Characterization of Sea Ice Surface Topography using Light Detection and Ranging (LiDAR)

by

Jack Christopher Landy

A thesis submitted to the Faculty of Graduate Studies of

The University of Manitoba

in partial fulfilment of the degree of

Doctor of Philosophy

Department of Environment and Geography

University of Manitoba

Winnipeg, Manitoba, Canada

Abstract

Where once the Arctic basin held predominantly old, thick perennial sea ice, it is now increasingly occupied by young, thin seasonal ice. The sea ice surface topography, which affects and is affected by many of the physical processes operating at the interface between ocean, sea ice and atmosphere, is closely related to the age and type of sea ice cover. In this thesis, new methods are presented for measuring and understanding sea ice topography using Light Detection and Ranging (LiDAR) technology.

A new technique is presented for parameterizing the micro-scale roughness of sea ice using terrestrial LiDAR. Field, laboratory and numerical experiments have been carried out to test the precision and accuracy of the technique, and calibrations have been developed for correcting field observations of surface roughness for known biases. Results obtained using this technique have been applied in several microwave remote sensing and electromagnetic-wave scattering model studies of snow-covered and melting sea ice.

Terrestrial and satellite LiDAR observations are acquired and combined in a further study to examine how sea ice surface topography regulates the melting of ice during the Arctic summer. Observations from a field program in the Canadian Arctic show that minor variations in the roughness of pre-melt sea ice topography can affect significant variations in the melt pond coverage at the ice surface in summer. Numerical simulations are used to develop a quantitative understanding of these findings and, when applied to satellite observations, explain most of the spatial variation in Arctic summer ice melting rates. Results suggest that a recent reduction in sea ice roughness, caused by progressive changes in the type of sea ice resident in the Arctic Ocean, has accelerated the summer melting and decline of the Arctic sea ice cover.

Acknowledgements

I have been lucky to receive the support of a great many people throughout the course of my Ph.D. studies. I am indebted to Megan Shields, Andrew Osipa, Jens Ehn, Aura Diaz, Sebastian Luque, Phillip Carew, Randy Scharien, Grant Gunn, Emme Wiley and Bruce Johnson, who each helped me to prepare for or collect data during fieldwork. In particular I am grateful to Megan Shields, who provided willing support above-and-beyond the call of duty during the intensive Arctic-ICE field campaign in 2012. I extend my thanks to all those who participated in the Arctic-ICE 2011 and 2012, and ICE-CAMPS 2014 field campaigns. Those long days in the field would have been far more challenging without the enthusiasm of a great bunch of people around me. To C.J. Mundy – a special thank you – your leadership, ideas and encouragement were vital in every one of these campaigns.

I have benefitted from stimulating scientific discussion with many colleagues, past and present, at the Centre for Earth Observation Science, including Dustin Isleifson, Alex Komarov, Brent Else, Dave Babb, Randy Scharien, Ryan Galley, David Landry, John Iacozza and Nari Firoozy. I have also received ideas and encouragement from my Ph.D. thesis advisory committee: Professor Lotfollah Shafai, Dr Lisa Loseto and Professor Jens Ehn, whenever needed. In particular, I want to thank Jens Ehn for extending me way too much of his time over the past four years: planning field sampling, analyzing data, brainstorming research ideas and editing manuscripts. You have been a source of inspiration throughout this process. To my supervisor, Professor David Barber, you have provided me with freedom, encouragement, your trust, and of course, a tremendous amount of funding, to pursue this research, and for that I am extremely grateful.

Financial support for this work came from a variety of sources, including: the Natural Sciences and Engineering Research Council of Canada, the ArcticNet Program of the Network of Centres of Excellence, the Polar Continental Shelf Program, and the Canada Foundation for Innovation, among others. This work is a contribution to the ArcticNet Program and to the Arctic Science Partnership. I personally received financial support from a University of Manitoba Graduate Fellowship, a V.E. Barber Memorial Fellowship, and from my supervisor David Barber. I received additional support for travel to and expenses at international scientific conferences from: the University of Manitoba Faculty of Graduate Studies Travel Award, the Graduate Student's Association Travel Award, the C.H. Riddell Endowment Fund, and the IGARSS Travel Award.

I arrived in Winnipeg in May 2011 to pursue my graduate studies without ever having visited Canada or knowing what to expect from the coming years. It is testament to the country and especially to the friends I have made here that Winnipeg now feels very much like home. I would like to thank the following people who have provided me with personal support during my time in Canada: Dave Babb, Julie Hauser, Paulo Guzzi, Geoff Gunn, Aurelie Delaforge, Matt Gale, Marc Cadieux, Jeremy Beller, Deland Wing, Megan Shields and Sarah Beattie, along with a great many others. I am grateful to Doug and Karen Campbell, who have taken me into their home, and the entire Campbell clan, who have treated me as part of the family ever since their daughter decided I was worth keeping around. To Karley Campbell, your determination and unwavering support have kept me going throughout my studies.

Finally, thank you to my parents for always believing in me and encouraging me to pursue adventure on the other side of the world, to my sister and brother for their affection, and to my friends back in England who would listen to me moan at all hours, in spite of the time difference.

Contents

List of Tables

List of Figures

List of Acronyms

AMSR-E	Advanced Microwave Scanning Radiometer – Earth Observing System
Arctic-ICE	Arctic Ice-Covered Ecosystems project
AVHRR	Advanced Very High Resolution Radiometer
BI	Bare ice
BRDF	Bi-directional reflectance distribution function
CAA	Canadian Arctic Archipelago
CLARA	Clouds Albedo and Radiation dataset
CSL	Constitutionally-supercooled layer
DFT	Discrete Fourier transform
EUMETSAT	European Organisation for the Exploitation of Meteorological Satellites
FF	Frost flowers
FFT	Fast-Fourier transform
FW	Full-width beam divergence
FWHH	Full-width at half-height beam divergence
FYI	First-year ice
GLA	Geoscience Laser Altimeter
GW	Gaussian-width beam divergence
HFOV	Horizontal field-of-view
ICE-CAMPS	Ice-Covered Ecosystems – Cambridge Bay Process Studies project
ICESat	Ice Clouds and Land Elevation Satellite
IEEE	Institute of Electrical and Electronics Engineers
LiDAR	Light Detection and Ranging
MODIS	Moderate-resolution Imaging Spectrometer
MYI	Multi-year ice
NCEP	National Centers for Environmental Prediction
NIR	Near infra-red
NSIDC	National Snow and Ice Data Center
OLSR	Orthogonal least-squares regression
OSA	Ocean-sea ice-atmosphere

PI	Pancake ice
PIOMAS	Pan-Arctic Ice Ocean Modelling and Assimilation System
RS	Refrozen slush
SAF	Network of Satellite Application Facilities
SI	Superimposed ice
TIN	Triangulated Irregular Network
VFOV	Vertical field-of-view
WMO	World Meteorological Organization

List of Notations

(n.b. List includes only notations used regularly throughout text)

ψ	Incidence angle
φ	Azimuth angle
σ	Root-mean square roughness height
λ	Wavelength
θ	Inclination angle
$\boldsymbol{\rho}$	Position vector in the horizontal plane
ε	Complex permittivity
δ	Laser beam divergence angle
γ	Overlap coefficient between adjacent laser beam profiles
ϕ	Solid ice fraction
α	Shortwave albedo
t	Time
n	Exponent of a generalized power-law spectrum
l	Correlation length
k	Fluid permeability
R	Laser range
N	Number of samples
L	Sampling extent (length of a profile or area of a surface)
D	Laser beam diameter
C	Correlation function
A	Area of site
Ω	Precision of laser ranging estimate
T	Shortwave transmittance
Δx	Sampling interval
Δx_{opt}	Optimum sampling interval
Δx_{max}	Critical maximum sampling interval
ΔV_{prod}	Volume of meltwater production per unit area
ΔV_{precip}	Volume of water added by precipitation per unit area
ΔV_{drain}	Volume of meltwater drainage per unit area

Δ	Angular sampling resolution
ϵ_l	Eccentricity of the correlation length
ψ_C	Inclination angle of sensor with respect to centre of rough surface
σ_{true}	True root-mean square height
σ_{obs}	Observed root-mean square height
σ_{mod}	Modelled root-mean square height
σ_{eff}	Effective root-mean square height
σ_{cal}	Calibrated root-mean square height
σ^0	Backscattering coefficient
ρ_w	Density of water
ρ_{si}	Density of sea ice
ρ_s	Snow density
ρ_i	Density of pure ice
α_{si}	Bare sea ice albedo
α_p	Pond-covered ice albedo
α_{ow}	Open water albedo
z_s	Snow surface level
z_{ref}	Reference level
z_p	Pond surface level
m_{total}	Total mass of snow, ice and meltwater
$m_{snow+ice}$	Mass of snow and ice
l_{true}	True correlation length
l_{obs}	Observed correlation length
l_{mod}	Modelled correlation length
l_{cal}	Calibrated correlation length
k_{si}	Thermal conductivity of sea ice
k_s	Thermal conductivity of snow
k_i	Thermal conductivity of pure ice
f_p	Melt pond fraction
f_c	Cutoff frequency
c_{si}	Specific heat of sea ice

c_i	Specific heat of pure ice
$V_{retained}$	Total volume of water retained per unit area at the sea ice surface
V_{lost}	Total volume of water lost per unit area from the sea ice surface
V_b	Brine volume fraction
V_a	Air volume fraction
T_{si}	Temperature of sea ice
T_s	Surface temperature
S_w	Salinity of water
S_{si}	Salinity of sea ice
R_C	Laser range to centre of rough surface
Q_l	Lateral heat flux at melt pond wall
Q^*	Net energy
L_u	Upwelling longwave radiation
L_{si}	Latent heat of fusion of sea ice
L_{min}	Critical minimum sampling extent
L_d	Downwelling longwave radiation
L^*	Net longwave radiation
F_u	Upwelling shortwave radiation
F_d	Downwelling shortwave radiation
F^*	Net shortwave radiation
D_f	Laser footprint diameter on target surface
$D_{f_{along}}$	Laser footprint diameter along the beam track
$D_{f_{across}}$	Laser footprint diameter across the beam track
C_{si}	Sea ice concentration
h_{si}	Snow-covered or bare sea ice thickness
h_s	Snow thickness
h_{pi}	Ponded-ice thickness
h_{pi}	Pond-covered sea ice thickness
h_p	Pond depth
h_{net}	Volume of meltwater per unit area in melt ponds
h_i	Bare-ice thickness

Use of Copyrighted Material

Chapter 3 of this thesis is reproduced with minor modifications from Landy et al. [2015, Parameterization of centimeter-scale sea ice surface roughness using terrestrial LiDAR, *IEEE Trans. Geosci. Rem Sens.*, 53(3), 1271-1286, doi.org/10.1109/TGRS.2014.2336833], with permission from the Institute of Electrical and Electronics Engineers.

Chapter 4 of this thesis is reproduced with minor modifications from Landy et al. [2015, Numerical and experimental evaluation of terrestrial LiDAR for parameterizing centimeter-scale sea ice surface roughness, *IEEE Trans. Geosci. Rem Sens.*, 53(9), 4887-4898, doi.org/10.1109/TGRS.2015.2412034], with permission from the Institute of Electrical and Electronics Engineers.

Chapter 5 of this thesis is reproduced with minor modifications from Landy et al. [2014, Surface and melt pond evolution on landfast first-year sea ice in the Canadian Arctic Archipelago, *J. Geophys. Res.*, 119, 3054–3075, doi.org/10.1002/2013JC009617], with permission from the American Geophysical Union.

Chapter 6 of this thesis is reproduced with minor modifications from Landy et al. [2015, Albedo feedback enhanced by smoother Arctic sea ice, submitted to *Geophysical Research Letters.*

Chapter 1. Introduction

1.1. Motivation

It is apparent that climate change will have, and may already be having, a measurable effect on the Arctic marine system. Not only is the geographic distribution of sea ice decreasing [Comiso, 2015], but evidence also suggests that with increasing annual proportions of seasonal rather than perennial ice [Maslanik et al., 2011; Stroeve et al., 2012], Arctic sea ice is thinning [Kwok and Rothrock, 2009]. As the extent, thickness and age of sea ice in the Arctic continues to change, the sea ice surface topography will also experience change. The surface topography is an important parameter affecting many geophysical sea ice processes; in particular, interactions between the sea ice and the atmosphere. It is therefore vitally important to accurately measure and understand changes in surface topography.

Conventional techniques for measuring the topography of natural surfaces, both *in situ* and from an airborne or satellite vantage point, are typically one-dimensional. However, the fundamental assumption of all these techniques, that one-dimensional measurements adequately represent the two-dimensional properties of a surface, is inherently limited. Measurements of surface topography from one-dimensional profiles are rarely stationary (i.e. samples are translationally variant), and cannot provide information on the directional properties (anisotropy) of a surface [Verhoest et al., 2008]. Moreover, the profiles obtained from conventional techniques often have a restricted sampling interval and extent, which can make the topography of a natural surface appear artificially fractal [Callens et al., 2006; Rees and Arnold, 2006].

Laser scanning, also referred to as Light Detection and Ranging (LiDAR), has become the preeminent method for acquiring three-dimensional geospatial data over the past few decades, and offers several improvements on the conventional techniques. Modern LiDAR instruments can be mounted terrestrially, or on an airborne or satellite platform, and are capable of providing tens to hundreds of thousands of measurements of the two-dimensional topography of a target every second. LiDAR can eliminate many of the geostatistical issues associated with conventional one-dimensional profiling techniques. However, the technology has been utilized only a handful of times in studies related to sea ice. State-of-the-art LiDAR instruments are expensive and, particularly with airborne systems which require auxiliary equipment, are bulky and challenging to use in harsh environmental conditions, such as the cold temperatures and exposure of the Arctic. In spite of these challenges, LiDAR technology is rapidly improving and, in future, instruments will become increasingly portable and cost-effective. A significant effort is therefore required to develop LiDAR technology as a practical and effective tool in the field of sea ice research. This will include developing methods for using LiDAR on sea ice, identifying the limitations of the technology, and applying LiDAR data for understanding geophysical sea ice processes.

This Ph.D. thesis includes a compilation of original research that is directed towards each of these goals. New methods are presented for using LiDAR technology and applying LiDAR data, over a wide range of spatial scales, for understanding various dynamic and thermodynamic processes operating at the OSA interface.

1.2. Thesis Objectives

The underlying goal of this thesis is to develop new methods for measuring and understanding sea ice surface topography, from spatial scales of millimeters to kilometers, using LiDAR. There are two separate parts to the thesis. In Part 1, terrestrial LiDAR is developed as a tool for parameterizing the two-dimensional centimeter-scale roughness of a multi-scale sea ice surface, in support of microwave remote sensing applications. In Part 2, terrestrial and satellite LiDAR are combined and applied to examine how meter- to kilometer-scale topography regulates sea ice melt during the Arctic summer. Each of these parts includes a set of research objectives, which are listed below.

Research Objectives – Part 1

1.1. Develop a method for deriving two-dimensional roughness parameters from three-dimensional terrestrial LiDAR data collected over a complex multi-scale natural sea ice surface

1.2. Compare the precision of the LiDAR method with conventional one-dimensional profile-based methods for deriving surface roughness parameters

1.3. Develop and validate a numerical model for simulating the LiDAR sampling process over a regular rough surface

1.4. Evaluate how the accuracy of *in situ* LiDAR observations depends on the sampling parameters of the LiDAR sensor and the intrinsic properties of a rough surface

1.5. Develop a set of calibration functions that can be used to correct *in situ* LiDAR observations for sampling bias

Research Objectives – Part 2

2.1. Monitor the surface topography, mass balance and physical properties of first-year sea ice during the spring-summer melt season using terrestrial LiDAR

2.2. Identify which physical mechanisms control spatial and temporal variations in melt pond coverage on landfast first-year sea ice

2.3. Develop and validate a numerical model to simulate the distribution of melt ponds on statistically-derived surface topographies

2.4. Examine whether winter (pre-melt) observations of Arctic sea ice surface topography, from satellite LiDAR, can be used to forecast the melt pond coverage in summer

2.5. Evaluate the implications of the observed transition from a multi-year to first-year ice dominated Arctic Ocean for changing sea ice surface topography and melt rates

1.3. Thesis Outline

This thesis includes seven chapters. In Chapter 2, we introduce background on: (i) the physical processes which give rise to the surface topography of snow-covered Arctic sea ice, across a range of space and time scales, (ii) the role of sea ice topography in microwave remote sensing, and (iii) Light Detection and Ranging technology. Chapters 3, 4 and 5 contain three separate original full-length research papers, each of which has been published in a peer-review journal. Chapter 6 contains an original full-length research letter, which is currently under review in a peer-review journal. Finally, in Chapter 7, we summarize our findings and offer recommendations for future work.

In the first research paper (Chapter 3), we describe a new method for parameterizing the centimeter-scale roughness of sea ice using terrestrial LiDAR and compare the new method with conventional techniques for measuring roughness. This work addresses objectives 1.1 and 1.2, and it has been peer-reviewed and published in *IEEE Transactions on Geoscience and Remote Sensing*:

> "**Landy, J.C.**, D. Isleifson, A.S. Komarov, and D.G. Barber (2015), Parameterization of centimeter-scale sea ice surface roughness using terrestrial LiDAR, *IEEE Trans. Geosci. Rem Sens.*, 53(3), 1271-1286, doi.org/10.1109/TGRS.2014.2336833."

In the second research paper (Chapter 4), we evaluate the accuracy of the LiDAR method for parameterizing sea ice surface roughness, using numerical modelling and laboratory experiments, and propose a set of calibration functions for correcting *in situ* LiDAR roughness observations for sampling bias. This work addresses objectives 1.3, 1.4 and 1.5, and it has been peer-reviewed and published in *IEEE Transactions on Geoscience and Remote Sensing*:

> "**Landy, J.C.**, A.S. Komarov, and D.G. Barber (2015), Numerical and experimental evaluation of terrestrial LiDAR for parameterizing centimeter-scale sea ice surface roughness, *IEEE Trans. Geosci. Rem Sens.*, 53(9), 4887-4898, doi.org/10.1109/TGRS.2015.2412034."

In the third research paper (Chapter 5), we describe a comprehensive field study to examine the physical mechanisms driving the formation and evolution of melt ponds on landfast first-year sea ice in the Canadian Arctic. This work addresses objectives 2.1 and 2.2, and it has been peer-reviewed and published in the *Journal of Geophysical Research – Oceans*:

> "**Landy, J.C.**, J.K. Ehn, M. Shields, and D.G. Barber (2014), Surface and melt pond evolution on landfast first-year sea ice in the Canadian Arctic Archipelago, *J. Geophys. Res.*, 119, 3054–3075, doi.org/10.1002/2013JC009617."

In the research letter (Chapter 6), we consider the influence of the roughness of winter sea ice surface topography on the spatial coverage of melt ponds in summer, through numerical modelling and using satellite observations, and examine whether recent changes in the roughness of the Arctic sea ice cover have accelerated the rate of summer ice melt. This work addresses objectives 2.3, 2.4 and 2.5, and it is currently under review in *Geophysical Research Letters:*

> "**Landy, J.C.**, J.K. Ehn, and D.G. Barber (2015), Albedo feedback enhanced by smoother Arctic sea ice, *Geophys. Res. Lett.*., In Review"

Chapter 2. Background

In this chapter we evaluate the critical role of sea ice surface topography in the Arctic marine system. In Section 2.1, we outline the characteristic scales of sea ice topography and describe the statistical properties of a random rough surface. In Section 2.2, we summarize the physical processes which give rise to sea ice topography through a range of spatial and temporal scales. This section covers the formation of sea ice, the internal properties of the ice cover, and the sea ice energy budget, in addition to the dynamic and thermodynamic processes controlling snow cover and melt pond evolution, and the dynamic processes leading to sea ice deformation. We explain how the sea ice internal and surface properties and processes combine to produce the sea ice thickness distribution, which is a proxy for the ice surface topography. In Section 2.3, we discuss the influence of surface topography on the microwave remote sensing of sea ice. Finally, in Section 2.4, we assess the existing techniques for measuring and understanding sea ice topography, and discuss the potential for LiDAR technology as an alternative.

The material in this chapter is largely derived from the author's Ph.D. Candidacy Exam paper, which was written in October 2014 in response to the following question:

> "Describe the physical processes giving rise to surface topography of snow covered sea ice through a full range of space and time scales. Assess the ability of terrestrial LiDAR to measure the topographic state of snow covered sea ice and explain how this helps us understand various dynamic and thermodynamic processes of snow covered sea ice."

2.1. Characterization of Sea Ice Surface Topography

2.1.1. Relevant Length Scales of Sea Ice Surface Topography

Throughout this thesis we refer to sea ice topography at a range of spatial scales. For simplicity, these scales are separated into three classes: micro-, meso- and macro-scale topography, based on the definitions of the World Meteorological Organization [2010]. Micro-scale topography (<0.1 m) describes the smallest deviations (roughness) of a sea ice surface, including bare ice, snow grains and frost flowers. Meso-scale topography (0.1-100 m) describes larger undulations and features of the sea ice surface, including snow drifts, deformed ice and melt ponds. Macro-scale topography (>100 m) describes sea ice floes and floe distributions. In spite of this classification, often, in reality, these scales cannot easily be separated.

2.1.2. Statistical Properties of a Random Rough Surface

The topography of a natural surface can be characterized by its statistical properties, including the parameters: root-mean square (rms) roughness height σ and correlation length l (Figure 2.1). For a two-dimensional random rough surface, $\zeta(\boldsymbol{\rho})$, with zero average $\langle\zeta(\boldsymbol{\rho})\rangle = 0$, where $\boldsymbol{\rho} = \{x, y\}$ is a position vector in the horizontal plane [Tsang et al., 2000]:

$$\sigma^2 = \langle\zeta^2(\boldsymbol{\rho})\rangle. \tag{2.1}$$

For a stationary random process, the normalized autocorrelation function, which defines the cross-correlation of a surface with itself as a function of displacement in the horizontal plane, is given by:

$$C(\boldsymbol{\rho}) = \frac{\langle \zeta(\boldsymbol{\rho} + \boldsymbol{\rho}')\, \zeta(\boldsymbol{\rho}') \rangle}{\langle \zeta^2(\boldsymbol{\rho}) \rangle}, \tag{2.2}$$

where $\boldsymbol{\rho}'$ is the shift vector in the horizontal plane. The correlation length is then a function defining the lag, l, with respect to the azimuth angle, φ, for which:

$$C(l(\varphi)\cos\varphi\,, l\,(\varphi)\sin\varphi) = e^{-1}. \tag{2.3}$$

The correlation length describes the maximum displacement between two interdependent samples of the same surface. The topography of a natural surface can generally be characterized using either the exponential or the Gaussian autocorrelation function [Fung and Chen, 2010] (equation 2.4). If l is independent of φ, i.e. the surface is isotropic, a generalized correlation function is [Fung and Chen, 2010]:

$$C(\boldsymbol{\rho}) = exp\left[-\left(\frac{\boldsymbol{\rho}}{l}\right)^{n}\right], \tag{2.4}$$

where $1 < n < 2$. Equation 2.4 converges to the exponential or the Gaussian function as n approaches 1 or 2, respectively. Sea ice surface topography can conform to either function [Drinkwater, 1989], but most often conforms to the exponential [Manninen, 1997].

In practice, the statistical parameters σ, l and C are calculated using discretized versions of equations 2.1-2.3, which depend on the sampling interval Δx and the sampling extent L. Numerical studies have shown that Δx must be at least $0.1l$ to differentiate between exponential and Gaussian C [Ogilvy and Foster, 1989], and that Δx must be at least $0.2l$ to accurately calculate l [Oh and Kay, 1998]. The minimum sampling extent should be at least

$40l$ and $200l$ for the determination of σ and l with an error <10%, respectively [Oh and Kay, 1998]. If L does not fulfill either of these criteria, σ and/or l can be severely underestimated because the measured sample cannot be assumed to be stationary [Verhoest et al., 2008].

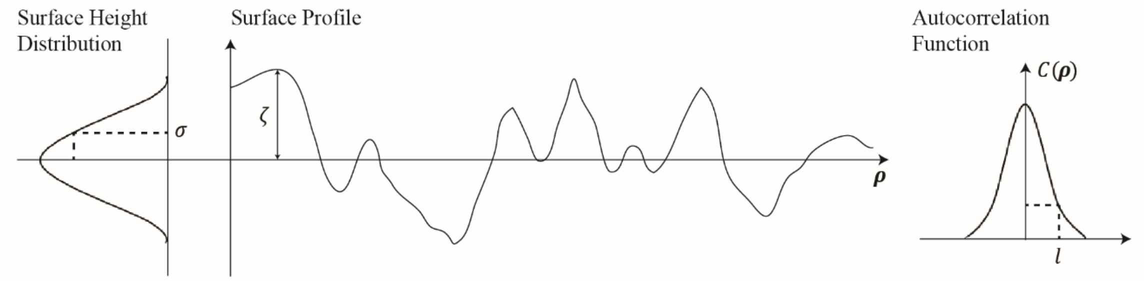

Figure 2.1 | Schematic diagram of a rough surface profile and its relevant statistical parameters.

2.2. Physical Processes Affecting and Affected by Sea Ice Topography

2.2.1. Sea Ice Formation, Growth and Physical Properties

2.2.1.1. Sea Ice Formation

The freezing temperature of seawater is a function of the salinity and density. At the sea surface, where the ocean pressure is zero, the freezing temperature can be calculated from: $T_f = -0.05S$, where the salinity S is in practical salinity units (psu). In autumn, sub-zero atmospheric temperatures cool the surface of the Arctic Ocean, leading to convective overturning as warmer sub-surface water replaces colder surface water. Only when the temperature of the entire ocean surface layer (i.e., above the pycnocline) cools to -1.8 °C does ice begin to form at the ocean-atmosphere interface [Wadhams, 2000].

The oxygen atoms of a pure ice crystal are arranged in the structure of a hexagonal prism [Weeks, 1998]. This anisotropic structure allows water molecules to be added more easily onto the crystal's basal plane (along crystallographic a and b axes) than perpendicular to the basal plane, onto the crystal's principal c-axis. The growth rate of the crystal is therefore asymmetrically large along the basal plane, which helps to explain the geometrical structure of newly-forming sea ice. Frazil ice is the earliest form of sea ice and begins to grow when the sea surface temperature drops to the freezing point. Frazil crystals grow laterally across the ocean surface (i.e., along a and b axes), with their c-axis oriented vertically, in a dendritic pattern which eventually becomes unstable at a crystal diameter >2-3 mm [Wadhams, 2000]. Above this size the arms of a crystal break apart leaving a thin suspension of randomly shaped and oriented ice crystals.

The fate of this frazil suspension depends on turbulence at the ocean surface. In calm conditions, the density of the frazil layer gradually increases until voids between individual crystals freeze up and the crystals aggregate into a slushy layer of grease ice with a highly saline surface. As the thickness of this layer increases, it eventually consolidates into a solid but elastic sheet of ice, termed nilas [WMO, 2010]. Further classes of newly-forming sea ice are defined by their thickness. For example, dark nilas, light nilas, grey ice and grey-white ice for thicknesses of <5, 5-10, 10-15 and 15-30 cm, respectively [WMO, 2010].

So called frost flowers (ice crystals with a fragile dendritic structure) can also form at the surface of young sea ice in calm conditions, when atmospheric temperatures and the near-surface wind speed are low. These crystals grow from local roughness discontinuities on the ice surface as air in the surface viscous layer, directly above the ice, becomes supersaturated [Style and Worster, 2009]. Isleifson et al. [2014] identified four distinct stages of frost flower formation. During Stage I, the thermo-molecular pressure gradient across the newly-forming ice cover drives brine transport, and a significant portion of the brine is expelled at the ice surface. During Stages II and III the brine is wicked up into the frost flowers by capillary suction, yielding salinities up to 120 psu [Douglas et al., 2012]. Frost flowers have been observed to grow up to a maximum height of approximately 3 cm [Douglas et al., 2012]. During the final stage (IV) the flowers are decimated as the ocean-atmosphere temperature gradient decreases sufficiently, or by strong winds. Observations have shown that the roughness height σ and correlation length l can change significantly, from 1 to 3 mm and 5 to 15 mm, respectively, as the frost flowers evolve [Landy et al., 2015a]. Frost flowers change the properties of sea ice significantly, insulating the ice by several degrees Celsius [Martin et al., 1996] and enhancing radar backscatter [Isleifson et al., 2014].

Turbulent conditions, characteristic of the Southern Ocean, can maintain a much higher density suspension of frazil ice and also broken grease ice and nilas. As this suspension undergoes cyclic compression and decompression, ice crystals aggregate into decimeter-scale pans which then collide and deform. Collisions raise frazil crystals onto the edges of pans, giving them the appearance of pancakes [Martin and Kauffman, 1981]. Individual pancakes can reach a diameter of 3-5 m and thickness of 0.5-0.7 m [Wadhams, 2000], but eventually consolidate into solid ice floes which are characterized by rough surface and bottom topography [e.g., Wadhams et al., 1987].

2.2.1.2. Supercooling and Congelation Ice Growth

Individual ice crystals at the base of consolidated nilas or pancake ice that are in contact with the ice-water interface grow as water molecules freeze onto crystal faces. The freezing process is easier for crystals with c-axis aligned horizontally, so these crystals grow at the expense of others before all crystals are oriented vertically below ~20 cm depth from the ice surface [Weeks and Wettlaufer, 1996]. The major ionic impurities (salts) in seawater are prevented from entering the crystal structure of pure ice and 60-90% of the total volume of salts is rejected from the crystal lattice as the ice grows [Petrich and Eicken, 2010]. The remaining 10-40% (depending on the ice growth rate) are entrained as brine or solid salt inclusions within the ice matrix.

Salt rejection creates a layer of seawater with enhanced salinity directly below the ice-water interface and consequently reduces the freezing/melting point at the ice bottom. The flux of salt from the ice to the ocean is sufficiently low to promote the formation of a strong, non-linear freezing temperature profile. A mm- to cm-thick layer of water at the interface is then cooled below the freezing point of ocean water, but is only slightly enriched in salinity (Figure 2.2) [Petrich and Eicken, 2010]. Ice crystals which protrude into this constitutionally supercooled layer (CSL) experience preferential growth with respect to adjacent crystals, so form ordered patterns of lamellar bulges at the ice bottom. The horizontal solid fraction (ϕ_h) of a lamellae section is between 0 and ~0.9 in the so-called skeletal layer. As the ice grows downward the lamellae become fully interlinked (when ϕ_h > ~0.9, illustrated by the horizontal dashed line in Figure 2.2), in the process of congelation (columnar) ice formation.

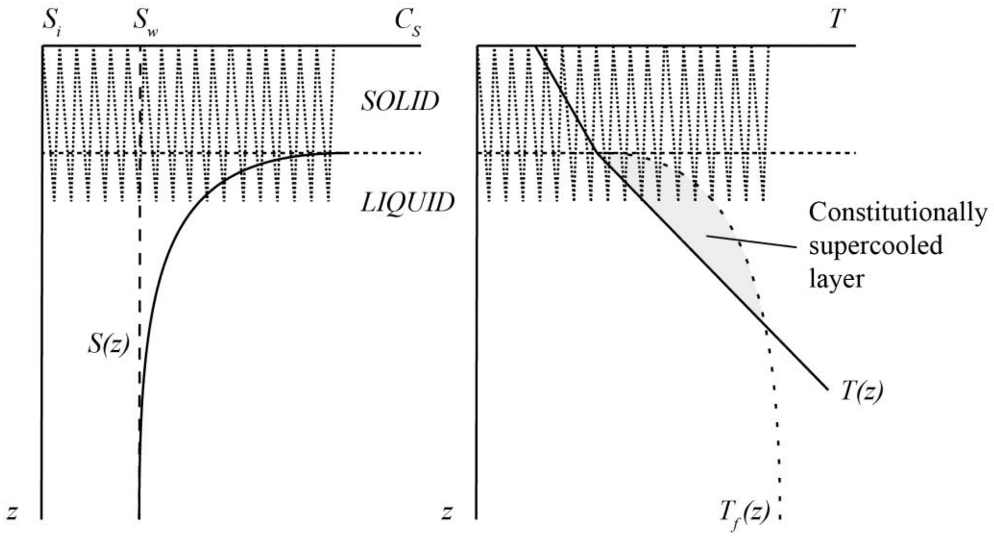

Figure 2.2 | Schematic diagram of the salinity (left) and temperature (right) profiles at the lamellar ice-water interface. The freezing temperature profile is given by the dashed line (right). After Petrich and Eicken [2010].

Fully formed sea ice comprises distinct layers which characterize the growth history of the ice cover. Granular ice zones are typically (but not only) found in the uppermost portion of the ice cover and characterize the formation of consolidated frazil ice into nilas or pancake ice. Granular ice can also be found within the central portion of the ice cover if the base of the ice becomes separated from the ocean by a low-salinity layer of freshwater during growth. Frazil/platelet ice can form in the freshwater layer and then be entrained within the congelation ice [Weeks, 1998]; however, this generally only occurs during the spring and summer when the ice is melting [Notz et al., 2003]. Congelation ice zones, characterizing the process described above, are found towards the base of the sea ice cover. Finally, transition zones with ice crystals that are increasingly aligned vertically with depth are found between granular and congelation ice zones.

Once fully formed, sea ice is commonly separated into one of two age classes: first-year ice (FYI), which is less than one year old, or multi-year ice (MYI), which has survived at least one melt cycle and is therefore greater than one year old.

2.2.1.3. Inclusions in Sea Ice

As the ice-water interface advances upwards during congelation ice growth, small bridges of ice periodically develop between lamellae when ϕ_h > ~0.9, trapping vertically aligned, parallel grids of inclusions within the sea ice matrix [Light et al., 2004]. These inclusions typically contain concentrated brine from the CSL. However, they can also contain bubbles of gas or solid salts. Bubbles can be entrained during congelation ice growth as well as or instead of brine, when gas that is dissolved in seawater comes out of solution. Alternatively, bubbles of air can fill voids that are left as brine drains from ice above freeboard during summer [Light et al., 2003]. Solid salts are only present if the temperature of brine within an inclusion drops sufficiently for salt crystals to precipitate out of solution. Assur [1958] examined the temperature-phase relations of various salts in standard seawater and demonstrated that ikaite (hydrous calcium carbonate), mirabilite (hydrous sodium sulphate) and hydrohalite (hydrous sodium chloride) crystals form at temperatures of -2.2, -8.2 and -22.9 °C, respectively. Other salts which precipitate at temperatures <-35 °C are rarely present in natural sea ice.

The fractional volume of brine, gas and/or solid salt in an inclusion and also the size and shape of an inclusion are determined by its temperature. As the temperature of an inclusion falls, pure water is removed from brine to freeze onto the surrounding ice and the inclusion either contracts in size or splits into multiple smaller spherical inclusions [Cole and

Shapiro, 1998; Light et al., 2003]. In contrast, as the temperature of an inclusion rises, the surrounding ice melts and the inclusion expands and can merge with other proximal inclusions to form elongated brine conduits [Perovich and Gow, 1996]. As the size and temperature of an inclusion decreases, the brine concentration increases, and vice versa, to maintain thermal equilibrium. Laboratory studies of brine inclusion populations in FYI have shown that mean inclusion length and aspect (major to minor axis) ratio γ increase non-linearly with temperature [Eicken et al., 2000]. Additionally, γ increases and the number-density of inclusions decreases non-linearly as a function of inclusion length [Light et al., 2003]. The length of a brine inclusion is characteristically between 0.01 and 10 mm [Light et al., 2003].

Brine can migrate within sea ice by several mechanisms:

(1) During winter, atmospheric temperatures in the Arctic are typically between 10 and 50 °C lower than upper ocean temperatures, so a strong vertical temperature gradient can develop through the ice cover. As this gradient acts across an individual inclusion, the inclusion experiences freezing at its upper surface, melting at its base and consequently migrates along the gradient [Wadhams, 2000].

(2) As the ice contracts around an inclusion at decreasing temperatures, pressure is exerted on the brine, which can then be expelled through microscopic cracks in the inclusion wall to nearby inclusions or to the ice surface or base [Notz and Worster, 2009].

(3) Pressure is also exerted on an inclusion if it is raised above sea level (i.e., it gains hydraulic head) as the ice thickens, driving gravitational drainage of brine downwards when inclusions become interconnected. This flow causes a density gradient to

develop within the ice, inducing cyclical convection of brine as buoyant forces act to replace brine that is dissipated at the base of the ice cover [Notz and Worster, 2009].

(4) As snow is deposited at the surface of the ice cover, brine can be raised up into the snowpack by capillary suction (wicking). Surface tension can drive a flow of brine through the interstitial voids between snow grains [Massom et al., 2001].

(5) During summer, meltwater from the ice surface can percolate down through connected brine channels, 'flushing' brine in its path towards the base of the ice cover [Vancoppenolle et al., 2007].

The rate of brine migration within sea ice depends on the level of connectivity between inclusions. Observations of FYI microstructure demonstrate that inclusions can become fully interconnected to form dendritic networks of brine channels [e.g., Cole and Shapiro, 1998]. These networks resemble vertically-oriented rivers, attended to by smaller tributary channels at angles generally <35 degrees to the vertical, which periodically eject brine from the base of the ice cover [Niedrauer and Martin, 1979]. Functional brine channels are typically found in the lowest portion of the ice cover [Cole and Shapiro, 1998], where the temperature is highest. Golden et al. [2007] were able to relate the vertical fluid permeability k of columnar sea ice (i.e., the connectedness of the brine network) to the sea ice solid fraction ϕ, by applying percolation theory to field measurements of k [Freitag, 1999]:

$$k = 3(1-\phi)^3 \cdot 10^{-10}\ \mathrm{m}^2,\ \phi > 0 \tag{2.5}$$

By assuming $(1-\phi)$ was equivalent to the brine volume fraction V_b, they used this relationship to support a 'law of fives', as originally suggested by Golden et al. [1998].

Columnar sea ice becomes permeable to gravitational brine transport when k ~ 2.4-2.6 x 10^{-10} m^2, which is, according to equation 2.5, approximately when V_b > 5%. This occurs if the temperature of sea ice with a bulk salinity of 5 ‰ (parts per thousand) rises above approximately -5 °C. A recent study has demonstrated that gravity drainage is initiated as V_b exceeds 5% with rising ice temperatures and is terminated as bulk ice desalination (through flushing) stabilizes the brine density profile [Carnat et al., 2013].

The salinity profiles of FYI and MYI reflect these processes of brine inclusion, migration and rejection. FYI has a C-shaped profile during winter, with a saline upper portion caused by high V_b in the granular ice layer, a lower salinity central portion caused by brine migration upwards and downwards and brine rejection during congelation ice growth, and a saline lower 20-40 cm portion caused by brine drainage to the base of the ice cover [Vancoppenolle et al., 2007]. The bulk salinity of the ice cover decreases as the thickness of the ice and of the lower salinity central portion increase, and also as meltwater flushes the ice in summer. MYI has a different profile to FYI as it has experienced melt at least once. The upper 50 cm section is almost fresh due to flushing and the salinity then increases steadily down to the base of the ice cover [Eicken et al., 1995].

2.2.1.4. Temperature and Salinity as State Variables

The thermal, structural, electrical and mechanical properties of sea ice are all governed by the relative fractions of salt and water in solid, liquid and gaseous phase within the ice [Hallikainen and Winebrenner, 1992; Wadhams, 2000; Feltham, 2008]. Cox and Weeks [1983] developed a set of continuity equations to calculate the fractional volumes of brine V_b and air V_a within sea ice as a function of two state variables: temperature T_{si} [°C] and salinity S_{si} [‰], based on the phase relations of Assur [1958]. Under the assumption that the total volume of sea ice V is isothermal, in thermodynamic equilibrium and contains a standard salt composition, V_b can be calculated as:

$$\frac{V_b}{V} = \frac{\rho_{si} S_{si}}{F_1(T_{si})}, \tag{2.6}$$

where ρ_{si} is the density of sea ice [Mg m^{-3}]. V_a can then be calculated as:

$$\frac{V_a}{V} = \frac{1 - \rho_{si}}{\rho_i + V_b F_2(T_{si})}, \tag{2.7}$$

where the density of pure ice $\rho_i = 917 - 0.14 T_{si}$ [kg m^{-3}]. F_1 and F_2 are empirically-derived polynomial functions from Cox and Weeks [1983] and Leppäranta and Manninen [1988] that vary for the temperature intervals: $0 > T_{si} \geq -2$, $-2 > T_{si} \geq -22.9$, and $-22.9 > T_{si} \geq -30$ °C. The boundaries between these intervals relate to the precipitation of ikaite and hydrohalite from brine, as described above. Although these equations offer a simple solution for estimating the phase relationships in sea ice, they are limited by the original assumptions. For instance, the ice is not always in thermodynamic equilibrium and does not always contain a constant chemical composition, especially at microscopic scales [Petrich and Eicken, 2010].

2.2.2. Sea Ice Energy Budget and Thermal Properties

Energy exchanges between the atmosphere, sea ice and ocean are primarily controlled by radiative, turbulent and conductive heat fluxes. The energy balance at the sea ice surface can be expressed as:

$$F_d - F_u + L_d - L_u + Q_H + Q_E + Q_C + Q_P = 0, \qquad (2.8)$$

where F is shortwave (wavelength, λ = 0.3-3 μm) and L longwave (λ > 3 μm) radiation, with subscripts d and u symbolizing downwelling and upwelling components, respectively, Q_H is the sensible heat flux, Q_E is the latent heat flux, Q_C is the conductive heat flux, and Q_P is the heat conducted by precipitation. The net energy balance is zero because the surface is massless and therefore cannot store energy [Oke, 1987].

2.2.2.1. Shortwave Flux

Shortwave radiation can be absorbed or scattered as it passes through and between the media contained within the sea ice cover: snow, pure ice, brine, gas, solid salt, water and organic material (e.g., algae). The degree of scattering and/or absorption in a volume depends on the composition of the volume and the size of scattering particles. For instance, brine and gas inclusions within sea ice are larger in diameter than the wavelength of sunlight, so cause Mie scattering [Light et al., 2004]. Algae cells at the base of the ice cover contain pigments with absorption peaks in the photosynthetically active radiation (PAR: 400-700 nm) region, and therefore absorb sunlight [Ehn et al., 2008].

The net shortwave flux F^* is a balance of downwelling and upwelling shortwave radiation. F_d is controlled by the solar azimuth and zenith angles relative to the horizon, with a maximum at local solar noon, and therefore varies on both annual and diurnal time-scales [Oke, 1987]. F_u depends on the fraction of incident radiation reflected by the sea ice. The fraction of the incident downwelling shortwave irradiance (solar radiance integrated over downward directions) that is reflected by the sea ice at wavelength λ is given by the spectral albedo [Perovich, 1996]:

$$\alpha(\lambda) = \frac{F_u(\lambda)}{F_d(\lambda)}. \tag{2.9}$$

The broadband albedo α is the albedo integrated over the wavelength range 0.3 to 3 μm. The value of α and the shape of the function $\alpha(\lambda)$ are both controlled by the sea ice surface and internal properties. As sea ice grows α increases from ~0.05 to 0.50 until the ice reaches a threshold thickness of approximately 0.8 m [Perovich, 1996]. α is unaffected as the ice grows beyond this thickness. As the ice grows the difference between α at short and long λ is also enhanced because green or blue (shorter) wavelengths are less easily absorbed by the sea ice than infra-red (longer) wavelengths [Perovich, 1996]. If snow falls on sea ice, shortwave radiation is effectively scattered by the snow grains causing $\alpha(\lambda)$ to increase at all wavelengths and α can rise above 0.9. Conversely, the evolution from snow-covered to melt pond-covered sea ice in the Arctic summer is accompanied by a decrease in area-averaged α to less than 0.5, as described in Section 2.2.4 [Perovich et al., 2002]. Visible radiation, especially at green or blue wavelengths, is transmitted very easily though surface water into the sea ice cover and ocean [Maykut and Grenfell, 1975].

The fraction of incident downwelling shortwave irradiance which is transmitted through the sea ice cover at wavelength λ to depth z is given by the spectral transmittance:

$$\mathrm{T}(z,\lambda) = \frac{F_d(z,\lambda)}{F_d(0,\lambda)} = F_d(0,\lambda)\exp\left(-\int_0^z \kappa\,dz\right). \tag{2.10}$$

The right-hand side of equation 2.10 is the Beer-Lambert law which parameterizes the attenuation of light (scattering and absorption) within the sea ice cover using a simple spectral extinction coefficient $\kappa(z, \lambda)$. The value of κ is orders of magnitude larger at 1400 nm (near infra-red) than 500 nm (green) [Perovich, 1996], which explains why green light is attenuated less easily by the sea ice cover and ocean. The broadband transmittance $\mathrm{T}(z)$ is the transmittance integrated over the wavelength range 0.3 to 3 μm. Although typically only visible light in the wavelength range 300-700 nm, coinciding with the PAR region, is transmitted through sea ice. All other wavelengths are easily scattered at the surface or by inclusions in the ice, or are absorbed within the sea ice cover [Perovich, 1996].

During the Surface Heat Budget of the Arctic Ocean (SHEBA) experiment K^* was close to zero from October through to February, before rising and falling from March through to September, with a daily average peak of approximately 120 W m^{-2} in early July [Persson et al., 2002]. This pattern followed the seasonal evolution of both F_d and sea ice α closely. Day-to-day fluctuations in F^* were based on fluctuations in F_d that were primarily caused by changes in cloud cover. A persistent thick cloud cover can reduce F_d by up to 90%, while increasing the proportion of diffuse rather than direct shortwave radiation reaching the sea ice, and preferentially absorbing wavelengths larger than 1400 nm [Grenfell and Perovich, 1984].

2.2.2.2. Longwave Flux

The net longwave flux L^* is a balance of downwelling and upwelling longwave radiation. L_d depends on atmospheric temperature and water vapour profiles, and is enhanced by cloud cover because L_u can be absorbed and re-emitted by clouds back to the sea ice surface [Oke, 1987]. L_u emitted from the sea ice depends on the surface temperature T_s and the emissivity ε of the ice (which is typically close to 1), according to the Stefan-Boltzmann law $L_u = \varepsilon\sigma_{SB}T_s^4$ (σ_{SB} = 5.67x10^{-8} W m^{-2} K^{-4}).

During the SHEBA experiment, minimum L^* (-70 W m^{-2}) occurred in early summer under a clear sky, when the ice surface temperature was high. In contrast, maximum L^* (~0 W m^{-2}) occurred during the melt season under persistent low-level clouds, when air temperatures were >0 °C and the surface temperature was fixed at 0 °C [Persson et al., 2002]. Ehn et al. [2006] and Else et al. [2014], among others, have shown that large values of downwelling longwave during persistent cloud cover, which delivers considerable energy to the snowpack, is the mechanism which characteristically triggers the onset of melt in spring.

2.2.2.3. Turbulent Fluxes

The sensible heat flux Q_H describes the transfer of energy by conduction and convection. The latent heat flux Q_E describes the transfer of energy through phase changes. Q_H and Q_E depend on turbulence in the atmospheric boundary layer, which affects and is affected by the sea ice surface topography. These fluxes can be related to the surface topography through the concept of aerodynamic roughness.

The aerodynamic roughness length z_0 is defined as the height above a surface at which the horizontal wind-speed profile extrapolates to zero [Oke, 1987]. Above z_0 air flow is turbulent and the transfer of momentum and heat through the boundary layer is controlled by the size of turbulent eddies. In general, a rougher surface produces larger eddies than a smoother surface, and the mean eddy diameter, along with the fluxes of heat and momentum, increase with height from z_0 [Andreas, 1987]. Lettau [1969] developed a simple empirical relationship between z_0 and the geometry of surface topography:

$$z_0 = 0.5h_{max}^{*}\left(\frac{s}{S}\right), \tag{2.11}$$

where h_{max}^{*} is the average maximum vertical extent, or effective obstacle height, of the surface roughness elements, and (s/S) is the silhouette area (average area of the upwind face of an element) per unit ground area occupied by each element. Observations of z_0 for sea ice surfaces range from 0.05 to 110 mm, for fresh snow through bare ice to multi-year sea ice containing multiple scales of topography [Banke et al., 1980; Guest and Davidson, 1991].

After specifying a reference height z for measuring the mean wind speed U_z, Q_H and Q_E can be parameterized with bulk formulas for the boundary layer at neutral stability [Andreas, 1987]:

$$Q_H = \rho_a c_p C_H U_z (T_s - T_z), \tag{2.12}$$

$$Q_E = \rho_a L_s C_E U_z (q_s - q_z), \tag{2.13}$$

where ρ_a is the air density, c_p is the specific heat of air, L_s is the latent heat of sublimation, C_H and C_E are the aerodynamic transfer coefficients for sensible and latent heat, respectively, T_s and q_s are the mean temperature and mean humidity at zero height (i.e., the sea ice surface), respectively, and T_z and q_z are the mean temperature and humidity at the reference height, respectively. C_H and C_E are related to z_0 by [Andreas, 1987]:

$$C_H = \frac{k{C_D}^{1/2}}{Pr\left[k{C_D}^{-1/2} - \ln(z_T/z_0)\right]}, \tag{2.14}$$

$$C_E = \frac{k{C_D}^{1/2}}{Sc\left[k{C_D}^{-1/2} - \ln(z_q/z_0)\right]}, \tag{2.15}$$

where k is the von Karman constant, Pr is the Prandtl number, Sc is the Schmidt number, C_D is the drag coefficient, and z_T and z_q are the roughness lengths for temperature and humidity, respectively. Andreas [1987] developed a surface-renewal model to determine z_T and z_q, and then used equations 2.14 and 2.15 to directly simulate the effect of sea ice surface topography on C_H and C_E. Both transfer coefficients decrease logarithmically with wind speed and increase linearly, at all wind speeds, as the roughness of the sea ice surface topography σ increases.

Q_H and Q_E between the sea ice and atmosphere are typically at least an order of magnitude smaller than the radiative fluxes. However, at times they can provide a significant contribution to the sea ice energy budget. Latent heat is typically lost from the sea ice surface during spring and summer, with a diurnal peak occurring shortly after solar noon [Persson, 2012]. Sensible heat exhibits a pronounced diurnal cycle during spring and summer, with energy lost from the surface during the night and gained by the surface during the day [Persson et al., 2002]. Q_H and Q_E are generally <10 W m^{-2}, although they can increase to >30 W m^{-2} during synoptic weather events when wind speeds are high, for instance during a cyclone [e.g., Else et al., 2014].

2.2.2.4. Conductive Flux

Q_C depends on the temperature gradient through the sea ice cover and the thermal conductivity of the ice k_{si}. The thermal conductivity of pure ice k_i is approximately 4 times higher than brine and 100 times higher than air [Wadhams, 2000]. Brine and air inclusions impede the flow of heat through the sea ice cover, so the thermal conductivity of sea ice k_{si} is directly proportional to the brine volume fraction V_b and air volume fraction V_a. Pringle et al. [2007] developed the following expression for k_{si} from the results of an effective-medium model for sea ice, which considered the temperature-dependent conductivity and thermal equilibrium volume fractions of ice, brine and air components:

$$k_{si} = \frac{\rho_{si}}{\rho_i}\left(2.11 - 0.011T_{si} + 0.09\frac{S_{si}}{T_{si}}\right), \tag{2.16}$$

where ρ_i is the density of pure ice (917 kg m^{-3}) and ρ_{si} is the density of sea ice (890-930 kg m^{-3}). This expression does not account for heat transferred throughout the sea ice cover by internal brine convection. However, observations suggest that brine convection contributes only a few percent of the heat transferred by conduction [Pringle et al., 2007]. From equation 2.16, k_{si} is between 1.88 and 2.22 W m^{-1} K^{-1} for the temperature range -5 to -25 K and salinity range 4 to 10 ‰.

Snow has a thermal conductivity k_s (0.1 to 0.4 W m^{-1} K^{-1}) [Sturm and Benson, 1997] which is approximately an order of magnitude lower than k_{si}, due to the large fraction of interstitial air between snow grains. This makes the snowpack a particularly efficient insulator, despite its relatively low volume (snow depth on smooth FYI is typically <0.5 m [Sturm et al., 2002]).

The conductive heat flux has been estimated using thermocouple dowels installed within the sea ice and snow cover [e.g., Else et al., 2014]. During the SHEBA experiment, Q_C was negative at the sea ice surface from winter through to spring, reflecting the conduction of heat from the ocean to the atmosphere as the sea ice grows, but low (0-10 W m^{-2}) due to the insulating effect of the snowpack [Persson et al., 2002]. In spring Q_C follows the solar zenith angle, removing energy from the surface during the day but contributing energy during the night [Else et al., 2014]. In summer, the sea ice cover becomes isothermal and Q_C drops close to zero [Persson et al., 2002].

2.2.2.5. Sea Ice Melt

In reality the energy budget is calculated for multi-layered media (i.e. atmosphere, snow, sea ice and ocean), rather than a massless surface, and is rarely balanced. A surplus of energy (Q^*) is produced, which is either reflected/emitted by the sea ice cover to the atmosphere (i.e., -Q^*) or transmitted/conducted from the atmosphere into the sea ice (i.e., +Q^*). During the SHEBA experiment Q^* was negative (down to -20 W m^{-2}) between November and February, close to zero in March and April, positive (up to 100 W m^{-2}) between May and August, and again close to zero in September [Persson et al., 2002]. For the duration of the melt season (+Q^*), energy that is conducted or transmitted into the sea ice can be absorbed by snow, meltwater or ice.

If the sea ice surface temperature is <0 °C, energy absorption within the snow or ice leads to an increase in temperature. A change in snow or sea ice temperature can be approximated as:

$$\frac{\Delta T}{\Delta t} = \frac{Q^*}{\rho h c}, \tag{2.17}$$

where ρ is the snow or ice density, h is the snow or ice thickness, and c is the specific heat capacity of pure ice c_i = 2110 J kg^{-1} K^{-1} or sea ice c_{si}. The specific heat of sea ice is the heat required to change the temperature of one gram of sea ice by one degree, and can be expressed as [Ono, 1967]:

$$c_{si} = c_i + 7.5T_{si} + 0.054L_i\frac{S_{si}}{T_{si}^2}, \qquad T_{si} > -8.2\ °C \tag{2.18}$$

where L_i = 334 kJ kg^{-1} is the latent heat of fusion of pure water. This expression assumes thermodynamic equilibrium and constant bulk salinity, and is only valid for T_{si} > -8.2 °C due to the precipitation of mirabilite from brine. If the sea ice surface temperature is at 0 °C, energy absorption leads to surface melt. The rate of surface ablation caused by snow or ice melt is given by:

$$\frac{\Delta h}{\Delta t} = \frac{Q^*}{\rho L}. \tag{2.19}$$

Since snow consists of pure ice crystals, the latent heat of fusion of snow is equal to L_i. The latent heat of fusion of sea ice L_{si} can be defined as the temperature integral of c_{si}. Hence, L_{si} varies as a function of the ice temperature and salinity, and can be expressed as [Ono, 1967]:

$$L_{si} = 79.68 - 0.505T_{si} - 0.0273S_{si} + 4.3115\frac{S_{si}}{T_{si}}. \qquad T_{si} > -8.2\ °C \tag{2.20}$$

For sea ice with an average temperature of -1 °C and salinity of 4 ‰ (typical of FYI in summer), L_{si} = 263 kJ kg^{-1}. If one assumes constant Q^* and representative values for ρ_s (300 kg m^{-3}) and ρ_{si} (900 kg m^{-3}), the rate of snow volume ablation would be approximately 2.5 times faster than sea ice volume ablation.

2.2.3. Snow on Sea Ice

Micro- and meso-scale sea ice topography can be modified significantly as snow accumulates and is redistributed across the ice surface throughout the autumn, winter and spring. The snow depth distribution on sea ice depends on a number of factors, including: (1) the growth history of the ice cover, (2) the age of the ice cover, (3) ice deformation, (4) the volume of precipitation deposited since the ice formed, (5) the surface wind speed, and (6) changes in the snowpack properties. The ice growth history, age and deformation can all modify the topography of the ice surface, thereby changing the overlying snow depth distribution and, by extension, the snow surface topography [Sturm et al., 2002]. On level first-year sea ice, the snow surface topography depends only on the redistribution of snow across the ice surface [Iacozza and Barber, 1999]. At low wind speeds, newly deposited snow accumulates at near-uniform depth, whereas at high wind speeds, snow is transported across the ice surface and accumulates in mobile drifts. The size and mobility of these drifts can then be influenced by changes in the snowpack as snow grains metamorphose over time [Colbeck, 1982; 1993].

In this section we outline the physical processes of snow deposition, transport and snow grain metamorphosis. We then describe the characteristic evolution of snow surface topography on sea ice, with a focus on snow-drift evolution on level FYI.

2.2.3.1. Snow Deposition and Transport

Snow accumulates on sea ice between autumn and spring. Snowfall generally does not occur continuously, over a long period of time. It rather occurs in discrete precipitation events (storms), which deliver a relatively large volume of precipitation over a few days [Sturm et al., 2002]. Once deposited, or during deposition, snow grains can be transported across the ice surface, primarily by saltation [Li and Pomeroy, 1997], but also by creeping or turbulent diffusion [Kobayashi, 1987]. An individual snow particle is subject to a variety of forces, including aerodynamic wind drag, which acts to entrain the particle in the atmospheric boundary layer, and gravity and cohesion (inter-crystal bonding), which both act to resist particle movement [Colbeck, 1982]. A particle at rest will be entrained by the wind if the drag force acting on it exceeds the particle's shear strength. This threshold force corresponds to a threshold in wind speed, commonly known as the shear velocity [Sozzi et al., 1998].

A wind speed (at a nominal height of 10 m above the surface, U_{10}) of 4.5 m s^{-1} has been observed to induce snow grain creep, i.e. rolling of snow grains, across level surfaces [Schmidt, 1982]. However, transport by saltation, i.e. bouncing of grains, which accounts for around 80% of snow transport over sea ice [Kobayashi, 1987], requires U_{10} exceeding 6-8 m s^{-1} [Li and Pomeroy, 1997; Massom et al., 2001]. Rapid consolidation of snow grains into large distinct formations (drifts) has only been reported for U_{10} exceeding 8-10 m s^{-1} [e.g. Massom et al., 2001; Iacozza and Barber, 2010]. Threshold U_{10} for saltation has also been shown to increase from approximately 8 to 10 m s^{-1} as the snowpack temperatures rise [Li and Pomeroy, 1997], because the cohesive force between snow particles increases as the water content in the snowpack increases up to 7% [Colbeck, 1982; Denoth, 1982]. Likewise, the saltation threshold has been shown to increase from approximately 7.5 m s^{-1} for fresh snow to 8 m s^{-1} for settled, dense wind-slab snow [Li and Pomeroy, 1997].

2.2.3.2. Snow Metamorphism

Snow grains can metamorphose in response to environmental forcing, thereby changing the thermophysical properties of the snowpack. When the temperature of the snowpack is close to 0 °C, liquid water is present and wet snow metamorphism occurs, whereas at temperatures <0 °C dry snow metamorphism occurs [Colbeck, 1982]. In the presence of brine, for instance in the basal snow layer on sea ice, wet snow metamorphism can occur at sub-zero temperatures. When dry snow metamorphism is active, two mechanisms typically dominate: (1) equilibrium growth (destructive) metamorphosis, and (2) temperature gradient (constructive) metamorphosis [Sommerfield and LaChappelle, 1970]. When the snowpack contains more than ~0.1% water by volume, wet snow metamorphism is active and one of two mechanisms typically dominates, depending on the water content: (1) equilibrium growth metamorphosis at low water content, and (2) melt-freeze metamorphosis at high water content [Colbeck, 1982]. These mechanisms all act to increase or decrease the bulk density of a snow layer by changing the size and/or shape of individual snow grains.

A snow grain in its original dendritic, crystalline form can be modified during deposition, as the arms of the snow crystal are broken by the wind or by colliding with other crystals. These arms can then be fused into the central portion of a snow grain, changing the shape of the crystal and reducing its specific surface area, in a process known as sintering [Colbeck, 1982]. Owing to the low thermal conductivity of snow (see Section 2.2.2), during winter the temperature gradient through the snowpack can be as high as 30 °C m^{-1} [e.g., Massom et al., 2001]. Colbeck [1982] showed that a temperature gradient increases the flux of water vapour through the snowpack J approximately as:

$$J = -D\frac{\partial \rho_a}{\partial T}\frac{\partial T}{\partial z} + V\rho_a, \tag{2.21}$$

where D is the diffusion coefficient for water vapour in snow, $\partial \rho_a / \partial T$ is the vapour density gradient, $\partial T / \partial z$ is the temperature gradient, and V is the mean air velocity. For instance, a 0.5-m thick snowpack with a base-to-surface temperature gradient of 30 °C will have a water vapour pressure gradient of 444 Pa m^{-1}, which is sufficient to drive upward water vapour fluxes through the snowpack, maintained by net sublimation of lower layers and net condensation of upper layers [Domine et al., 2008].

Dry snow metamorphism is separated into equilibrium growth and temperature gradient metamorphism depending on the value of J, and by extension the magnitude of $\partial T / \partial z$ [Sommerfield and LaChappelle, 1970]. Equilibrium growth metamorphism typically occurs at low $\partial T / \partial z$ when vapour pressure gradients only exist in the interstitial cavities between grains and are dependent on the specific surface area of the snow crystals [Colbeck, 1993]. Mass is redistributed from the convex arms of the crystal (higher pressure) to the concave central portion of the crystal (lower pressure) by sintering and the crystal develops a smaller rounded shape [Colbeck, 1986]. Temperature gradient metamorphism typically supersedes equilibrium growth when $\partial T / \partial z$ exceeds a limit in the range 9 to 20 °C m^{-1} [Armstrong, 1980; Colbeck, 1982; Domine et al., 2008]. Snow crystals then experience kinetic growth as a function of the vapour flow rate J [Colbeck, 1982; 1993], caused by supersaturation at the crystal protrusions, and develop a faceted shape [Colbeck, 1986]. This mechanism of growth is rapid relative to equilibrium growth and leads to the formation of depth hoar.

With the introduction of liquid water in the snowpack in spring, wet snow metamorphism prevails. When liquid water is only located in the disconnected meniscuses between adjacent snow grains, e.g. in early spring, it is immobile and grains experience little modification. However, at higher liquid water content, during the pendular regime (2-7% liquid by volume) [Denoth, 1982], the convex arms of a crystal melt and the meltwater is redistributed within the interstices between neighbouring crystals to re-freeze on the concave central portions. Like the equilibrium growth process in dry snow, this leads to a rounded crystal form which minimizes the specific surface area of the grain [Colbeck, 1982]. At even higher liquid water content, during the funicular regime (7-15% liquid by volume) and saturation regime, rapid grain growth can occur as the snow is continually melted and refrozen during diurnal freeze-thaw cycles [Denoth, 1982]. This can also lead to the formation of ice lenses within the snowpack [Sturm et al., 2002].

2.2.3.3. Snow-Drift Topography

A complex relationship between the variable boundary layer wind speed, ice surface topography and evolving snowpack properties produces a variety of snow-drift formations. The earliest-forming features are ripples, typically less than 5 cm in height and aligned to the wind direction at the time of snow deposition [Doumani, 1966]. The wind velocity field in the boundary layer is then modified by these features (equation 2.11), in turn eroding the upwind ripple faces and re-depositing grains on the slip faces. Ripples migrate and grow and, as this cycle is repeated, the wind-parallel features are transformed into wind-perpendicular drifts similar to barchan sand dunes [Massom et al., 1997]. At particularly high wind speeds, slight variations in snow surface hardness can also lead to the non-uniform erosion of drifts and subsequent formation of small wind-aligned ridges, known as sastrugi [Kuchiki et al., 2011].

Although snow grain metamorphosis within a drift can reduce the density of the lowest (oldest) snow layers, size-sorting of grains and compaction by the wind can increase the density of the upper layers by several times following deposition [Sturm et al., 2002]. A snow density profile measured on landfast FYI in Resolute Passage, NU in 2011 is shown in Figure 2.3 and illustrates these contrasting snow properties with depth. The formation of well-bonded wind slab snow layers acts to slow the migration and increase the size of drifts. Orientation of the long-axes of large drifts along the prevailing wind direction has then been observed to occur as grains are eroded from the upwind side of a drift and re-deposited on the downwind side [Iacozza and Barber, 2010; Petrich et al., 2012].

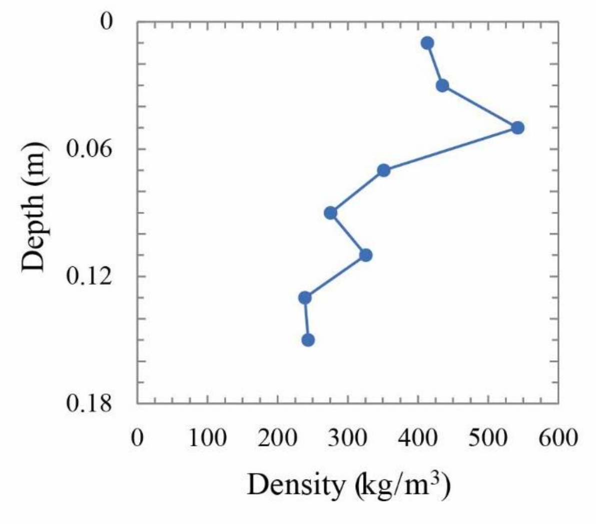

Figure 2.3 | Snow density profile from a 0.16-m deep snow pit on landfast FYI showing the impact of snow grain metamorphism on the lower layers and wind compaction & grain sorting on the upper layers. From Landy et al. [2014].

Three groups have tracked long-term seasonal changes in the snow depth distribution on level FYI and all observed a similar trend [Sturm et al., 2002; Iacozza and Barber, 2010; Petrich et al., 2012]. Initially strong unimodal distributions in autumn/winter, characterizing a snowpack with near-uniform depth or single scale of drifts, became increasingly multimodal into the following spring as several secondary snow-drift scales were superimposed onto the primary snow-drift scale. However, the correlation length of the dominant (primary) scale of snow-drifts barely changed over time [Sturm et al., 2002; Petrich et al., 2012]. Massom et al. [1997] have suggested that the deposition of wind slab snow layers during discrete, high-velocity wind events will eventually restrict the migration of large snow-drifts completely and 'lock' the meso-scale snow surface topography in place. Incidentally, snow-drift positions in as early as March were closely co-located with the initial positions of melt ponds in June at Barrow, Alaska [Petrich et al., 2012]. This indicates that the spatial distribution of ponds at melt onset can be preconditioned by the formation of a semi-rigid, meso-scale snow surface topography many months before.

2.2.4. Melt Ponds on Sea Ice

At the transition between spring and summer, the surface of sea ice in the Arctic becomes heterogeneous with the melting of snow and formation of meltwater ponds. Wherever these ponds form, the ice surface albedo drops from typical winter snow values >0.8 to around 0.2-0.4 [Perovich et al., 2002a]. A larger fraction of the incident solar irradiance is absorbed within the ice and transmitted through to the ocean [Ehn et al., 2011], thereby accelerating melt. This leads to a reduction in the thickness of the ice and further pond growth [Curry et al., 1995]. In contrast, wherever ponds do not form, melting surface ice is drained of meltwater to expose a layer of bubble-rich superimposed ice [Hanesiak et al., 2001; Granskog et al., 2006] or forms a surface layer of disaggregated, snow-like ice crystals [Perovich et al., 2002a]. Both of these surfaces retain a relatively high albedo despite extensive melting. These self-perpetuating and self-reciprocating phenomena are important components of the ice-albedo feedback mechanism [Curry et al., 1995].

Climate model projections of sea ice volume and extent are particularly sensitive to variations in prescribed albedo [Curry et al., 2001; Wang et al., 2006]. Some recent progress has been made, at computational cost, to create physically based numerical models of melt pond coverage [e.g., Scott and Feltham, 2010] and incorporate melt pond physics into albedo parameterizations for global climate models [e.g., Flocco et al., 2010; 2012]. However, limited melt pond observations have shown that seasonal coverage can vary by as little as 25% [Barry, 1983; Perovich et al., 2002b] or by as much as 85% [Holt and Digby, 1985], that diurnal coverage can vary by as much as 35% [Scharien and Yackel, 2005], and that interannual maximum coverage for ice in the same general location can vary by as much as 20% [Landy et al., 2014]. Physically based albedo parameterizations suffer from a lack of validation data and from our incomplete understanding of the variability associated with melt pond formation and evolution. This variability is driven by a history of physical forcing mechanisms (including air temperatures, wind speeds, snowfall or rain events, ice growth conditions and ice deformation) experienced by the ice cover since its formation. Each of these forcing mechanisms can be highly variable over space and time.

In this section we explain how melt ponds form at the transition between spring and summer and introduce a simple hydrological model for melt ponds on sea ice. We then explain the characteristic evolution of melt ponds on undeformed first-year sea ice and, finally, discuss which mechanisms control spatial and temporal variations in melt pond coverage, including the critical role of sea ice topography.

2.2.4.1. Melt Pond Formation

Snow melt in Arctic locations begins as daylight hours increase in spring and the net daily flux of radiative energy from the atmosphere to the sea ice becomes positive [Persson et al., 2002]. This typically occurs when longwave radiation is trapped between the sea ice and a persistent cloud cover [Ehn et al., 2006; Else, et al., 2014] (Section 2.2.2.2). The liquid water content in the snowpack increases as snow grains absorb energy. However, air temperatures are typically still below zero, so any meltwater produced will percolate down to the snow-ice interface to refreeze as a layer of superimposed ice [Granskog et al., 2006]. Further increases in liquid water content result in the pendular and funicular regimes (Section 2.2.3.2), but water is only present close to or at the snow surface when the snowpack becomes saturated. This lowers the albedo of the snow from around 0.8-0.9 to below 0.7 [Perovich, 1996], accelerating solar energy absorption and instigating surface ablation. Meltwater generated in thicker drifts will percolate downwards with gravity, thereby returning the snow surface to a relatively high albedo (although not as high as original winter values). However, melt within thinner snow (or bare ice) patches, in the interstices between drifts, permanently and irreversibly reduces the surface albedo, accelerating further melt and creating the first ponds [Iacozza and Barber, 1999].

2.2.4.2. Hydrological Melt Pond Model

A melt pond is a body of meltwater whose depth and geometry are determined by the local sea ice surface topography and whose volume is determined from a balance of water inflows and outflows. The rate of inflow depends on the rate of snow and ice melt, precipitation, and the size of the pond's catchment basin. The rate of outflow depends on the pond's hydraulic head (the pressure potential accumulated as the melt pond fills and its surface is elevated above sea level), and the presence of outflow pathways. Lateral flow of meltwater across the ice surface towards macroscopic flaws (such as ice floe edges, cracks, seal breathing holes and enlarged brine drainage channels) and vertical percolation through the ice cover can both contribute to surface water drainage [Holt and Digby, 1985; Eicken et al., 2002].

Eicken et al. [2004] developed a simple hydrological model to predict melt pond fraction f_p, and hence surface albedo, from the rate of surface melt and drainage. In steady state, the hydrological balance of pond-covered sea ice is given by:

$$\left[\frac{\rho_{si}}{\rho_w}\right]\left[\left(1-f_p\right)\frac{dh_i}{dt}+f_p\frac{dh_{pi}}{dt}\right]=\frac{f_p k \rho_w}{\eta}\frac{z_h}{h_{pi}}, \tag{2.22}$$

where ρ_{si} is the density of sea ice, ρ_w is the density of pure water, h_i is the bare ice thickness, h_{pi} is the ponded ice thickness, k is the permeability of sea ice, z_h is the hydraulic head, and η = 10^{-6} m^2 s^{-1} [Taylor and Feltham, 2004] is the kinematic viscosity of water. The left-hand side of equation 2.22 gives the rate of meltwater production per unit area through ice melt at the surface and at melt pond bases, and the right-hand side is Darcy's law which generally describes flow through a porous medium – in this case the flow of meltwater through permeable sea ice under melt ponds.

Eicken et al. [2004] assumed that the effect of meltwater production on f_p is essentially instantaneous, i.e. melt ponds have a connectivity close to one. Under this assumption they could use a frequency distribution function of ice surface elevation (a hypsographic curve) to describe the surface topography statistically, rather than explicitly, and calculate meltwater production. Without measurements of pond base elevations, ice melt at pond bases (the second term in equation 2.18) could not be calculated and was neglected. They found reasonable agreement between modelled and observed f_p when the rate of meltwater production per unit area was 0.01 m d^{-1} and the sea ice permeability was 10^{-12} m^2. However, observations have shown that the true rate of meltwater production is typically between 0.02-0.06 m d^{-1} [Landy et al., 2014] and the permeability of summer sea ice is $>10^{-11}$ m^2 [Eicken et al., 2002]. The physical mechanisms controlling melt pond fraction are clearly not as straightforward as suggested by equation 2.22. This is discussed in the following section.

2.2.4.3. Physical Mechanisms Controlling Melt Pond Evolution

After initial formation, melt ponds generally develop over four consecutive stages [Eicken et al., 2002]. These stages are characterized by: (I) topographic control, (II) meltwater balance, (III) ice freeboard control, and finally (IV) fall freeze-up or ice break-up (Figure 2.4).

Stage I is characterized by increasing melt pond fractional coverage as meltwater fills topographic depressions and remains there with limited drainage. Pond surfaces are typically well above sea level (positive hydraulic head) and surface meltwater progressively fills higher areas of topographic relief as pond coverage increases [Holt and Digby, 1985; Fetterer and Untersteiner, 1998]. On relatively smooth first-year sea ice, where the effects of deformation, aging and previous melt are either small or negligible, past studies have shown that snow drifts control the spatial distribution and shape of newly-forming melt ponds [Barber and Yackel, 1999; Petrich et al., 2012]. Stage I culminates with the seasonal peak in pond coverage over both first- and multi-year sea ice [Perovich and Polashenski, 2012].

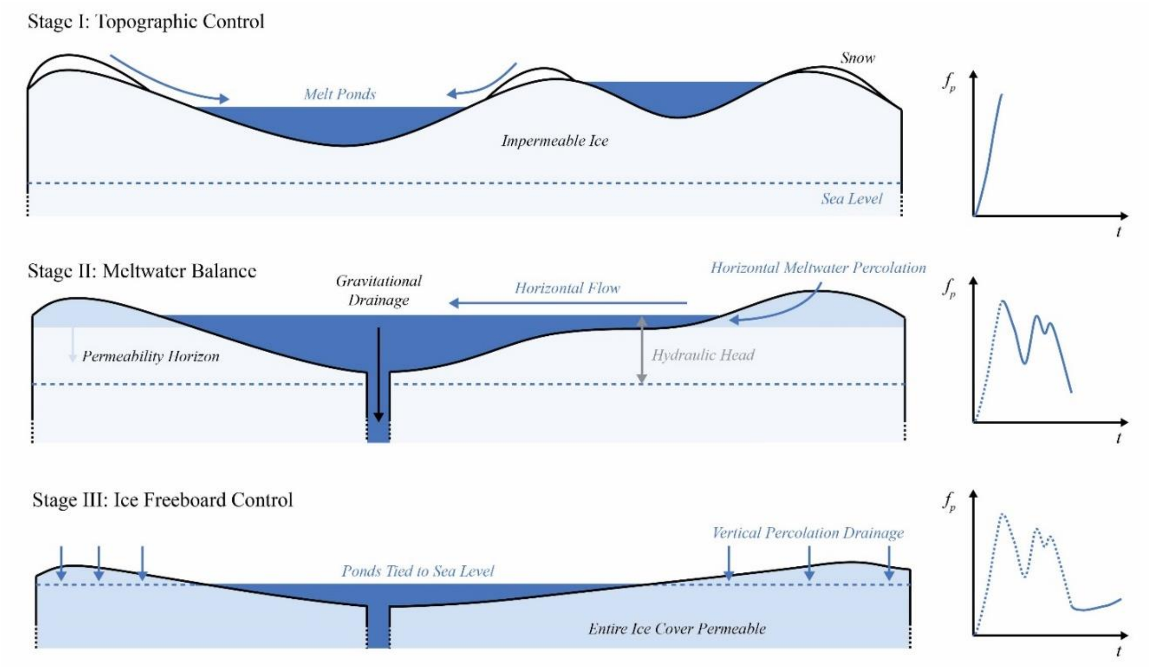

Figure 2.4 | Stages I, II and III of melt pond evolution, as identified by Eicken et al. [2002]. The graphs on the right illustrate how the melt pond fraction f_p develops during each stage.

Stage II is characterized by a hydrostatic balance between meltwater production and its drainage. Holt and Digby [1985] noted that melt channels, connecting ponds that were previously isolated during Stage I, could transport water several hundred meters to a drainage flaw as melt ponds evolved throughout Stage II. However, they also collected ice cores during Stage II which demonstrated that bulk salinity within the ice cover was too high for the fresh surface meltwater to have drained through it. During Stage II the lateral flow of meltwater across the ice surface promotes the formation of melt channels and ponds become interconnected, forming large networks [e.g., Hohenegger et al., 2012]. Melt ponds covering some of the lowest-lying pre-melt areas can rapidly drain as they become elevated above these deepening channels [Landy et al., 2014]. Stage II ends when the hydraulic head has decreased to zero and melt pond surface levels match the sea level. The final geometrical structure of the melt pond cover is established at this time. Pond coverage generally declines slowly during Stage II. However, observations indicate that coverage (and hydraulic head) can vary substantially on daily time scales, due to fluctuations in the meltwater balance [Landy et al., 2014].

According to the 'law of fives' suggested by Golden et al. [1998], sea ice should undergo a permeability transition when V_b > 5%, after which gravity drainage is initiated and brine and surface meltwater begin to percolate through the ice cover (Section 2.2.1.3). Polashenski et al. [2012] observed that V_b was well above the 5% threshold throughout the entire ice cover several weeks prior to the formation of melt ponds. Eicken et al. [2004] and others have suggested that a layer of superimposed ice forming at the snow-ice interface could effectively seal melt pond bases early in the melt season. However, Polashenski et al. [2012] also observed that most of the superimposed ice on pond bases melted several days before the transition in ice cover permeability. Instead, Polashenski et al. attributed the delay in the permeability transition to fresh meltwater percolating into the ice shortly after pond formation, subsequently refreezing during its migration towards the coldest portion of the ice cover (that remains below the freezing point of the surface meltwater), to form interposed ice plugs, and limiting further infiltration until Stage III.

During **Stage III** the permeability of the sea ice to vertical meltwater drainage increases such that melt pond surface levels remain tied to sea level and horizontal discharge to and drainage at macroscopic flaws become small. Changes in pond coverage during Stage III depend on changes in surface topography and the freeboard of the ice cover [Eicken et al., 2002]. Pond-covered ice generally absorbs more solar radiative energy than white ice and thus experiences preferential ablation [Hanson, 1965; Perovich et al., 2003; Hudson et al., 2013]. As the ice below sea level, i.e. at melt pond bases and at the ice bottom, melts and is removed more rapidly than adjacent bare ice above sea level, the ice surface gradually sinks. Consequently, the ice freeboard decreases and ponds expand as a function of surface topography [Landy et al., 2014]. Observations have shown that ponds deepen and can also widen during this period as ice is preferentially melted from pond bases and eroded from pond walls [Eicken et al., 2004].

Stage IV characterizes either fall freeze-up, as ponds refreeze from their surface down to their base and accumulate snow, or ice break-up. Since refreezing and break-up can occur at any time, this stage is not necessarily restricted to the end of the season.

The four stage model of Eicken et al. [2002] has been supported by recent quantitative analysis [Petrich et al., 2012; Polashenski et al., 2012; Landy et al., 2014]. However, available melt pond observations demonstrate considerable variability within these idealized developmental stages [e.g., Derksen et al., 1997; Eicken et al., 2004]. This suggests that pond coverage is strongly dependent on variability in weather, snowpack and ice cover properties, ice age, ice growth history, and other physical forcing mechanisms. Here we discuss how these mechanisms can affect changes in melt pond coverage.

The weather affects the sea ice surface energy balance and by extension the rate of meltwater production. It can be highly variable over space and time, especially during the Arctic spring and summer, due to variable cloud cover [Kay and Gettelman, 2009] and the passing of storms [Zhang et al., 2004]. It has been suggested that cyclones passing over sea ice in spring can increase the turbulent heat fluxes sufficiently to hasten melt onset by more than one week [Else et al., 2014].

The thickness of the spring snowpack can affect the rate of meltwater production and the cumulative volume of meltwater produced at the sea ice surface during the melt season. Eicken et al. [2004] suggested that the eventual peak in melt pond fractional coverage increases as the thickness of the snowpack increases, from 0 up to a threshold mean thickness of approximately 0.5 m. This was attributed to the formation of superimposed and interposed ice delaying the permeability transition of the sea ice cover. Above this 0.5 m threshold the peak melt pond coverage can drop significantly because meltwater continually drains to the base of the thick snowpack, renewing the high snow surface albedo and delaying the exposure of lower albedo bare ice and pond-covered ice.

Ice cover properties, including the structure of the ice and the thermodynamic development of the ice, affect the rate of meltwater drainage from the sea ice surface to the ocean. For instance, observations have shown that the rate of drainage can be increased dramatically in areas of sea ice with a high density of cracks, flaws and seal holes, or at the edges of floes, which reduces surface melt pond coverage [Holt and Digby, 1985; Fetterer and Untersteiner, 1998; Eicken et al., 2002].

If sea ice survives the first year of melt, non-uniform ablation will have increased the roughness of the ice surface topography. Consequently, in the following spring, new melt ponds will be confined to a smaller area of the ice surface and although they will be deeper, they will not be able to spread or recede as much as on smooth, level FYI. As the age of MYI increases, the roughness of the topography will increase further, due to multiple seasons of uneven melt, and pond coverage will fall [Eicken et al., 2004; Perovich and Polashenski, 2012]. Ice deformation also increases the roughness of the surface topography (Section 2.2.5.3) and, additionally, tends to increase the density of flaws and cracks through the ice cover [Eicken et al., 2002], which both lead to a reduction in melt pond coverage.

2.2.5. Sea Ice Dynamics and Deformation

Sea ice that has been subject only to thermodynamic processes is described as having ‘level’ surface topography. However, it is not only thermodynamic processes that modify the topography. An unrestricted sea ice floe will move in the ocean, primarily owing to wind and water drag acting on the surface and base of the floe, respectively. Incidentally, the drag force acting on the surface of a mobile ice floe, in response to wind forcing, depends on the drag coefficient C_D which increases as a function of the sea ice surface roughness (Section 2.2.2.3). Under divergent forcing, an ice floe can be divided and fragmented, with open water leads forming in the interstices between floe fragments [Leppäranta, 2011]. Under convergent forcing, colliding ice floes can be mechanically deformed, leading to the formation of rafted ice, rubble fields and pressure ridges [Wadhams, 1994]. These dynamic processes can significantly modify the sea ice surface topography.

In this section we give a brief overview of sea ice strength and rheology, which both influence the rate of ice deformation, before discussing the physical mechanisms that cause sea ice to deform and the characteristic size and spacing distributions of pressure ridges.

2.2.5.1. Sea Ice Strength and Rheology

Sea ice is strongest in compression, strong in shear and weak in tension, because ice crystals are vertically aligned [Feltham, 2008]. These properties are reflected in rheological models, which use a constitutive law to characterize the rate of strain within sea ice under applied stress. The rheology of drift ice is complicated because different laws apply to different ice states (i.e., to different ice concentrations and floe thicknesses). Stress-generating mechanisms in sea ice include: (1) floe collisions, (2) floe break-up, (3) shear friction between floes, (4) friction between ice blocks during ridge formation, and (5) potential energy (PE) production during ridge formation [Leppäranta, 2011].

Below an ice concentration of around 0.7-0.8, applied stresses do not typically exceed a critical ‘sub-yield’ stress, and sea ice behaves as an elastic [Coon et al., 1974] or viscous material [Hibler, 1979]. As ice concentration approaches unity, friction between ice blocks and PE production during ridging become important, and applied stresses exceed the sub-yield stress. Sea ice then behaves like a plastic, yielding permanent and irreversible deformation [Feltham, 2008]. Consequently, an isotropic elastic-plastic or viscous-plastic rheology is commonly used to simulate rates of ice deformation in the sea ice component of climate models [e.g., Lipscombe et al., 2007]. However, recent progress has been made to develop anisotropic sea ice rheologies for high-resolution (< 100 km grid scale) climate model simulations that consider lead formation and the influence of one or several leads on the local plastic failure stress [e.g., Wilchinsky and Feltham, 2012]. As leads are oriented features, high shear rates can be included along specific failure lines that better replicate observed ice kinematics [Kwok and Sulsky, 2010].

2.2.5.2. Mechanisms of Sea Ice Deformation

The three key mechanisms of deformation include: (1) lateral rafting of thin ice under compression, (2) hummocking of fractured ice blocks in rubble fields with no regular geometry, and (3) ridging of ice blocks into defined piles with quasi-regular geometry. Hopkins [1994; 1998] used a two-dimensional particle simulation technique to model the ridging process and found that ridge growth exhibits a cyclic alteration between periods of sustained sail growth (accompanied by a low lateral 'ridge-building' force and low kinetic energy (KE) expenditure) and keel growth (accompanied by spikes in lateral force and high KE expenditure). Four stages of ridge growth could be identified:

(1) Thin ice (in open water or newly-formed within a lead) converges on a thick floe, the ridge sail and keel grow vertically at a similar rate until the sail reaches a critical maximum slope, after which the friction between blocks and gravity prevent blocks from riding up any higher.

(2) The ridge keel deepens and widens until the sail reaches a critical maximum slope, and the ridge settles in isostatic equilibrium.

(3) A rubble field grows lead-ward with approximately uniform thickness until the supply of thin ice is exhausted.

(4) Under further compressive forcing the ridge barely changes, but the rubble field is compressed onto the ridge and the ridge widens.

Integrated KE expenditure over these four stages was found to be an order of magnitude greater than the potential energy stored in the ridge.

Pressure ridges comprise a sail (ice blocks above sea level) and keel (ice blocks below sea level), in isostatic equilibrium with respect to sea level (Figure 2.5). The isostatic balance can be written in terms of the geometrical parameters and density of a ridge as:

$$(\rho_w - \phi\rho_i)h_k^2 \cot\varphi_k = \phi\rho_i h_s^2 \cot\varphi_s, \tag{2.23}$$

where ρ_w is the density of seawater, ρ_{si} is the density of sea ice, ϕ is the solid fraction of sea ice, and h_k and h_s are the heights, and φ_k and φ_s are the slopes, of the keel and sail, respectively. The bulk porosity of a ridge sail is typically between 0.2 and 0.4, whereas the porosity of the keel can be 0.2, or as low as zero, because ice can grow down from sea level to the base of a ridge, thereby consolidating the keel [Leppäranta, 2011]. The ratio of keel depth to sail height $\gamma = h_k/h_s$ is approximately 4-5 for FYI ridges and 3 for MYI ridges [Wright et al., 1978].

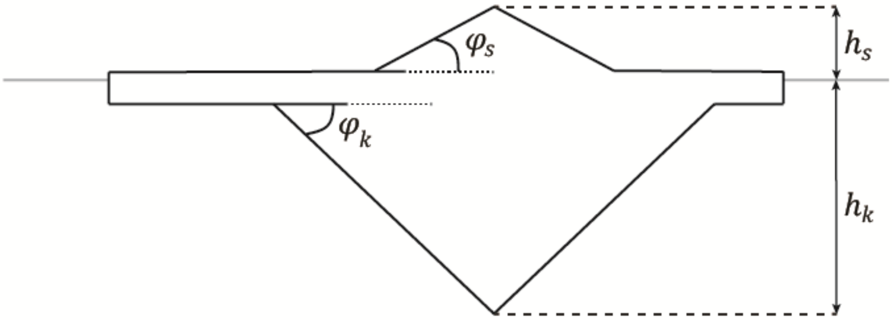

Figure 2.5 | Simplified structure of a sea ice pressure ridge. After Leppäranta [2011].

2.2.5.3. Size and Spacing Distributions of Pressure Ridges

The size or spacing distribution of pressure ridges can be characterized by an exponential probability density function of the form [Wadhams, 1980]:

$$p(h^*) = \lambda \exp[-\lambda(h^* - h_c)]\,, h^* \geq h_c \tag{2.24}$$

where h^* is the sail height [m], keel depth [m] or ridge spacing in [m^{-1}], h_c is a cutoff representing the minimum permitted height for a sail, and λ is a distribution shape parameter, where the mean size or spacing is $h_c + \lambda^{-1}$ and the standard deviation is λ^{-1}. The thickness of a ridge is typically between 5 and 30 m, and it has been suggested that closely spaced and thick ridges, in areas of particularly deformed sea ice, may account for up to one half of total ice volume [Leppäranta, 2011]. In a recent study, Tan et al. [2012] demonstrated that three distinct regions of sea ice surface topography could be identified from the intensity (mean sail height/spacing) of ridges in the Weddell Sea: (1) broken level ice in the MIZ and level polynya ice (sail height = 0.99 m, sail spacing = 232 m), (2) deformed FYI and SYI (height = 1.12 m, spacing = 54 m), and (3) heavily deformed ice outflowing from the Weddell Gyre (height = 1.17m, spacing = 31 m).

2.2.6. The Sea Ice Thickness Distribution

The thickness of the sea ice cover within a region depends on the history of dynamic and thermodynamic processes to which it has been subject. The probability density function of sea ice thickness $g(R, h, t)$ was defined by Thorndike et al. [1975], with $g\ dh$ the fractional area of region R covered by ice whose thickness lies between h and $h + dh$ at time t and, by definition, $\int_0^\infty g\ dh = 1$ (Figure 2.6). The governing equation for the thickness distribution is:

$$\frac{\partial g}{\partial t} = -\nabla \cdot (\boldsymbol{v}g) - \frac{\partial (fg)}{\partial h} + \Psi, \tag{2.25}$$

where $\boldsymbol{v}$ is a horizontal velocity vector ($-\nabla \cdot (\boldsymbol{v}g)$ is therefore the divergence (i.e., flux) of the thickness distribution out of R), f is the thermodynamic growth or melt rate, and ψ is a redistribution function that takes into account the formation of pressure ridges following convergent sea ice deformation [Thorndike et al., 1975].

Equation 2.25 takes into account most of the dynamic and thermodynamic processes that modify the ice thickness distribution (many of which have been described in this chapter). The equation can be solved to a reasonable approximation by dividing and solving each term (i.e. thermodynamic, divergence and deformation terms) in succession, and it is therefore commonly used in the sea ice component of climate models [e.g., Lipscombe, 2001]. The contribution of each term to $g(h)$ is illustrated in Figure 2.6. Thermodynamic ice growth or melt redistributes thin ice to thick ice classes, and vice versa. In purely divergent conditions, open water (leads) fills the area exported from region R. In purely convergent conditions, thin ice from a range of the lowest thickness classes is redistributed to the thicker classes, with the cut off between negative and positive Ψ determined by the ice rheology.

There is no simple, general form for $g(h)$ because it exhibits strong spatial and temporal variability. However, the upper tail of the distribution is typically well represented by a negative exponential curve, because pressure ridge formation acts to distribute thin ice area to thicker classes [Leppäranta, 2011] (Figure 2.6). The shape and properties of the thickness distribution offer some information on the surface topography of sea ice. Level FYI has a low narrow mode and few ridges contributing to the tail, whereas deformed ice has a larger tail and smaller secondary peaks at low thickness caused by new ice formation in leads. MYI has a wide mode with several secondary peaks, owing to variable rates of ice growth and deformation, and a strong peak at low thickness, representing the growth of seasonal lead ice. Melt pond formation acts to roughen the distribution by selectively redistributing ice area from higher to lower classes [Haas, 2010]. Satellite altimeter observations have shown that sea ice surface roughness height σ varies between approximately 2 cm, for level young ice, and 30 cm, for rough deformed MYI, at a 25-km length scale [Kwok et al., 2006].

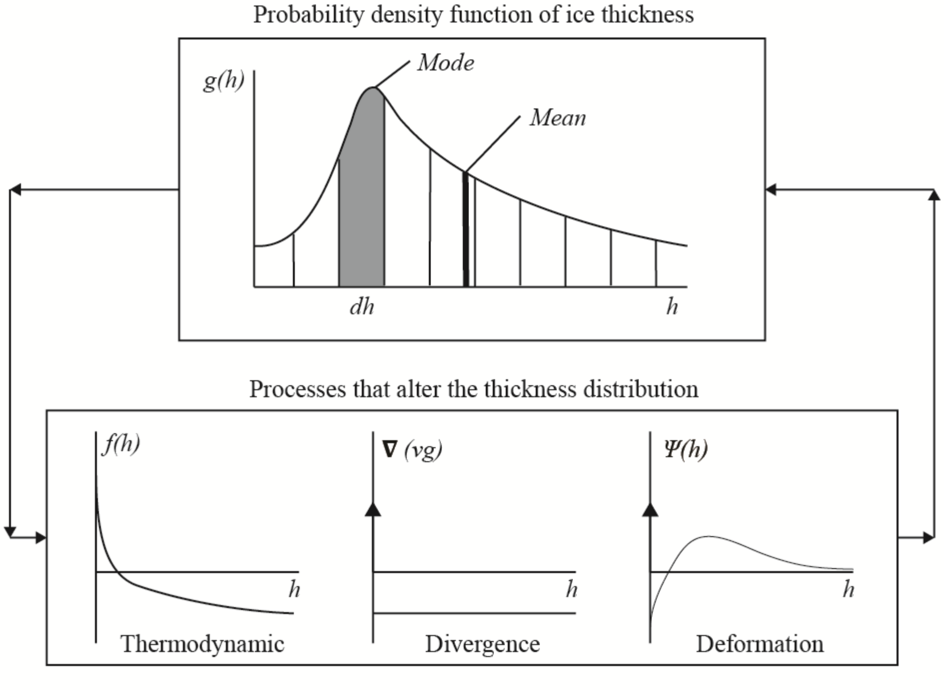

Figure 2.6 | Schematic diagram of the contributions of thermodynamic growth or melt, ice divergence, and ice deformation to the probability density function of sea ice thickness. After Haas [2010].

2.3. Microwave Scattering from Sea Ice Topography

Microwave remote sensing can be a powerful tool for studying Arctic sea ice. Microwave radiation is affected by both the geophysical structure and thermo-physical state of snow and sea ice, and can therefore be used to interrogate the sea ice cover remotely. Sea ice properties are estimated from passive microwave sensors by comparing the amount of electromagnetic (EM) radiation that is emitted from sea ice at various frequencies (in the range 7-85 GHz) [Comiso, 2010]. In contrast, active microwave sensors (radars) both emit and receive EM radiation, and sea ice properties are estimated from changes in the amount and type of energy that is backscattered from the ice [Barber, 2005]. The backscatter is not only dependent on the physical parameters of the snow and ice, but also on the frequency (typically in the range 1-18 GHz), polarization and inclination angle of the radar with respect to the ice cover. Here we focus on active microwave remote sensing of sea ice.

In this section we discuss the physical basis for active microwave remote sensing of snow-covered sea ice. We then contrast surface and volume EM scattering within sea ice, and explain the role of sea ice topography in driving surface scattering, before discussing the inversion of sea ice parameters using radar.

2.3.1. Physical Basis

Sea ice is a heterogeneous mixture of ice, brine, air and solid salt inclusions, as discussed in Section 2.2.1. Although sea ice does not conduct electricity, the ice and brine are dielectric materials which can be polarized by the electric field of an EM wave. The ‘polarizability’ of a material, or extent to which it is polarized by an applied field, is known as the complex permittivity: $\varepsilon = \varepsilon' + i\varepsilon''$, including real ($\varepsilon'$) and imaginary ($\varepsilon''$) parts [Hallikainen and Winebrenner, 1992]. The real part (or relative permittivity) is related to the energy stored within the material relative to the absolute permittivity of a vacuum ($\varepsilon_0 = 1$). The imaginary part is related to the loss of energy within the material.

The dielectrics of snow and sea ice depend on the properties and relative proportions of the constituting materials: pure ice, brine, pure water and air, and the properties of the EM radiation. Pure ice ε' is weakly dependent on temperature and is almost frequency independent [Mätzler and Wegmuller, 1987]. Pure water ε' and ε'' are dependent on both temperature and frequency and, with the introduction of dissolved salts, increase non-linearly as a function of salinity [Stogryn and Desargent, 1985]. Consequently, the dielectric of dry snow is effectively governed by the density and shape of snow grains, whereas the dielectric of wet snow is governed by the liquid water content and the presence of brine in the snow basal layer. The dielectric of sea ice is based on the number and distribution of inclusions hosted by the pure ice cover. Brine ε' and ε'' are dependent on both temperature and frequency, and generally brine ε' is 3-30 times greater than pure ice [Jin, 1993]. Brine inclusions act to scatter EM radiation within the ice cover because the dielectric contrast between pure ice and brine is very large. Air ε' is approximately 3 times smaller than pure ice ε', so EM radiation can also be scattered by air bubbles in the sea ice (typical of a multi-year ice cover) and by the snow-air or ice-air interface.

2.3.2. Surface and Volume Scattering

An EM wave incident upon the surface of a medium can be scattered by dielectric discontinuities at the surface or transmitted across the boundary into the medium. Once transmitted the wave can pass through the medium and also be scattered by dielectric discontinuities within the medium. Scattering which takes place at an interface between two media is known as surface scattering, whereas scattering which takes place within a medium is known as volume scattering. The penetration depth of the EM radiation which enters a medium is the depth at which the wave power drops to $1/e$ (37%). In practical terms, the penetration depth of sea ice can be defined as the maximum depth which contributes to backscattering of radiation in the z-direction [Hallikainen and Winebrenner, 1992].

The upper portion of multi-year sea ice is generally quite fresh (less than 2 psu), the brine having been drained as surface water flushed the ice cover during previous melt seasons [Petrich and Eicken, 2010]. Consequently, the penetration depth of multi-year ice can be as high as 5 m at L-band radar frequency [Hallikainen and Winebrenner, 1992] and a significant fraction of the incident EM radiation is scattered by inclusions within the sea ice volume. Volume scattering, rather than surface scattering, dominates [Barber, 2005]. However, the penetration depth of new and young first-year ice is typically close to zero because the surface is saline and the brine volume within the upper portion of the ice cover is high [Hallikainen and Winebrenner, 1992]. The dielectric contrast between the air and sea ice is strong. In this situation backscatter at C-band radar frequency depends almost entirely on surface scattering at the air-ice interface. If the snowpack on first-year ice is cold and dry, EM radiation can be transmitted through the snow, but the backscatter signal is still dominated by scattering at the snow-ice interface. Only when the ice is sufficiently thick and cold does penetration occur at C-band and volume scattering become significant [Onstott, 1992].

Surface scattering depends on the micro-scale topography or roughness at an interface. A surface appears rough to microwave illumination when the height variations of the surface (σ; see Section 2.1.2) are larger than a fraction of the radar wavelength λ. This fraction is qualitative and can be shown to increase as the incidence angle of the radar increases, but commonly the surface is assumed to be rough if it exceeds the Raleigh criterion: $\sigma > \lambda/8\cos\theta$, where θ is the inclination angle [Ulaby et al., 1990]. A wave is backscattered only when the surface is 'radar rough'.

A widely used method for determining scattering from slightly rough surfaces is the small perturbation method (SPM). SPM approximates an exact analytical solution to the scattering of waves from a perturbed flat surface separating two adjacent media with homogeneous dielectrics. Scattered and transmitted fields are expanded in perturbation series, with the small parameter $k\sigma$ (wave number multiplied by rms height) quantifying the deviation of the approximate solution from the exact solution [Winebrenner et al., 1992]. SPM only applies for surfaces with a limited (small) roughness height: $k\sigma < 0.3$, and correlation length: $kl < 3$ [Fung and Chen, 2010].

Past observations of sea ice σ and l range from 0.01 to 5 cm and 0.4 to 20 cm, respectively [Onstott, 1992]. The upper limits of these observations, which have typically been collected over deformed and/or multi-year sea ice [e.g., Drinkwater, 1989], or superimposed ice [Onstott, 1992], exceed the SPM criteria at C-band and L-band. However, a recent study has indicated that all sea ice surfaces, including multi-year and superimposed ice (Figure 2.7), have roughness properties that are within the limits of the SPM [Landy et al., 2015a]. The high values for σ and l presented in past studies are thought to have been biased by inadequate field measurement techniques, such as pin or laser profiling. These inadequacies are discussed in greater detail in Section 2.4.1.

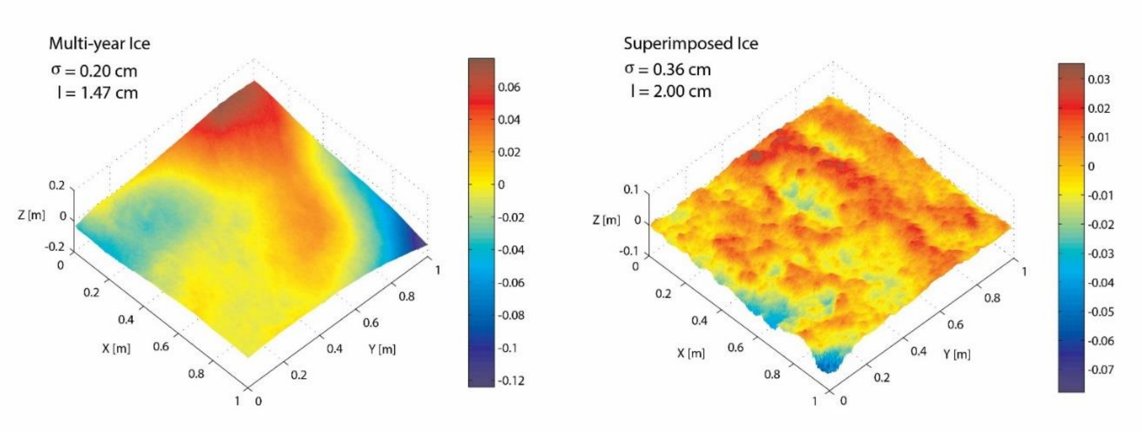

Figure 2.7 | Digital surface models of multi-year sea ice and superimposed ice, along with measured σ and l for the micro-scale surface roughness. Following Landy et al. [2015a].

Macro- and meso-scale sea ice topography also affect scattering by altering the orientation of a surface with respect to the incident EM wave. Natural sea ice surfaces are generally inclined in a range of directions by snow drifts, deformed ice and/or due to non-uniform ablation in previous melt seasons (e.g., the multi-year ice surface in Figure 2.7). However, the SPM can be extended to multi-scale surfaces by separately considering the backscattering from micro-scale surface roughness and larger-scale topography [e.g., Ulaby et al., 1990].

2.3.3. Inversion of Physical Parameters using Radar

Physical parameters such as the type, thickness and thermo-physical state of sea ice can be inverted from radar measurements with sufficient knowledge of the sea ice dielectrics and scattering behaviour. A radar measures the backscattering cross-section of a target, which is the portion of the outgoing signal that is redirected by the target back towards the radar antenna. The normalised radar cross-section (NRCS) is the backscattering cross-section per unit area, i.e. for an area-extensive target, and is otherwise known as the backscattering coefficient σ^o [Onstott, 1992]. The NRCS of sea ice depends on both the system parameters of the radar, i.e. frequency, polarization, incidence angle and azimuth angle of the incident radiation, and the scattering properties of the ice, which have been discussed above.

Polarimetric radar systems can transmit and receive EM waves which are vertically or horizontally polarized. The VV-channel transmits and receives vertically-polarized EM waves, the HH-channel transmits and receives horizontally-polarized EM waves, and the VH-channel transmits and receives cross-polarized EM waves (HV is redundant). Ground-based scatterometers can be used to collect the ‘radar signature’ of a target, which is the variation of σ^o with incidence angle in each of these channels. Fully-polarimetric scatterometers have been deployed over sea ice in the Arctic from the side of a ship [Isleifson et al., 2010] or from an aircraft, and over sea ice which has been grown artificially in a tank [Isleifson et al., 2014]. In each of these studies a series of accompanying *in situ* measurements were taken of the sea ice, including: snow and ice temperature, salinity, and density, roughness at air-ice/snow and/or snow-ice interfaces, among others; to characterize the physical and dielectric properties of the snow and ice.

Relationships have been identified between radar parameters, such as the total power, co-polarization or cross-polarization ratio, and phase difference between the co-polarized channels, and the geophysical properties of the sea ice or changes in thermo-physical state. These relationships can be derived purely from observational data [e.g., Isleifson et al., 2014], or by using observational data to validate numerical models of wave scattering [e.g., Komarov et al., 2014]. Existing relationships between radar signatures and sea ice geo-thermo-physical parameters can be scaled for satellite earth observation. For instance, Geldsetzer and Yackel [2009] demonstrated that the co-polarized ratio $\gamma_{co} = \sigma^o_{HH}/\sigma^o_{VV}$ could be used to differentiate between FYI with smooth and rough surface topography, as well as open water and MYI, in ENVISAT ASAR (synthetic aperture radar) imagery. However, there is currently no established technique for deriving quantitative estimates for sea ice surface roughness, i.e. in terms of the parameters described in Section 2.1.2.

2.4. Techniques for Measuring and Understanding Sea Ice Topography

2.4.1. Existing Techniques

The techniques used to measure sea ice surface topography, and attempt to capture the dynamic and thermodynamic processes which affect it, have typically involved traditional surveying methods such as profiling or levelling. In the last decade or so airborne and satellite altimeters have also been developed to measure sea ice topography over regional scales. In this section we provide an overview of these *in situ* and remote sensing techniques.

2.4.1.1. In Situ Techniques

Field- or laboratory-based measurements of micro-scale surface topography (roughness) have generally been made along discrete one-dimensional profiles, using either contact or non-contact instruments. Detailed descriptions of the methods used to collect surface roughness data over snow and sea ice are rare, so studies targeting soil or outcrop roughness are included here. Contact instruments include the stylus profilometer [Mathia et al., 2011], meshboard [Mattia et al., 2003], and pin profiler [Bryant et al., 2007]. The key disadvantage of a contact instrument is that it can interfere with the physical properties of the surface, especially if the surface comprises fragile structures, such as newly fallen snow grains. Moreover, these instruments typically also have limited sampling resolution and extent, for example standard pin profilers include pins with 1 cm spacing [Jester and Klik, 2005] and both these and stylus profilometers are generally limited to 1 m-long transects [Manninen, 1997]. Non-contact techniques include photographing a surface against a background grid [Paterson et al., 1991; Manes et al., 2008] and most commonly laser profiling [Drinkwater, 1989; Callens et al., 2006; Gupta et al., 2012]. These instruments do not disturb the surface, and can generally sample at spatial resolutions of <1 cm, but only the laser profiler can measure transects with a length greater than ~1 m.

Traditionally linear profiles (or transects) have also been used to measure meso-scale topography, for example to track the evolution of snow-drifts [e.g., Iacozza and Barber, 1999; Iacozza et al., 2010] or melt ponds [e.g., Eicken et al., 2001; Perovich et al., 2002a; 2009] at the sea ice surface. Typically measurements are taken using a laser profiler [Eicken et al., 2001] or dumpy level [Iacozza and Barber, 1999], at a horizontal resolution of 0.1-

2.5 m, and located relative to sea level or a fixed reference level within the ice cover to a vertical precision of ~0.1 m.

However, all of these techniques suffer from a number of problems. One-dimensional surveying techniques (i.e., that measure $Z(x)$) are assumed to characterize two-dimensional (i.e., $Z(x, y)$) surface properties, which is not always the case [Callens et al., 2006]. Individual profiles across a surface may not be stationary, causing measurements to vary considerably between adjacent profiles. One-dimensional profiles also fail to identify anisotropy in surface conditions, although Iacozza and Barber [1999] sampled along multiple radial profiles in their study areas to attempt to account for this. Additionally, the length of a profile or sampling interval may be inadequate to capture the length scale of the *in situ* topography [Verhoest et al., 2008]. If the sampling interval or extent is insufficient to characterize the surface correlation function, the statistical parameters describing the rough surface will be inaccurate (Section 2.1.2).

2.4.1.2. Remote Sensing Techniques

Measurements of sea ice surface topography can theoretically be inverted from radar data if surface scattering presides over volume scattering, for instance over saline FYI or wet snow with a high dielectric constant [Barber, 2005] (Section 2.3). Under this condition, an increase in the roughness of micro-scale topography produces an increase in backscatter, which is especially clear at higher radar frequencies (e.g., X-band or Ku-band). An increase in the roughness of meso- and macro-scale topography (i.e., greater deformation) also produces an increase in backscatter, which is especially clear at lower frequencies (e.g., L-band) [Onstott, 1992]. Wohl [1995] demonstrated that linear-polarization C-band synthetic aperture radar (SAR) could be used to discriminate between young ice, smooth FYI and rough FYI, for this very reason. Development of polarimetric SAR (e.g., RADARSAT-2) may also improve our ability to detect FYI roughness remotely [Gupta et al., 2012]. However, the complexity involved in interpreting spatial and temporal variations in SAR backscatter has prevented attempts to directly link backscatter to surface topography statistics.

Airborne laser altimeters (ALAs) have regularly been used to measure the surface elevation of sea ice, typically in combination with a radar altimeter for mapping snow depth or electromagnetic induction (EMI) system for mapping ice thickness. Standard ALAs sample elevation along one-dimensional profiles, with a horizontal resolution of 0.1-5 m and vertical precision of 0.15 m [Doble et al., 2011]. However, few studies have examined higher order moments of elevation measurements obtained with an ALA (i.e., surface topography). Rivas et al. [2006] collected altimeter tracks over FYI and MYI to investigate the power spectral density (PSD) of meso-scale sea ice topography. Their results showed that the spectral shape of the topography of all sea ice types (young ice, level FYI, deformed FYI, and MYI) was best represented by a Lorentzian PSD model, and that young and level FYI had a distinctly lower rms height σ (0.03-0.10 m) and marginally lower correlation length l (3-7 m) than deformed FYI and MYI σ (0.1-0.4 m) and l (4-9 m).

Satellite altimeters, such as the laser altimeter ICESat or radar altimeters Cryosat-1 and -2, have also regularly been used to measure the surface elevation of sea ice but, like the ASAs, rarely used to investigate surface topography. The principal focus of the satellite altimeters has been estimating ice thickness from the difference between sea ice and sea surface elevations (i.e., ice freeboard), based on an assumption that the sea ice cover is in isostatic equilibrium, and using parameterizations for snow thickness and density [Laxon et al., 2013]. Two exceptions are the studies of Kwok et al. [2006] and Kurtz et al. [2014], in which the sea ice surface roughness height σ was estimated from the spread of ICESat and Cryosat-2 echo waveforms, respectively.

2.4.2. Light Detection and Ranging (LiDAR)

Laser scanning, also referred to as LiDAR, has become the preeminent technique for acquiring three-dimensional geospatial data over the past few decades. Although the laser was invented late in the 1950s, and was integrated into surveying instruments (laser rangefinders and theodolites) the following decade, it was not until the 1980s that it was combined with automated scanning apparatus.

Modern laser scanners simultaneously measure the range of a target and the two angles (inclination and azimuth) which locate the target in horizontal and vertical planes, centered on the laser origin. Ranging is accomplished by measuring either the time-of-flight for consecutive discrete pulses of radiation to be emitted and received by the instrument or the phase difference between transmitted and received waveforms of a continuous beam of radiation [Baltsavias, 1999]. Static terrestrial laser scanners, i.e. scanners operating from a fixed origin (as opposed to airborne laser scanners, which require a GPS and inertial measurement unit (IMU) to continuously track the sensor origin), typically utilize the pulse ranging method [Petrie and Toth, 2008]. By systematically deflecting the laser beam in equal increments of arc along a series of profiles, the scanner can measure the range, direction and thus three-dimensional coordinates of thousands of points across a target.

In this section we review the basic theory associated with static terrestrial laser scanning, including laser ranging and precision, angular resolution and beam divergence, and the factors affecting the sampling resolution. We then describe techniques for registering and filtering laser scan data, and modelling terrain.

2.4.2.1. Laser Ranging, Precision and Target Surface Reflectivity

The range R and range resolution ΔR of a pulsed laser are [Baltsavias, 1999]:

$$R = c\frac{t}{2}, \qquad \Delta R = c\frac{\Delta t}{2}, \tag{2.26}$$

where the time t is measured by an interval counter relative to a specific point on the pulse, e.g. the leading edge, and c is the speed of light in air. Because the leading edge is occasionally not well-defined, t is typically recorded when the signal voltage passes a pre-determined (constant) fraction of the signal amplitude [Beraldin et al., 2010]. Ambiguity in this threshold (Δt) is translated to the range measurement and defines the range resolution ΔR.

The precision of a range measurement is based on the ratio between the peak signal power collected by the receiver optics of the LiDAR sensor and the noise input bandwidth. For a laser pulse incident on a diffuse circular target with a diameter equal to the diameter of the laser footprint, the ratio between the power collected by the receiver optics P_r and the power transmitted P_t (otherwise known as the intensity, I) is given by [Baltsavias, 1999]:

$$I = \frac{P_r}{P_t} = \frac{\rho}{\pi}\frac{M^2 A_r}{R^2}, \tag{2.27}$$

where ρ/π is an assumed Lambertian (diffuse) bidirectional reflectance distribution function (BRDF), M is the atmospheric transmission, and A_r is the receiver area. Essentially if the dimensions of the sensor optics are fixed and atmospheric transmission is constant, the intensity depends on the range of a target and its reflectivity.

Natural surfaces can produce diffuse, specular, or diffuse *and* specular reflection, at different laser wavelengths λ, depending on the surface rms roughness height σ. In general, an optically smooth surface ($\sigma < \lambda$) causes specular reflection and an optically rough surface ($\sigma \geq \lambda$) causes diffuse reflection [Ogilvy, 1991]. The underlying condition for active optical geometrical measurements is that the measured surface is opaque, diffusely reflecting and uniform at the wavelength of interest.

Modern, medium-range terrestrial laser scanners commonly use a laser with a wavelength between 500 nm (green) and 1050 nm (near infrared, NIR). Laser pulses at both green and NIR consistently experience diffuse reflection from snow and ice, although the surface reflectivity of snow and ice is higher at green than at NIR [Perovich, 1996; Wehr and Lohr, 1999; Prokop, 2008]. In spite of this, pulses at green wavelengths will penetrate the surface of snow or white ice by a few mm/cm, with volume scattering therefore contributing to laser returns. The reflectance of snow, expressed as the fraction of reflected versus emitted radiation, is >0.95 at 500 nm but is only 0.40-0.85 at 1050 nm, and decreases with snow grain size. Laser pulses at NIR wavelengths consistently experience specular reflection from water surfaces. Although laser pulses at green wavelengths also experience specular reflection from water surfaces at low incidence angles, they typically penetrate water when the incidence angle is close to nadir [Wozencraft and Millar, 2005].

2.4.2.2. Angular Resolution and Beam Divergence

The spatial distribution of LiDAR measurements acquired over a surface normal to the scan origin is controlled by the angular sampling resolution Δ and the diameter of the laser beam D. The beam diameter expands from the radius at the origin (or 'beam waist') ω_0 as [Weichel, 1990]:

$$D = 2\omega_0 \sqrt{1 + \left(\frac{\lambda R}{\pi \omega_0}\right)^2}. \tag{2.28}$$

If $D \ll R$, the laser footprint diameter on the surface across the scanning track of the beam $D_{f_{across}}$ can be expressed as a function of R and the far-field laser beam divergence δ [Baltsavias, 1999]:

$$D_{f_{across}} = 2R \tan\left(\frac{\delta}{2}\right), \tag{2.29}$$

For a Gaussian-shaped transversal beam profile, δ is given by Beraldin et al. [2010]:

$$\delta = \frac{\lambda}{\pi n \omega_0}, \tag{2.30}$$

where n is the refractive index of the propagation medium ($n_{air} \sim 1$). δ is characterized by the laser wavelength and focusing optics of a LiDAR system and is typically reported by the instrument manufacturer. For a surface which is normal to the scan origin (i.e., at nadir), the laser footprint diameter on the surface along the scanning track $D_{f_{along}}$ is equal to $D_{f_{across}}$. However, if the scan origin is inclined by angle θ from nadir:

$$D_{f_{along}} = \frac{2R\cos\theta\sin\delta}{\cos 2\theta + \cos\delta}. \tag{2.31}$$

The laser footprint on the surface becomes elongated along the track of the beam when θ > 0. At sufficient R and/or θ, the footprint diameter exceeds the minimum distance between independent LiDAR samples (which is defined by the smallest available angular sampling resolution Δ), and the true spatial resolution is then limited by Δ. Fine details are effectively blurred as sequential laser footprints overlap beyond a threshold optimal spacing Δx_{opt} (or in the frequency domain, above the cut-off frequency μ_c).

Lichti and Jamtsho [2006] modelled the spread of LiDAR points from a terrestrial scanning location as a function of both the angular sampling interval and laser beam diameter using average modulation transfer functions (AMTFs). By equating μ_c for the sampling interval and beam diameter AMTF they identified Δx_{opt} as 86% of the laser beam diameter.

2.4.2.3. Factors Affecting the Sampling Resolution

Equations 2.29 and 2.31 can be used to calculate the maximum density of LiDAR measurements P_{max} projected onto a level surface from a single terrestrially-located scan position as:

$$P_{max} = \frac{\cos\theta}{\left(0.86\, D_{f_{across}}\right)\left(0.86\, D_{f_{along}}\right)}, \tag{2.32}$$

based on the optimum point spacing Δx_{opt} criterion of Lichti and Jamtsho [2006]. As a case study, and following Polashenksi [2011], the density of measurements projected onto a 100 x 100 m surface are estimated from a total of four scan positions, one located at each corner of the surface. For the *Leica Scanstation C10* laser scanner the (Gaussian-width) beam divergence δ is 0.14 mrad and, since the instrument is typically mounted on a tripod while scanning, it is assumed that the instrument origin is fixed at a height of 2.5 m above the surface. The farthest range from any single scan position is approximately 70 m at the centre of the surface (Figure 2.8a). P_{max} is at least 68 points per m^2, equating to a mean horizontal spacing between LiDAR measurements of at most 0.12 m, at the centre of the surface (Figure 2.8b).

However, natural surfaces are rarely level, typically containing topography with various length scales. This includes sea ice surfaces, as described in this chapter. The incident laser beam angle θ is decreased if the surface topography is inclined toward the scanner but is increased if the topography is inclined away from the scanner. If the surface is inclined from horizontal greater than $(90-\theta)°$ in the opposite direction to the scanner, the surface will be occluded (shadowed) from the scanner's perspective.

An estimate of the cumulative surface slope distribution of undeformed first-year sea ice was obtained by the author from LiDAR measurements of sea ice topography collected in Resolute Bay, Nunavut in June 2011. The probability that a 1 x 1 m grid cell of the case study surface will be completely shadowed could then be calculated by comparing the slope distribution with θ (Figure 2.8c). Over the entire surface, <0.5% is in shadows of 1 m^2 size. In other words, one can expect less than 50 of 10,000 grid cells to be shadowed.

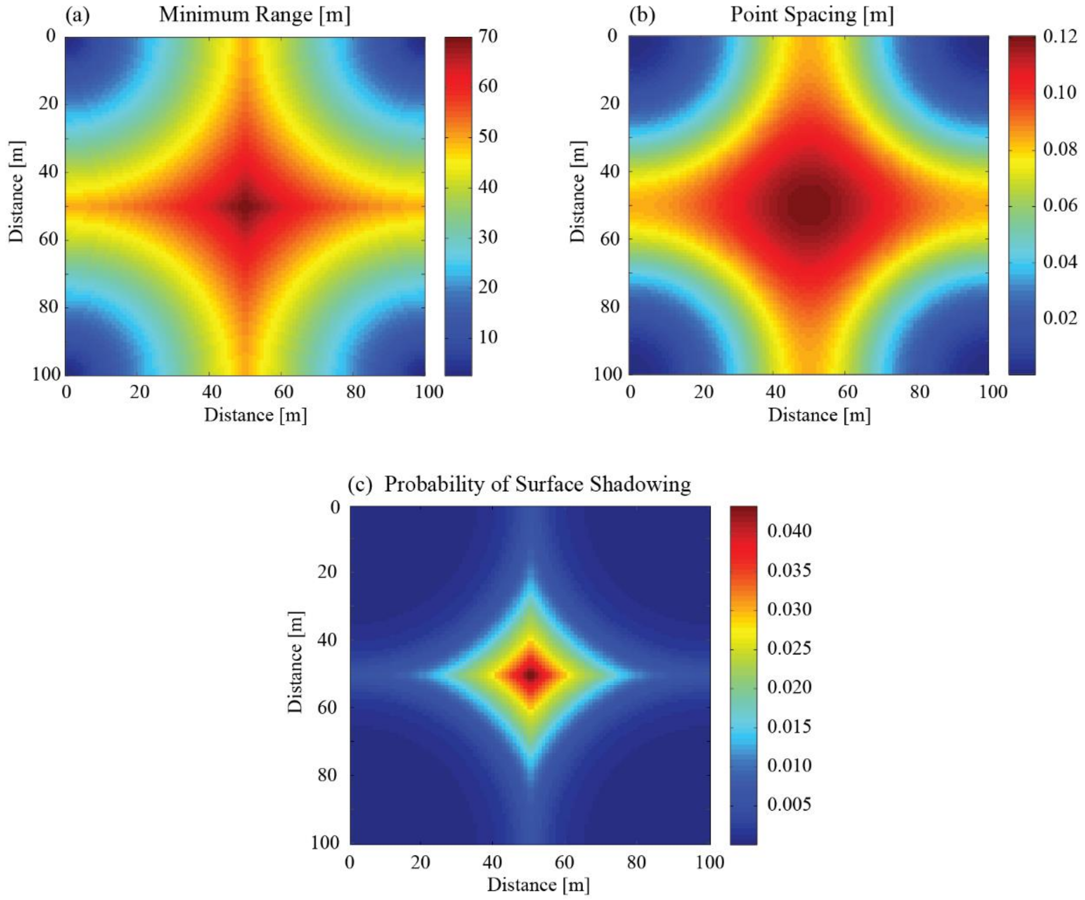

Figure 2.7 | LiDAR sampling parameters projected onto a 100 x 100 m surface: (a) minimum range; (b) mean point spacing; (c) probability of surface shadowing.

2.4.2.4. Registration

The first step after acquiring LiDAR data is to merge individual scans of the same area (taken from different azimuth angles) by registering the scans to a single global coordinate system (GCS). This is usually achieved by manually locating a set of reflective targets in each scan that were mounted inside or adjacent to the target area while scanning. A transformation matrix is then created which fits each individual scan into the GCS by translating and rotating points in three dimensions, while minimizing the root mean square of the residual distances between real target positions and their ideal virtual positions in the GCS [Beraldin et al., 2010].

Alternatively, multiple scans can be registered without targets using (mostly proprietary) algorithms that perform automated ‘cloud-to-cloud’ matching. Here the term cloud refers to a so-called ‘cloud’ of raw, unprocessed LiDAR points. Cloud-to-cloud matching algorithms typically require the user to select a few tie-points between different scans (i.e., points from approximately the same xyz location) and then iteratively translate and rotate the point clouds so as to minimize the root mean square of the orthogonal distances between all points. Such algorithms can only be successful when a significant number of matches (i.e., analogous points from different scans) are available [Bae and Lichti, 2008].

2.4.2.5. Filtering

At this stage, a registered LiDAR data set may be suitable for use. However, a data set will still typically contain outlying points and/or points from objects within the target area that are either redundant or prevent further analysis. For instance, outlying points located well above or below the true level of a surface can be produced by multi-path errors [Petrie and Toth, 2008], and have to be removed. If the objective of a LiDAR scan is to measure the local terrain elevation, points generated as the scanner interacts with e.g. overlying vegetation, buildings or precipitation, must also be removed. Of course there is no vegetation and there are no buildings on sea ice in the Arctic, but precipitation, in the form of snow or rain, can produce thousands of unwanted points above the ice surface.

The process of removing unwanted LiDAR points from a raw point cloud is described as filtering [Sithole and Vosselman, 2004]. Simple threshold-based algorithms can be used to filter points above or below a specified elevation. However, in the case of precipitation on sea ice, a selection of points will be located below the elevation of the tallest feature (e.g., snow drift or pressure ridge) at the ice surface, when snowflakes or rain drops are just above the terrain (Figure 2.8a). In this case, sophisticated algorithms are required to remove unwanted points while retaining points on the terrain. A wide variety of filtering algorithms have been developed, commonly with the aim of removing vegetation and buildings from scans of temperate and urban landscapes. These algorithms generally use mathematical morphology, clustering, or segmentation [Sithole and Vosselman, 2004], to separate terrain points from non-terrain points.

Here the two most suitable algorithms for filtering precipitation from an undulating, snow drift covered sea ice surface are described in detail:

Morphological Slope-based Filter [Vosselman, 2000]

This filter approximates the local geometrical structure of the terrain using a morphological structuring element, usually in the form of an inverted funnel (Figure 4.4b). The structuring element defines the maximum permitted height difference between two points with respect to the distance between them. A sharply inclined funnel is less tolerant to discontinuities in terrain elevation. At *(i)* in Figure 4.4b a LiDAR return from precipitation is incorrectly classified as terrain because it is within the bounds of the structuring element. At *(ii)* a LiDAR return from steep terrain is incorrectly classified as non-terrain because it is outside the bounds of the structuring element.

Progressive TIN Densification Filter [Axelsson, 2000]

This filter first derives a sparsely populated TIN (triangular irregular network) from LiDAR points located at neighbourhood minima (Iteration 0 in Figure 4.4c). In each subsequent iteration, a point is added to the TIN if it meets certain criteria in relation to the triangle which contains it, thereby progressively densifying the TIN. These criteria are that a point must be within a minimum inclination angle φ and distance r of the nearest triangle node. At the end of each iteration the TIN is recomputed and new criteria are obtained from the frequency distributions of the angular and dimensional properties of the new TIN's facets. The iterative process ends when no more points are classified below these thresholds. At *(iii)* and *(iv)* in Figure 4.4c two LiDAR returns from the terrain are still classified as non-terrain at the current iteration (Iteration 3) because they are not within φ or r of their closest TIN nodes.

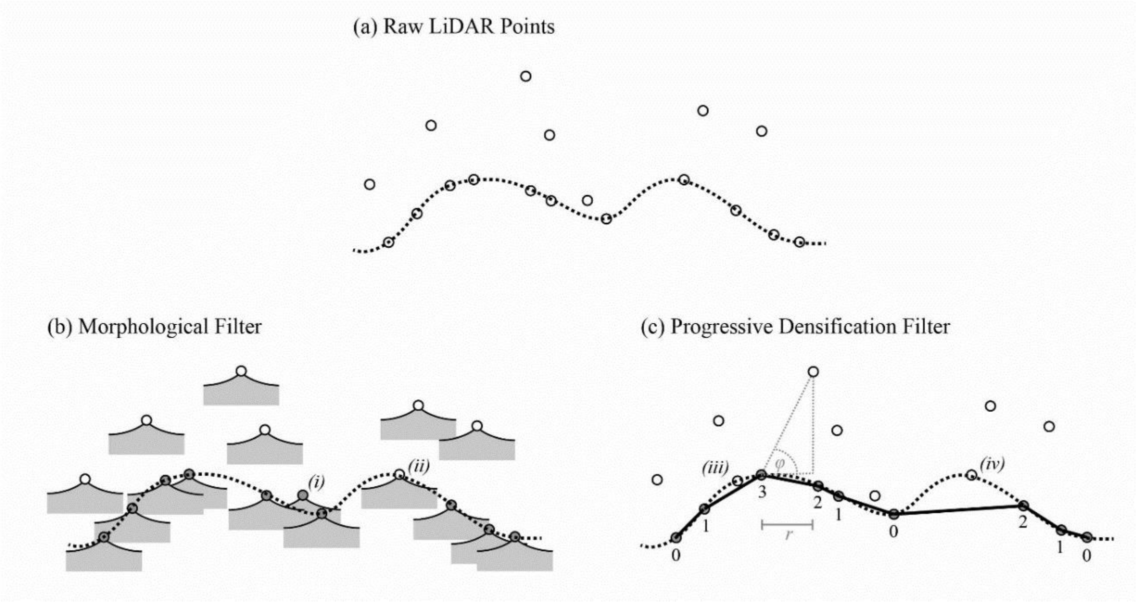

Figure 2.8 | Schematic diagrams of: (a) LiDAR returns (circles) from the surface of sea ice (dotted line) and falling snow; (b) the morphological slope-based filter of Vosselman [2000]; and (c) the progressive TIN densification filter of Axelsson [2000]. LiDAR returns are highlighted as either terrain in grey or non-terrain (i.e., precipitation) in white. In (b) the morphological structuring element is illustrated by the inverted grey funnel, and the annotations *(i)* and *(ii)* are referred to in the text. In (c) points are classified as terrain or non-terrain at sequential iterations of the algorithm (numbers below points), and the annotations *(iii)* and *(iv)* are referred to in the text.

2.4.2.6. Terrain Modelling

The only way to preserve all of the information in a filtered LiDAR data set is to keep it in its original three-dimensional form. However, it is usually desirable to resample the points to a regular two-dimensional gridded surface of the form $Z(x, y)$, commonly referred to as a digital terrain model (DTM), for further analysis. If the data is kept in its original form, further analysis may be biased by: (1) outliers that were not removed at the filtering stage, and/or (2) areas that were under- or over-sampled with respect to the mean point density [Smith et al., 2005].

Terrain modelling is implemented by arranging a regular grid over the LiDAR data and calculating the elevation of each grid cell as the maximum, minimum or mean of point elevations within the cell, or by interpolating between points. Studies have shown that sophisticated interpolation techniques such as kriging or tension splines are most suitable for modelling geospatial data when the sampling interval between points is larger than the grid cell size [Smith et al., 2005]. However, when the sampling interval between points is smaller than the grid cell size, linear interpolation is more suitable than either of these methods, as it is not predisposed to fit a smooth surface between points and therefore helps to preserve most of the information in the original data.

2.5. Conclusion

In this chapter we have evaluated the critical role of sea ice surface topography in the Arctic marine system. The surface topography evolves as the sea ice cover forms, ages and is affected by various dynamic and thermodynamic processes.

The topography of new ice depends on the conditions present during ice formation. For instance, a calm ocean promotes the formation of nilas and frost flowers, whereas a turbulent ocean promotes the formation of pancake ice. The energy budget of the sea ice cover controls how the initial surface topography changes as the sea ice grows and decays. Snow is deposited and redistributed at the sea ice surface between autumn and spring, modifying the surface topography considerably. The snowpack physical properties change as snow grains metamorphose in response to air temperatures and boundary-layer winds drive the formation of snow drifts. Snow-drift topography at the onset of melt controls the initial locations of melt ponds at the sea ice surface. Melt ponds then generally evolve in stages which depend on the sea ice energy budget, the permeability of the ice cover, and changes in the surface topography. The dynamic flow of meltwater across the sea ice surface, and differential melt caused by variations in surface albedo between white ice and melt ponds, both affect changes in surface topography throughout the summer melt season. When a sea ice floe is unrestricted it moves on the ocean, and the velocity of motion primarily depends on wind-drag, which increases as the roughness of the surface topography increases. Collisions between mobile ice floes can cause the ice cover to deform, creating pressure ridges of ice blocks that increase the roughness of the macro-scale topography considerably.

Active microwave remote sensing (radar) measurements of sea ice are affected by the sea ice topography. Microwaves can be scattered at the interface between layers of the sea ice cover (air-snow, snow-ice, or air-ice) if the dielectric contrast is sufficiently high. The degree of backscattering can significantly depend on the roughness of the micro- and meso-scale surface topography, if the scale of roughness is similar to the frequency of the microwave radiation.

Traditional techniques for measuring surface topography at the relevant scales for sea ice research, including micro-scale (<0.1 m) and meso-scale topography (0.1-100 m), are limited. In situ profile-based measurements of the surface topography are characteristically imprecise. On the other hand, satellite data typically do not have adequate spatial or temporal resolution to resolve changes in surface features, such as snow drifts and melt ponds, which affect and are affected by the topography.

Light Detection and Ranging (LiDAR) offers an effective solution to these challenges. State-of-the-art terrestrial LiDAR systems can be used to obtain three-dimensional measurements of surface topography over areas >10,000 m^2 in size, at sub-centimeter sampling resolution and precision, in just a few hours. The key benefit of terrestrial LIDAR is that it provides a rapid and effective option for characterizing (i.e. measuring and understanding) the physical properties of a surface, which cannot be achieved using traditional in situ or remote sensing techniques. LiDAR can therefore be exploited to verify and support remotely sensed satellite data, which is the subject of the following four chapters.

Chapter 3. Parameterization of Centimeter-Scale Sea Ice Surface Roughness using Terrestrial LiDAR

A peer-reviewed scientific research paper published in:

IEEE Transactions on Geoscience and Remote Sensing, 53(3), 1271-1286,

doi.org/10.1109/TGRS.2014.2336833

Jack C. Landy[*1], Dustin Isleifson[1,2,3], Alex S. Komarov[1,2], David G. Barber[1]

[*] Corresponding Author

[1] Centre for Earth Observation Science, Department of Environment and Geography, University of Manitoba, Winnipeg, Manitoba, Canada.

[2] Department of Electrical and Computer Engineering, University of Manitoba, Winnipeg, Manitoba, Canada.

[3] now at: Radarsat Constellation Mission, Magellan Aerospace, Winnipeg, Manitoba, Canada.

Abstract

Microwave scattering from sea ice is partially controlled by the ice surface roughness. In this paper we propose a technique for calculating two-dimensional centimeter-scale surface roughness parameters, including the rms height, correlation length and form of autocorrelation function, from three-dimensional terrestrial Light Detection and Ranging (LiDAR) data. We demonstrate that a single scale of roughness can be extracted from complex sea ice surfaces, incorporating multiple scales of topography, after sophisticated two-dimensional detrending, and calculate roughness parameters for a wide range of artificial and natural sea ice surface types. The two-dimensional technique is shown to be considerably more precise than standard one-dimensional profiling techniques and can therefore characterize surface roughness as a stationary single-scale process, which a one-dimensional technique typically cannot do. Sea ice surfaces are generally found to have strongly anisotropic correlation lengths, indicating that microwave scattering models for sea ice should include surface spectra that vary as a function of the azimuthal angle of incident radiation. However, our results demonstrate that there is no fundamental relationship between the rms height and correlation length for sea ice surfaces if the sampling area is above a threshold minimum size.

3.1. Introduction

Active microwave remote sensors can provide valuable insight into the geo-thermo-physical conditions of snow-covered sea ice [Barber, 2005]. Radar scattering signatures are linked to geophysical parameters through microwave scattering models [Winebrenner et al., 1992], which can include separate formulations for surface and volume scattering within layered snow and ice media [Fung, 1994]. Modeled backscatter is particularly sensitive to variations in roughness at the air-snow or snow-ice interface, when the dielectric contrast between layers is high. So it is important that the statistical parameters characterizing surface roughness correctly describe the physical properties of a rough interface. However, conventional techniques for in situ measurement and analysis of surface roughness are limited [Ogilvy, 1991; Verhoest et al., 2008], and incorrect values for the surface roughness parameters introduce significant bias into modeled backscatter [Verhoest, et al. 2008].

Surface roughness is generally treated as a stationary, single-scale random process, describing height deviations from a reference level, in microwave scattering models [Ogilvy, 1991]. In reality, natural surfaces are characterized by an aggregate of several superimposed scales of roughness, created by various physical forcing mechanisms. Sea ice comprises three general length scales: macro (>100 m; level or ridged ice), meso (0.1-100 m; snow drifts), and micro (<0.1 m; frost flowers, snow grains or bare ice) [Manninen, 1997; Paterson et al., 1991]; and roughness at each of these scales is a product of dynamic and/or thermodynamic forcing. For instance, strong winds can cause ice ridging, snow drift redistribution and snow or ice surface scouring, potentially modifying surface roughness at all three scales.

It is common practice to remove or ‘detrend’ large-scale topography from a natural surface and consider micro- and meso-/macro-scales of roughness separately in scattering models [Ogilvy, 1991]. The single-scale assumption is then valid for small-scale roughness, and large-scale topography can be characterized as a distribution of surface slopes (or inclination angles) on which the small-scale roughness is superimposed. In other words, rough surfaces are tilted towards or away from the incident radiation beam and the reference level for characterizing small-scale roughness is represented by large-scale topographic trend.

The goal of this study is to develop a method for calculating surface roughness parameters from three-dimensional elevation data acquired with a terrestrial LiDAR instrument. In Section 3.2 we review surface roughness theory and the conventional techniques for measuring surface roughness. In Section 3.3 we outline a procedure for collecting and preprocessing the LiDAR data and introduce two 2-D detrending algorithms for removing large-scale topography. In Section 3.4 we present roughness parameters calculated from natural and artificial snow and sea ice surfaces, in both one and two dimensions, and evaluate the sensitivity of calculated roughness parameters to variations in the sampling approach. In Section 3.5 we discuss potential sources of error in the LiDAR measurements and roughness parameters, and the implications of our results for microwave scattering from sea ice. Finally, in Section 3.6 we conclude.

3.2. Background

For a two-dimensional random rough surface, $\zeta(\boldsymbol{\rho}')$, with zero average value $\langle\zeta(\boldsymbol{\rho}')\rangle = 0$, where $\boldsymbol{\rho}' = \{x, y\}$ is a position vector in the horizontal plane [Tsang et al., 2000]:

$$\sigma^2 = \langle\zeta^2(\boldsymbol{\rho}')\rangle \tag{3.1}$$

where σ is the root-mean square (rms) roughness height. For a stationary random process, the normalized autocorrelation function is given by:

$$C(\boldsymbol{\rho}) = \frac{\langle\zeta(\boldsymbol{\rho} + \boldsymbol{\rho}')\, \zeta(\boldsymbol{\rho}')\rangle}{\langle\zeta^2(\boldsymbol{\rho}')\rangle} \tag{3.2}$$

where $\boldsymbol{\rho}$ is the shift vector in the horizontal plane. The correlation length, l, is the absolute value of $\boldsymbol{\rho}$ for which $C(\boldsymbol{\rho}) = e^{-1}$. l can then be defined with respect to the azimuth angle, φ, as follows:

$$C(l(\varphi)\cos\varphi\, , l\,(\varphi)\sin\varphi) = e^{-1} \tag{3.3}$$

The eccentricity of the surface correlation, a measure of the roughness isotropy, is:

$$\epsilon_l = \sqrt{1 - \left(\frac{\min(l)}{\max(l)}\right)^2} \tag{3.4}$$

Following the notation of [Fung et al. 1994], if l is independent of φ, i.e. the surface is isotropic, the exponential correlation function is given by:

$$C(\boldsymbol{\rho}) = exp\left(-\frac{\rho}{l}\right) \tag{3.5}$$

and the Gaussian correlation function is given by:

$$C(\boldsymbol{\rho}) = exp\left(-\frac{\rho^2}{l^2}\right) \tag{3.6}$$

A generalized power-law correlation function is therefore:

$$C(\boldsymbol{\rho}) = exp\left[-\left(\frac{\rho}{l}\right)^n\right] \tag{3.7}$$

where $1 < n < 2$, so that the function converges to the exponential or Gaussian as n approaches 1 or 2, respectively.

Drinkwater [1989] found that the rough surface of level undeformed ice was best described by exponential $C(\boldsymbol{\rho}')$ (hereafter referred to only as C), whereas deformed ice was best described by Gaussian C. It was assumed that the exponential function, which is characterized by smaller correlations at shorter lag distances than the Gaussian function, was identifying micro-scale roughness features over the undeformed ice that were not present over the deformed ice. But a later study showed that rough surfaces from both level and deformed ice mostly conformed to exponential C [Manninen, 1997], which suggests that the sampling interval used by Drinkwater to discretize roughness on the ice surface (~1 cm) may not have been small enough to properly characterize the measured correlation function [Drinkwater, 1989].

The choice of the sampling interval (Δx) and the sampling extent (L), can have a profound effect on the derived roughness parameters. Several groups have used numerical methods to simulate the effect of sampling interval on roughness parameters. Ogilvy and Foster determined that a sampling interval of $0.1l$ is required to differentiate between exponential and Gaussian C [Ogilvy and Foster, 1989] and a later study has shown that an interval of $0.2l$ is required to accurately calculate the correlation length [Oh and Kay, 1998]. Ulaby et al. suggested that the sampling interval should be no higher than 0.1 of the microwave observable wavelength (i.e. the wavelength at C-band is ~5.5 cm, so the sampling interval should be no more than ~5.5 mm) [Ulaby et al., 1982].

Numerous studies have also demonstrated that roughness parameters are dependent on sampling extent (the length of a profile or area of a surface) up to a limit (L_{min}), approached asymptotically with increasing extent [Manninen, 1997; Oh and Kay, 1998; Nishimoto, 2010]. Below L_{min} the rms height and correlation length are underestimated because the measured profile fails to capture surface height extrema and cannot be assumed to be stationary [Ogilvy, 1991; Vehoest et al., 2008]. If the measured profile is not stationary, σ and l will change when shifted in space. Estimates for L_{min} from numerical simulations are not in agreement, however, with Oh and Kay [1998] reporting that L_{min} should be at least $40l$ and $200l$ for the determination of σ and l with an error of <10%, respectively, and Nishimoto [2010] reporting the same criteria as $240l$ and $458l$, respectively. Owing to the dependency of σ and l on L, attempts have been made to characterize rough surfaces using band-limited fractals, e.g. [Manninen, 1997; Mattia and LeToan, 1999]. However, backscatter models typically require that surface roughness is treated as a single-scale process, so research into this area has not been widely pursued.

Field- or laboratory-based surface roughness measurements have generally been made along discrete one-dimensional profiles, using either contact or non-contact instruments. Detailed descriptions of the methods used to collect surface roughness data over snow and sea ice are rare, so we include studies targeting, for example, soil or outcrop roughness, as we review these techniques. Contact instruments include the stylus profilometer [Manninen, 1997; Mathia et al., 2011], meshboard [Mattia et al., 2003], and pin profiler

[Bryant et al., 2007]. The key disadvantage of a contact instrument is that it can interfere with the physical properties of the surface, especially if the surface comprises fragile structures, such as newly fallen snow. Moreover, these instruments typically also have limited horizontal resolution and extent, for example standard pin profilers include pins with 1 cm spacing [Jester and Klik, 2005] and both these and stylus profilometers are generally limited to 1-m long transects [Manninen, 1997]. Non-contact techniques include photographing a surface against a background grid [Paterson et al., 1991; Manes et al., 2008] and, most commonly, laser profiling [Drinkwater, 1989; Callens et al., 2006; Gupta et al., 2012]. These instruments do not disturb the surface, and can generally sample at spatial resolutions of <1 cm, but only the laser profiler can measure transects with a length greater than ~1 m.

The vast majority of these techniques, both contact and non-contact, are vulnerable to errors introduced by inadequate sampling interval and/or extent [Callens et al., 2006]. But a fundamental limitation of all profiling techniques is that one-dimensional statistics are assumed to represent two-dimensional surface properties, which is not always the case [Callens et al., 2006]. Individual profiles across a surface may not be translationally invariant (causing roughness statistics to vary considerably between adjacent profiles) and, consequently, the surface cannot be assumed to be stationary [Ogilvy, 1991]. One-dimensional profiles also fail to identify anisotropy in surface roughness which, for example, has previously been measured over snow on sea ice [Manninen, 1997].

So a few groups have started to experiment with techniques such as photogrammetry [Warner, 1995; Jester and Klik, 2005], and dual-axis laser scanning (or LiDAR) [Jester and Klik, 2005; Vryant et al., 2007; Gutierrez et al., 2007; Pollyea and Fairley, 2011], for characterizing surface roughness in two-dimensions. But the methods for analyzing surface roughness from the three-dimensional elevation data obtained with these instruments vary. For instance, Bryant et al. [2007] calculated σ as the mean of 20 (or more) 1-m profiles extracted from LiDAR elevation models, whereas Jester and Klik [2005] calculated σ as the overall rms roughness height of a two-dimensional surface grid, obtained with a downward-looking, traversing laser scanner. These are preliminary studies and, to our knowledge, there has not yet been any research published on the extraction of complex roughness parameters, such as C and l, from two-dimensional LiDAR data.

It is not only the measurement technique but also the method for detrending surface roughness data that varies between studies. Many groups implicitly assume that surface height only varies in one direction, i.e. perpendicular to the principal plane, within the sampling extent. So data are detrended by fitting a mean line through a profile by ordinary least-squares regression (OLSR) and assessing surface roughness with respect to this local datum [Manninen, 1997; Bryant et al., 2007; Gupta et al., 2012]. These regression lines can be fit through the entire profile or multiple smaller segments [e.g. Bryant et al., 2007]. Pollyea and Fairley [2011] updated this approach by considering orthogonal distance regression (ODR) planes, rather than OLSR planes, through three-dimensional LiDAR surface elevation data, that are robust to principal axis orientation. These techniques can introduce erroneous ‘jumps’ between profiles or segments at the intersection between adjacent regression lines, over surfaces with high topographic relief [Callens et al., 2006]. Higher-order polynomials have been used to detrend non-linear topography from surface profiles [Callens et al., 2006; Verhoest et al., 2008]. However, the natural surfaces of agricultural fields or sea ice, for example, rarely demonstrate topographic trends that can be described by linear or non-linear functions. And, in these circumstances, a highpass filter based on the Fast Fourier Transform (FFT), which removes all spatial frequencies lower than a specified cutoff frequency from the topography, has proved to be more effective than linear or polynomial detrending techniques [Callens et al., 2006]. In any case, incorrect detrending introduces systematic bias into surface roughness statistics.

3.3. Methods

3.3.1. Data Collection and Preprocessing

A Leica Scanstation C10 laser scanner was used to measure snow and sea ice surface roughness at an experimental ice tank facility (SERF: Sea-ice Environmental Research Facility) on the University of Manitoba Campus (Winnipeg, Canada) and at three locations in the Canadian High Arctic (Table 3.1). The SERF is an outdoor pool containing artificial seawater that was used to grow various types of sea ice during the winters of 2012 and 2013. Because the laser scanner is highly sensitive to movement and vibrations, it cannot be mounted to a ship or drifting station, and is therefore only a practical option for measuring surface roughness when ice is thick enough to support the weight of the scanner directly (above ~20 cm). But the SERF poolside provided a stable vantage point for scanning newly-formed ice with a thickness of less than a centimeter. Surface roughness measurements were obtained from four types of sea ice grown in the SERF pool: (1) bare congelation ice, (2) refrozen slush, caused by seawater flooding bare ice, (3) pancake ice, and (4) frost flowers (Figure 3.1a-d). Ice physical properties depended on variations in environmental forcing mechanisms, such as temperature and wind speed at the air-pool interface, especially during the earliest stages of ice formation. For more information on the diverse processes contributing to sea ice formation and growth, see Petrich and Eicken [2010].

Table 3.1 | Properties of forty LiDAR sections, collected over various types of sea ice at different stages of evolution, used in the study to investigate snow and ice surface roughness. 'Thickness' refers to the approximate mean sea ice thickness at the time of acquisition. 'Stage' and 'Hour' refer to the stage of ice development and number of hours since initial ice formation, respectively. 'No. Sections' refers to the number of individual LiDAR sections obtained for an ice type or stage of evolution.

Snow/Ice Type	Code	Location	Thickness [cm]	Stage (Hour)	No. Sections
Bare Congelation Ice	BI	SERF	7		3
Refrozen Slush	RS	SERF	8		3
Pancake Ice	PI	SERF	5	I (15)	3
			9	II (37)	3
			11	III (61)	3
Frost Flowers	FF	SERF	0.5	I (9)	4
			1	II (11)	3
			2	III (16)	3
			5	IV (64)	4
Wet Snow	S	Resolute*	100		1
Superimposed Ice	SI	Resolute*	100		1
First-Year White Ice	FYI	Resolute*	100		5
Multi-Year White Ice 1	MYI1	Beaufort Sea**	430		2
Multi-Year White Ice 2	MYI2	Beaufort Sea***	360		2

Approx. Lat/Lon: * 74.73 N 95.58 W, **74.86 N 128.30 W, ***75.03 N 128.98 W.

Surface roughness measurements were obtained in the field by mounting the laser scanner directly on natural sea ice and sampling adjacent areas. Three field locations were selected, including: landfast seasonal (or ‘first-year’) sea ice in Resolute Passage, Nunavut, sampled in the early melt season during June 2012, and two perennial (or ‘multi-year’) sea ice floes in the Beaufort Sea, sampled late in the melt season during August 2011 (Table 3.1). In Resolute Passage we first measured the roughness of the wet snowpack surface on June 9 (Figure 3.1e), then carefully cleared the snow to expose and sample a layer of superimposed ice [Granskog et al., 2006] at the snow-ice interface (Figure 3.1f). After the snow cover melted completely, we measured the roughness of drained white ice [Maykut and Grenfell, 1975] at the sea ice surface on June 19 (Figure 3.1g). We could only measure the roughness of white ice hummocks on multi-year sea ice in the Beaufort Sea (Figure 3.1h), as the snowpack had melted long before we sampled in August.

The experimental setup was kept consistent between locations to ensure that results from the ice tank and field sites were comparable. Before sampling, the instrument was heated in a custom-built case to an operational temperature above 0 °C, and then mounted on a level tripod. At the ice tank, the scanner and tripod were set up on a scaffold next to the pool, whereas at the field sites they were set up on a custom-made platform directly on the ice. In both situations the scanning origin was elevated to a height of 2.5-3 m above the target surface. The maximum range of the target surface from the scanner was consistently ~10 m.

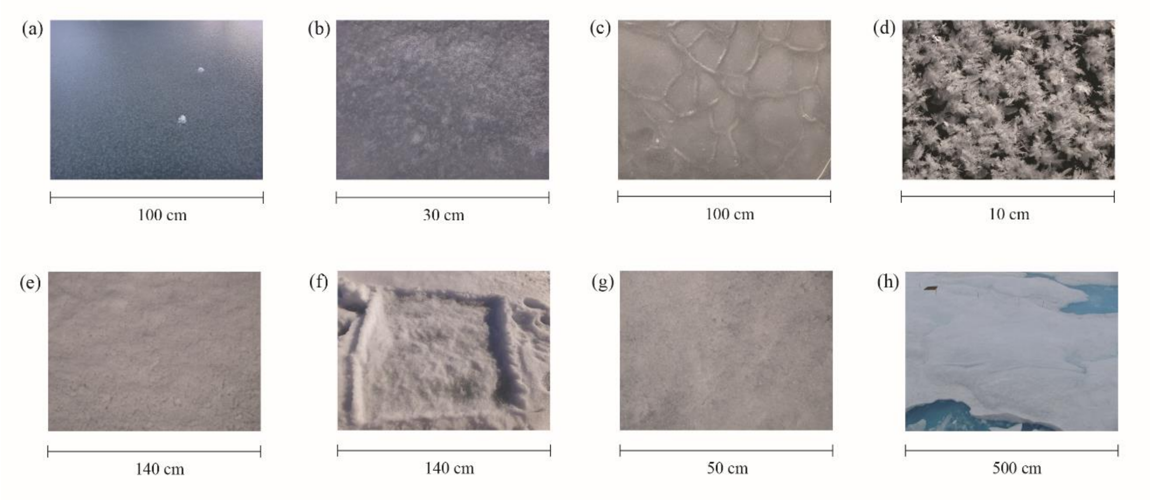

Figure 3.1 | Photographs of sea ice surfaces measured for roughness, including the following: (a) bare congelation ice, (b) refrozen slush, (c) pancake ice (at stage II, hour 38), (d) frost flowers (at stage III, hour 16), (e) wet snow on FYI, (f) superimposed ice cleared of the snow in photograph (e), (g) drained white ice surface on FYI, and (h) drained white ice surface on MYI. Approximate scales are given under each photograph.

The Scanstation C10 is a discrete-pulse laser scanner that emits pulses of energy (532 nm wavelength) at a pulse repetition frequency of up to 50 kHz. It subsequently records the time-of-flight for each pulse to be reflected by objects in the target area and return to the scanner, thereby mapping the target in three dimensions. However, the snow and ice surfaces of interest in this study are not entirely opaque to the green light of the Leica C10, but rather reflect by backscattering from a transparent media [Perovich, 1996]. The laser may penetrate into the snow or ice several mm, and multi-path interactions will then spread the pulse return in time. The scanner computes the range from the first pulse return that has a backscattering intensity above an instrument-defined threshold. The method presented herein makes the fundamental assumption that the main source of the backscatter is from the surface of the medium, so the first valid return must generally be from surface rather than volume scattering. This assumption is supported by measurements of the reflectance and polarization of light from sea ice and by empirical experiments which are outlined below. Past observations have demonstrated that green light which is reflected from a variety of ice types (including: glazed melting snow, melting white ice, blue ice, bare congelation ice, and pancake ice), at a low incidence angle, is strongly polarized [Perovich, 1994; 1998]. This implies a substantial contribution from specular reflection in the direction of the light source [Perovich, 1994]. The small amount of light which experiences volume scattering within the upper portion of the ice would be backscattered approximately uniformly over the hemisphere. Therefore the returning laser pulse would include a strong defined front from surface backscatter and a long undefined tail from volume backscatter. The sensor would routinely compute a ranging estimate from the time-of-flight of the pulse front.

The minimum sampling interval of the scanner depends on the range of the target R, the inclination of the target surface with respect to the scanning origin θ, and the beam divergence of the laser δ. If the laser footprint diameter D_f is small compared to R [Baltsavias, 1999]:

$$D_f = 2Rtan\left(\frac{\delta}{2}\right) \tag{3.8}$$

The cross-section of the laser beam's power distribution is Gaussian and therefore it is beneficial that the angular sampling interval of the scanner Δ is smaller than δ, to yield a higher Nyquist frequency. Licthi and Jamtsho [2006] have demonstrated that the optimal angular sampling interval Δ_{opt} = 0.859δ. Using this criteria, the optimal horizontal sampling interval of the C10 scanner x_{opt} is 2.06 mm at a range of 10 m. However, along the track of the laser beam D_f becomes elongated if $\theta > 0$ and, in our scans, θ ranged from approximately 45-70°. We can derive the along-track footprint diameter $D_{f_{along}}$ as:

$$D_{f_{along}} = \frac{2R \cos\theta \sin\delta}{\cos 2\theta + \cos\delta}. \tag{3.9}$$

$D_{f_{along}}$ is approximately 2 mm at a range of 5 m (when $D_{f_{across}}$ is 1.2 mm) and is approximately 8 mm at a range of 10 m (when $D_{f_{across}}$ is 2.1 mm). The optimal along-track sample spacing x_{opt} is therefore 1.7 mm at a range of 5 m and 6.8 mm at 10 m range, using the criteria of Lichti and Jamtsho [2006]. Based on these calculations, consecutive samples may have become slightly correlated in the along-track direction during scanning, which could have affected the isotropy of the roughness calculations (see Section 3.5.1).

As a compromise between the theoretical optimal along- and across-track sample spacing, scanning area, scanning time, and the sampling interval criteria [Ulaby et al., 1982; Ogilvy and Foster, 1989; Oh and Kay, 1998], the scanner was configured so that the spacing between points along- and across-track was 2 mm at the selected maximum range (typically around 10 m). Preliminary analysis of test scans showed that regular mm-cm scale physical features of the sea ice surface (e.g. frost flowers) could be observed with this spatial resolution. The time required to scan a single ~25-50 m^2 target at this resolution ranged from 30 to 60 minutes. Reported values for the correlation length of Arctic sea ice are generally above one centimetre [Onstott, 1992], so a sampling interval of at least 2 mm satisfies the requirements given above for identifying the correlation length [Oh and Kay, 1998], in addition to the criteria of Ulaby et al. [1982].

The vertical precision of the instrument was tested by repeatedly scanning two different target surfaces, both of which were assumed to have an effective rms height σ_{eff} of zero.

In other words, σ_{eff} is assumed to be more than an order of magnitude lower than the range resolution of the laser scanner. The target was scanned at a similar range and inclination angle to the artificial and natural sea ice surfaces, to keep the ranging and pointing errors consistent. The first target was a smooth, laminate office floor and the second target was a thin sheet of smooth sea ice grown from artificial seawater and stored in a cold laboratory at -20 °C at the University of Manitoba. Three 1 x 1 m floor sections were each scanned three times and, between the nine samples, the average standard deviation in the elevation of points with respect to a fixed reference level through the floor was 0.8 ± 0.3 mm. The ~1 x 1 m sheet of sea ice was scanned three times from different orientations and the average standard deviation of points through the ice surface was 1.4 ± 0.2 mm. However, the sea ice sheet could not be kept entirely smooth, but was rough to touch and the measured error was overestimated by the presence of larger ice crystals which grew at the surface as the ice formed. Therefore, σ_{eff} was above zero for the sea ice sheet. Between the two experiments, we can estimate that the noise floor of our measurements – incorporating the ranging precision of the sensor and volume scattering within the upper portion of the sea ice cover – is around 1 mm.

After data collection was complete, several pre-processing steps were performed on the LiDAR point clouds in preparation for calculating surface roughness parameters. To ensure that roughness parameters were calculated from the same area of the SERF pool, each scan in a series was registered to an arbitrary coordinate system that was consistently maintained by locating a number of fixed reflective targets, mounted around the edge of the pool, while scanning. Select scans from both the SERF and field sites contained outlying points located well above or below the true pool surface, caused by laser reflections from precipitation or multi-path errors [Petrie and Toth, 2009]. These outliers were removed using in-house algorithms based on the morphological [Vosselmann, 2000] and adaptive TIN (triangulated irregular network) [Axelsson, 2000] filters. The two filters iteratively removed points from scans that were outside a minimum user-defined inclination angle and/or distance from an initial estimate of the terrain.

A number of individual square sections, with a width of 1 to 3 m, were then extracted from each scan (Table 3.1), and, finally, points were resampled to a regular grid made up of 2 mm x 2 mm cells using linear interpolation. We chose to use linear interpolation, rather than a more sophisticated method of interpolation, because the sampling interval between raw LiDAR points was at most 2 mm. Therefore basic linear interpolation helped to retain most of the information from the original data while resampling to a grid with cells typically larger in width than the sampling interval of the raw data points.

3.3.2. Detrending Algorithms

We present two detrending algorithms that remove the underlying topography from natural surfaces, leaving a single scale of roughness. Both algorithms are two-dimensional, removing topographic trends from a surface in its original two-dimensional form, rather than from individual profiles across it. The first is a two-dimensional adaptation of the commonly-used OLSR method, developed as a baseline for assessing the second algorithm, which uses two-dimensional FFT to separate different wavelengths of roughness from a surface.

3.3.2.1. Ordinary Least-Squares Regression (OLSR) Planes

The OLSR algorithm consists of a sequence of routines that: (1) segment the original surface grid into a regular grid of lower spatial resolution, (2) establish local reference levels within each low-resolution grid cell by fitting OLSR planes to subsections of the original surface, and (3) reconstruct the surface after removing local reference levels from each grid cell. By varying the cell size of the low resolution grid, the user can adjust the scale of roughness (or topography) removed from the original surface.

The local reference datum within each low resolution grid cell, C_x, is defined as the plane for which

$$z = \beta_0 + \beta_1 x + \beta_2 y \tag{3.10}$$

where x, y and z are coordinates of cells in the original surface grid and β_0, β_1 and β_2 are plane coefficients. These coefficients are found using ordinary least-squares regression, which identifies a local reference plane that minimizes vertical cell-to-plane distances. Original surface grid cells are then projected onto a new, reconstructed grid – which retains the same x and y coordinates – by translating grid heights in the z-dimension.

3.3.2.2. Fast-Fourier Transform (FFT) Filter

The FFT-based algorithm consists of a sequence of routines that: (1) take the two-dimensional discrete Fourier transform (DFT) of the original surface grid, (2) identify and filter the frequencies of roughness below a specified cutoff frequency (f_c), and (3) reconstruct the surface using the inverse DFT. By varying the cutoff frequency, the user can again adjust the scale of roughness (or topography) removed from the original surface.

3.3.2.3. Identifying the Cutoff Frequency

Whilst the OLSR and FFT-based algorithms are fairly simple to compute and operate, the challenge with both is to select an appropriate low-resolution grid cell size or cutoff frequency, respectively, so as to retain all frequencies of roughness that affect microwave backscatter, but also remove all frequencies that do not affect backscatter and therefore introduce errors into calculated surface roughness parameters. So we attempted to characterize the full range of roughness scales associated with a natural sea ice surface, from millimeters up to tens of meters, to identify a length scale separating micro- from meso-/macro-scale roughness.

In addition to collecting LiDAR data at the mm-cm scale over first-year ice in Resolute Passage in 2012, we also collected data at a lower spatial resolution (5 cm) over a much larger 100 x 100 m site to investigate geometric roughness at the snow-drift scale. The size of the site was selected to be >5 times the characteristic length of snow drifts to provide a representative sample of the surface. Since areas of a large site such as this can be 'shadowed' behind objects, such as snow drifts, in the laser scanner's field-of-view, a total of four scans were collected from each corner of the site. These scans were subsequently registered to a single, global coordinate system, to generate a point cloud with a uniform distribution of measurements across the full site. The rms height and correlation length of topography within this site were calculated as 0.1 and 4.9 m, respectively, using the 2-D technique outlined in Section 3.3.3.1. Hereafter, all of the roughness parameters reported in this study (Tables 3.2-3.4) were derived from the smaller 1-3 m diameter sections, rather than the larger 100 x 100 m site.

We combined a 10 x 10 m section of topography, with these σ and l values, with a small-scale (2 x 2 m) high-resolution scan from a white ice hummock (FYI) taken a few days later, which contained micro-scale roughness *and* underlying meso-scale topography, into a single surface grid. With this grid we could analyze the power spectral density of the full range of roughness elements contained within a natural sea ice surface. The circular power spectrum can be estimated from the Fourier transform, $F(f_r, f_s)$, of the rough surface, $\zeta(\boldsymbol{\rho}')$, using the periodogram method, as [Lin et al., 1993]:

$$P\left(f_{r,}f_s\right) = |F(f_r, f_s)|^2 + \left|F(f_{N-r,}f_{M-s})\right|^2 + |F(f_{N-r}, f_s)|^2 + |F(f_r, f_{M-s})|^2 \qquad (3.11)$$

where:

$$f_r = \frac{r}{N\Delta x}, \qquad f_s = \frac{s}{M\Delta y} \qquad 0 < r < \frac{N}{2}, 0 < s < \frac{M}{2} \qquad (3.12)$$

Here f_r and f_s are the frequency components along two coordinate axes. N and M are the number of grid cells on the x- and y-axes, respectively, and Δx and Δy are the sample spacing on x- and y-axes, respectively. $P\left(f_{r,}f_s\right)$ can be interpreted as the accumulation of power spectra distributed around the four quadrants of the spectral matrix $F(f_r, f_s)$ for a given frequency $f = (f_r^2 + f_s^2)^{1/2}$.

Lin et al. [1993] demonstrated that the cutoff frequency (f_c) for removing low-frequency components (i.e. underlying topography) from a surface can be identified as a significant change in the quantity of power in the distribution of surface spectra. We conduct a basic sensitivity analysis of the grid cell size C_x of the OLSR algorithm and the cutoff frequency f_c of the FFT-based algorithm on σ and l in Section 3.4.2.

3.3.3. Surface Roughness Parameterization

3.3.3.1. Extraction of One- and Two-Dimensional Roughness Parameters

After detrending the natural sea ice surfaces, we consider all surface grids as single-scale and extract roughness parameters in both one and two dimensions. We implement the discrete version of equation 3.1 to calculate σ for a two-dimensional surface grid with extent, L, and N x M cells. Since calculating σ from the entire surface is identical to calculating it from a series of adjacent profiles across it, we do not discriminate between one- and two-dimensional (1-D and 2-D) variations of the rms height.

However, for the autocorrelation function and correlation length, we can discriminate between 1-D and 2-D forms. In the 1-D case we separately calculate the autocorrelation function for each profile across the surface in x and y dimensions (i.e. $N + M$ profiles in total) using the discrete, one-dimensional version of equation 3.2, and then determine the normalized autocorrelation function of the surface as the average of individual functions. Likewise, we determine the surface correlation length as the mean l calculated from each individual function in x and y dimensions, using the one-dimensional version of equation 3.3. In contrast, in the 2-D case we calculate a single autocorrelation function from the discrete, two-dimensional version of equation 3.2. The two-dimensional correlation length is then a function describing the contour of the 2-D autocorrelation function with a normalized correlation of e^{-1}, as defined in equation 3.3. Because the 2-D form of l varies with azimuth angle, we can also evaluate the eccentricity, ϵ_l, of the surface correlation, using equation 3.4.

3.3.3.2. Form of Rough Surface Autocorrelation Function

Besides the rms height and correlation length, the form of the surface autocorrelation function (C) – whether conforming to an exponential, Gaussian, or other model – is a vital parameter in microwave scattering models. Scattering models for sea ice typically use an exponential function, since level and smooth ice surfaces have many scales of roughness, which make the correlation appear exponential-like [Fung, 1994]. But we have found only one study that includes a comprehensive evaluation of C for sea ice surfaces, using a database of one-dimensional surface profiles [Manninen, 1997]. So, in addition to σ and l, we also calculated a number of parameters that (1) describe whether experimental autocorrelation functions extracted from our forty LiDAR surface sections conform to the exponential or Gaussian model, and (2) characterize the exponent, n, of the generalized power law spectrum, given by equation 3.7, fit to the data.

We fit the exponential, Gaussian and generalized model to each experimental C from individual one-dimensional profiles, and also to radial profiles across the two-dimensional C, through artificial and natural sea ice surface sections, by minimizing the coefficient of determination (r^2) between the observations and model. From this we obtained both 1-D and 2-D parameters for the surface autocorrelation function. Since the experimental C begins to oscillate after several correlation lengths, typically at a correlation of around zero, we restricted the model fit to a lag distance of $3l$. The entire processing chain, including: data collection, pre-processing and analysis for the extraction of surface roughness parameters, is summarized in Figure 3.2.

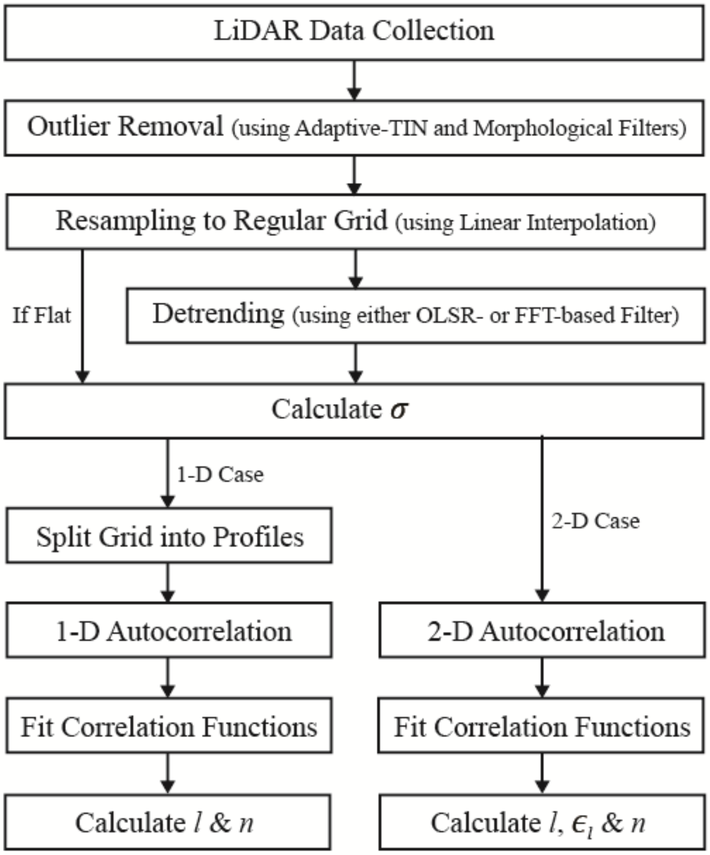

Figure 3.2 | Summary of the processing chain for extracting surface roughness measurements from terrestrial LiDAR data.

3.3.3.3. Algorithm Training using Artificial Surfaces

To ensure the processing algorithms do not adversely affect the roughness parameters calculated from a natural surface, we generated a series of artificial surfaces for training. We followed the method of Ogilvy and Foster [1989] to generate ten random isotropic surfaces with predetermined σ and l (ranging from 0.15 to 0.35 cm, and 1.0 to 3.0 cm, respectively). 'Observed' roughness parameters were then calculated from each of these surfaces with our processing algorithms and compared with the original (true) parameters. The average root mean square error (RMSE) between observed and true σ was 0.005 cm, and between observed and true l was 0.02 cm, in each case at least one order of magnitude lower than the true values of σ and l.

3.4. Application and Results

3.4.1. Detrending

We assumed that the surface of young, artificial ice grown in the SERF pool was uniform and flat, so the ice surface mean level corresponded to a fixed principal plane through x- and y-dimensions, parallel to the pool surface. Surface roughness of the artificial ice was therefore based only on variability in the z-dimension and roughness parameters could be extracted directly from the original gridded data. However, the surfaces of natural sea ice (S, SI, FYI, MYI1 & MYI2) contained several superimposed scales of roughness and had to be detrended before extracting roughness parameters.

Combined circular spectra for the large-scale 100 x 100 m and small-scale 3 x 3 m LiDAR scans from first-year ice in Resolute Passage are presented in Figure 3.3 as a plot of the squared amplitude of surface heights versus wavelength. Figure 3.3 illustrates a significant change in power at approximately 0.25 m, corresponding to a separation between micro- and meso-/macro-scales of sea ice surface roughness. So we use this value as a standard for both the grid cell size in the OLSR algorithm and the cutoff wavelength in the FFT-based algorithm, to detrend the surfaces of natural ice.

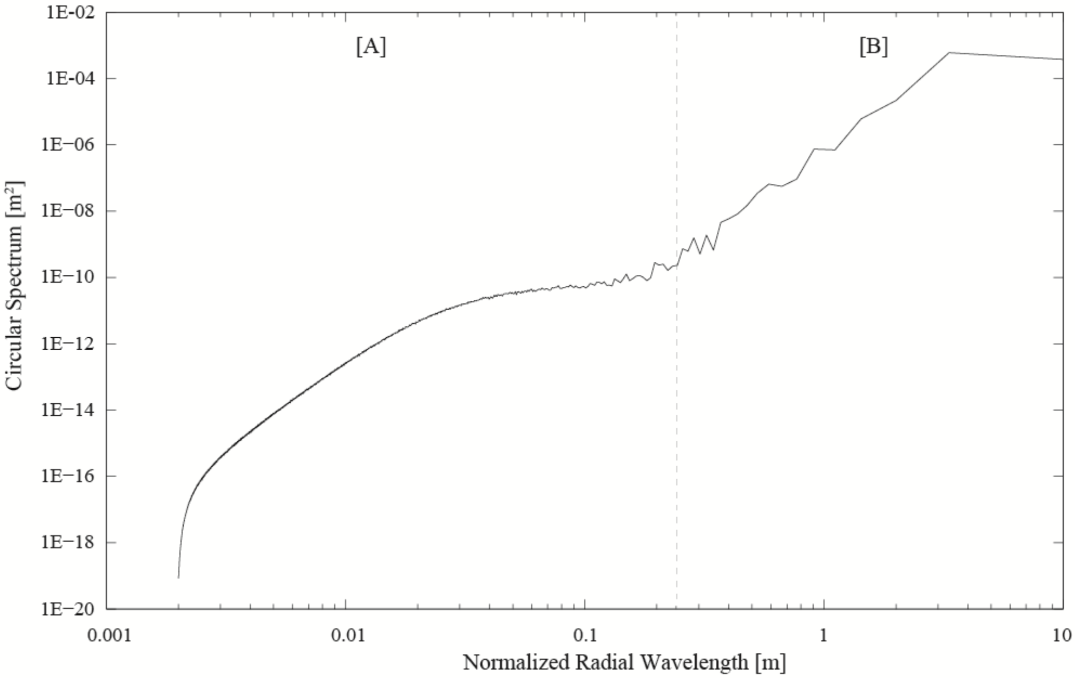

Figure 3.3 | Circular power spectra of combined micro- and meso-/macro-scales of sea ice surface roughness. The dashed line marks a transition at approximately 0.25 m between group [A], which includes micro-scale roughness (assumed to interact with microwave radiation at C-band), and group [B], which includes meso- and macro-scale roughness, e.g., snow drifts, deformed ice, and other elements contributing to underlying surface topography.

An illustration of the differences between detrending with: (1) the OLSR algorithm with 1-m grid cells, (2) the OLSR algorithm with 0.25-m grid cells, and (3) the FFT algorithm with a 0.25-m cutoff wavelength, is presented in Figure 3.4. Artificial 'jumps', such as those at around 1.9 m in Figure 3.4b and c, are introduced into detrended surfaces at the edges of plane segments using both versions of the OLSR algorithm, although detrending is clearly improved by using 0.25-m, rather than 1-m, plane segments. However, the FFT-based algorithm provides the best approximation for the surface mean line of first-year ice in Figure 3.4a and generates flat surfaces containing only single-scale roughness elements (Figure 3.4d).

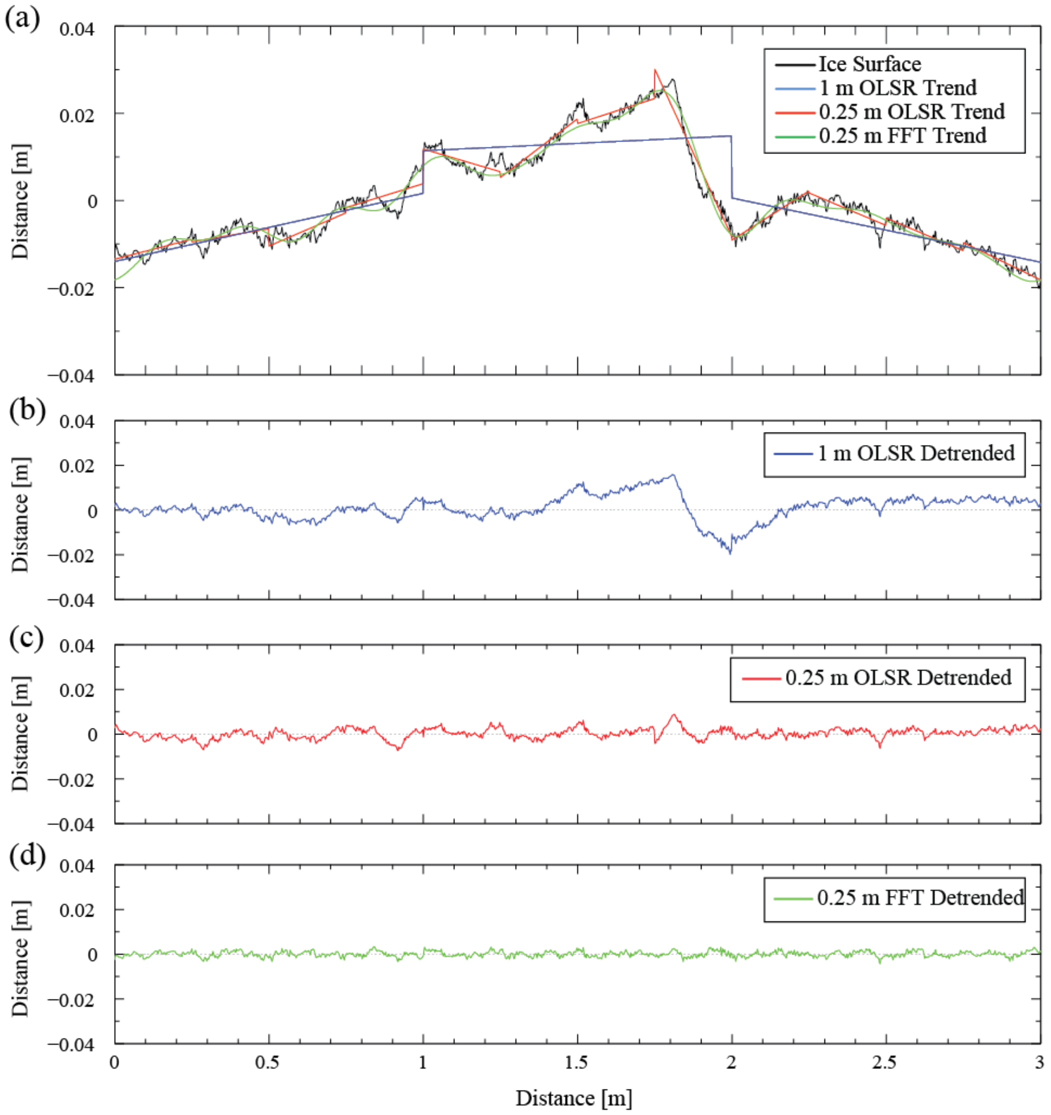

Figure 3.4 | (a) Reference levels calculated through a profile across first-year sea ice (FYI subsection 5) using three detrending algorithms: OLSR with 1-m plane segments (blue), OLSR with 0.25-m plane segments (red), and FFT with a 0.25-m cutoff (green); in addition to three subsequent plots (b-d) showing the height deviations from each reference level.

3.4.2. Surface Roughness

One- and two-dimensional roughness parameters extracted from the nine artificial sea ice surfaces are presented in Table 3.2. The rms height varies by only 0.13 cm between all ice types, in the range 0.13 to 0.26 cm, which lies towards the center of σ values compiled for laboratory-grown, young sea ice in [Onstott, 1992], which range from 0.02 to 0.34 cm. While σ for the pancake ice remains fairly stable at around 0.20 cm through Stages I to III, σ for the frost flowers increases steadily from 0.13 to 0.26 cm from Stage I to III, before dropping to 0.21 cm at Stage IV. These changes in frost flower roughness are related to processes of crystal growth, brine rejection and decimation modifying the ice surface conditions, as reported in Isleifson et al. [2014], while the slight drop in σ for the pancake ice between Stages I and II may be related to a ‘flattening’ of pancake rims as the ice consolidated over time. The correlation length varies by around two centimeters, from 0.27/0.19 to 2.14/2.25 cm (1-D/2-D), between all artificial ice types, which again lies in the approximate range of l values compiled in [Onstott, 1992], from 0.45 to 3.65 cm. l is notably different between ice types and different stages of development for the same ice type. For example the bare ice has a 2-D l of only 0.19 cm whereas the refrozen slush has a 2-D l of 2.25 cm, despite both surfaces having similar σ. The pancake ice also demonstrates a significant ‘roughening’ between Stage II and III with a reduction in 2-D l from 1.36 to 0.27 cm.

Table 3.2 | Compilation of surface roughness parameters extracted from artificial sea ice. Values for each surface are averages from multiple LiDAR sections (see Table 3.1).

Code	σ [cm]	l [cm] (1-D)			l [cm] (2-D)	
		Mean & Std	Min	Max	Mean & Std	ϵ_l
BI	0.23	0.27 ± 0.46	0.09	5.01	0.19 ± 0.00	0.19
RS	0.25	2.14 ± 1.19	0.62	11.12	2.25 ± 0.26	0.69
PI-I	0.23	1.15 ± 0.82	0.14	6.83	1.27 ± 0.11	0.63
PI-II	0.19	1.20 ± 0.66	0.16	4.69	1.36 ± 0.11	0.61
PI-III	0.21	0.37 ± 0.39	0.12	5.27	0.27 ± 0.04	0.73
FF-I	0.13	0.71 ± 0.14	0.57	1.90	1.01 ± 0.32	0.90
FF-II	0.19	0.44 ± 0.23	0.17	2.91	0.70 ± 0.47	0.98
FF-III	0.26	0.59 ± 0.58	0.30	5.46	0.85 ± 0.50	0.93
FF-IV	0.21	1.28 ± 0.34	0.57	6.61	1.36 ± 0.34	0.86

BI = bare ice; RS = refrozen slush; PI = pancake ice; FF = frost flowers

Surface roughness parameters extracted from natural sea ice, after detrending with the OLSR and FFT-based algorithms, are presented in Table 3.3. It is clear that OLSR detrending with 1-m grid cells (OLSR-1) consistently produces values for σ and l that are several times higher than OLSR detrending with 0.25-m grid cells (OLSR-0.25). Both σ and l for OLSR-1 are close to the highest values reported for first- and multi-year sea ice in Onstott [1982] and Drinkwater [1989]. But the profile for OLSR-1 in Figure 3.4b illustrates that background trend from a surface with high topographic relief is not fully removed with this algorithm, causing σ and l to be severely overestimated. A lack of (or inadequate) detrending, in this manner, may also explain the 1.5-4.5 cm rms heights and 4-20 cm correlation lengths measured over FYI and MYI in past studies [Drinkwater, 1989; Farmer et al., 1991; Manninen, 1997]. The same is true for OLSR-0.25, but to a lesser degree, with irregular jumps between grid planes introducing false ‘topography’ into the surface roughness (Figure 3.4b and c).

Table 3.3 | Variation in surface roughness parameters extracted from natural sea ice after detrending using: (1) the OLSR algorithm with 1 m grid cells (OLSR-1), (2) the OLSR algorithm with 0.25 m grid cells (OLSR-0.25), and (3) the FFT-based algorithm with a 0.25 m cutoff wavelength (FFT-0.25). Values for each surface are averages from multiple LiDAR sections, with the exception of S and SI (see Table 3.1).

Code	σ [cm]			l [cm] (1-D)			l [cm] (2-D)		
	OLSR-1	OLSR-0.25	FFT-0.25	OLSR-1	OLSR-0.25	FFT-0.25	OLSR-1	OLSR-0.25	FFT-0.25
S	1.89	0.32	0.18	17.42	3.67	0.97	29.34	3.91	0.96
SI	0.85	0.64	0.36	5.73	3.86	1.87	6.65	3.70	2.00
FYI	0.45	0.31	0.20	7.17	2.97	1.56	7.99	2.96	1.68
MYI1	1.83	0.47	0.20	17.76	4.40	1.29	22.18	4.03	1.47
MYI2	2.01	0.38	0.16	17.01	4.49	1.46	21.06	4.27	1.72

S = glazed snow; SI = superimposed ice; FYI = first-year ice; MYI = multi-year ice

Figure 3.5a demonstrates the sensitivity of calculated σ and 1-D l to variations in the size of grid cells (C_x) in the OLSR detrending algorithm and cutoff frequency (f_c) in the FFT-based detrending algorithm, and Figure 3.5b demonstrates the sensitivity of calculated σ and 2-D l to variations in C_x and f_c. Both σ and l are reduced significantly as C_x or f_c decreases, but their sensitivity to changes in f_c in the FFT-based algorithm is lower than their sensitivity to changes in C_x in the OLSR algorithm, especially close to the selected f_c or C_x of 0.25 m. Detrending using the FFT-based algorithm with a 0.25 m cutoff wavelength (FFT-0.25) produces the lowest values for σ and l, but these values are closer to the roughness parameters calculated in this study for artificial sea ice (Table 3.2). Figure 3.4a also shows that the FFT-based algorithm identifies a trend or reference level that closely follows the true ice topography. <u>The FFT-based algorithm is clearly more suitable than the OLSR-based algorithm for detrending natural sea ice surfaces</u>.

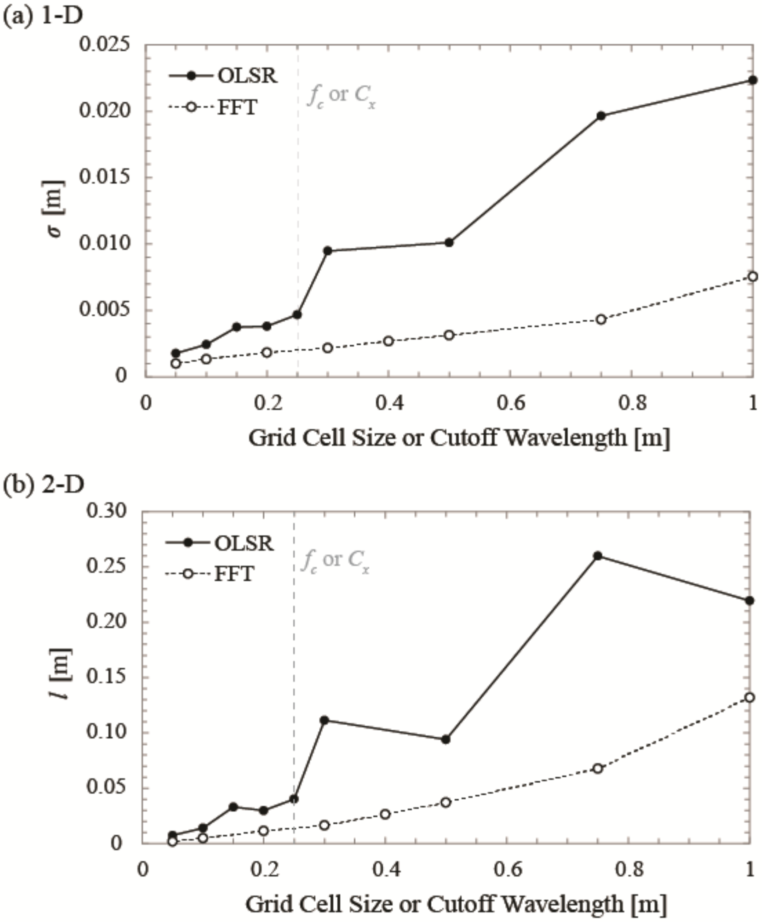

Figure 3.5 | Sensitivity of σ (a) and 2-D l (b) for MYI1 to variations in the grid cell size of the OLSR detrending algorithm and the cutoff wavelength of the FFT-based detrending algorithm. The grid cell size and cutoff wavelength of 0.25 m used in this study is given by the dashed grey lines.

One- and two-dimensional roughness parameters extracted from the five natural sea ice surfaces using the FFT-0.25 detrending algorithm are presented in Table 3.4. The rms height varies by 0.20 cm between all ice types, in the range 0.16 to 0.36 cm, which again lies towards the center of σ values compiled for first- and multi-year sea ice in Onstott [1992], which range from 0.05 to 0.89 cm. MYI is generally considered to be rougher than FYI during spring and summer, as supported by a few isolated measurements [e.g. Drinkwater, 1989; Paterson et al., 1991], contrary to our results which suggest FYI and MYI have similar (i.e. indistinguishable) σ around 0.2 cm. Superimposed ice has by far the highest σ of all measured sea ice types, both natural and artificial, at 0.36 cm, whereas the snow surface has a predictably low σ of 0.18 cm. The correlation length varies by around one centimeter, from 0.97/0.96 to 1.87/2.00 cm (1-D/2-D), between all natural sea ice types, which lies towards the lower end of the range of l values compiled in Onstott [1992] for FYI and MYI, from 0.54 to 6.02 cm. Like σ, l is similar between first- and multi-year ice surfaces, at around 1.5 cm. The superimposed ice demonstrates a relatively high l of around 2 cm, consistent with the only published measurement we could find for superimposed ice of 2.7 cm [Onstott, 1982], and the snow demonstrates a relatively low l of around 0.96 cm, which is almost a centimeter lower than the few reported values [Farmer et al., 1991; Nghiem et al., 1995].

There appears to be no bias toward either 1-D or 2-D forms of the correlation length for all sea ice types (natural and artificial), i.e. one does not consistently under-or over-estimate the other. However, the average standard deviation of the 1-D form of l is 0.49 cm, which is more than twice the equivalent value for the 2-D form at 0.22 cm. Given that microwave scattering models require a single value for l that characterizes the entire surface, increasing variability in l introduces increasing variability in calculated backscatter. Indeed, this issue is emphasized when we consider the vast differences between minimum and maximum measured 1-D correlation lengths (4.34 cm on average) (Tables 3.2 and 3.4). For instance, if a single profile is extracted from the refrozen slush surface, as if it had been collected with a laser or pin profiler, the measured correlation length could range from 0.62 to 11.12 cm (Table 3.2).

Table 3.4 | Compilation of surface roughness parameters extracted from natural sea ice after detrending using the FFT-based algorithm with a 0.25 m cutoff wavelength. Values for each surface are averages from multiple LiDAR sections, with the exception of S and SI (see Table 3.1).

Code	σ [cm]	l [cm] (1-D)			l [cm] (2-D)	
		Mean & Std	Min	Max	Mean & Std	ϵ_l
S	0.18	0.97 ± 0.40	0.16	2.93	0.96 ± 0.18	0.81
SI	0.36	1.87 ± 0.47	0.14	3.41	2.00 ± 0.07	0.44
FYI	0.20	1.56 ± 0.25	0.82	2.51	1.68 ± 0.21	0.70
MYI1	0.20	1.29 ± 0.35	0.31	2.92	1.47 ± 0.33	0.85
MYI2	0.16	1.46 ± 0.51	0.22	3.52	1.72 ± 0.20	0.69

S = glazed snow; SI = superimposed ice; FYI = first-year ice; MYI = multi-year ice

A fraction of this variability in l is caused by surface anisotropy and this is captured by the eccentricity of the 2-D correlation length. Of the artificial ice surfaces, the bare ice is near-isotropic, but the refrozen slush, pancake ice, and especially frost flowers are clearly anisotropic (Table 3.2). In the case of the pancake ice this may have been caused by the linear rims (see Figure 3.1c), whereas after examining the frost flowers, it appears that surface winds may have arranged the crystal structures into a linear pattern that was subsequently measured with the laser scanner. Of the natural ice surfaces, the superimposed ice is close to isotropic, but the first- and multi-year ice and snow are anisotropic. These results are consistent with the results of Manninen [1997], who found that sea ice and especially snow regularly showed strong anisotropy.

3.4.3. Form of Rough Surface Autocorrelation Function

One- and two-dimensional parameters describing the form of autocorrelation for the nine artificial sea ice surfaces are presented in Table 3.5. Profiles across all nine surfaces largely conform to the exponential function, in both 1-D and 2-D forms, with the exception of the 1-D form for Frost Flowers Stage I (FF-I), which demonstrates a 70% to 30% split between exponential and Gaussian functions. The exponent of the x-exponential function, n, is close to 1 across all nine surfaces, again with the exception of FF-I, which has 1-D and 2-D n of 1.26 and 1.18, respectively, and generally the goodness-of-fit (r^2) is high for profiles fit to the x-exponential function. The r^2 values for 2-D x-exponential functions are all above 0.75, excluding Pancake Ice Stage I (PI-I), which has an r^2 of 0.55 and does not demonstrate a strong agreement with either the exponential nor Gaussian function. It is possible that the rims around individual, consolidated pancakes – defined and a few centimeters high at Stage I, but increasingly flattened thereafter – distorted the correlation function (likely exponential, given the form of C for PI-II and PI-III) at this early stage.

Table 3.5 | The form of surface autocorrelation for artificial sea ice surfaces, including the fraction of observed one- and two-dimensional autocorrelation functions conforming to either the exponential ('Exp', equation 3.5) or Gaussian ('Gauss', equation 3.6) model, and the mean and standard deviation of the exponent (n) of a generalized power-law model (equation 3.7) fit to observed autocorrelation functions, along with the average coefficient of determination (r^2) of the fit.

Code	1-D ACF		n		2-D ACF		n	
	Exp	Gauss	Mean & Std	r^2	Exp	Gauss	Mean & Std	r^2
BI	0.98	0.02	1.14 ± 0.12	0.96	1.00	0.00	1.02 ± 0.03	0.98
RS	1.00	0.00	1.00 ± 0.01	0.80	1.00	0.00	1.00 ± 0.00	0.75
PI-I	1.00	0.00	1.00 ± 0.02	0.65	1.00	0.00	1.00 ± 0.00	0.55
PI-II	0.99	0.01	1.01 ± 0.06	0.80	1.00	0.00	1.00 ± 0.00	0.80
PI-III	1.00	0.00	1.01 ± 0.03	0.77	1.00	0.00	1.00 ± 0.00	0.81
FF-I	0.70	0.30	1.26 ± 0.19	0.98	0.96	0.04	1.18 ± 0.06	0.99
FF-II	0.96	0.04	1.07 ± 0.12	0.94	1.00	0.00	1.01 ± 0.02	0.94
FF-III	1.00	0.00	1.03 ± 0.07	0.91	1.00	0.00	1.00 ± 0.00	0.90
FF-IV	0.93	0.07	1.09 ± 0.14	0.96	1.00	0.00	1.01 ± 0.01	0.98

BI = bare ice; RS = refrozen slush; PI = pancake ice; FF = frost flowers

Parameters describing the form of autocorrelation for the five natural sea ice surfaces, after detrending with the OLSR and FFT-based algorithms, are presented in Table 3.6. Four of the surfaces: S, FYI, MY1 and MYI2, demonstrate enormous variation in n when detrending with the OLSR-1, OLSR-0.25 and FFT-0.25 algorithms. The least successful algorithm, OLSR-1, generates surfaces that principally conform to the Gaussian correlation function, producing minimum 1-D and 2-D n of 1.91 and 1.85, respectively, for MYI1, due to the widening of the observed autocorrelation function and diminished influence of the smallest-scale surface roughness elements. The OLSR-0.25 algorithm generates surfaces somewhere between exponential and Gaussian. But the FFT-0.25 algorithm, which is shown in Figure 3.4a to generate the best reference level through natural sea ice topography, produces surfaces largely conforming to the exponential correlation function, with maximum 1-D and 2-D n of 1.23 and 1.04, respectively, between these four surface types. This variation in modeled C with the choice of detrending algorithm reveals the importance of both performing detrending in the first place and then selecting a sophisticated enough technique, such as FFT-based filtering.

Table 3.6 | The form of surface autocorrelation for natural sea ice surfaces after detrending (DT) using: (1) the OLSR algorithm with 1 m grid cells (OLSR-1), (2) the OLSR algorithm with 0.25 m grid cells (OLSR-0.25), and (3) the FFT-based algorithm with a 0.25 m cutoff wavelength (FFT-0.25); including the fraction of observed one- and two-dimensional autocorrelation functions conforming to either the exponential ('Exp', equation 3.5) or Gaussian ('Gau', equation 3.6) model, and the mean and standard deviation of the exponent (n) of a generalized power-law model (equation 3.7) fit to observed autocorrelation functions, along with the average coefficient of determination (r^2) of the fit.

Code	DT	1-D ACF		n		2-D ACF		n	
		Exp	Gau	Mean & Std	r^2	Exp	Gau	Mean & Std	r^2
S	(1)	0.04	0.96	1.92 ± 0.18	0.76	0.00	1.00	1.98 ± 0.06	0.79
	(2)	0.63	0.37	1.32 ± 0.31	0.92	0.53	0.47	1.35 ± 0.15	0.94
	(3)	0.94	0.06	1.08 ± 0.14	0.91	1.00	0.00	1.01 ± 0.02	0.91
SI	(1)	0.26	0.74	1.63 ± 0.33	0.89	0.24	0.76	1.53 ± 0.22	0.97
	(2)	0.33	0.67	1.58 ± 0.33	0.93	0.13	0.87	1.57 ± 0.12	0.97
	(3)	0.18	0.82	1.65 ± 0.26	0.88	0.56	0.44	1.39 ± 0.16	0.96
FYI	(1)	0.36	0.64	1.58 ± 0.36	0.91	0.52	0.48	1.33 ± 0.24	0.98
	(2)	0.50	0.50	1.40 ± 0.25	0.96	1.00	0.00	1.24 ± 0.05	0.99
	(3)	0.80	0.20	1.23 ± 0.20	0.94	1.00	0.00	1.03 ± 0.09	0.97
MYI1	(1)	0.03	0.97	1.91 ± 0.17	0.80	0.06	0.94	1.85 ± 0.18	0.90
	(2)	0.51	0.49	1.39 ± 0.29	0.93	0.62	0.38	1.39 ± 0.13	0.97
	(3)	0.80	0.20	1.23 ± 0.22	0.95	1.00	0.00	1.04 ± 0.06	0.97
MYI2	(1)	0.04	0.96	1.87 ± 0.21	0.79	0.12	0.88	1.71 ± 0.19	0.92
	(2)	0.32	0.68	1.51 ± 0.27	0.93	0.64	0.36	1.36 ± 0.06	0.97
	(3)	0.79	0.21	1.20 ± 0.21	0.93	1.00	0.00	1.01 ± 0.03	0.92

S = glazed snow; SI = superimposed ice; FYI = first-year ice; MYI = multi-year ice

The exception to this trend of a Gaussian-to-exponential shift with improving detrending is the Superimposed Ice (SI) surface, which remains primarily Gaussian as the detrending algorithm is changed from OLSR-1 through to FFT-0.25. This indicates that, of all natural and artificial sea ice surface types, superimposed ice, exclusively, has a Gaussian autocorrelation function. This observation is in agreement with the results of Manninen [1997] who measured hundreds of profiles of small-scale roughness across Baltic sea ice and found that only around 10% conformed to the Gaussian, rather than exponential, correlation function. The goodness-of-fit (r^2) for profiles fit to the x-exponential function is high for all surfaces, detrended with all three algorithms, with r^2 values for 2-D x-exponential functions above 0.91 after detrending with FFT-0.25 for all five surfaces. However, the average 1-D standard deviation of n for both natural and artificial sea ice surfaces is noticeably higher than equivalent average 2-D standard deviation (after detrending with FFT-0.25: 0.21 versus 0.07) (Tables 3.5 and 3.6). Like the vast differences in minimum and maximum measured 1-D correlation lengths (discussed above), the much wider variation in 1-D rather than 2-D n illustrates the lack of precision associated with using a 1-D approach, for example laser or pin profiling, to measure surface roughness.

3.4.4. Sensitivity of Surface Roughness Parameters to the Sampling Interval & Extent

To examine the dependency of roughness parameters σ, l and C on the sampling interval, Δx, and extent, L, we performed two simple experiments on select ice surface sections, including Bare Congelation Ice (BI) Subsection 1 and Pancake Ice Stage I (PI-I) Subsection

1. In the first we reduced the spatial resolution of the grid, resampled from original LiDAR points, at regular intervals of 1 mm from the highest resolution of 2 mm down to 20 mm, and calculated 1-D and 2-D surface roughness parameters at each iteration. For both PI-I and BI, σ barely changes as the grid is down-sampled; but l and the form of C vary dramatically and quite differently between the two surface types (Figures 3.6 and 3.7). For both surfaces l increases and the fraction of observed C conforming to the exponential model decreases as Δx is reduced, but the critical maximum sampling threshold, Δx_{max}, above which l increases, varies between the two surfaces. To estimate Δx_{max} we calculate the relative percentage change of l with respect to l at the highest grid resolution of 2 mm:

$$\Delta l_{\%} = \frac{(l - l_{2\,mm})}{l_{2\,mm}} \cdot 100, \tag{3.13}$$

as the grid is down-sampled. Δx_{max} is then identified as the lowest resolution where $\Delta l_{\%} \leq$ 10%.

Whereas l remains almost constant from 2 mm up to Δx_{max} of 10 mm (1-D) and 13 mm (2-D) for the pancake ice (Figure 3.6), it rapidly increases after Δx_{max} of 3 mm in both 1-D and 2-D cases for the bare ice (Figure 3.7). The fraction of exponential C also decreases more rapidly with decreasing Δx for the bare ice rather than pancake ice. This can be explained by the differences in measured l between the two surface types, which, using the 2-D measurements from Table 3.2, show that pancake ice has a correlation length of 1.27 cm, almost an order of magnitude higher than the bare ice at 0.19 cm. A sampling interval of 2 mm would provide over six data points within one correlation length of PI-I, but only around one data point within one correlation length of BI, so any further reduction in Δx has a greater impact on measured l and C from BI than PI-I.

(a) 1-D

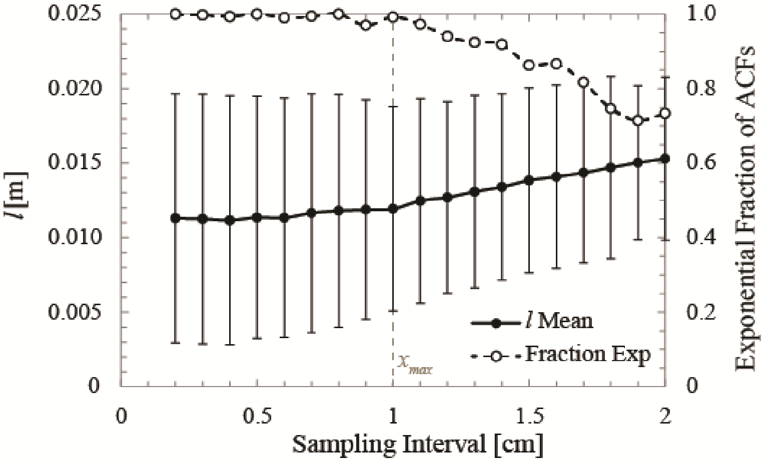

(b) 2-D

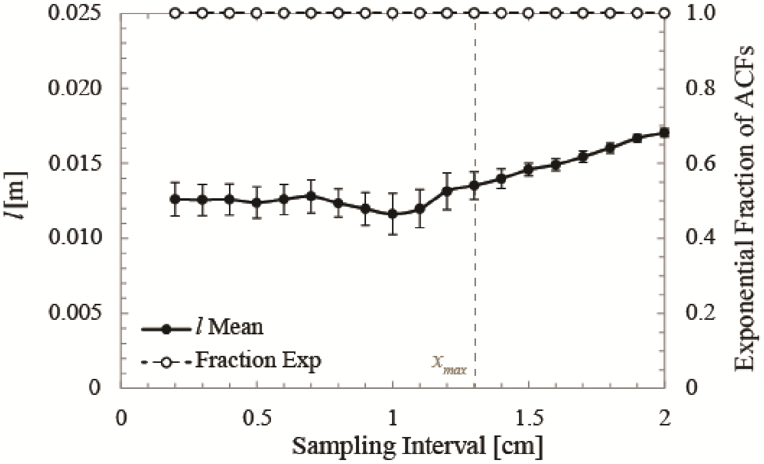

Figure 3.6 | Change in the one- (a) and two-dimensional (b), mean and standard deviation correlation length (bold points, bold line), and exponential fraction of curves fit to experimental auto-correlation functions (hollow points, dashed line), for Pancake Ice Stage 1 (PI-I) Subsection1, as the sampling interval is varied. The threshold maximum sampling interval, Δx_{max}, is given by a dashed grey line.

(a) 1-D

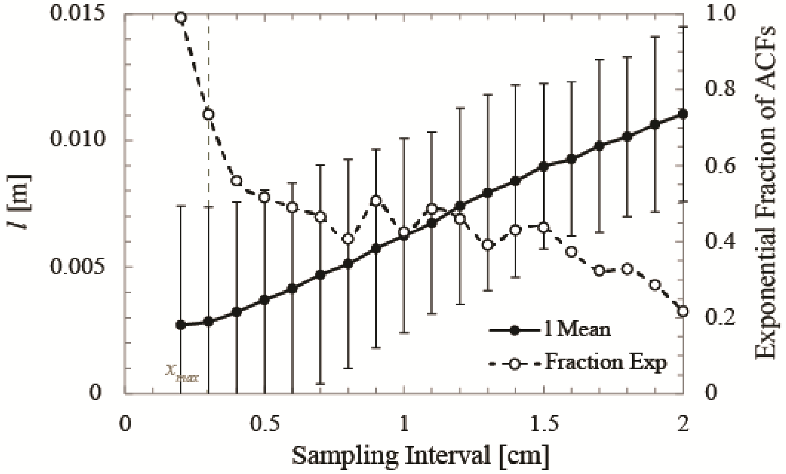

(b) 2-D

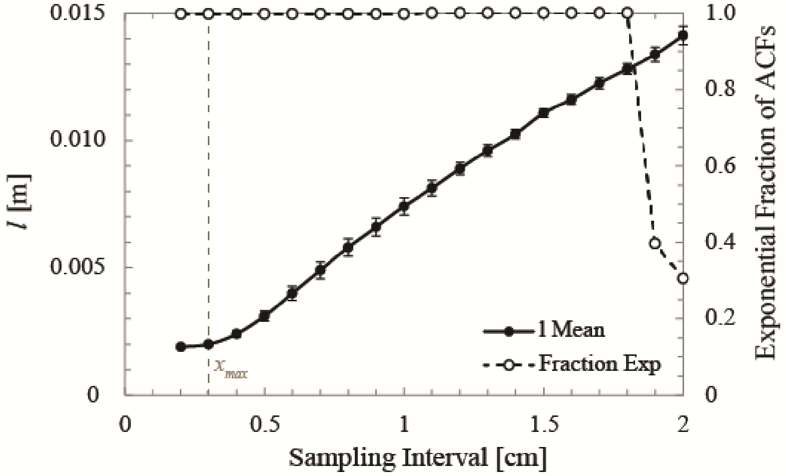

Figure 3.7 | Change in the one- (a) and two-dimensional (b), mean and standard deviation correlation length (bold points, bold line), and exponential fraction of curves fit to experimental auto-correlation functions (hollow points, dashed line), for Bare Ice (BI) Subsection1, as the sampling interval is varied. The threshold maximum sampling interval, Δx_{max}, is given by a dashed grey line.

In the second experiment we kept the grid resolution at 2 mm but gradually reduced the sampling extent from the full 3 x 3 m section down to 1.5 x 1.5 m, then to 1 x 1 m and so on to only 5 x 5 cm, and calculated 1-D and 2-D surface roughness parameters at each iteration. At 3-m extent, a single set of parameters were calculated for the section, but at subsequent iterations the roughness parameters were calculated as an average of subsections, for example 4 x 1.5 m sections or 9 x 1 m sections, within the larger 3-m section. We observe that σ does not change as L decreases, but for both surfaces l decreases in a similar manner as L drops, and the result for PI-I is illustrated in Figure 3.8. To estimate the critical minimum threshold for the sampling extent, L_{min}, we calculate the relative percentage change of l as L decreases, in the same manner as equation 3.13, but with respect to l at the largest 3 x 3 m extent. Again we identify L_{min} as the largest extent where $\Delta l_{\%} \leq 10\%$. For the 1-D measurements, l decreases exponentially from 3-m extent, and even the second-largest extent (1.5-m) provides $\Delta l_{\%} > 10\%$, indicating that $L_{min} > 1.5$ m (Figure 3.8a). In contrast, for the 2-D measurements, l only starts to decrease significantly at L_{min} under 0.25 m (Figure 3.8b).

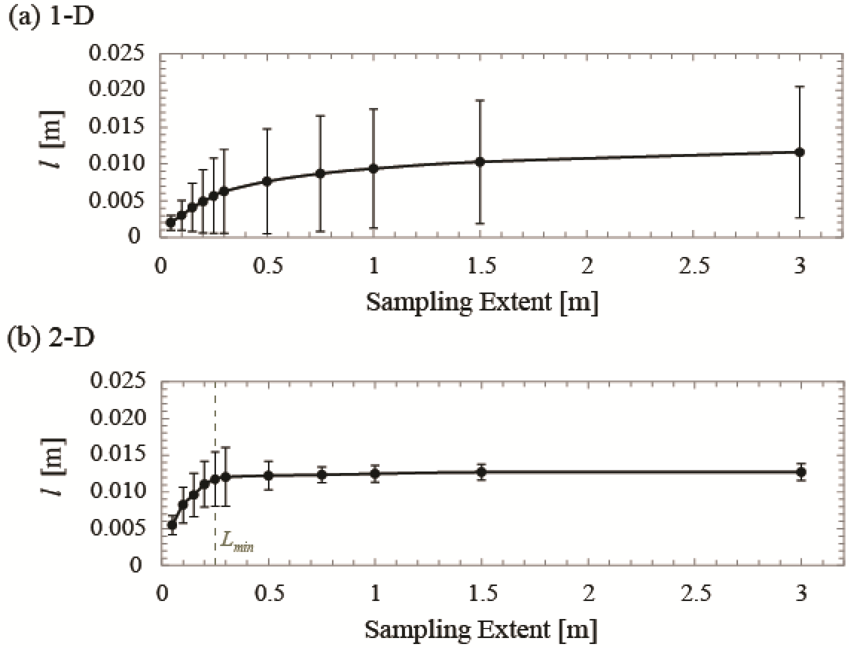

Figure 3.8 | Change in the one- (a) and two-dimensional (b), mean and standard deviation correlation length for Pancake Ice Stage 1 (PI-I) Subsection 1, as the sampling extent is varied. The threshold minimum sampling extent, L_{min}, is given by a dashed grey line in the 2-D case (b), but since $L_{min} > 1.5$ m in the 1-D case (a), it is left unmarked.

A noticeable result from both of these experiments is that the standard deviation of l is typically several orders of magnitude higher using the 1-D approach rather than the 2-D approach, even as the two sampling parameters are varied (Figures 3.6-3.8). We have already demonstrated that the average standard deviation of 1-D correlation lengths measured over sea ice surfaces in this study is more than twice equivalent 2-D correlation lengths (see Section 3.4.2). Both results support the argument that the 2-D approach is considerably more precise than the 1-D approach and is therefore able to characterize the surface correlation length as a single-scale, stationary process for microwave scattering models, which the 1-D approach cannot do.

3.4.5. Relationship between σ and l

Figure 3.9 illustrates the relationship between the rms height and two-dimensional correlation length of measurements acquired over fourteen sea ice surface types in this study, in the context of literature values obtained from past studies [Drinkwater, 1989; Farmer et al., 1991; Onstott, 1992; Swidt et al., 1992; Beaven et al., 1993; Fung, 1994; Nghiem et al., 1995; Manninen, 1997; Nassar, 1997]. Although the literature values appear to demonstrate a weak non-linear trend of increasing l with increasing σ, our measurements suggest that no such relationship exists. Our lowest measured value for σ, over FF-I, has a moderate corresponding l and, similarly, our lowest measured value for l, over BI, has a moderate corresponding σ; though one of our highest measured values for σ, over SI, also has a particularly high l. These results indicate that there is no clear dependency of l on σ, or vice versa, which suggests that the geophysical processes controlling surface roughness as an ice sheet forms and evolves can *independently* modify σ or l, not necessarily both simultaneously. This contrasts the result of Manninen [1997], who found an exponential relationship between l and σ, obtained from hundreds of short (0.1-1 m) one-dimensional profiles recorded over Baltic sea ice. However, we believe their relationship characterizes the sensitivity of σ and l to the sampling extent and fractal nature of ice surface roughness within a small area, which is especially significant for a 1-D approach (Figure 3.8a), and is shown by our results to break down as L exceeds L_{min} (Section 3.4.4).

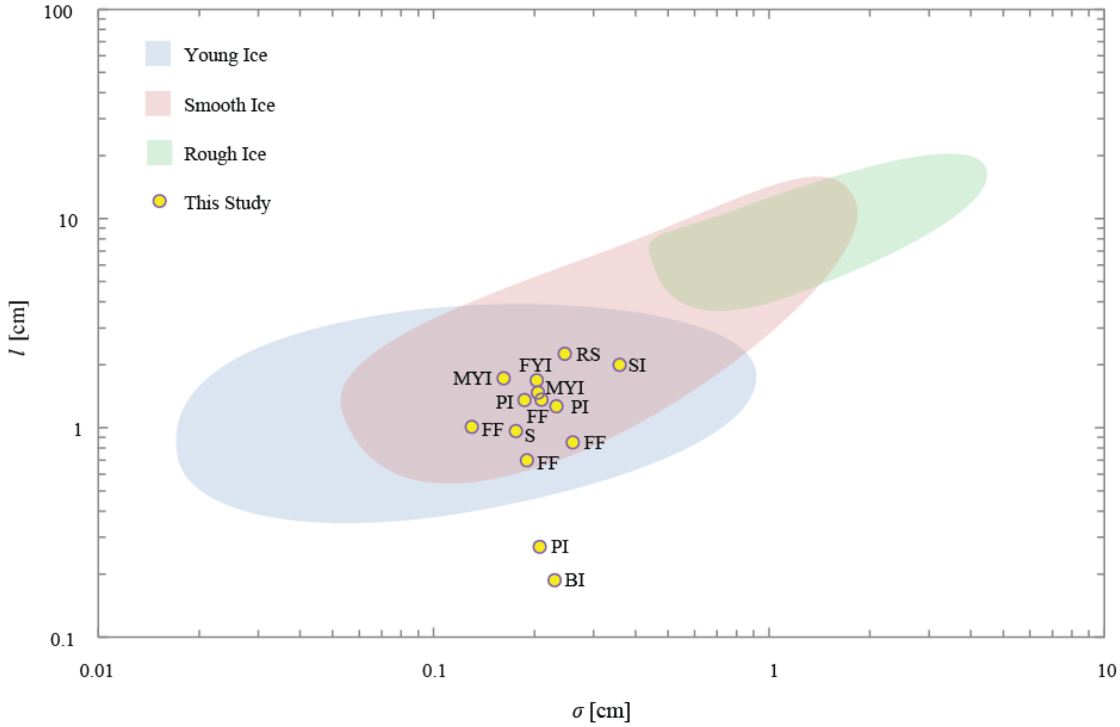

Figure 3.9 | Comparison between the RMS height and two-dimensional correlation length of sea ice surfaces examined in this study. Literature values, grouped as young ice (obtained in the laboratory or field), smooth ice (FYI or MYI, obtained in the field only), and rough ice (FYI or MYI, obtained in the field only), are presented as shaded zones in the background.

3.5. Discussion

3.5.1. Potential Sources of Error

Terrestrial laser scanning delivers several advantages over conventional techniques for measuring surface roughness at radar-observable scales. However, it is not without limitation. The Leica C10 is limited by the diameter of the laser footprint and, even at the lowest ranges, cannot resolve elements of the target surface that are smaller than ~ 1 mm. Snow and ice grains are often smaller than 1 mm [Swift et al., 1992]; however, an electromagnetic wave at C-band does not interact with surface roughness at this scale [Ulaby et al., 1982]. At a scanning range of approximately 20 m, $D_{f_{across}}$ of the Leica C10 exceeds 5 mm, which is approximately the criteria of Ulaby et al. [1982] for C-band. Above this range consecutive samples may become correlated if $\Delta < 0.859\delta$ [Lichti and Jamtsho, 2006]. In other words, the Gaussian peaks of adjacent laser pulses may cross, and the scanner won't resolve elements of the surface between these samples.

If the target surface is inclined with respect to the scanning origin ($\theta > 0$), $D_{f_{along}}$ will also be larger than $D_{f_{across}}$. The laser footprint will become increasingly elliptical in the along-track direction as θ rises. θ can be reduced by either elevating the scanner to a greater height above the target surface, or restricting the range. Terrestrial laser scanners have a limited field-of-view in the zenith angles, including the Leica C10, which is constrained to $\theta > 45°$. However, we have demonstrated that, by restricting the maximum range of the C10 to approximately 10 m, at a mounting height of 3 m, x_{opt} in the along-track direction is at most 6.8 mm for a scan with a maximum range of 10 m. If the scan were restricted to a maximum range of 8 m, maximum x_{opt} along-track would fall to 4.4 mm.

When the scanner operates at a low incidence angle, it also preferentially samples high points of the local surface topography and slopes with an aspect toward the scanner. Consequently, the observed anisotropy in surface roughness (Tables 3.2 and 3.4) may partially be an artefact of the scanning perspective. The anisotropy cannot entirely be attributed to the scanning perspective because the axis of highest correlation (i.e. the a-axis of the 1/e contour of 2-D C) was rarely oriented parallel or perpendicular to the scanning origin, and varied considerably between scans of different ice surfaces (data not shown). Besides this, satellite radars are intentionally ‘looking’ at the ice from an oblique perspective in the same way the terrestrial LiDAR system is.

As explained in Section 3.3.1, the laser may penetrate into the snow or sea ice surface several mm and the pulse return will therefore be a time-spread combination of surface and volume backscatter. Past observations indicate that green light is primarily backscattered by surface specular reflection from most of the snow and ice types measured in this study [Perovich 1994; 1998]. However, observations have also shown that light reflected from cold, dry snow has a strong volume scattering component [Perovich, 1994]. A terrestrial LiDAR sensor with a green laser may not be able to accurately measure the surface roughness of dry snow, although for radar remote sensing at C-band, the radar wave penetrates into the dry snowpack and the snow surface roughness is inconsequential [Onstott, 1982]. In spite of this, the extinction coefficients for sea ice are larger at 1000 nm wavelength (near-infrared; NIR) than at 500 nm (green) [Perovich, 1996], meaning that a NIR laser would penetrate into the snow or ice to a shallower depth than a green laser. A

LiDAR sensor with a NIR laser is therefore advantageous over a system with a green laser (such as the Leica C10) for measuring snow and sea ice surface roughness at short range.

3.5.2. Implications for Microwave Scattering from Sea Ice

The small perturbation model (SPM) has been widely used to simulate the scattering of electromagnetic waves from a rough interface separating two media [Fung, 1994]. In the SPM, beside the frequency, incidence angle, polarization and dielectric properties of the media, the backscattering coefficient strongly depends on the rms height, correlation length, and correlation function, which together characterize the rough surface. Our results have shown that the technique used to measure surface roughness in the field, and the procedures used to post-process the field data, can affect derived σ, l and C considerably. One-dimensional profiling versus two-dimensional surface-based measurement affects the precision of σ and l. Insufficient detrending causes σ and l to be overestimated, and C to be incorrectly classified. Two-dimensional measurements allow l to be characterized as a function of azimuth angle φ for sea ice surfaces that are typically anisotropic.

To demonstrate the sensitivity of the backscatter to these factors, we have used SPM theory to calculate the relative change in HH or VV backscatter σ^0 associated with a minor change in l that might be caused by errors in the field measurement technique, inhomogeneity of the surface, or surface anisotropy. The sensor parameters: frequency, polarization, and incidence angle, and surface parameters: permittivity and rms height are fixed. Then the relative change in σ^0 associated with a change in l for the exponential correlation function is [Fung, 1994]:

$$\alpha(l) = \frac{\sigma^0(l)}{\sigma^0(l_0)} = \left(\frac{l^2}{l_0^2}\right)\left[\frac{1+(2kl_0 sin\theta)^2}{1+(2klsin\theta)^2}\right]^{1.5} \tag{3.14}$$

where k is the wave number ($k = 2\pi/\lambda$ = 114 m^{-1} at C-band), θ is the incidence angle, and l_0 is a reference correlation length of 1 cm, corresponding to approximately the lowest observed value in this study. The relative change in σ^0 for a 1.5 cm change in l is between 2 and 3 dB, increasing at higher incidence angles (Figure 3.10).

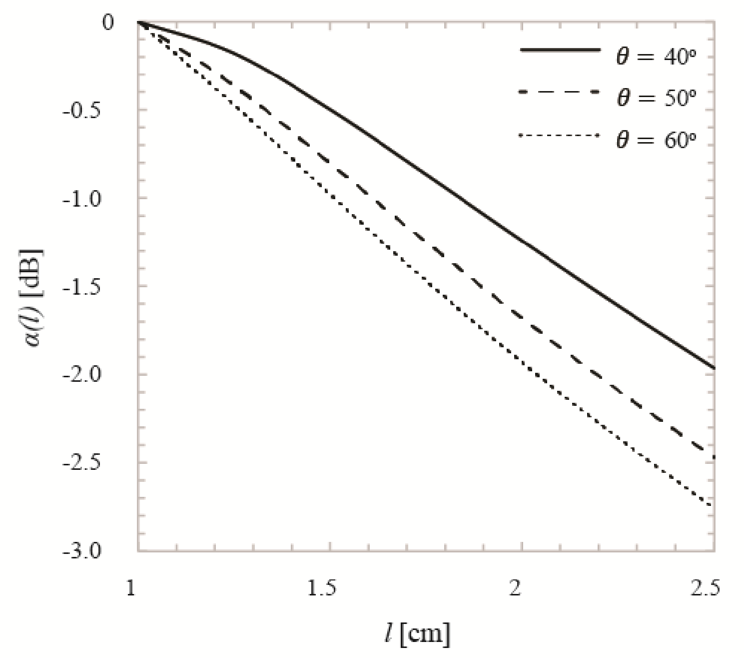

Figure 3.10 | Sensitivity of $\alpha(l)$ (relative change in σ^0) to variations in l, for the exponential correlation function, at 40°, 50° and 60° incidence angles.

It is not only the mm-cm scale roughness that affects the radar backscatter, but also the larger (meter) scale topographic roughness of the sea ice surface. SPM theory can be extended to a case where the small-scale roughness is modulated by large-scale topography. In this situation, the large-scale topography is characterized as a distribution of surface slopes [Ulaby et al., 1982]. The technique that we have developed in this study could be scaled up to examine the two-dimensional, large-scale roughness of sea ice. However, airborne LiDAR would be a more suitable tool than terrestrial LiDAR for measuring roughness at this scale [Rivas et al., 2006].

3.6. Conclusion

A technique has been developed for calculating surface roughness parameters from three-dimensional elevation data acquired with a terrestrial LiDAR system. The technique includes several steps, involving (1) raw data pre-processing, (2) resampling of data to a regular grid, (3) detrending (where necessary), and (4) two-dimensional autocorrelation, to characterize the surface rms height, correlation length and autocorrelation function. We have introduced a pair of two-dimensional detrending algorithms that can be used to remove macro-scale topography from a surface section and evaluated their capacity to detrend natural sea ice surfaces, leaving a single-scale of roughness suitable for extracting roughness parameters. We have then presented surface roughness parameters for various types of sea ice, some at different stages of physical development, calculated using this technique.

Our main conclusions are as follows:

- Terrestrial LiDAR can be used to measure surface roughness at mm-cm scale, provided the LiDAR system is elevated to a height of 2.5-3 m above the surface and the range is restricted to approximately 10 m.

- Terrestrial LiDAR is most suitable for measuring the roughness of snow and sea ice types which demonstrate strong surface specular reflection at visible or near-infrared wavelengths, including: glazed snow, melting white ice, blue ice, pancake ice, frost flowers and young congelation ice. More research is required to evaluate the suitability over dry snow, where volume scattering may bias the ranging estimate of the sensor.
- The 2-D approach for parameterizing surface roughness is considerably more precise than the traditional 1-D profiling approach and is therefore able to characterize a surface while satisfying an underlying assumption of stationarity, required by most backscatter models, which the 1-D generally cannot do.
- An absence of, or inadequate, detrending retains macro- and/or meso-scale topography in surface roughness calculations, leading to an overestimation of σ and l, and, typically, also erroneously classifies the surface correlation function as Gaussian rather than exponential. Of the fourteen sea ice surface types examined in this study, thirteen, including first- and multi-year ice, could be characterized with the exponential function and only one with the Gaussian.
- The critical maximum sampling interval and minimum sampling extent are dictated by the surface correlation length. The correlation length of pancake ice, typical of most sea ice surfaces at around 1.5 cm, provides Δx_{max} ~ 1 cm and L_{min} ~ 30 cm, but the correlation length of bare congelation ice, at around 0.3 cm, provides similar x_{max} to l of approximately 0.2 cm. We have demonstrated that the 2-D sampling approach increases Δx_{max} and decreases L_{min}, but clearly when $\Delta x \rightarrow l$, e.g. for bare ice when Δx = 2 mm, the sampling interval is inadequate for characterizing the correlation function.

- The correlation functions of most natural and artificial sea ice surfaces examined in this study, including first- and multi-year ice, are strongly anisotropic, indicating that a sea ice surface cannot generally be treated as an isotropic scattering interface in backscatter models (as is typically the case). Rather the correlation length should vary as a function of the azimuth angle, so that backscatter depends on both the radar incidence angle and the azimuth angle of surface correlation with respect to the incident beam [Fung, 1994].
- Our results demonstrate that there is no fundamental relationship between σ and l at the cm scale for sea ice surfaces. We speculate that earlier studies indicating such a relationship have actually characterized the fractal nature of surface roughness within a small area, i.e. the association between the rms height, correlation length and sampling extent when $L < L_{min}$, rather than a more general relationship.

Chapter 4. Numerical and Experimental Evaluation of Terrestrial LiDAR for Parameterizing Centimeter-Scale Sea Ice Surface Roughness

A peer-reviewed scientific research paper published in:

IEEE Transactions on Geoscience and Remote Sensing, 53(9), 4887-4898,

doi.org/10.1109/TGRS.2015.2412034

Jack C. Landy[*1], Alex S. Komarov[1,2], David G. Barber[1]

* Corresponding Author

[1] Centre for Earth Observation Science, Department of Environment and Geography, University of Manitoba, Winnipeg, Manitoba, Canada.

[2] Department of Electrical and Computer Engineering, University of Manitoba, Winnipeg, Manitoba, Canada.

Abstract

Terrestrial Light Detection and Ranging (LiDAR) offers significant advantages over conventional techniques for measuring the centimeter-scale surface roughness of natural surfaces, such as sea ice. However, the laser scanning technique is inherently limited, principally by: (1) the high inclination scanning angle of the sensor with respect to nadir, (2) the precision of the laser ranging estimate, and (3) the beam divergence of the laser. In this paper we introduce a numerical model which has been designed to simulate the acquisition of LiDAR data over a regular rough surface. Results from the model compare well (r^2 = 0.97) with LiDAR observations collected over two experimental surfaces of known roughness that were constructed from medium-density fibreboard (MDF) using a computer numerical control (CNC) three-axis router. The model demonstrates that surface roughness parameters are not sensitive to minor variations in the LiDAR sensor's range and laser beam divergence, but are slightly sensitive to the precision of the ranging estimate. The model also demonstrates that surface roughness parameters are particularly sensitive to the inclination angle of the LiDAR sensor. The surface rms height is underestimated and correlation length is overestimated as either the inclination angle of the sensor or the true roughness of the surface increases. An isotropic surface is also increasingly observed as an anisotropic surface as either the inclination angle or the true surface roughness increases. Based on the model results, we propose a set of calibration functions which can be used to correct *in situ* LiDAR measurements of surface roughness.

4.1. Introduction

The centimeter-scale surface roughness of sea ice is an important parameter for two different physical processes. Radar backscatter is sensitive to variations in roughness at either the air-snow or snow-sea ice interface, when the dielectric contrast between layers is high [Ulaby et al., 1982; Komarov et al., 2014]. Surface roughness also influences turbulent heat and mass exchanges between the sea ice and the atmosphere, thereby affecting both the ice surface energy balance [Andreas, 1987] and the exchange of climatically significant gases [Sørensen et al., 2014; Barber et al., 2014].

Centimeter-scale roughness characterizes surface macroscopic irregularities (e.g. visible roughness), but does not include microscopic roughness (<0.01 cm) or large-scale surface topography (>1 m). Conventional instruments for measuring mesoscale roughness in the field, including the pin profiler, meshboard, laser profiler, and stylus profilometer, are limited [Verhoest et al., 2008; Landy et al., 2015a]. For instance, the parameters derived from these instruments are assumed to represent the two-dimensional roughness properties of a surface, but are obtained from one-dimensional measurements (i.e. profiles). If the roughness parameters vary considerably between adjacent profiles, the one-dimensional measurements are not stationary [Callens et al., 2006]. The profiles obtained from these instruments also have a restricted sampling interval and sample length. In the case of the pin profiler and meshboard, the minimum sampling interval is typically > 5 mm and maximum sample length is ~ 1 m, which are inadequate to characterize mm-cm scale surface roughness [Landy et al., 2015a]. Roughness measurements obtained from small sampling profiles can make a natural surface appear fractal, i.e. roughness parameters depend on the length of the profile [Manninen, 1997]. Errors in roughness parameterizations can introduce significant bias into the results of microwave scattering models [Verhoest et al., 2008; Landy et al., 2015a] or energy balance calculations [Rees and Arnold, 2006].

A new technique has been developed for measuring and analyzing surface roughness using terrestrial laser scanning (or LiDAR), which offers several improvements on the conventional techniques [Landy et al., 2015a]. State-of-the-art discrete-pulse laser scanners operate with a pulse repetition frequency up to 1 MHz (one million points per second) [Leica Geosystems, 2013], measuring the time-of-flight for each laser pulse to be reflected by a target and return to the scanner, thereby mapping the target in three dimensions. A dual-axis scanner can rapidly collect two-dimensional surface roughness data at a mm-scale sampling interval, over an area that is > 5 x 5 m in size. Consequently, the two-dimensional measurements of surface roughness derived from a laser scanner are considerably more precise than one-dimensional profile-based measurements [Landy et al., 2015a]. Furthermore, the correlation function and correlation length of mm-cm scale surface roughness are accurately characterized by the high-frequency sampling interval and large sample area. Azimuthal variations in the roughness of an anisotropic surface can also be identified from the two-dimensional measurements.

There are, however, caveats to this technique. The laser scanner does not measure the range to a single point on the target surface, rather the laser has a finite beam divergence δ and the scanner therefore measures the range within a portion of the laser's footprint on the surface. If the angular sampling interval of the scanner Δ is below δ, sequential footprints will overlap, which may lead to correlated sampling. However, the irradiance profile of the laser beam typically resembles a Gaussian distribution, so it is actually beneficial that $\Delta =$

$\gamma\delta$, where $\gamma < 1$, to yield a higher Nyquist frequency [Lichti and Jamtsho, 2006]. The value of γ is uncertain, but numerical and experimental studies have demonstrated that it lies between approximately 0.6 and 0.9 [Lichti and Jamtsho, 2006; Pesci et al., 2011]. Uncertainty in γ is related to an ambiguous definition of the laser beam divergence. δ can be defined by the manufacturer of a LiDAR system as either the full-width (FW), Gaussian-width (GW), or full-width at half-height (FWHH) of the laser beam's irradiance profile [Jacobs, 2006].

Another potential limitation is the ranging precision of the laser scanner. The precision depends on the range and reflectivity (backscattering properties) of the target surface. Higher range and lower target reflectivity decrease the signal-to-noise ratio of the returning laser pulse, thereby reducing the precision of the ranging estimate [Wehr and Lohr, 1999]. However, at low range (≤10 m), the ranging noise of a state-of-the-art laser scanner can be < 1 mm, even for a target with a reflectivity as low as 10% [Leica Geosystems, 2013].

Perhaps the most significant limitation of terrestrial LiDAR for measuring surface roughness is the high inclination scanning angle from the sensor to the target surface, with respect to nadir. Laser scanners are generally restricted to an inclination angle $\psi > 45°$, and this has three repercussions. First, the laser footprint becomes elongated on the target surface along the track of the laser beam, meaning that sequential samples can become correlated in the along-track direction if Δ is sufficiently low compared to δ. Second, the number of samples acquired per unit area (sample density) for the same angular sampling interval decreases. Finally, positive projections ('hills') in a rough surface may obstruct the line-of-sight of the laser, shadowing negative projections ('valleys'), resulting in oversampling of the positive and undersampling of the negative projections [Pollyea and

Fairley, 2012]. This phenomenon has been referred to as surface ‘self-shadowing’ and introduces occlusion bias into surface roughness measurements [Pollyea and Fairley, 2012].

The goal of this study is to evaluate the accuracy of cm-scale sea ice surface roughness measurements derived from terrestrial LiDAR data. This is accomplished through laboratory-based experiments and numerical simulations, using artificially generated rough surfaces. In Section 4.2 we introduce a numerical model to simulate the acquisition of terrestrial LiDAR data over a 1 x 1 m regular rough surface, and outline a laboratory experiment designed to validate the model. In Section 4.3 we use the model to examine the sensitivity of statistical roughness parameters to the range, beam divergence, ranging precision, and inclination angle of the LiDAR sensor. In Section 4.4 we discuss which of these factors significantly influence surface roughness measurements and develop empirical functions for calibrating *in situ* field measurements of roughness. In Section 4.5 we conclude.

4.2. Methods

4.2.1. Numerical LiDAR Model

The purpose of the model is to simulate the spatial distribution of LiDAR points across a 1 x 1 m regular rough surface with predetermined statistical properties, as if the points had been collected using a terrestrial laser scanner. The statistical parameters characterizing the rough surface are the rms (root mean square) roughness height, σ, correlation length, l, and autocorrelation function, c [Ogilvy, 1991]. We describe these as the ‘surface’ variables. In addition, the following 'sensor' variables can be modified in the model: the two angles φ and θ which define the rotation of the surface about the (surface-parallel horizontal) y-axis and (vertical) z-axis, respectively, from nadir, the range from the sensor origin to the centre of the surface, R_C, the angular sampling interval, Δ, the beam divergence of the laser, δ, and one sigma of the ranging precision (i.e. the ranging noise), Ω (Figure 4.1).

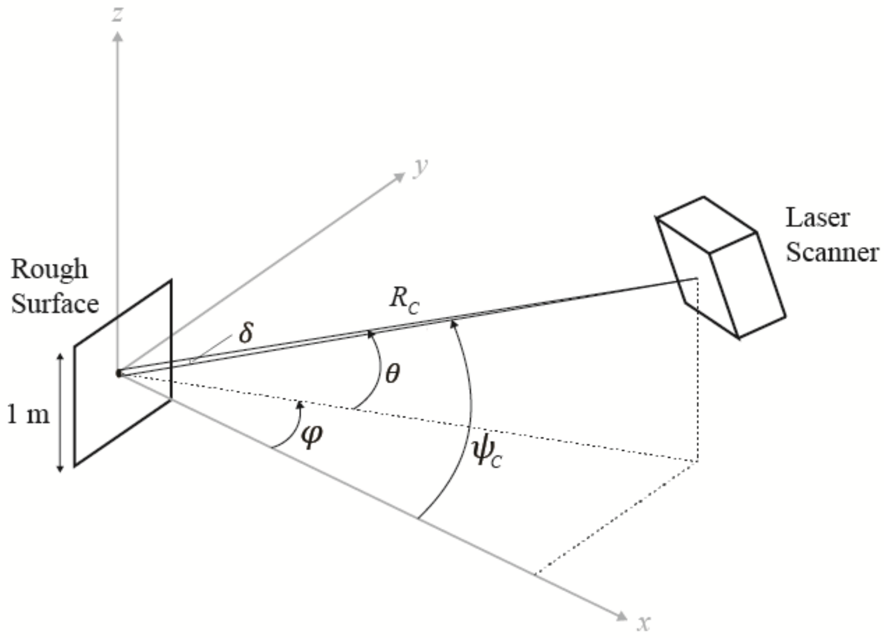

Figure 4.1 | Schematic diagram of the experimental and numerical model setup.

The model domain is based on a spherical coordinate system whose origin is located at the centre of the rough surface. The surface is located at $x = 0$ and extends from -0.5 to 0.5 m along y and z axes. The Cartesian coordinates of the sensor origin (x_s, y_s, z_s) can be defined in terms of spherical geometry as:

$$x_S = R_C \cos\varphi \cos\theta \tag{4.1}$$

$$y_S = R_C \cos\varphi \sin\theta \tag{4.2}$$

$$z_S = R_C \sin\theta, \tag{4.3}$$

where:

$$R_C = \sqrt{x_s^2 + y_s^2 + z_s^2}. \tag{4.4}$$

The inclination angle from the sensor to the centre of the rough surface ψ_C (Figure 4.1) can be defined in terms of φ and θ as:

$$\cos\psi_C = \cos\varphi \cos\theta. \tag{4.5}$$

Isotropic random rough surfaces are generated with predetermined statistical parameters as follows. Initially, an uncorrelated random surface $f_u(y, z)$ is created with Gaussian distribution, zero mean and standard deviation σ. Landy et al. [2015a] have demonstrated that sea ice surfaces at mm-cm scale are generally best characterized using the exponential correlation function. An isotropic exponential correlation function is:

$$c(\rho) = \exp\left(-\frac{\rho}{l}\right), \tag{4.6}$$

where $\rho = \sqrt{y^2 + z^2}$ is the absolute value of the position vector $\boldsymbol{\rho} = \{y, z\}$ in two dimensions. To generate the correlated rough surface $f(\boldsymbol{\rho})$ with pre-determined correlation function $c(\rho)$ we introduce the uncorrelated rough surface $f_u(\boldsymbol{\rho})$. The correlation function of $f_u(\boldsymbol{\rho})$ is the Dirac delta-function. It is possible to show that Fourier transforms of $f(\boldsymbol{\rho})$ and $f_u(\boldsymbol{\rho})$ are linked as follows:

$$F(\boldsymbol{k}) = F_u(\boldsymbol{k})\sqrt{C(\boldsymbol{k})}, \tag{4.7}$$

where $F(\boldsymbol{k})$ is the Fourier transform of $f(\boldsymbol{\rho})$, $F_u(\boldsymbol{k})$ is the Fourier transform of $f_u(\boldsymbol{\rho})$, $C(\boldsymbol{k})$ is the Fourier transform of the autocorrelation function $c(\rho)$, and $\boldsymbol{k} = \{k_y, k_z\}$ is the position vector in the Fourier domain. The correlated rough surface $f(\boldsymbol{\rho})$ is derived by applying the inverse Fourier transform to equation 4.7. In practice, the discrete Fourier transform is applied through the fast Fourier transform algorithm.

The simulated roughness parameters σ and l for a particular surface depend on how the sampling interval and area are discretized [Ogilvy and Foster, 1989]. For the surfaces generated here, a sampling interval of 2 mm and area of 1 x 1 m are used, which produce σ and l up to 10% different from predetermined σ and l, in the worst cases. Increasing the size of the surface to 2 x 2 m would reduce these errors by several times; however, an associated increase in computation time for the LiDAR model is prohibitive. Therefore, random synthetic surfaces are repeatedly generated by computer and tested until the errors in both σ and l with respect to the predetermined parameters are <1%. The key point is that σ and l are known for each generated surface, even if they are slightly different from the predetermined parameters. Hence, a change in σ or l as simulated by the LiDAR model is reported as the difference between the true and modelled roughness parameter.

LiDAR pulses are generated as a series of vectors with infinite range that extend out from the sensor origin in equal horizontal and vertical increments of Δ. The total number of pulses generated in horizontal and vertical directions (conventionally referred to as the number of columns and rows, respectively, in a LiDAR scan) are equal to the horizontal field-of-view (HFOV) or vertical field-of-view (VFOV) divided by Δ. HFOV is defined as the arc between lines that bisect the sensor origin and the minimum and maximum extent of the surface along the y-axis. VFOV is defined in the same manner along the z-axis.

Four attributes are calculated for each LiDAR pulse: (1) the across-track laser footprint diameter on the surface; (2) the along-track laser footprint diameter on the surface; (3) ranging noise; and (4) the location where the pulse intersects the surface plane. If the laser footprint diameter is small compared to the range, the across-track footprint diameter on the surface, $D_{f_{across}}$, is given by [Baltsavias, 1999]:

$$D_{f_{across}} = 2R\tan\left(\frac{\delta}{2}\right), \tag{4.8}$$

where R is the range from the sensor origin to the surface. The laser scanner used for the experimental assessment in this study was a *Leica Scanstation C10*, which has a FW δ of 0.24 mrad. For δ = 0.24 mrad, $D_{f_{across}}$ is 1.2 mm at 5 m range and 2.4 mm at 10 m range. In addition to the FW δ, the manufacturer also provides GW and FWHH beamwidths of the Leica C10 at 50 m range of 7 and 4.5 mm, respectively [Leica Geosystems, 2009]. These values equate to a GW δ of 0.14 mrad and a FWHH δ of 0.09 mrad, which would clearly provide smaller $D_{f_{across}}$ than the FW δ. The along-track footprint diameter on the surface, $D_{f_{along}}$, can be adapted from Sheng [2008] as:

$$D_{f_{along}} = \frac{2R\cos\psi\sin\delta}{\cos 2\psi + \cos\delta}, \tag{4.9}$$

where:

$$\tan\psi = \frac{\sqrt{(y_i - y_s)^2 + (z_i - z_s)^2}}{x_s}, \tag{4.10}$$

and y_i and z_i are coordinates of a LiDAR point on the surface. For ψ = 45° and (FW) δ = 0.24 mrad, $D_{f_{along}}$ is 1.7 mm at 5 m range and 3.4 mm at 10 m range. Again the GW and FWHH δ would provide smaller $D_{f_{along}}$ than the FW δ.

The precision of the laser scanner's range estimate is modelled as Gaussian noise, with one standard deviation Ω, following Pesci et al. [2011]. The true range of a single laser pulse is equal to $R + r$, where r is a random entry from the probability distribution function:

$$G(r) = \frac{1}{\Omega\sqrt{2\pi}} e^{-\frac{r^2}{2\Omega^2}}. \tag{4.11}$$

The manufacturer report 'modelled' Ω as ≤ 2.0 mm at 50 m range for the Lecia C10 [Leica Geosystems, 2009], although Ω has been measured as 0.8 mm in a practical experiment for a surface with high reflectivity at R < 10 m [Landy et al., 2015a].

Before we can evaluate the location where the laser pulse footprint intersects the surface and compute a range, we must identify elements of the surface that are shadowed from the sensor's perspective. This is accomplished by establishing whether there is a line-of-sight between the sensor origin and each grid node of the rough surface. For each grid node we perform the following, in order: (1) calculate the inclination angle between the sensor and primary node; (2) identify secondary grid nodes that lie on the line in the y-z plane between the sensor and primary node, within a specified distance of the primary node; and (3) calculate the inclination angle between the sensor and each secondary node. The inclination angles are calculated using equation 4.10 but, in this case, y_i and z_i are coordinates of a grid node. If the primary node angle is larger than all of the secondary node angles, the surface element is visible from the sensor's perspective. Conversely, if the primary node angle is smaller than any of the secondary node angles, the surface element is obscured from the sensor's perspective. An illustration of the relationship between the LiDAR sensor's inclination angle and surface self-shadowing from the sensor's perspective is shown in Figure 4.2.

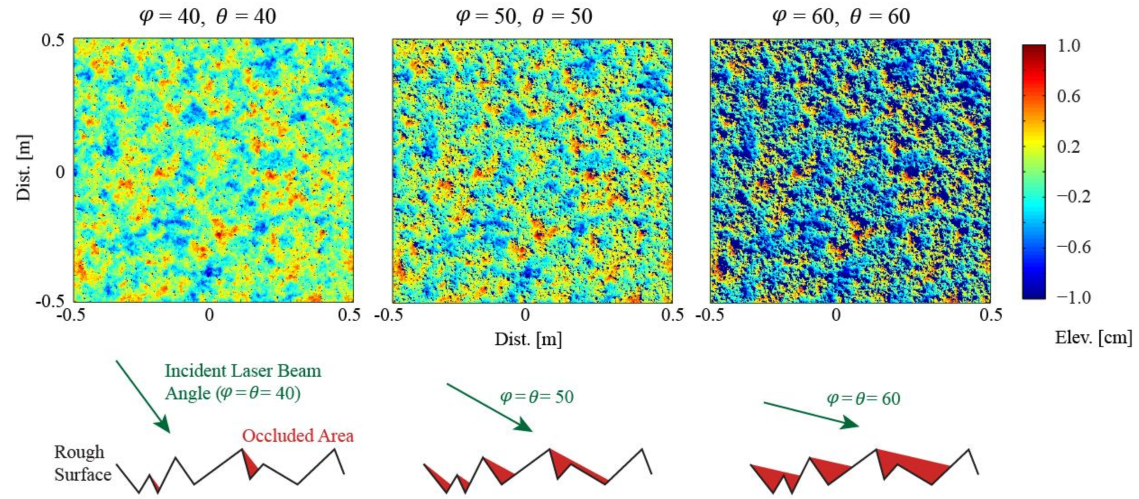

Figure 4.2 | Surface self-shadowing modelled from three different sensor perspectives. Surface σ = 0.2 cm and l = 2.0 cm. The sensor is located to the bottom-left of the surface and shadowed areas are shown in dark blue. Schematic diagrams illustrating the increase in occluded area as sensor inclination rises are given below each surface.

The y and z coordinates of a single LiDAR point are calculated as the centre of the laser footprint on the rough surface, plus y and z coordinate-vectors of the ranging noise. The x coordinate of the point is computed from the mean elevation of all unobscured surface elements within the laser footprint, plus the x coordinate-vector of the ranging noise. Therefore, as R_C and ψ increase, the size of the laser footprint on the surface grows and the footprint becomes increasingly ellipsoidal in the along-track direction, covering more surface elements and 'blurring' the final range estimate. Equally, as the surface becomes rougher (i.e. σ increases and/or l decreases), more surface elements are obscured within the laser footprint which biases the final range estimate.

The final distribution of LiDAR points is used to calculate single values for σ and l, as 'observed' by the laser scanner. The eccentricity of l in the y-z plane, ϵ_l (a measure of the anisotropy in surface roughness), is also calculated as:

$$\epsilon_l = \sqrt{1 - \left(\frac{\min(l)}{\max(l)}\right)^2}. \tag{4.12}$$

For instance, if the difference between maximum and minimum l is 50%, then ϵ_l ~ 0.75. These three parameters: σ, l and ϵ_l are obtained through linear interpolation of LiDAR points to a regular grid and two-dimensional autocorrelation, following the technique of Landy et al. [2015a].

4.2.2. Experimental Assessment

Two rough surface boards with predetermined σ, l, and exponential c, were manufactured from MDF to evaluate the validity of the numerical LiDAR model (Figures 4.3a and b). Two surfaces were initially generated by computer using the method described in Section 4.2.1. The statistical properties of the surfaces were representative of measurements from a relatively smooth and a relatively rough type of sea ice: bare white ice (σ = 0.16 cm, l = 1.72 cm) and frost flowers (σ = 0.26 cm, l = 0.59 cm), respectively. The boards were manufactured from the two synthetic surfaces using a computer numerical control (CNC) three-axis router, which removes material from a flat panel of MDF to a horizontal and vertical accuracy of 0.025 mm [Bourgouin, pers. comm., 2013]. Despite this level of accuracy, the two surfaces could not be kept absolutely isotropic. The standard deviation of the correlation length was 0.07 cm (0.04l) for the smooth surface and 0.03 cm (0.05l)

for the rough surface. However, these minor variations in l were not large enough to affect the results of the model validation (Section 4.3.1).

Figure 4.3 | (a) A close-up of the ‘rough’ MDF board used in the experimental assessment, **(b)** the ‘smooth’ MDF board, and **(c)** the rough board mounted to a frame which allowed dual-axis rotation about vertical (φ) and horizontal surface-parallel (θ) axes.

In turn, each board was mounted to a steel frame that allowed dual-axis rotation about horizontal and vertical surface-parallel axes (Figure 4.3c). The scanning origin of the Leica C10 was positioned exactly 5 m from the centre of the board, and both the sensor and centre of the board were elevated to a height of 1.6 m above the floor. The experimental setup was designed to exactly replicate the conditions of the numerical model.

For each scan, the point acquisition spacing Δx was set to 2 mm horizontally and vertically at a range of 5 m, corresponding to Δ of 0.4 mrad. For a detailed study of the sensitivity of surface roughness parameters to Δx, see Landy et al. [2015a]. Following the procedure of Pollyea and Fairley [2012], individual scans of each board were acquired for 24 dual-axis rotations about the vertical axis φ and/or surface-parallel horizontal axis θ. A set of scans were acquired with φ = 0 and θ varying in 10° increments from 0 to 80°, another set with θ = 0 and φ varying in 10° increments from 10 to 80°, and a final set with both φ and θ varying in equal 10° increments from 10 to 70°. A total of 48 scans were acquired between the two boards.

For each scan, single values for the roughness parameters σ, l, and ϵ_l, were calculated from the LiDAR points, following the technique of Landy et al. [2015a]. These parameters could then be compared to parameters generated from the model.

4.3. Application and Results

4.3.1. Model Validation

Observed roughness parameters σ_{obs} and l_{obs} from scans of the two experimental surfaces are compared with modelled roughness parameters σ_{mod} and l_{mod} in Figure 4.4. R_C was fixed at 5 m in the model runs to imitate the experimental setup. The model runs that were found to best predict the observed changes in σ and l with varying φ and θ were configured with Ω = 1 mm and the Gaussian-width δ of the Leica C10 (0.14 mrad).

The model well characterizes the observed changes in σ and l as either φ, θ or both angles vary from 0 to 80°. σ_{mod} follows σ_{obs} closely for both the smooth and rough surfaces, although σ_{mod} overestimates σ_{obs} by 0.1-0.2 mm (3-7%) for the rough surface when φ or θ rises above approximately 50° (Figure 4.4a). l_{mod} follows l_{obs} closely in both cases, although l_{mod} tends to underestimate the rate of increase in l_{obs} by up to 1.5 mm (8%) for the rough surface, when φ or θ rises above approximately 50° (Figure 4.4b). l_{mod}

also overestimates l_{obs} by almost 2 mm (10% and 26%, respectively) for both smooth and rough surfaces, when $\varphi = \theta = 70°$.

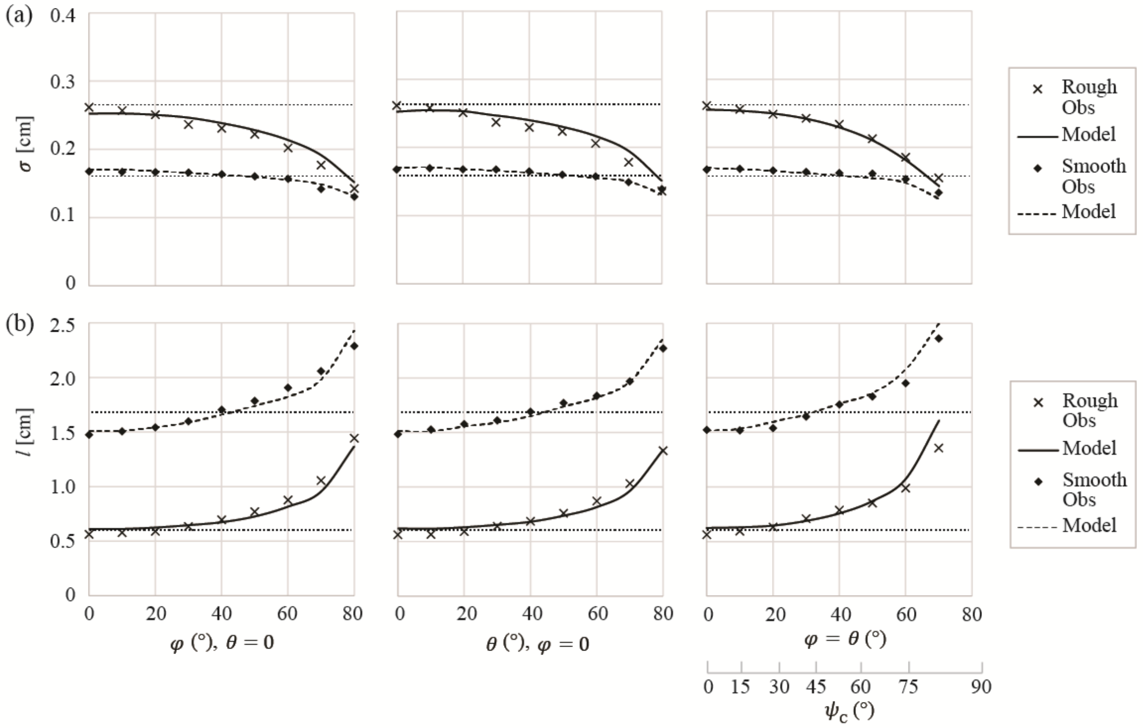

Figure 4.4 | Comparison between observed and modelled changes in **(a)** σ, and **(b)** l, as φ and θ are varied between 0 and 80°. The inclination angle ψ_C is calculated using equation 4.5. Horizontal dashed lines indicate σ_{true} and l_{true}.

The average coefficients of determination (r^2) between observed and modelled σ, for changes in φ, θ or φ and θ, are 0.97 and 0.98, for the smooth and rough surfaces, respectively. The average r^2 between observed and modelled l, for changes in φ, θ or φ and θ, are 0.97 for both the smooth and rough surfaces. The average root mean square errors (RMSE) between observed and modelled σ, for changes in φ, θ or φ and θ, are 0.034 and 0.074 mm, for the smooth and rough surfaces, respectively. The average RMSE between observed and modelled l, for changes in φ, θ or φ and θ, are 0.56 and 0.63 mm, for the smooth and rough surfaces, respectively. These errors are at least one order of magnitude lower than the typical values of σ and l in the mm-cm scale roughness range for sea ice [Onstott, 1992].

4.3.2. Sensitivity of σ, l and ε_l to the Sensor's Beam Divergence, Noise and Range

We examine the sensitivity of the modelled surface roughness parameters to variations in δ, Ω or R_C. For each sensitivity study, all of the sensor and surface parameters are identical to the following standard case, unless otherwise specified. The sensor inclination (φ, θ) is fixed at either (0, 0) or (45°, 45°), and the true surface roughness parameters σ_{true} and l_{true} are fixed at 0.25 and 1.5 cm, respectively. The sensor's beam divergence is fixed at the Gaussian-width (GW) of the Leica C10 (0.14 mrad), the ranging noise at 1 mm, and the range at 5 m.

To examine the sensitivity of the roughness parameters to the LiDAR sensor's beam divergence, δ is varied between FW, GW and FWHH cases (i.e. from 0.24 to 0.09 mrad). At a sensor inclination of φ = 0 and θ = 0, σ_{mod} and l_{mod} are independent of δ. σ_{mod} is almost identical to σ_{true} (Figure 4.5a), and l_{mod} is almost identical to l_{true} (Figure 4.5b), as δ is varied. At a sensor inclination of φ = 45° and θ = 45°, σ_{mod} and l_{mod} are also independent of δ. σ_{mod} consistently underestimates σ_{true} by around 0.14 mm (6%) (Figure 4.5a), and l_{mod} consistently overestimates l_{true} by around 1.9 mm (13%) (Figure 4.5b), as δ is varied. When the sensor is located at nadir, or inclined with respect to the rough surface, small variations in the beam divergence do not affect the modelled roughness parameters.

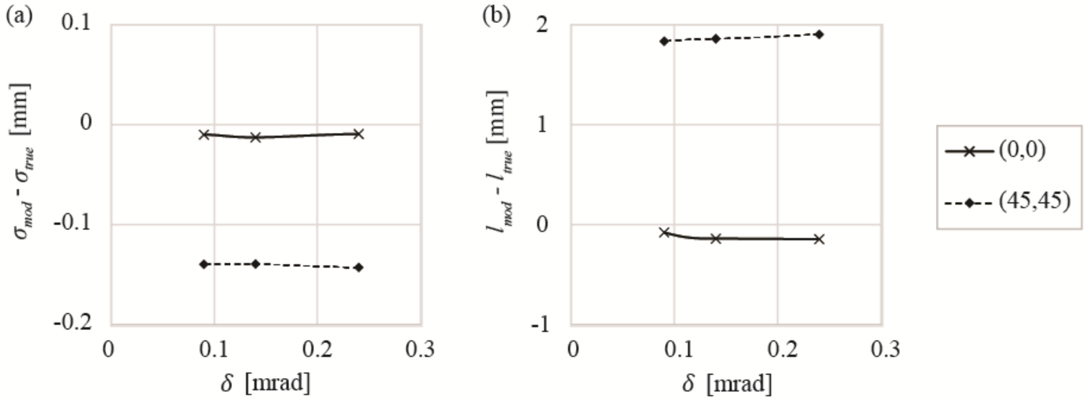

Figure 4.5 | Absolute errors of **(a)** σ, and **(b)** l, as δ is varied between FW, GW and FWHH cases (i.e. from 0.24 to 0.09 mrad).

To examine the sensitivity of the roughness parameters to the LiDAR sensor's ranging noise, Ω is varied between 0.5 and 2.0 mm, which covers the value of Ω reported by the manufacturer of the Leica C10 [Leica Geosystems, 2009] and values obtained through experimentation with the instrument [Landy et al., 2015a]. At a sensor inclination of $\varphi = 0$ and $\theta = 0$, σ_{mod} and l_{mod} clearly depend on Ω. σ_{mod} underestimates σ_{true} by up to 0.05 mm (2%) when Ω < 1.0 mm, but increasingly overestimates σ_{true} as Ω rises, up to 0.26 mm (10%) when Ω = 2.0 mm (Figure 4.6a). l_{mod} slightly overestimates l_{true} when Ω < 0.75 mm, but increasingly underestimates l_{true} as Ω rises, by up to 3.4 mm (23%) when Ω = 2.0 mm (Figure 4.6b). At a sensor inclination of $\varphi = 45°$ and $\theta = 45°$, σ_{mod} and l_{mod} are also clearly dependent on Ω. σ_{mod} underestimates σ_{true} by 0.17 mm (7%) when Ω = 0.5 mm, but decreasingly underestimates σ_{true} as Ω rises, and is very close to σ_{true} when

Ω = 2.0 mm (Figure 4.6a). l_{mod} overestimates l_{true} by almost 2.2 mm (15%) when Ω = 0.5 mm, but decreases as Ω rises (Figure 4.6b). Variations in the ranging precision of the sensor affect the modelled roughness parameters at nadir and when the sensor is inclined with respect to the rough surface.

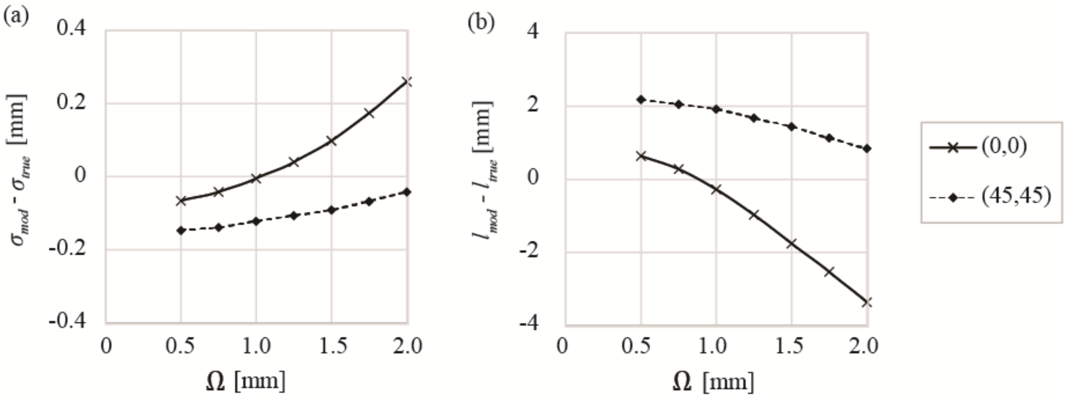

Figure 4.6 | Absolute errors of **(a)** σ, and **(b)** l, as Ω is varied between 0.5 and 2.0 mm.

To examine the sensitivity of the roughness parameters to the LiDAR sensor's range, R_C is varied between 3 and 10 m. These limits are based on the practical scanning range of the Leica C10 in the field for sea ice surfaces, which is restricted to a minimum of approximately 3 m, owing to the height of the laser scanner, and also to a maximum of approximately 10 m, owing to the increase in $D_{\updownarrow}$ with range and sensor inclination. Sea ice surfaces contain high-frequency (1-2 mm scale) roughness which can only be resolved at short scanning range (i.e. <10 m); however, the maximum range could potentially be extended beyond 10 m when scanning alternative natural surfaces containing lower-frequency roughness (e.g. >5-10 mm). Note that Δ is varied between model runs, so that the across-track sample spacing is always 2 mm at R_C. At a sensor inclination of φ = 0 and θ = 0, σ_{mod} and l_{mod} are independent of R_C. σ_{mod} is almost identical to σ_{true} (Figure 4.7a), and l_{mod} consistently underestimates l_{true} by around 0.3 mm (2%) (Figure 4.7b), as R_C is varied. At a sensor inclination of φ = 45° and θ = 45°, σ_{mod} and l_{mod} are also independent of R_C. σ_{mod} consistently underestimates σ_{true} by around 0.14 mm (6%) (Figure 4.7a), and l_{mod} consistently overestimates l_{true} by around 1.8 mm (12%) (Figure 4.7b), as R_C is varied. When the sensor is located at nadir, or inclined with respect to the rough surface, variations in the sensor's range (within 10 m) do not affect the modelled roughness parameters.

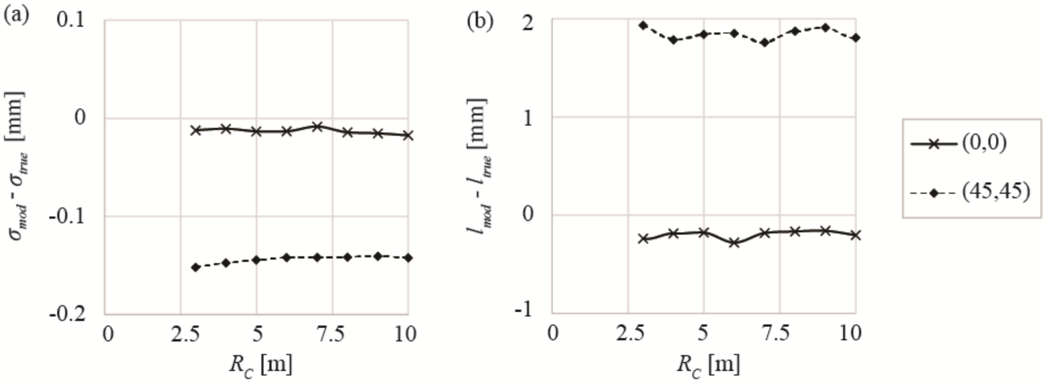

Figure 4.7 | Absolute errors of **(a)** σ, and **(b)** l, as R_C is varied between 3 and 10 m.

In addition to the roughness parameters σ_{mod} and l_{mod}, we also examine the influence of δ, Ω and R_C on the eccentricity in correlation length, ε_l. Our results demonstrate that ε_l is independent of each of these sensor parameters (data not shown). An isotropic rough surface does not become artificially observed as an anisotropic rough surface by the laser scanner as δ, Ω or R_C is varied.

4.3.3. Sensitivity of σ, l and ε_l to the Sensor's Inclination Angle

The key objective of this study is to examine the sensitivity of the surface roughness parameters to the LiDAR sensor`s inclination angle. Figure 4.4 demonstrates the influence of increasing ϕ and θ on σ_{mod} and l_{mod} for two surfaces with roughness parameters equal to those used in the experimental assessment. In both the smooth and rough cases, σ_{mod} decreases non-linearly as φ, θ or φ and θ increase, whereas l_{mod} increases non-linearly as φ, θ or φ and θ increase. However, the rate of change in σ_{mod} or l_{mod} is different between the two cases. σ_{mod} decreases more rapidly, and begins to decrease at a lower inclination angle, for the rough rather than smooth surface. l_{mod} increases more rapidly, and begins to increase at a lower inclination angle, for the rough rather than smooth surface. Additionally, at nadir, σ_{mod} overestimates σ_{true} for the smooth surface but underestimates σ_{true} for the rough surface. In contrast, at nadir, l_{mod} is almost identical to l_{true} for the smooth surface but overestimates l_{true} for the rough surface.

To examine the sensitivity of σ_{mod} and l_{mod} at different inclination angles ψ_C to variations in the true surface roughness parameters, σ_{true} and l_{true}, we use a GW δ, and fix Ω at 1 mm and R_C at 5 m, following the results of the model validation in Section 4.3.1. Rough surfaces are generated for σ_{true} at 0.05 cm intervals from 0.15-0.5 cm and for l_{true} at 0.5 cm intervals from 0.5-5.0 cm. These limits in σ and l were determined from published measurements of sea ice surface roughness (see Landy et al. [2015a] and references therein). We then simulate σ_{mod} and l_{mod} for each surface and for each regular 10° interval of ψ_C from 0 to 80°.

Variations in the absolute error of σ as a function of σ_{true}, for different φ_C and l_{true}, are shown in Figure 4.8. The modeled rms height clearly depends on both the inclination angle of the sensor and the true rms height and correlation length of the rough surface. When ψ_C is close to nadir, σ_{mod} overestimates σ_{true} slightly at low σ_{true} and l_{true}. However, when ψ_C > 40°, σ_{mod} tends to underestimate σ_{true} at all σ_{true} and l_{true}. σ_{mod} consistently decreases as σ_{true} rises, at all inclination angles and correlation lengths, although the rate of decrease in σ_{mod} with σ_{true} is greater for low l_{true}. For instance, at ψ_C = 80°, σ_{mod} underestimates σ_{true} by almost 0.25 cm (50%) when σ_{true} = 0.5 cm and l_{true} = 0.5 cm, whereas σ_{mod} underestimates σ_{true} by only 0.07 cm (14%) when σ_{true} = 0.5 cm but l_{true} = 5.0 cm.

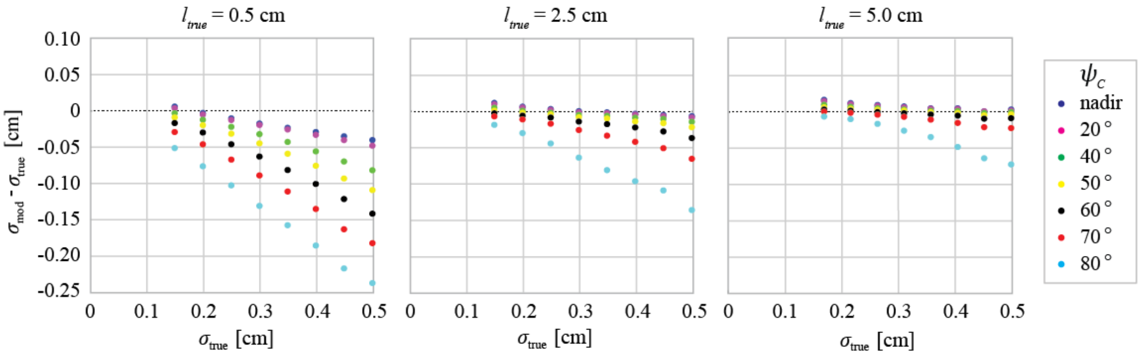

Figure 4.8 | Absolute error of σ as a function of σ_{true} and ψ_C, for l_{true} = 0.5, 2.5 and 5.0 cm.

Variations in the absolute error of l as a function of l_{true}, for different ψ_C and σ_{true}, are shown in Figure 4.9. The modeled correlation length depends on both the inclination angle of the sensor and the true rms height and correlation length of the rough surface. However, the relationships in Figure 4.9 are not as clear as they are for the modeled rms height in Figure 4.8. When ψ_C is greater than approximately 60°, l_{mod} overestimates l_{true} at all σ_{true} and l_{true}. In contrast, when ψ_C is less than 60°, l_{mod} can underestimate l_{true} at low σ_{true} and high l_{true}, but can overestimate l_{true} at high σ_{true} and low l_{true}. In general, l_{mod} decreases as a function of l_{true} at all ψ_C and σ_{true}. The exception to this is for the highest inclination angle (ψ_C = 80°), where l_{mod} remains consistently high as l_{true} rises when $\sigma_{true} \geq 0.3$ cm, although there is considerable scatter in the results for l_{mod} at ψ_C = 80°.

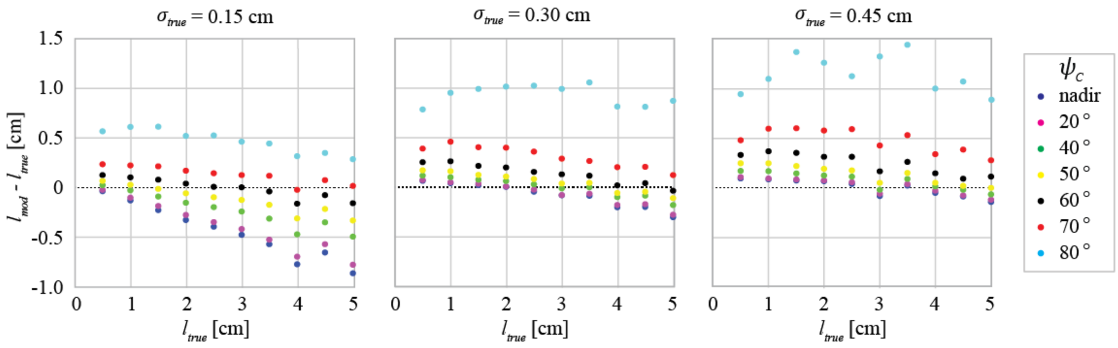

Figure 4.9 | Absolute error of l as a function of l_{true} and ψ_C, for σ_{true} = 0.15, 0.30 and 0.45 cm.

Variations in $\varepsilon_{l_{mod}}$ as a function of σ_{true}, for different ψ_C and l_{true}, are shown in Figure 4.10. When $\psi_C < 60°$, $\varepsilon_{l_{mod}}$ is below 0.4 regardless of the value of σ_{true} and l_{true}, which demonstrates that the rough surface is accurately ‘observed’ as an isotropic surface by the laser scanner. However, when $\psi_C \geq 60°$, $\varepsilon_{l_{mod}}$ increases as a function of σ_{true} and generally decreases as a function of l_{true}. For l_{true} = 1.0 cm, the rate of increase in $\varepsilon_{l_{mod}}$ with σ_{true} rises as ψ_C increases from 50 to 70°. At ψ_C = 80°, $\varepsilon_{l_{mod}}$ is relatively high (0.6) even when σ_{true} is only 0.15 cm. For l_{true} = 2.5 cm, $\varepsilon_{l_{mod}}$ only increases as a function of σ_{true} when ψ_C = 80°. For l_{true} = 5.0 cm, $\varepsilon_{l_{mod}}$ varies randomly with σ_{true} at all inclination angles, but is consistently between 0.3 and 0.5. An isotropic rough surface is ‘observed’ by the laser scanner as an increasingly anisotropic surface as the true rms height of the surface rises, the true correlation length falls, and/or the inclination angle of the sensor rises above approximately 50°.

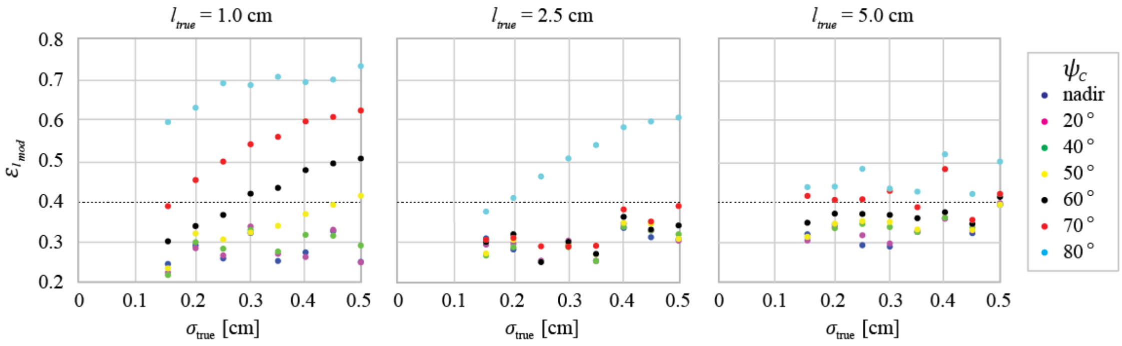

Figure 4.10 | Variations in ε_l as a function of σ_{true} and ψ_C, for l_{true} = 1.0, 2.5 and 5.0 cm. A surface with a difference between maximum and minimum l < 10% (i.e. the surface is close to isotropic) has ε_l < 0.4, which is marked by the dashed line.

4.4. Discussion

4.4.1. Factors Affecting Surface Roughness Measurements

Our results demonstrate that the accuracy of LiDAR-derived surface roughness measurements depends on complex relationships that exist between the sampling parameters of the LiDAR sensor and the inherent (unknown) roughness properties of the target surface. In this section, we explain why the relevant sensor and surface parameters affect the roughness measurements.

The roughness measurements are insensitive to minor variations in the laser beam divergence of the LiDAR sensor, depending on which definition of δ is used. As explained above, δ can be defined as the full-width, Gaussian-width, or full-width half-height of the beam divergence. LiDAR manufacturers generally specify the full-width δ, although it has not yet been identified which of these definitions is the most practical. We found that Gaussian-width δ gave the best fit between observed and modelled surface roughness parameters using the Leica C10 (Section 4.3.1). However, we also found that variations in δ between definitions were not large enough to change how well roughness elements were resolved within the laser footprint, at our scale of interest (Figure 4.5).

The roughness measurements are also insensitive to the sensor’s range, within a practical limit of approximately 10 m. In our experiments with the Leica C10, changes in the diameter of the laser footprint (both along and across the track of the laser beam) caused by variations in the range were not large enough to change how well roughness elements were resolved within the laser footprint (Figure 4.7).

However, the roughness measurements are sensitive to the ranging precision (noise floor) of the LiDAR sensor. The measured rms height is increasingly overestimated as Gaussian noise is added to LiDAR points, because increasing noise widens the vertical height distribution of surface roughness elements. This effect is reduced as the inclination angle of the sensor increases, owing to two processes. (1) Occlusion errors proliferate (i.e. the surface becomes increasingly self-shadowed) (Figure 4.2). (2) Ranging noise is added in the direction of the laser beam, so the component of the noise which is normal to the surface decreases. Both processes act to narrow the height distribution and reduce the rms height. The measured correlation length is increasingly underestimated as noise is added to LiDAR points, because the Gaussian noise which is added to adjacent samples is uncorrelated. This acts to increase the mean slope between adjacent roughness elements, thus reducing the correlation length. The effect is more pronounced if the true surface rms height is lower, because the mean slope between adjacent elements of the rough surface is initially small. For instance, the correlation length is severely underestimated when σ_{true} = 0.15 cm in Figure 4.9, but is not when σ_{true} = 0.45 cm. Despite the sensitivity of measured σ and l to the sensor's ranging precision, modelled changes in either parameter were typically more than one order of magnitude lower than true σ or l, when Ω was varied within a reasonable range for the Leica C10 (between 0.5 and 2.0 mm) (Figure 4.6).

The roughness measurements are particularly sensitive to the LiDAR sensor's inclination angle. The measured rms height decreases as the inclination angle increases (Figure 4.8), for three reasons. (1) The along-track laser footprint diameter lengthens, blurring roughness elements within the footprint and reducing the precision of the range estimate. (2) The total number N of LiDAR samples acquired over the surface decreases non-linearly as ψ_C rises [Pollyea and Fairley, 2012] (Figure 4.11). As N decreases, the sampling interval on the surface Δx increases and surface height extrema (the highest positive or negative projections of the topography) are undersampled [Verhoest et al., 2008]. (3) Occlusion errors proliferate and the ranging estimate is biased towards positive projections in the topography [Pollyea and Fairley, 2012]. These effects are all more pronounced if the true rms height of the surface is higher and/or the true correlation length is lower (i.e., the surface is rougher; Figure 4.8), because the mean slope between adjacent elements of the surface is larger. This result supports the conclusion of Pollyea and Fairley [2012] who found that σ is increasingly underestimated as the inclination angle of the LiDAR sensor rises.

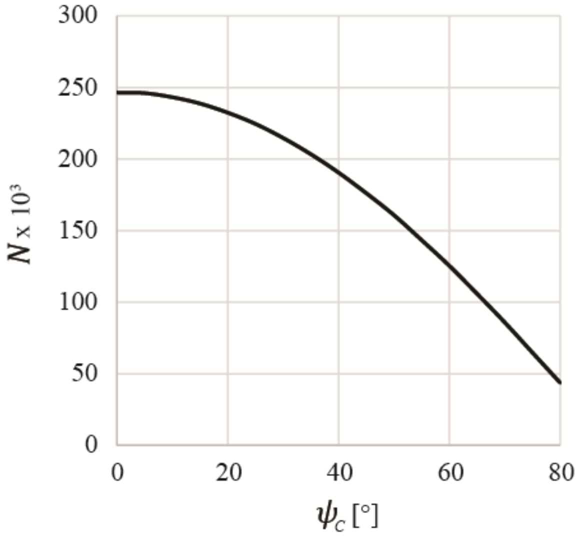

Figure 4.11 | The effect of ψ_C on the number N of LiDAR samples acquired over a 1 x 1 m surface, when the angular sampling interval Δ is 0.4 mrad.

In contrast to the rms height, the measured correlation length increases as the inclination angle increases (Figure 4.9), again owing to the three reasons stated above. As the laser footprint on the surface lengthens, adjacent samples can eventually become correlated in the along-track direction. Additionally, as N decreases, Δx increases, so that roughness elements at a scale which is smaller than either the footprint diameter or sampling interval cannot be resolved. Most importantly, as the occlusion errors proliferate, the LiDAR sensor cannot measure the intervening 'negative' topography between adjacent positive projections, and positive elements of the surface thus appear correlated to the sensor.

The measured eccentricity in the correlation length also increases as the inclination angle increases, because the laser footprint becomes increasingly elliptical, elongated in the along-track direction, which eventually leads to correlated sampling, and the total number of LiDAR samples on the surface decreases. The measured correlation length appears larger along the axis parallel to the sensor than perpendicular to it. This effect is more pronounced when the true rms height of the surface is higher and/or the true correlation length is lower (i.e., the surface is rougher; Figure 4.10), because the mean slope between adjacent elements of the surface is larger. For instance, laser profiling measurements have appeared to show that snow roughness is strongly anisotropic [Manninen, 1997], but at least part of this 'observed' anisotropy may have been artificially introduced by the high laser scanning angle. However, even at an inclination angle as high as 80°, rms height as high as 0.5 cm and correlation length as low as 1.0 cm, this phenomenon only produces artificial eccentricity in l of around 50% (i.e., ε_l ~ 0.75). Consequently, if measured ε_l is greater than approximately 0.75, it is safe to assume that the roughness of the surface is truly anisotropic.

A significant point to note here is that it is not only the statistical roughness properties of the target surface which affect the LiDAR measurements, but also the reflective properties of the material. For instance, in the case of sea ice, the green laser beam of the Leica C10 (wavelength = 512 nm) may penetrate slightly into the snow or ice, and the backscattered laser pulse will then combine light originating from both surface and volume scattering. It would have been impossible to create experimental surfaces with predetermined roughness parameters from sea ice in this study. Therefore we used MDF, which was expected to provide a strong pulse return (especially at short range) using the Leica C10, to validate our numerical model. For the model results to be applicable to a natural surface (such as sea ice), we make the fundamental assumption that the laser scanner typically records the range of a target from the front of a returning laser pulse, and thus the effect of volume scattering is negligible. This assumption is supported, in the case of sea ice, by observations of the polarization of light reflected from various types of ice [Perovich, 1994; 1998], as discussed in Landy et al. [2015a]. Further experiments are required to verify this assumption empirically, for both sea ice and other natural surfaces (such as soil or rock). In any case, a LiDAR system with a near-infrared (NIR) laser could be used to avoid this issue, since NIR light typically does not penetrate natural materials such as sea ice, snow, soil or rock.

4.4.2. Calibrations for *In-Situ* Roughness Measurements

The accuracies of measured σ and l principally depend on the true roughness properties of the surface and the inclination angle of the LiDAR sensor. We can attempt to use these relationships, illustrated in Figures 4.8 and 4.9, to develop empirical calibration functions for correcting the measured roughness parameters. The true rms height and correlation length each depend on the measured (or 'observed') parameters: σ_{obs}, l_{obs} and ψ_C, obtained with the LiDAR sensor, through non-linear relationships. However, the specific form of each of these non-linear relationships is unknown.

We use a genetic algorithm to optimize the functional form of a multi-dimensional polynomial fit to the parameters: σ_{obs}, l_{obs} and ψ_C, for each of the dependent variables: σ_{cal} and l_{cal}, which are the accurate (calibrated) roughness parameters. The genetic algorithm tests the least-square fit of an initial population of candidate polynomial functions on the data, then iteratively optimizes the functions by 'mutating' or altering their properties [Clegg et al., 2005]. At each iteration (commonly referred to as a 'generation'), functions which provide a poor fit on the data are rejected whereas functions which provide a good fit on the data are modified slightly and re-tested. Modifications include crossover, which combines two 'parent' functions and produces a single merged 'child' function at the next generation, and mutation, which alters one part of a parent function to produce a new child function. In our algorithm, these modifications can change the number of terms and/or power of a term in the polynomial. The algorithm is terminated when the difference in the 'goodness of fit' from one generation to the next is negligible. However, the mutation rate is kept sufficiently large to ensure that the algorithm does not converge to a local minimum, rather it converges to the global optimum

The calibration functions for correcting the rms height and correlation length, based on the measured parameters: σ, l and ψ_C, are as follows. The maximum number of terms in each polynomial was set as six and the maximum value of the sum of powers in a term group was also set as six to avoid polynomial ‘ringing’ (unreasonably large model inflexions).

$$\sigma_{cal} = \alpha_1 l^2 \psi_C^2 + \alpha_2 \sigma \psi_C^5 + \alpha_3 l + \alpha_4 \sigma l \psi_C^3 + \alpha_5 \sigma + \alpha_6 l \psi_C^4. \tag{4.13}$$

$$l_{cal} = \beta_1 l + \beta_2 \sigma \psi_C^4 + \beta_3 \psi_C^2 + \beta_4 \sigma^3 l^2 + \beta_5 \sigma l + \beta_6 \sigma \psi_C^5. \tag{4.14}$$

The coefficients α_n in equation 4.13 and β_n in equation 4.14 are given in Table 4.1. The confidence intervals for the coefficients in Table 4.1 provide a measure of the precision of the model estimates. There is a 99% probability that the calculated confidence interval encompasses the true value for each coefficient. We can verify the two statistical models by applying these coefficients and comparing the calibrated parameters to the values of σ_{true} and l_{true} shown in Figures 4.8 and 4.9. The r^2 between the predicted (calibrated) roughness parameters and the true roughness parameters is 0.99 for both models. The RMSE between the predicted (calibrated) roughness parameters and the true roughness parameters are 0.11 and 0.91 mm for the two models, respectively. For comparison, the RMSE between the measured and true roughness parameters are 0.40 and 4.06 mm for the two models, respectively; so the calibrated parameters are a significant improvement.

The benefit of these empirical calibration functions is that they require no advanced knowledge of the true roughness properties of the surface. LiDAR data can be collected over a target surface, preprocessed using the technique of Landy et al. [2015a] to calculate roughness parameters as ‘observed’ by the LiDAR sensor, and then calibrated using the above functions to calculate accurate roughness parameters. The three variables required by the calibration functions: σ, l and ψ_C, can be obtained through basic preprocessing of the raw LiDAR data. No advanced modelling is required. However, it is important to note that these functions can only be used if the measured surface roughness is within the validity range of the model predictions reported in this study, i.e. 0.15 cm ≤ σ ≤ 0.5 cm, and 0.5 cm ≤ l ≤ 5 cm.

Table 4.1 | Calibration coefficients for correcting measured σ and l, using equations 4.13 and 4.14. The upper and lower bounds of the 99% confidence interval are also provided for each coefficient.

	Coefficient	99% Confidence Interval	
		Lower	Upper
$\boldsymbol{\alpha_1}$	1.810×10^{-4}	1.803×10^{-4}	1.816×10^{-4}
$\boldsymbol{\alpha_2}$	4.022×10^{-10}	4.015×10^{-10}	4.029×10^{-10}
$\boldsymbol{\alpha_3}$	-9.401×10^{-3}	-9.437×10^{-3}	-9.365×10^{-3}
$\boldsymbol{\alpha_4}$	-4.149×10^{-5}	-4.160×10^{-5}	-4.137×10^{-5}
$\boldsymbol{\alpha_5}$	1.081	1.080	1.082
$\boldsymbol{\alpha_6}$	-1.424×10^{-9}	-1.428×10^{-9}	-1.419×10^{-9}
$\boldsymbol{\beta_1}$	1.245	1.244	1.246
$\boldsymbol{\beta_2}$	2.903×10^{-7}	2.892×10^{-7}	2.914×10^{-7}
$\boldsymbol{\beta_3}$	-1.240×10^{-6}	-1.244×10^{-6}	-1.236×10^{-6}
$\boldsymbol{\beta_4}$	2.594×10^{7}	2.579×10^{7}	2.609×10^{7}
$\boldsymbol{\beta_5}$	-7.539×10^{1}	-7.564×10^{1}	-7.514×10^{1}
$\boldsymbol{\beta_6}$	-4.143×10^{-9}	-4.155×10^{-9}	-4.131×10^{-9}

4.5. Conclusion

Numerical simulations and laboratory experiments were performed to evaluate the accuracy of cm-scale surface roughness measurements derived from terrestrial LiDAR data. A numerical model was developed to simulate the acquisition of LiDAR data over a regular rough surface, artificially modelled and based on sea ice roughness statistics. The model could accurately simulate: (1) the size and shape of the laser footprint on the surface, (2) ranging noise in the sensor, and (3) occlusion errors caused by surface self-shadowing from the sensor's perspective. A laboratory experiment was then designed to validate the model. Two surfaces with predetermined statistical roughness parameters were machined from MDF using a CNC three-axis router and mounted to a frame that allowed the surface to be rotated around horizontal and vertical surface-parallel axes. A *Leica Scanstation C10* terrestrial laser scanner was used to collect LiDAR data across each MDF surface at a range of inclination angles. Comparisons between the experimental and model results showed that the model accurately predicted changes in the surface roughness parameters as the inclination angle of the sensor was varied.

Further model runs were performed to assess the sensitivity of predicted surface roughness parameters to a variety of 'sensor' and 'surface' variables. The predicted roughness parameters were found to not be sensitive to minor changes in the laser beam divergence, depending on which of the manufacturer's definitions (full-width, Gaussian-width, or full-width half-height) were used. The predicted roughness parameters were also found to not be sensitive to the range of the LiDAR sensor, within a maximum scanning range of approximately 10 m. However, the predicted roughness parameters were found to be only moderately dependent on the ranging precision of the sensor. Higher ranging noise artificially increased the rms height and decreased the correlation length of the rough surface.

The predicted roughness parameters were primarily dependent on the inclination angle of the sensor and the true roughness parameters of the surface. As the inclination angle increased, the rms height dropped but the correlation length and the anisotropy in the correlation length rose, because the LiDAR data increasingly oversampled positive (higher) and undersampled negative (lower) projections of the rough surface. This caused the vertical distribution of surface roughness elements to become narrowed, biasing the rms height and correlation length. Since the sensor's ranging noise is always added in the direction of the laser beam, an increase in the inclination angle also reduced the effect of noise on the LiDAR data, enhancing the decrease in the rms height. As the true roughness of the surface increased, i.e. the rms height increased or correlation length decreased, this phenomenon became even more pronounced. A greater fraction of the surface became shadowed from the sensor's perspective, causing the modelled rms height to drop and the correlation length to rise.

By modelling these scenarios we were able to identify non-linear relationships between the accuracy of measured roughness parameters and both the inclination angle of the sensor and true roughness parameters of the surface. Multivariate polynomial regression was then used to develop empirical calibration functions for correcting measured roughness parameters, using only information that is available through basic preprocessing of the raw LIDAR data. The functions can be used to correct roughness parameters derived from any surface which provides a strong backscatter response to the LiDAR sensor and is rough on the order of a few mm to a few cm.

The confidence intervals of the model coefficients can then be used to obtain a measure of the precision of the model estimate. However, the coefficients reported in this study for the calibration functions were developed from a model that was based on the *Leica Scanstation C10* laser scanner. These coefficients may vary slightly for a different laser scanning system, particularly if the beam divergence or noise floor of the system is substantially different from the Leica C10. For instance, the *Optech ILRIS HD* has Gaussian-width δ = 0.15 mrad (Ω is not reported by the manufacturer) [Optech Inc., 2015], and may potentially produce similar results to the Leica C10. However, *the Riegl VZ-400* has larger δ = 0.30 mrad and Ω = 3 mm (at 100 m range) [Riegl LMS, 2014] than the Leica C10, which may cause a larger and more rapid loss of accuracy of the obtained roughness parameters as a function of the inclination angle than presented here. If required, the model presented here can be run with alternative parameters to obtain calibration coefficients for a different laser scanning system.

This novel technique for characterizing the statistical roughness of natural surfaces has already been applied in several studies. It has been used to develop a small database of sea ice surface roughness statistics [Landy et al., 2015a] and to monitor changes in the roughness of both young and mature sea ice over time [Isleifson et al., 2014; Scharien et al., 2014]. Although these studies were applied to sea ice, the technique is also suitable for measuring the roughness of other surfaces, such as soil and rock.

Chapter 5. Surface and Melt Pond Evolution on Landfast First-Year Sea Ice in the Canadian Arctic Archipelago

A peer-reviewed scientific research paper published in:

Journal of Geophysical Research – Oceans, 119, 3054-3075,

doi.org/10.1002/2013JC009617

Jack C. Landy*, Jens K. Ehn, Megan Shields, David G. Barber

* Corresponding Author

Centre for Earth Observation Science, Department of Environment and Geography, University of Manitoba, Winnipeg, Manitoba, Canada.

Abstract

The evolution of landfast sea ice melt pond coverage, surface topography and mass balance were studied in the Canadian Arctic during May-June 2011 and 2012, using a terrestrial laser scanner, snow and sea ice sampling, and surface meteorological characterization. Initial melt pond formation was not limited to low-lying areas, rather ponds formed at almost all pre-melt elevations. The subsequent evolution of melt pond coverage varied considerably between the two years owing to four principle, temporally-variable factors. First, the range in pre-melt topographic relief was 0.5 m greater in 2011 (rougher surface) than in 2012 (smoother surface), such that a seasonal maximum pond coverage of 60% and maximum hydraulic head of 204 mm were reached in 2011, versus 78% and 138 mm in 2012. A change in the meltwater balance (production minus drainage) caused the ponds to spread or recede over an area that was almost 90% larger in 2012 than in 2011. Second, modification of the pre-melt topography was observed during mid-June, due to preferential melting under certain drainage channels. Some of the lowest-lying pre-melt areas were subsequently elevated above these deepening channels and unexpectedly became drained later in the season. Third, ice interior temperatures remained 1-2 °C colder later into June in 2012 than in 2011, even though the ice was 0.35 m thinner at melt onset, thereby delaying permeability increases in the ice that would allow vertical meltwater drainage to the ocean. Finally, surface melt was estimated to account for approximately 62% of the net radiative flux to the sea ice cover during the melt season.

5.1. Introduction

Energy exchanges across the ocean-sea ice-atmosphere interface are poorly understood during the Arctic melt season, when the sea ice surface becomes heterogeneous with the melting of snow and formation of meltwater ponds. Wherever these ponds form, ice surface albedo drops from typical winter snow values of > 0.8 to around 0.2-0.4 [Perovich et al., 2002a], and a larger fraction of the incident solar radiation is absorbed within the ice and transmitted through to the ocean [Ehn et al., 2011], thereby accelerating melt. This leads to a reduction in the thickness of the ice and further pond growth [Curry et al., 1995]. In contrast, wherever ponds do not form, melting surface ice is drained of meltwater to expose a layer of bubble-rich superimposed ice [Hanesiak et al., 2001; Granskog et al., 2006] or form a surface layer of disaggregated, snow-like ice crystals [Perovich et al., 2002a], both of which retain a relatively high albedo despite extensive melting. These self-perpetuating and -reciprocating phenomena are important components of the ice-albedo feedback mechanism [Curry et al., 1995].

Climate model projections of sea ice volume and extent are particularly sensitive to variations in prescribed albedo [Pederson et al., 2009; Flocco et al., 2012]. Some recent progress has been made to create physically-based numerical models of melt pond coverage [e.g. Skyllingstad et al., 2009; Scott and Feltham, 2010] and incorporate melt pond physics into albedo parameterizations for global climate models [e.g. Flocco et al., 2010; Hunke and Lipscombe, 2010; Flocco et al., 2012]. However, limited melt pond observations have shown that seasonal coverage can vary by as little as 25% [Barry, 1983; Perovich et al., 2002b] or by as much as 85% [Holt and Digby, 1985], that diurnal coverage can vary by as much as 35% [Scharien and Yackel, 2005], and that interannual maximum coverage for ice in the same general location can vary by as much as 20-25% [Polashenski et al., 2012]. Physically-based albedo parameterizations suffer from a lack of validation data and from our incomplete understanding of the variability associated with melt pond formation and evolution. This variability is controlled by a history of physical forcing mechanisms (including air temperatures, winds, snowfall or rain events, ocean heat flux, ice growth conditions, and ice deformation) experienced by the ice cover since its formation. Each of these forcing mechanisms can be highly variable over space and time.

After initial formation, melt ponds generally develop over four consecutive stages [Eicken et al., 2002]. These are: (I) topographic control, (II) hydrostatic balance, (III) ice freeboard control, and finally (IV) fall freeze-up or ice break-up. Such a sequence of stages has been supported by recent observations [e.g. Nicolaus et al., 2010; Ehn et al., 2011; Petrich et al., 2012; Polashenski et al., 2012]. However, available observations, including those in this study, demonstrate considerable deviation from and variability within these ideal developmental stages.

Stage I is characterized by increasing melt pond coverage as meltwater fills topographic depressions and remains there with limited drainage. Pond surfaces are typically well above sea level (positive hydraulic head) and pond coverage is largely controlled by pre-melt ice topography. Surface meltwater preferentially accumulates in topographic depressions on the ice surface at melt onset and then progressively fills higher areas of relief as pond coverage increases. [Holt and Digby, 1985; Fetterer and Untersteiner, 1998]. On relatively smooth first-year sea ice, where the effects of deformation, aging and previous melt are either small or negligible, past studies have shown that snow drifts control the spatial distribution and shape of newly-forming melt ponds [Barber and Yackel, 1999; Eicken et al., 2004; Petrich et al., 2012; Polashenski et al., 2012]. Stage I culminates with the seasonal peak in pond coverage over both first- and multi-year sea ice [Perovich and Polashenski, 2012].

Stage II is characterized by a hydrostatic balance between meltwater production and its drainage. Lateral flow of meltwater across the ice surface towards macroscopic flaws (such as ice floe edges, cracks, seal breathing holes and enlarged brine drainage channels) and vertical percolation through the ice cover both contribute to surface water drainage, in a complexly evolving manner [Eicken et al., 2002; 2004]. Holt and Digby [1985] noted that melt channels, connecting ponds that were previously isolated during Stage I, could transport water several hundred meters to a drainage flaw as melt ponds evolved throughout Stage II. However, they also collected ice cores during Stage II which demonstrated that bulk salinity within the ice was too high for meltwater to have drained through it. During Stage II the lateral flow of meltwater across the ice surface promotes the formation of melt channels and ponds become interconnected, forming large networks [e.g. Hohenegger et al., 2012]. Stage II ends when the hydraulic head has decreased to zero and melt pond surface levels match the sea level. Although there are ponds, typically on MYI which remain above sea level for the duration of the melt season. The final geometrical structure of the melt pond cover is established at this time.

During Stage III the permeability of the sea ice to vertical meltwater drainage has increased such that melt pond surface levels remain tied to sea level and horizontal discharge to and drainage at macroscopic flaws become small [Polashenski et al., 2012]. Changes in pond coverage during Stage III depend on changes in surface topography and the freeboard of the continuously melting and thinning ice cover [e.g. Eicken et al., 2002].

Observations show that melt ponds deepen during this period due to preferential melting and can gradually expand, either through the erosion of pond walls or changes in topography, as the ice freeboard decreases [Eicken et al., 2004].

Stage IV characterizes either fall freeze-up, as ponds refreeze and accumulate snow, or ice break-up. Since refreezing and break-up can occur at any time, this stage is not necessarily restricted to the end of the melt season.

The goal of this study is to use *in situ* field data, collected over undeformed first-year sea ice in Resolute Passage in the Canadian Arctic, to examine seasonal, interannual and spatial variability in the development of melt ponds on landfast sea ice. We separately consider four physical processes that control melt pond coverage: (i) pre-melt surface topography, (ii) non-linear evolution of surface topography, (iii) ice permeability, thickness reduction and freeboard, and (iv) surface energy balance. We conclude by evaluating the timing of Stages I-IV and their utility as a descriptor of the seasonal evolution of melt pond coverage, within both our study area and the wider Canadian Arctic Archipelago (CAA).

5.2. Material and Methods

As part of the Arctic-ICE (Arctic – Ice-Covered Ecosystem) project, field data were collected in Resolute Passage, Nunavut, in 2011 and 2012, to study the formation and evolution of surface melt ponds. The Arctic-ICE project was a three-year study (2010-2012) in Resolute Passage to examine physical and biological coupling within the ice-covered marine ecosystem. Sampling sites were located 3 km off Cornwallis Island inside Allen Bay, close to 74.723 N 95.176 W, in 2011, and out in the passage between

Sheringham Point and Griffith Island, close to 74.726 N 95.576 W, in 2012 (Figure 5.1). Each location was selected in the field to represent undeformed, snow-covered first-year ice that was characteristic of both level ice in the surrounding area and typical first-year landfast ice in the CAA.

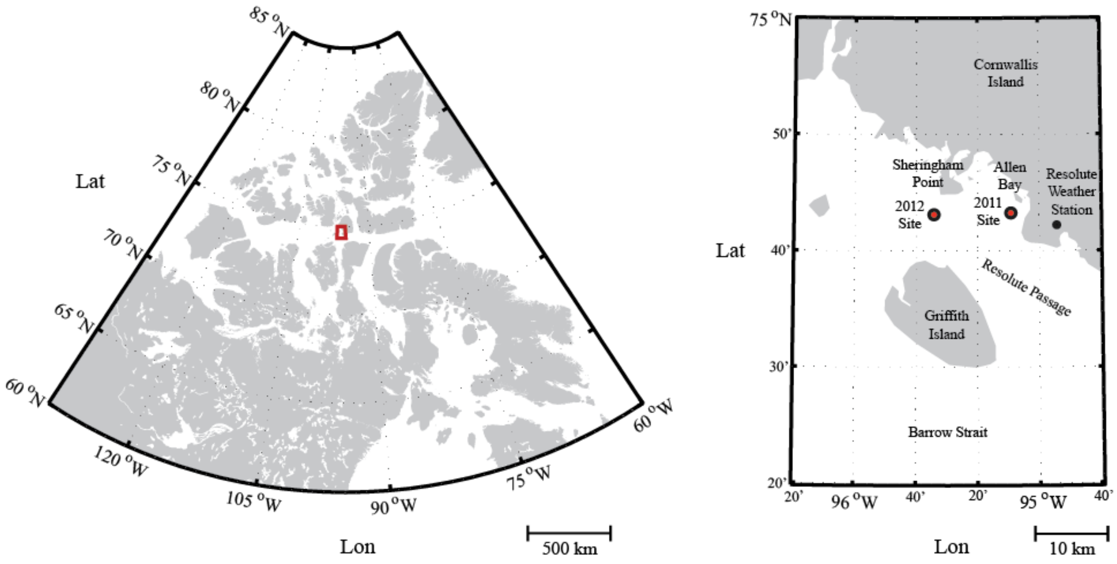

Figure 5.1 | Map of the Canadian Arctic Archipelago (CAA) and study area, including 2011 and 2012 primary field site locations and the Environment Canada Resolute Weather Station.

5.2.1. Field Observations

LiDAR (Light Detection and Ranging) data were acquired near-daily in 2011 and approximately every other day in 2012 at selected areas of the ice surface from mid-May to late-June with a Leica Scanstation C10 discrete-pulse terrestrial laser scanner. Selected areas were carefully marked out using surveying apparatus at the start of each sampling period and then left untouched throughout the duration of our experiments, as the laser scanner was able to collect a wealth of information from the sea ice surface remotely. The laser scanner emits pulses of energy and subsequently records the time-of-flight for each pulse to be reflected by surrounding objects and return to the scanner, thereby mapping objects, in our case surface topography, in three-dimensions. The Scanstation C10 operates at a frequency up to 50 kHz (50,000 pulses emitted and received per second) and can therefore capture hundreds of thousands of measurements from a target area in a matter of minutes.

Four scans were acquired, one from each site corner of the sampling areas, and subsequently registered to a single, global coordinate system, to provide as close to uniform coverage across the sites as possible and remove occlusions from single scan directions. Following Polashenski [pers. comm., 2011] and Polashenski et al. [2012], sampling platforms were frozen into the ice cover at site corners, prior to melt onset, so that the laser scanner mounted on these platforms remained at fixed positions relative to the ice interior throughout the sampling periods. The collection of a set of four scans took 3-4 hours and we ensured that each set was acquired between 08:00 and 12:00 (local time) for consistency between sampling days.

The exact arrangement of the sampling site was based on the characteristics of the ice surface and therefore varied slightly between years. Snow drifts were elongated and aligned to the prevailing wind direction in 2012, so we set up a rectangular 80 x 160 m site for laser scanning whose long-axis was parallel to the drifts and was bounded, at the northwest corner, by a transect constituting one 100 m drift-parallel arm and one 60 m drift-perpendicular arm, to account for the directional component of the ice surface (Figure 5.2).

In 2011, snow drifts were not directionally-dependent, so we set up a square 100 x 100 m site bounded by a single 100 m transect line along the western edge.

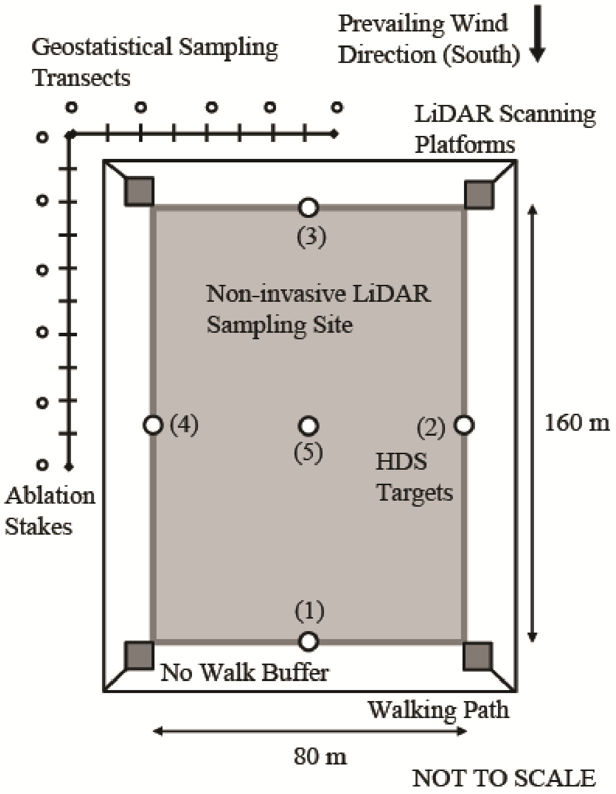

Figure 5.2 | Schematic diagram of the primary sampling site in 2012, which included an area for remote measurement of surface mass balance with the laser scanner and adjacent transect line for direct measurement of geophysical variables. The general arrangement of the 2011 sampling site was almost identical to the 2012 site.

The scanner was heated in a custom-built case to raise it to an operational temperature above 0 °C, mounted on a tripod and positioned on a platform, before a scan was taken. Individual scans were tied together using a set of reflective targets that were mounted and frozen into the ice prior to sampling, and acted as constant reference points that could be located by the instrument in every scan (Figure 5.2). Scans were merged by minimizing the root mean square of the residual distances between targets, which never exceeded 15 mm, indicating that the ice did not deform within either year's site throughout the duration of sampling. Merged scans were then registered to a global coordinate system covering the whole sampling period, i.e. first scan until last, that was based on the positions of the targets prior to sampling (at t=0). Total compound error in the elevation of target positions on each sampling day compared to the positions of targets in the global coordinate system was only 50 mm in 2011 and 40 mm in 2012. Lowest measurement densities within merged scans were approximately 250 points per m^2, close to the center of the sampling areas.

It was important to relate the LiDAR scans to sea level, so that we could analyze changes in ice freeboard and melt pond hydraulic head. Therefore, measurements of ice freeboard, ice thickness, snow depth, and the height of the scanner above sea level, were collected at white ice patches close to each scanning platform while the LiDAR system was running. The height of a merged LiDAR scan above sea level was thus calculated as an average of the four samples from each platform.

Several geophysical variables, complementary to the LiDAR data, were regularly sampled directly along a transect line set up adjacent to the laser scanning site, either during or shortly after laser scanning, to ensure that measurements from the whole site were directly relatable (Figure 5.2). Snow thickness or pond depth was sampled at 1 m intervals (where appropriate) and surface ablation was sampled at 10 m intervals at an array of stakes frozen into the ice (i.e. 11 stakes in 2011 and 17 in 2012). The ice surface was classified into one of five distinct categories every 1 m in 2011 and every 0.1 m in 2012, and photographed using a hand-held digital camera every 2.5 m, to support post-field analysis of surface classes. The five surface categories included: snow; white ice – a drained and deteriorated bare ice surface that is snow-like in appearance [Maykut and Grenfell, 1975]; blue ice – bare ice without a drained surface optical scattering layer, i.e. with low freeboard or otherwise water saturated inclusions at the surface [Maykut and Grenfell, 1975]; melt pond; and melt pond lined with superimposed ice.

Furthermore, auxiliary data sets, targeting changes in atmospheric variables and snow and ice properties, were collected at nearby field sites to provide the context for identifying the mechanisms driving melt pond evolution at the primary site. A surface meteorological tower was installed on the ice, approximately 1 km away from the primary field site, to monitor air temperature, relative humidity, and downwelling radiation fluxes, among other variables, at one-minute intervals for the duration of each year's field study. Precipitation could not be monitored at the micro-meteorological tower, but daily snow or rainfall data were available from the Resolute Bay Weather Station, operated by Environment Canada, which is terrestrially located (68 m a.s.l.) on Cornwallis Island (74.72 N, 94.97 W) (Figure 5.1).

Snowpack properties, including temperature, salinity, density and grain size, were measured in snow pits with depths selected to be close to the regional average (0.05-0.15 m) at distributed sites in the kilometre or so area surrounding the primary field site, following Eicken and Salganek [2010].

Sea ice cores were taken approximately every 4 days with a Kovacs Mark II 9-cm diameter coring system to track the evolution of ice temperature and salinity throughout each year's field study, following Eicken and Salganek [2010]. Before melt pond onset, ice cores were taken under regional-average snow thicknesses over undeformed level ice that was representative of the primary field site, whereas after melt pond onset, cores were taken under both white ice patches and, occasionally, also under melt ponds.

Ice temperature profiles were also recorded continuously using thermocouple arrays (thermocouples Type T, Omega Inc.), installed vertically through the ice cover prior to melt onset. In 2011 one array was installed under an initial snow depth of 0.08 m and in 2012 two arrays were installed, under 0.03 and 0.40 m snow depths. The 2011 array and 0.03-m depth 2012 array were covered by melt ponds on 11 and 15 June, respectively, but the 0.40-m depth 2012 array remained unponded (i.e. under white ice) for the duration of the sampling period.

5.2.2. LiDAR Data Postprocessing

LiDAR data were postprocessed using computer software including: Cyclone, Matlab, QT Modeler and ArcGIS, to calculate mass and meltwater balance at the sea ice surface. A few registered LiDAR scans contained outlying points located well above or below the ice surface, caused by laser reflections from precipitation or multi-path errors [Pfeifer and Mandlburger, 2008], that were removed using algorithms based on the adaptive triangular irregular network (A-TIN) and morphological filters of Axelsson [2000] and Vosselman [2000]. The Scanstation C10 laser pulses at 532 nm (green) consistently experienced diffuse reflection from (and did not penetrate) surfaces such as snow and ice [e.g. Prokop, 2008], but experienced specular reflection from water surfaces. Melt pond surfaces therefore stood out from the surrounding snow and ice surface as empty ‘holes’ in the LiDAR scans, save for a few artefacts existing just below melt pond surfaces caused by specular reflection and backscattering from ice at the far edges of ponds. These artefacts were systematically removed by cropping points from a scan below a threshold level defined by the ring of laser reflections marking the perimeter of a melt pond. In no instance were we able to detect the melt pond bottom using LiDAR. Processed LiDAR scans were then converted to a regular grid of 0.05 x 0.05 m cells using kriging interpolation. This method of interpolation was considered most suitable for modelling the densely populated LiDAR scans, as it was not predisposed to fit a smooth surface between points, yet still modelled melt pond surfaces as a series of flat planes.

By analysing changes in ice surface topography and melt pond hydraulic head between consecutive LiDAR grids, we could estimate mass balance and meltwater production and drainage, following Polashenski et al. [2012]. Each grid cell contained a column of either snow-covered ice or pond-covered ice, between the surface and a horizontal reference level fixed at an arbitrary depth within the centre of the ice cover (Figure 5.3).

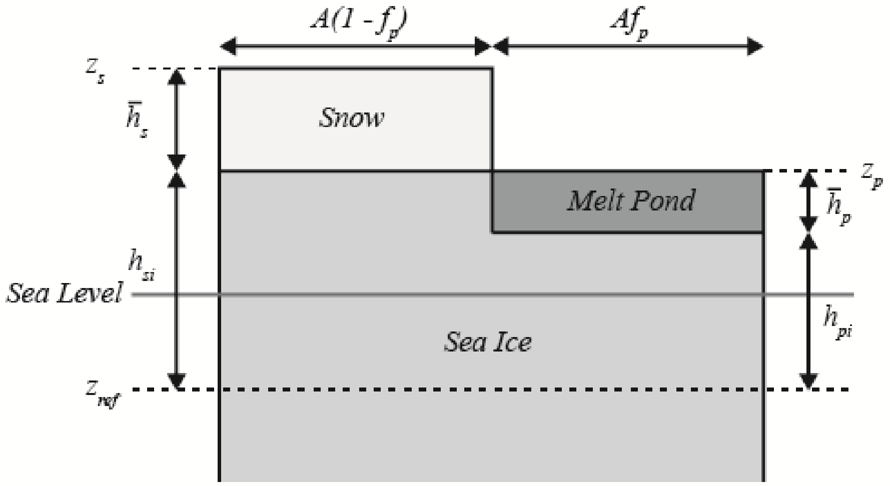

Figure 5.3 | Schematic diagram of the variables measured directly with the laser scanner (A, f_p, z_s, z_p and z_{ref}), estimated from measurements collected at the sampling transects ($\overline{h}_s$ and $\overline{h}_p$), or estimated using the LiDAR surface grids (h_{si} and h_{pi}).

Since the laser scanner could not differentiate between snow and ice at the surface, bare ice was included as snow-covered ice with a snow depth of zero. A column of snow-covered ice could be defined as:

$$z_s - z_{ref} = h_s + h_{si}, \tag{5.1}$$

where z_s was the snow surface level, z_{ref} was the reference level, h_s was the snow thickness, and h_{si} was the (snow-covered) ice thickness (Figure 5.3). Likewise, a column of melt pond-covered ice could be defined as:

$$z_p - z_{ref} = h_p + h_{pi}, \tag{5.2}$$

where z_p was the pond surface level, z_{ref} was again the reference level, h_p was the pond depth, and h_{pi} was the (pond-covered) ice thickness (Figure 5.3). The laser scanner measured only surface topography and could not measure snow thickness or melt pond depth. We estimated h_s and h_p for each grid cell from mean snow thickness ($\bar{h}_s$) and mean melt pond depth ($\bar{h}_p$) recorded at the transect line on the same date as the LiDAR scan. After the snow cover had melted completely, $\bar{h}_s$ was kept at a constant thickness of 5 mm, which characterized the granular, snow-like surface optical scattering layer of white ice. This layer had different properties to the bulk sea ice and was therefore treated separately.

The total mass of water in snow and ice forms ($m_{snow+ice}$) above the reference level for a surface grid was calculated as:

$$m_{snow+ice} = f_p A\left[h_{pi}\rho_i\right] + f_p(1 - A)\left[\bar{h}_s\bar{\rho}_s + h_{si}\rho_i\right], \tag{5.3}$$

where A was the area of the site, f_p was the melt pond fraction, ρ_i was the density of ice (estimated as 900 kg m^{-3}), and $\bar{\rho}_s$ was the mean snow density on or on the closest date to the scanning date (varying between approximately 100 and 600 kg m^{-3}). After the snow had completely melted, $\bar{\rho}_s$ was maintained at a constant density of 600 kg m^{-3} for the white ice surface optical scattering layer [Perovich et al., 2009]. The rate of surface meltwater production per unit area (ΔV_{prod}), expressed as a depth of water equivalent (w.e.) produced at the ice surface per day, i.e. m d^{-1}, could then be determined from equation 5.3 as:

$$\Delta V_{prod} = \frac{\Delta m_{snow+ice}}{\rho_w \Delta t}, \tag{5.4}$$

where ρ_w was the density of water (taken as 1000 kg m^{-3}). The total mass of water in all forms (snow, ice and liquid) (m_{total}) above the reference level for a surface grid was calculated as:

$$m_{total} = f_p A\left[\bar{h}_p \rho_w + h_{pi}\rho_i\right] + f_p(1-A)\left[\bar{h}_s \bar{\rho}_s + h_{si}\rho_i\right]. \tag{5.5}$$

The rate of surface meltwater drainage per unit area (ΔV_{drain}), again expressed as a depth of water equivalent produced at the ice surface per day, i.e. m d^{-1}, could then be determined from equation 5.4 as:

$$\Delta V_{drain} = \frac{\Delta m_{total}}{\rho_w \Delta t} + \frac{\Delta V_{precip}}{\Delta t}, \tag{5.6}$$

where ΔV_{precip} was the volume of water per unit area added to the site by precipitation between scans. The mass added through precipitation never exceeded 8% of Δm_{total}, and only once exceeded 2%.

We could also calculate the total volume of meltwater lost from the ice per unit area (V_{lost}), at any given time (t), during the melt season as:

$$V_{lost} = \int_{t_0}^{t} \Delta V_{drain}\, dt. \tag{5.7}$$

And, finally, we could calculate the volume per unit area of meltwater retained at the ice surface in melt ponds as:

$$V_{retained} = \bar{h}_w f_p A. \tag{5.8}$$

5.3. Results and Discussion

5.3.1. Seasonal Development of the Sea Ice Cover

5.3.1.1. Pre-Melt Snow and Ice Conditions

At the winter baseline in both 2011 and 2012, level fast ice fully covered the region surrounding Resolute Passage. Pre-melt ice thicknesses at the laser scanning sites were measured as 1.6 ± 0.1 m on 8 June 2011 and 1.25 ± 0.05 m on 4 June in 2012. Average ice cover freeboards (the distance from the snow-ice interface to the seawater level) on these dates were measured as 0.18 m and 0.07 m, respectively. The pre-melt snowpack was also thicker in 2011 than in 2012, with average thickness recorded as 0.14 ± 0.07 m and 0.11 ± 0.05 m, respectively, along each year's transect line. These differences in average ice and snow thicknesses are corroborated by the significant difference between 2011 and 2012 pre-melt snow surface height distributions (Figure 5.4). Both distributions are log-normal in form, positively skewed, and characteristic of the thickness distribution of a drifted snowpack on level sea ice [Iacozza and Barber, 1999; Sturm et al., 2002]. However, surface heights varied by 0.8 m in 2011, compared to 0.3 m in 2012. Consequently, with both a higher freeboard and a thicker snowpack, the pre-melt surface in 2011 was elevated to a greater average height above sea level than the 2012 surface (Figure 5.4).

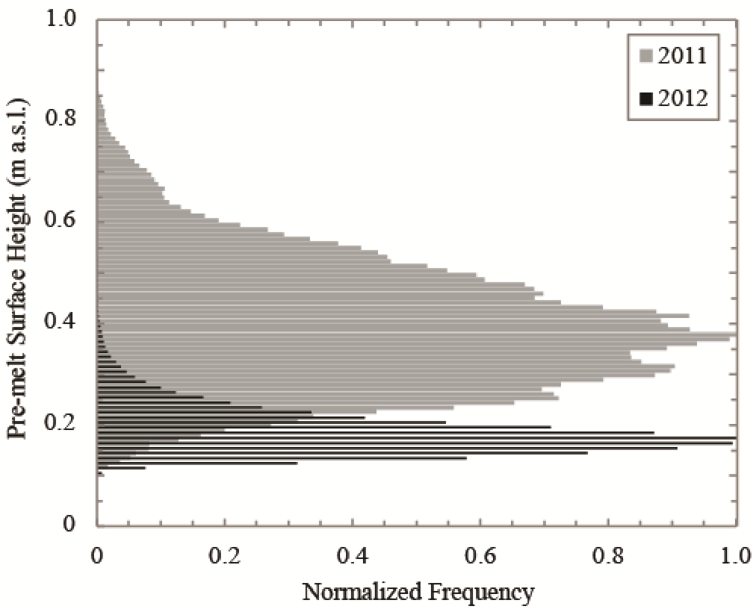

Figure 5.4 | Normalized pre-melt surface height distributions from the laser scanning sites. Surface height classes represent the snow surface height in metres above sea level within a sampling site. The 2011 pre-melt snow surface was measured on 8 June and the 2012 pre-melt surface was measured on 4 June.

Ice core temperature profiles measured prior to melt pond onset in both years show that ice temperatures increased throughout May. In mid-May the ice had a positive temperature gradient, which is typical of sea ice in winter (Figures 5.5a and c), whereas in late-May the ice had evolved to a more uniform temperature profile throughout the ice cover. Temperatures within the upper 0.2 m of the ice cover had also begun to swing towards zero by the end of May in both years, and particularly in 2012, in response to increasing air temperatures and incoming solar radiation. Pre-melt salinity profiles for both years, combined from multiple ice cores, were C-shaped with depth, as is typical of winter sea ice [Schwerdtfeger, 1963], and generally above 4.5 psu (Figures 5.5b and d).

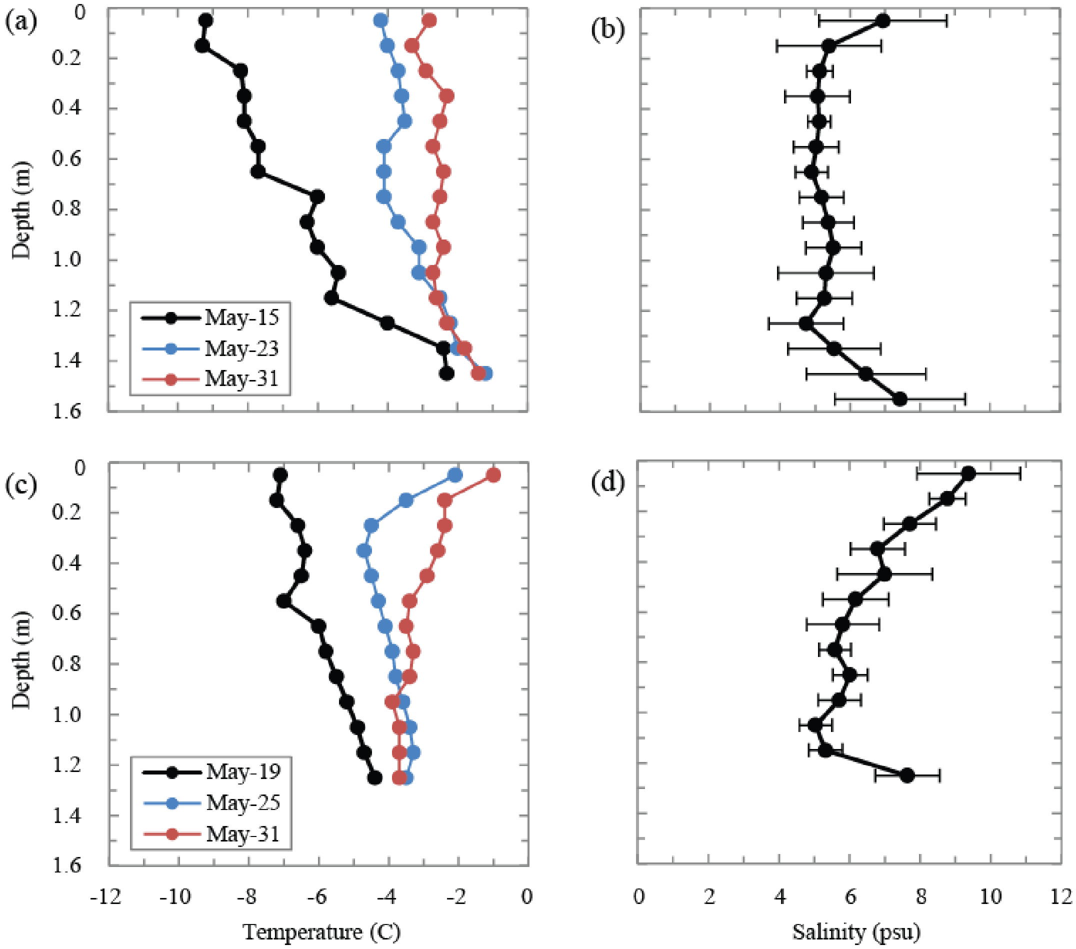

Figure 5.5 | Sea ice properties prior to melt pond formation, including temperature and salinity. Select temperature profiles from ice cores are presented for 2011 in (a) and 2012 in (c). Salinity profiles are presented for 2011 in (b) and 2012 in (d) as the average of measurements from ice cores (10 cores collected between 27 April and 4 June in 2011 and 8 cores collected between 19 May and 2 June in 2012), with the standard deviation of measurements between cores given by the error bars.

Measurements at two snow pits, collected prior to melt pond formation, showed that snow temperature and salinity profiles varied slightly between the two years, but were characteristic of first-year sea ice in this region (Figure 5.6a and b). However, snow density varied considerably between the years (Figure 5.6c) and measurements from these two pits were comparable to others made at snow pits located around the field sites in the first week or so of June each year. Snow density increased down through the surface layer of the 2011 pack, due to the consolidation of freshly fallen snow, and then steadily decreased from a depth of 50 mm to the snow-ice interface, due to snow grain metamorphosis that occurred over winter [Colbeck, 1991]. This suggests that the majority of the 2011 snowpack had been deposited a considerable time before we sampled on 7 June. But snow density was uniform and low throughout the 2012 pack when we sampled on 4 June, and had a high and constant temperature profile (Figure 5.6a), which suggests that the snow had been deposited recently. Almost 0.3 m of snowfall was recorded at the Resolute Weather Station during two significant deposition events around the start of May in 2012 and these probably contributed to the observed temperature and density profiles.

The varying history of the snowpack may also explain the observed interannual differences in the salinity profiles. The basal salinity in 2011 was almost twice the basal salinity in 2012, and measurements from these two pits were again comparable to others made at snow pits located around the field sites each year. If the bulk of the 2011 snowpack had been deposited earlier than the bulk of the 2012 snowpack, there would have been longer for brine at the ice surface to be wicked up into the snow. Alternatively, there may have been highly saline frost flowers present as the ice cover formed in 2011, which were then incorporated into the snowpack [Perovich and Richter-Menge, 1994].

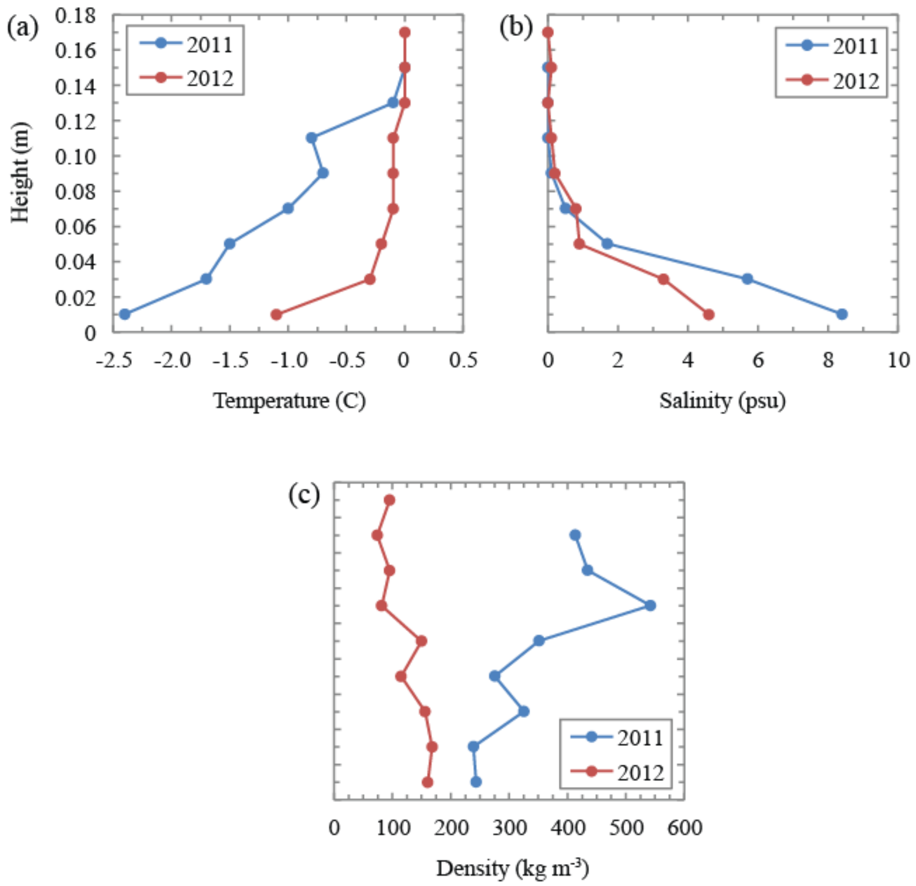

Figure 5.6 | Snow properties prior to pond formation, including (a) temperature, (b) salinity and (c) density. Profiles were measured at 0.02 m intervals from the snow-ice interface (at height = 0) to the air-snow interface, at a 0.16 m deep pit on 7 June in 2011 and at an 0.18 m deep pit on 4 June in 2012.

5.3.1.2. Evolution of Melt Pond Coverage

The first melt ponds formed on 10 June in both 2011 and 2012 as thin areas of the snowpack rapidly ablated, leaving flooded meltwater on the ice surface. This match in the date of pond formation disguises the fact that snow melt onset occurred several days earlier on 2 June in 2012 rather than on 8 June in 2011 (Figure 5.7a). In this study, snow melt onset is defined as the first date that the snow surface temperature rose to the melting point. Moreover, at the location of the 2011 field site in Allen Bay, ponds were observed to have formed by 8 June in 2012. Pond coverage rapidly increased to a seasonal peak of 60% by 12 June in 2011 and remained > 50% until 16 June, after which coverage dropped and fluctuated between 24% and 46% from 17 June until we left the field on 26 June. In 2012, pond coverage rose less rapidly than in 2011, but on 15 June it had reached a seasonal peak of 78% and remained above 50% until we left the field on 25 June.

In both years, the observed evolution of melt pond coverage appeared, in general, to conform to the stages outlined by Eicken et al. [2002]. Pond coverage rose from zero up to a seasonal peak within six days (Stage I) and then decreased over the next two weeks (Stage II), as meltwater drainage from the ice surface increased. A gradual increase in pond coverage was also observed after 21 June in 2011 (Stage III), after melt pond surfaces had dropped to sea level (i.e. hydraulic head became zero) (Figure 5.7c), but not in 2012. The date of melt pond onset was within a week of past observations from the same region of the CAA [Derksen et al., 1997; Scharien and Yackel, 2005]. The length of Stage I (less than one week) was also similar to past observations of first-year ice [Derksen et al., 1997; Eicken et al., 2004; Polashenski et al., 2012] and multi-year ice [Perovich et al., 2002b; Sankelo et al., 2010] from across the Arctic. Rösel and Kaleschke [2012] used MODIS data to estimate that the 2011 peak in melt pond coverage was ~50% in the CAA and occurred around 18 June, which agrees closely with our observations.

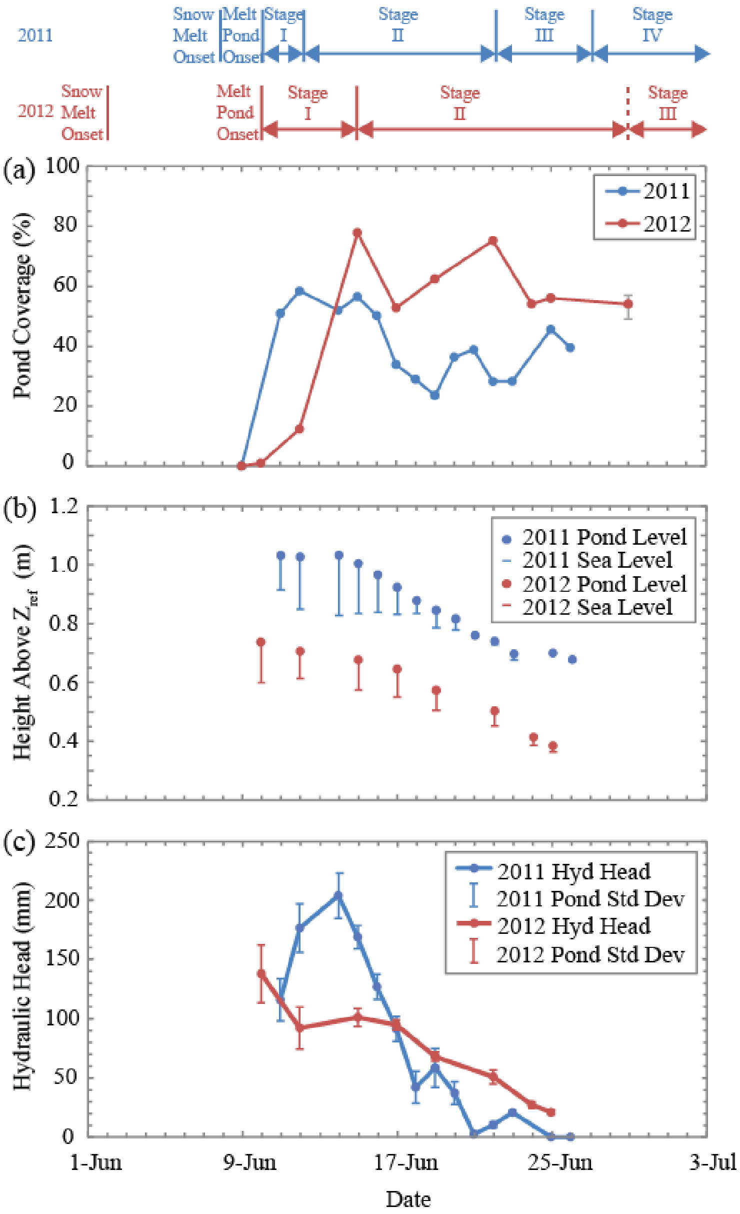

Figure 5.7 | Evolution of: (a) melt pond coverage; (b) the average melt pond surface level and sea level with respect to z_{ref}; and (c) the average hydraulic head of pond water above sea level (i.e. the difference between pond level and sea level in (b)) and the standard deviation of pond surface levels. The final measurement of pond coverage in the 2012 series in (a) is obtained from an aerial photograph taken over the site on June 29, with the error bars illustrating change in coverage associated with a ± 5% variation in the intensity threshold selected to classify ice and melt pond surfaces.

However, the evolution of pond coverage through Stages II and III varied considerably between the two years of our study, and compared to past observations of melt pond evolution on sea ice. For instance, Polashenksi et al. [2012] (2008 and 2009 data) and Eicken et al. [2004] (2001 data) have shown that pond coverage on undeformed, first-year ice at Barrow, Alaska has generally fallen considerably (from 50-70% to <20%) as ponds have drained during Stage II and has remained low throughout Stage III. In contrast, pond coverage varied by more than 20 pp (percentage point, i.e. absolute percentage change) during Stages II and III in both years of our study and, in 2012, hadn't fallen below 50% by the end of June. Remote sensing measurements covering much larger areas than these *in situ* studies have demonstrated that variability in melt pond coverage following Stage I is symptomatic not only of first-year ice in the CAA, but of mixed sea ice types across the Arctic [Tschudi et al., 2008].

5.3.1.3. Topography Evolution

A selection of hypsographic curves illustrate the evolution of unponded surface topography and melt pond depth throughout the melt season each year (Figure 5.8). The volume of snow and ice above sea level decreased throughout June each year, as the mass of the sea ice cover declined through melting and the drainage of retained meltwater to the ocean. By 25 June in 2011, melt pond surface levels had fallen to sea level and the majority of the pond water was located below sea level, whereas by 25 June in 2012, pond surfaces remained a few centimetres above sea level and a large fraction of the pond water was therefore also located above sea level. Meltwater located above sea level will contribute to the weight of the ice cover and thus affected the overall freeboard.

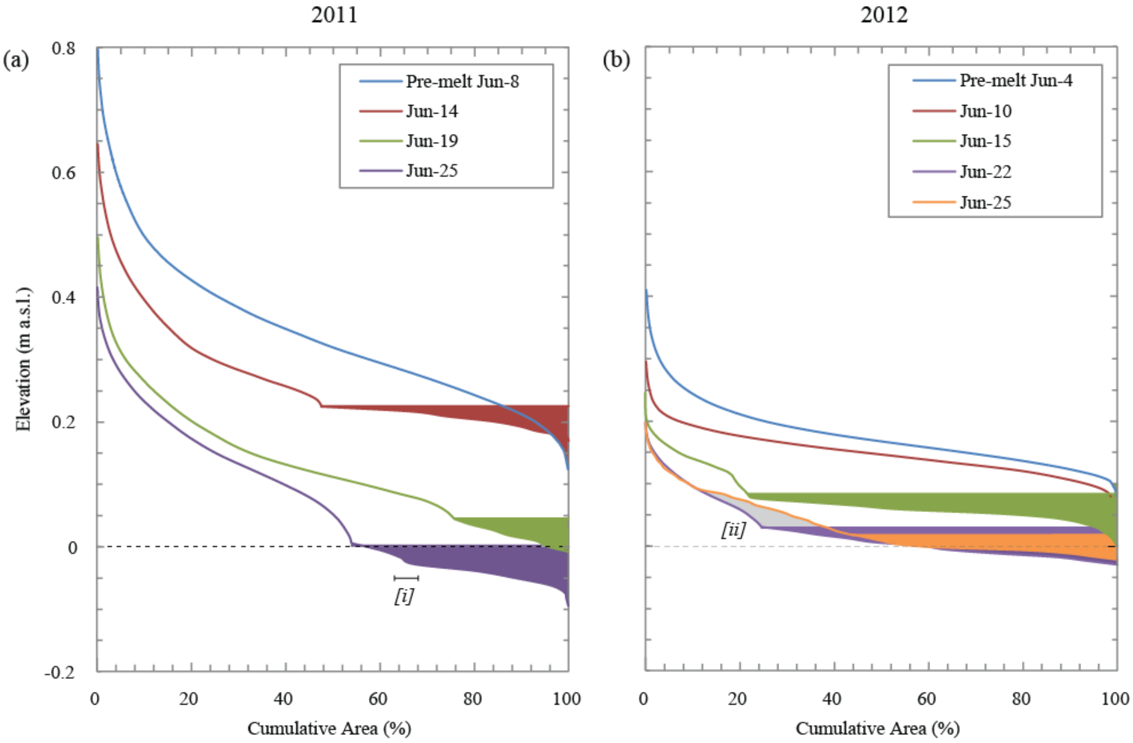

Figure 5.8 | Hypsographic curves of surface topography (coloured lines) and melt pond depth (coloured blocks), above and below the mean elevation of surface melt ponds, respectively, for select dates in (a) 2011 and (b) 2012. Curves for surface topography were produced from the LiDAR data and distributions of pond depth were produced from *in situ* measurements collected at the sampling transects. Sea level is given by the dashed line at zero elevation. Steepening of pond walls late in the 2011 melt season is highlighted by *[i]*. Re-exposure of ice on 25 June that was previously covered by meltwater on 22 June in 2012 is highlighted by the shaded zone at *[ii]*.

The significant difference in topographic relief between the two years is further evidenced in Figure 5.8. The hypsographic curves show that snow or ice surface topography was steeper and the dispersion of melt pond water was confined to a smaller area of the sea ice surface in 2011 than in 2012. A notable consequence of this apparent lack of restriction on pond growth, and the rapid and considerable changes in melt pond coverage observed in 2012, can be seen in Figure 5.8b. A subsection of ponded ice in the

22 June curve was re-exposed by 25 June, as melt pond coverage dropped from 75 to 56%. The hypsographic curves also demonstrate that melt pond bottom topography was steeper and ponds were generally deeper in 2011 than in 2012. Furthermore, the steepening of pond walls late in the 2011 melt season is noticeable in the 25 June curve in 2011 (Figure 5.8a), but is not apparent in any of the 2012 curves (Figure 5.8b).

5.3.1.4. Meltwater Balance and Melt Pond Hydraulic Head

Past observations have shown that the effective hydraulic gradient between meltwater production and drainage at the ice surface drives the expansion and contraction of ponds over local topography throughout the melt season [Eicken et al., 2002]. Since the LiDAR data could be used to calculate meltwater production, storage and drainage at the ice surface, following equations 5.1 to 5.8, we can evaluate how this occurred at our field sites.

In the few days following melt pond formation (Stage I), in both 2011 and 2012, drainage pathways to the ocean were restricted and meltwater filled topographic depressions on the ice surface mainly as a function of production (Figures 5.9d and h). In 2011, Stage I proceeded rapidly so that between 10 and 12 June pond coverage increased from zero to the seasonal maximum. During this period, meltwater was produced on the ice surface at a rate of up to 20 mm water equivalent (w.e.) per day, coinciding with the onset of positive air temperatures, and negligible meltwater drained (Figures 5.9a and d). Between 12 and 14 June, temperatures decreased below freezing and the downwelling shortwave irradiance dropped to just over 100 W m^{-2} (Figures 5.9a and b), resulting in a near-total loss of meltwater production. Nevertheless, pond coverage stayed close to the seasonal maximum because the drainage of meltwater from the surface remained negligible (Figure 5.9d).

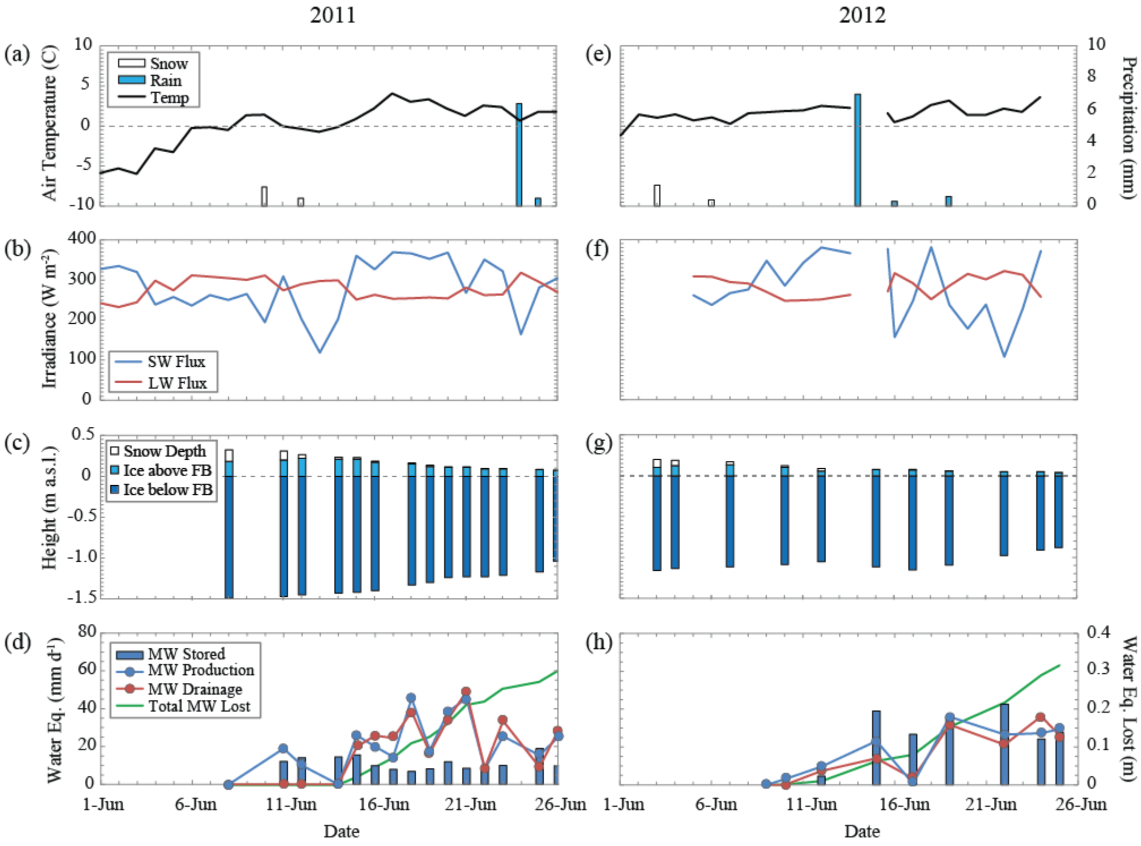

Figure 5.9 | Composite of meteorological and geophysical variables recorded during the 2011 (a-d) and 2012 (e-h) field studies: (a) and (e) air temperature and precipitation; (b) and (f) incident short- and long-wave irradiance; (c) and (g) sea ice thickness, including mean snow depth measured at the transect line and mean ice thickness, both above and below freeboard, measured at laser scanning platforms; and (d) and (h) rates of meltwater production and drainage at the laser scanning site (in mmd^{-1}), meltwater stored in ponds (in mm), and cumulative meltwater lost from the ice surface (in m). The short gap in meteorological measurements between 13 and 15 June 2011 was caused by a severe storm that prevented us from accessing the ice and shut down the met tower.

In 2012, air temperatures were above zero from 2 June and the downwelling shortwave irradiance rose steadily after 5 June (Figures 5.9e and f). However, meltwater was not produced sufficiently to initiate pond formation until 10 June (Figure 5.9h). Although meltwater production increased to almost 10 mm d^{-1} by 12 June, melt pond coverage remained below 15% because drainage was not entirely restricted, as it had been in the thicker and rougher ice cover in 2011. Furthermore, melt ponds were evidently connected to an outflow pathway (or pathways) by 12 June in 2012, with meltwater drainage exceeding 7 mm d^{-1} (Figure 5.9h).

In the first 4-5 days following pond formation each year, the mean level of melt pond surfaces remained at a fairly constant height above the fixed reference level within the centre of the ice cover and well above sea level (Figures 5.7b and 5.8). However, the standard deviation of pond surface levels was relatively high (typically >20 mm), compared to later in the season (Figure 5.7c), indicating that melt ponds were present at varying elevations on the surface. In 2011, the standard deviation of pond levels remained >9 mm until 20 June, after which it declined to <0.5 mm as ponds dropped to sea level. The particularly high standard deviations in melt pond levels for 10 and 12 June 2012 were associated with the small pond coverage on these two dates (1.0 and 12.3%, respectively). However, by 15 June 2012 the standard deviation of pond surface levels had dropped to 7.5 mm, and by the end of our sampling period, on 25 June, it had dropped to <2 mm (Figure 5.7c). These interannual differences in the variation of melt pond levels suggest that ponds were less interconnected in 2011 than in 2012. This was likely caused by the rougher ice surface in 2011 (Figure 5.3), which we expect would have provided greater restriction to the horizontal meltwater percolation, compared to the smooth ice surface in 2012.

In 2012, surface meltwater was first observed to be draining at a hole through the ice in the area surrounding the field site on 11 June (1 day after pond onset), whereas the same phenomenon was not observed until 15 June in 2011 (6 days after pond onset). Ringed seals were visibly present at a number of breathing holes within a kilometre of the 2012 field site as early as May and one such hole was observed about 50 m south of the laser scanning site. Surface meltwater could therefore drain as soon as a hydraulic gradient developed between melt ponds in the field site and the seal hole, which occurred shortly before or on 11 June. Several studies have reported extensive meltwater drainage at seal breathing holes [Holt and Digby, 1985; Fetterer and Untersteiner, 1998], including one in the Resolute Passage region [Barber and Yackel, 1999]. Aerial photographs collected over the region surrounding the field site on 24 June in 2012 demonstrated that, by the end of the sampling period, up to 25 drainage holes had opened through the ice per square kilometre. These may have all originated from seal holes, many having been covered with snow and obscured earlier in June, although additional drainage holes may have formed through the widening of brine channels, as observed by Polashenski et al. [2012].

Pond coverage declined rapidly between 16 and 18 June in 2011 as a drainage network developed and further melt holes formed close to the field site. Throughout the same period the pressure potential accumulated as melt pond surface levels rose above sea level during Stage I, i.e. hydraulic head, decreased rapidly from 200 mm on 14 June to around zero by 21 June as meltwater drained from the ice surface (Figure 5.7c). In contrast, melt pond hydraulic head decreased from 140 mm on 10 June in 2012 to around 20 mm by 24 June, but had not yet dropped to sea level when we left the ice on 25 June.

In spite of these variations in the evolution of hydraulic head, a similar total depth of water equivalent was lost from the ice surface in both years (approximately 0.30 m) (Figures 5.9d and h). By comparing the thickness of the pre-melt ice and snow cover with the total depth of water lost, we can estimate that approximately 20% of the pre-melt sea ice mass was lost from the surface through melt and drainage in 2011, whereas 27% was lost in 2012.

5.3.1.5. Ice Break-Up

After leaving the ice we were unable to directly observe the final stages of ice melt (end of Stage III) and break-up (Stage IV); nonetheless, through analysis of sequential cloud-free MODIS and Landsat 7 satellite images, we established the fate of the ice in the region of the field site each year.

In 2011, Barrow Strait opened up as early as 15 May and only a bridge of landfast ice between the south side of Griffith Island and Cornwallis Island prevented ice break up in Resolute Passage. The bridge was removed on 26-27 June and strong offshore winds rapidly and dynamically broke up ice in the passage, including Allen Bay, on 27 June (Figure 5.7a).

In 2012, open water was present in Wellington Channel, on the far northeast side of Cornwallis Island, in May, but not in Barrow Strait. Two polynas, one off the north side of Griffith Island and one off Sheringham Point (Figure 5.1), began to form on 26 June and had intersected by 2 July, covering the field site. The ice cover broke away from the coast inside Allen Bay on 30 June. However, in the absence of strong winds and open water clearing the passage, as in 2011, the sea ice cover melted in place until it broke up on 5 July, i.e., nine days after it broke up in 2011.

5.3.2. Physical Mechanisms Controlling Melt Pond Coverage

To understand why melt pond evolution progressed differently at the 2011 and 2012 field sites, we separately examine the roles of: (i) pre-melt surface topography; (ii) topography evolution; (iii) ice permeability and freeboard; and (iv) the surface energy balance; in controlling melt pond coverage.

5.3.2.1. Pre-Melt Snow and Ice Surface Topography

The initial formation of melt ponds was not strictly confined to the lowest pre-melt elevations (Figure 5.10). In fact, throughout the entire melt season, ponds were present on nearly the full range of pre-melt elevations, excluding only the highest elevations each year. At the onset of ponding, pond coverage fractions were generally highest at the lowest pre-melt surface elevations, and vice-versa. If pond coverage at a certain height simply were a function of meltwater filling areas of the surface lower than or equal to that height, the distributions would resemble step functions with 100% pond coverage below a certain pre-melt elevation and zero coverage above it. In 2011, between 11 and 14 June, pond coverage was indeed 100% for the lowest pre-melt surface heights. However, instead of a sudden reduction to zero, pond coverage decreased gradually with increasing pre-melt height (Figure 5.10a). In 2012, on 10 and 12 June, pond coverage was highest for the lowest pre-melt elevations, but reached only 20% and 70%, respectively, before obtaining 100%

coverage on 15 June (Figure 5.10b). We note that the secondary peak in the 12 June 2012 distribution (Figure 5.10b) is related to the most common pre-melt surface height of about 0.17 m a.s.l. (Figure 5.4), suggesting that when meltwater exceeded this level, it resulted in a peak. Likewise a number of smaller local peaks in the 2011 pre-melt surface correspond to secondary peaks in the 2011 distributions (Figure 5.10a).

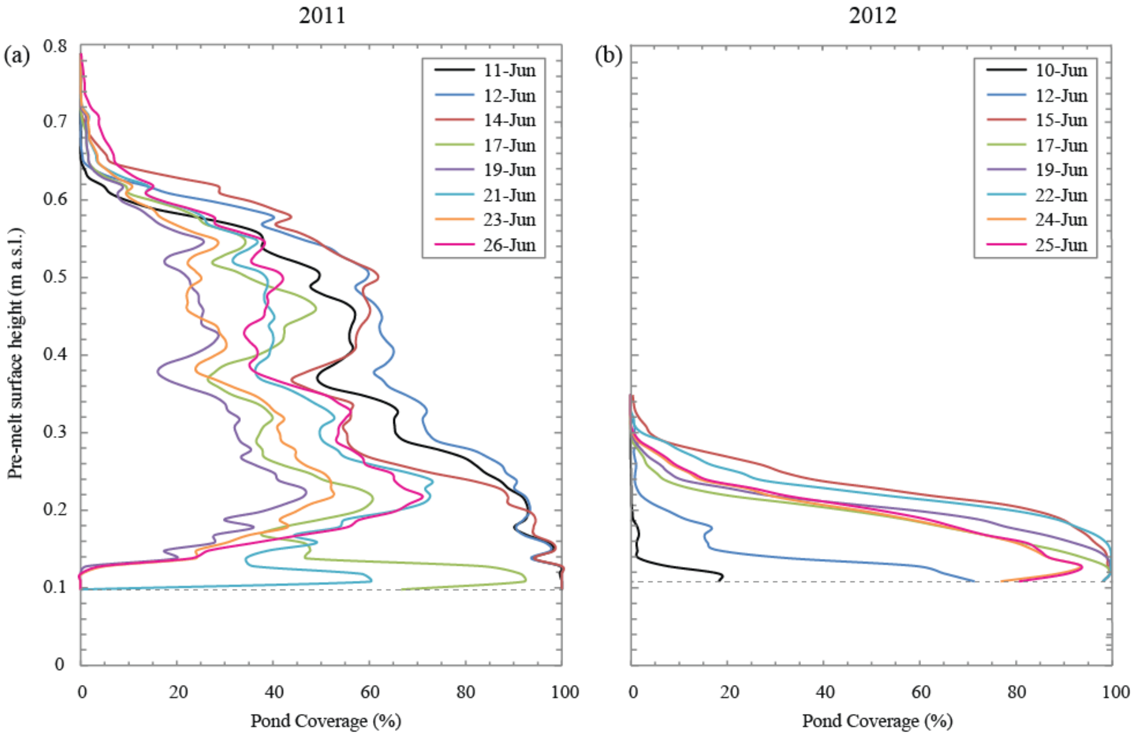

Figure 5.10 | Distributions showing the fraction of pre-melt surfaces of a given height above sea level that are ponded at a subsequent date in (a) 2011 and (b) 2012. The dashed lines mark the lowest elevations of the pre-melt surfaces. Pre-melt surface height distributions are given in Figure 5.4.

Excluding the first two distributions of 2012 (for 10 and 12 June), melt pond coverage appears to decrease at an almost linear rate with increasing pre-melt surface height, up to a threshold height, after which coverage decreases exponentially. Within the central portions of the 2011 distributions, between around 0.20 and 0.55 m pre-melt surface height, an increase in height of 0.1 m results in a drop in pond coverage fraction of approximately 10 pp (percentage point), and this rate of change is reduced by only 2 pp between 15 and 25 June. In contrast, for the smoother 2012 distributions, within the central portions between 0.15 and 0.25 pre-melt surface height, an increase in height of 0.1 m results in a drop in pond coverage of approximately 80 pp, and this rate of change is reduced by only 4 pp between 12 and 26 June. The difference in the relationship between pre-melt surface height and coverage fraction reflects the difference in topographic relief between the two years. Melt ponds were confined within a narrow 0.2 m band of pre-melt surface topography on the smoother sea ice in 2012, compared to a wider 0.6 m band of topography on the (relatively) rougher ice in 2011.

It is interesting that the rate of change in pond coverage with increasing pre-melt surface height did not drop significantly throughout the course of the melt season. Initial pond formation appeared to have occurred in local depressions regardless of the larger scale topography, at a time when the horizontal percolation of meltwater across the ice surface was restricted. This supports the findings of Petrich et al. [2012], who showed that snow drift locations pre-condition the initial (Stage I) distribution of melt ponds on first-year ice. When horizontal percolation was initiated and melt ponds became interconnected, which was observed during Stage II, we might have expected meltwater to recede from ponds located at higher pre-melt elevations and the rate of decline in coverage with elevation to increase dramatically over time. Instead, the fact that pond coverage remained high across a wide range of pre-melt elevations throughout the melt season (Figure 5.10) indicates that, once formed, ponds must have increased sufficiently in depth with respect to surrounding unponded surfaces to remain fixed for the remainder of the season. Furthermore the bases of melt ponds located at higher pre-melt elevations must have eventually dropped below the surfaces of ponds located at lower pre-melt elevations so that the standard deviation in melt pond hydraulic head could become zero (Figure 5.7c).

5.3.2.2. Non-Linear Evolution of the Surface Topography

The 2011 distributions of pre-melt surface heights that were subsequently ponded reveal a marked ‘drop-off’ after 17 June in pond coverage fractions located at the lowest pre-melt surface height classes below 0.24 m a.s.l. (Figure 5.10a). The magnitude of the drop-off fluctuates, but these fluctuations appear to match the overall variability in coverage recorded on the same dates. For instance, between 17 and 19 June pond coverage decreased by approximately 90 pp at ~0.12 m a.s.l. when the overall coverage at the laser scanning site decreased by 18 pp, whereas between 19 and 21 June pond coverage increased by approximately 60 pp at ~0.12 m a.s.l. when the overall coverage increased by 15 pp. This same phenomenon occurred in 2012, but to a lesser degree, with a minor drop-off in pond coverage at the lowest pre-melt height classes commencing 24 June (Figure 5.10b). That meltwater appeared to have preferentially drained from the lowest pre-melt surface heights seems counterintuitive, but we will discuss a number of potential mechanisms that may have caused it.

First, the pre-melt surface topography, which described the snow distribution overlying the ice surface, may not have represented the ice surface distribution. Thicker snow drifts may not have always overlain hummocks in ice topography, so that the relationship between snow drift locations and the spatial distribution of melt ponds [Petrich et al., 2012] became less pronounced after the snowpack ablated following Stage I. Indeed, several snow drifts can be identified in the 8 June (pre-melt) profile (Figure 5.11c) across a subsection of the 2011 laser scanning site (Figure 5.11a), for example at distances of 5-10 m, 18-32 m, and 56-73 m. However, although the first two coincided with hummocks in ice topography at later dates, i.e. after snow had melted entirely, the final one appeared to have overlain an almost uniformly level area of ice. We cannot discriminate between snow and ice surface melt using the laser scanner, but the differential surface ablation observed between these areas was more likely caused by a thicker snow drift at 56-73 m ablating faster than thinner snow at 5-10 and 18-32 m, rather than differential rates of ice melt. Non-uniform surface ablation in this manner was characteristic of the early period (i.e. first 10 days or so) of melt in both years, suggesting that the snow surface topography was not entirely representative of the ice surface topography. This also helps to explain why such broad distributions of pond coverage at varying pre-melt surface heights could be maintained throughout the melt season (Figure 5.10).

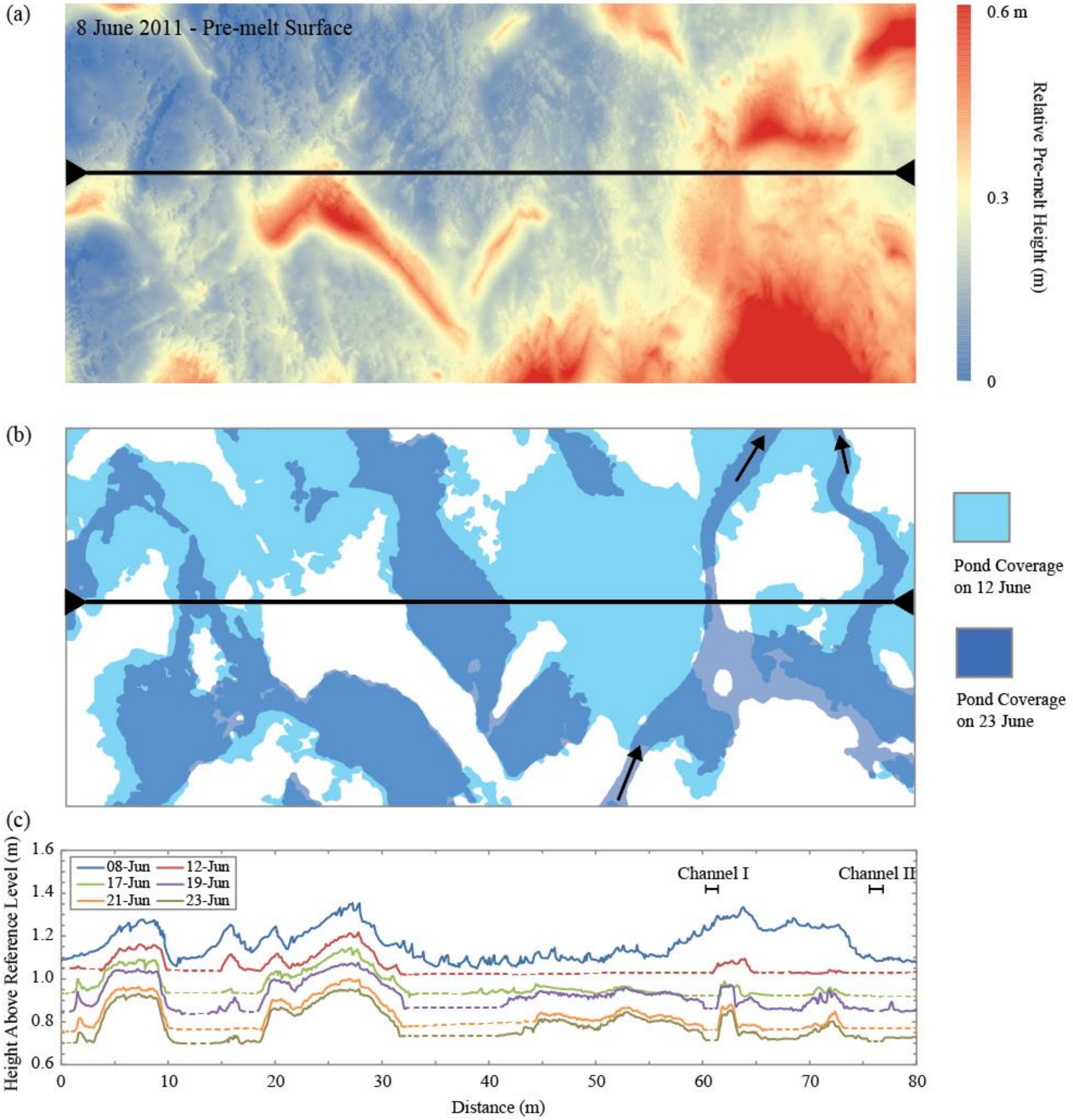

Figure 5.11 | Maps of an 80-m wide subsection located at the northeast corner of the 2011 laser scanning site, showing (a) pre-melt surface topography on 8 June, and (b) melt pond coverage on 12 and 23 June. A series of 80-m length profiles across the surface between 8 and 23 June are shown in (c) and give the height of the surface above the fixed reference level within the centre of the ice cover. The location of the profiles is illustrated by the black transect lines in (a) and (b), and the directions of meltwater flow within channels on the ice surface on 23 June are illustrated by the black arrows in (b). Snow or ice surface elevation is given by the full lines in (c) whereas water surface, i.e. melt pond or meltwater channel, elevation is given by the dashed lines.

However, it is unlikely that differences between the snow and ice surface topography led to the significant drop in coverage observed at low pre-melt height classes in the 17-26 June 2011 distributions in Figure 5.10a and the 24 and 25 June distributions in Figure 5.10b. This must have been caused by a modification of ice topography in low-lying areas. We speculate that meltwater flowing at greater velocity will preferentially melt and/or erode underlying ice, thus forming deep channels and generally altering the pond bottom topography. Indeed, an increasing proportion of the available meltwater became retained within drainage channels throughout Stage II in both years. Melt pond coverage at any location is then not only dependent on local topography and the meltwater balance, but also on the proximity to a drainage channel. Areas of the ice surface close to a drainage channel will experience preferential drainage as opposed to areas located away from a channel. After a channel develops at the ice surface, the meltwater in an adjacent pond will percolate into the permeable upper layer of the ice cover and drain into the channel via gravity. As soon as pond coverage is lost, the rate of surface ablation slows and the area adjacent to the channel remains elevated compared to pond-covered areas. Unless the rate of meltwater production is higher than the maximum potential rate of gravitational drainage to sustain pond coverage, this location will remain unponded, perhaps indefinitely.

The sequence of processes described above is consistent with the ice surface evolution shown in Figure 5.11. A melt flaw formed <30 m outside the northeast corner of the laser scanning site on 16 June 2011. In the next few days, an interconnected network of drainage channels had developed between ponds in the >100 m area surrounding the flaw, including the subsection presented in Figure 5.11. The impact this had on the retention of meltwater on the ice surface was immediate, with a decrease in pond coverage of 12 pp between 17 and 19 June (Figure 5.7a). Melt ponds had drained from distributed puddles, visibly controlled by local topography on June 12, into discrete channels by 23 June. But, interestingly, this process of drainage was not restricted to areas of high pre-melt elevation. Melt ponds did not recede in the same manner they had occupied topography, rather sufficient surface modification had taken place such that the recession of meltwater appeared to depend more on the proximity of a pond to a high-order drainage channel.

The argument that ice under drainage channels may have preferentially eroded, thereby influencing pond coverage at adjacent locations, is supported by observations from the profiles shown in Figure 5.11c. On 12 June, melt ponds were present along much of the section, including both low pre-melt heights (e.g., at 32-55 m) and higher pre-melt heights (e.g., at 55-62 and 65-68 m). Areas of the ice surface that remained covered with meltwater (whether melt pond or drainage channel) between 17 and 23 June were a subset of the areas that were ponded on 12 June. As the ice melt progressed, the ponds located at 32-62 and 73-80 m disappeared and two channels formed, the first at approximately 61 m (Channel I) and the second at 76 m (Channel II). Notably, both channels were located along paths that followed the locally lowest pre-melt topography and adjacent to high topography features (Figure 5.11a and b). After meltwater drained from the ice surface at 42-60 m by 17 June, the rate of surface ablation at this location clearly decelerated compared with other locations that were ponded on 12 June, and it remained unponded thereafter (Figure 5.11c). In contrast, despite the formation of Channel II by 19 June and drainage of the ice surface at 73-80 m (Figure 5.11c), pond coverage at this location fluctuated as the meltwater balance swung from net production on 20 June to net drainage on 23 June (Figure 5.9d).

5.3.2.3. Ice Permeability Increase

After the melting of the sea ice renders it permeable enough to support vertical drainage through the ice cover, outflow pathways become unrestricted and the hydraulic head will gradually decrease thereby reducing horizontal flow towards macroscopic flaws [Eicken et al., 2002; Polashenski et al., 2012]. Once pond levels settle at the sea level no further horizontal gravity drainage can occur. However, pond expansion can still occur due to freeboard loss from a decline in buoyancy as the ice thins and lateral melt or erosion at pond walls.

According to Golden et al. [1998] and Golden [2001], sea ice should undergo a permeability transition at ~ 5% brine volume after which brine and meltwater percolation through the ice is possible. Brine volume fractions calculated using the equations of Cox and Weeks [1983] show that the entire ice cover passed this threshold as early as 23 May in 2011 (Figure 5.12c), which is several weeks before melt ponds began to form at the ice surface. A similar transition past this threshold could be identified during May in 2012 as well. Yet, significant hydraulic heads were observed in both years when melt ponds formed (Figure 5.7c). Eicken et al. [2004] and others have suggested that a layer of impermeable superimposed ice forming at the snow-ice interface could seal pond bases early in the melt season. But we recorded little of this type of ice in 2011 and, although it was prevalent in 2012, most had broken away from pond bases at the transect line by 16 June when bulk salinity in the ice column was still >4 psu (Figure 5.12d).

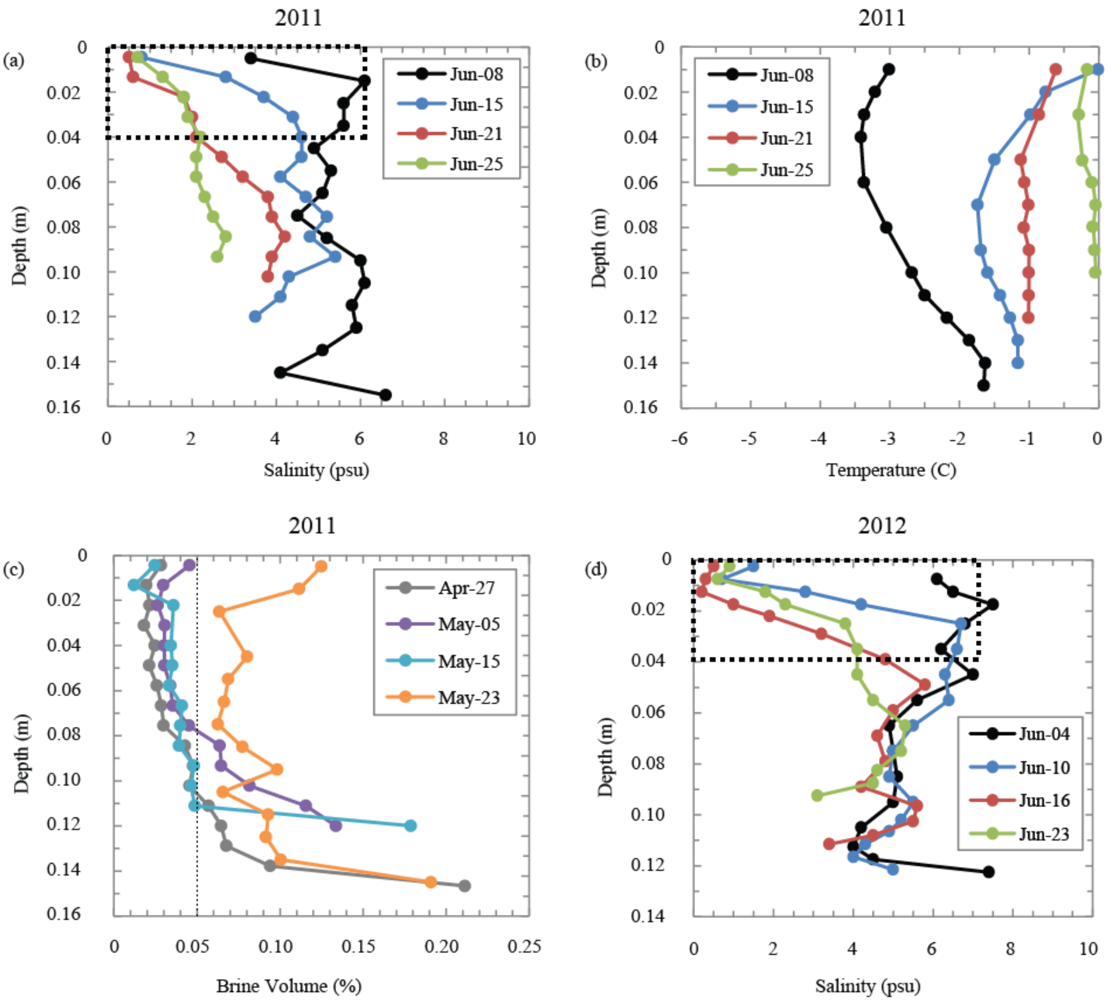

Figure 5.12 | A selection of (a) ice core profiles of salinity, (b) thermocouple profiles of temperature, and (c) ice core profiles of brine volume, from the 2011 field study, and (d) a selection of ice core profiles of salinity, from the 2012 field study. All thermocouple profiles were obtained at midday. The upper portion of the ice column became desalinized after melt onset in early June each year (highlighted by the dashed boxes in (a) and (d)), several weeks after bulk brine volume passed the 5% percolation threshold predicted by Golden et al. [1998] (highlighted by the dashed line in (c)). However, percolating meltwater appeared to only 'flush' the entire ice cover in 2011, by late-June.

The upper 0.3-0.4 m portion of the ice cover became increasingly desalinized throughout June in both years, but fresh meltwater appeared to only percolate through the entire cover in 2011, as the full salinity profile dropped to between 0 and 2 psu by 25 June

(Figure 5.12a). These observations indicate that meltwater was not able to penetrate the central portion of the ice cover, which was also the coldest portion of the ice (Figure 5.12b), until approximately 21 June in 2011. This supports one hypothesis, suggested by Polashenski et al. [2012], that water percolating into the ice shortly after pond formation will refreeze inside this section and form interposed ice plugs to limit further infiltration until later in the melt season. Ice core salinity profiles from 2012 indicate that this mechanism of refreezing ensured the ice remained impermeable for the duration of the 2012 sampling period (Figure 5.12d).

Although melt ponds had dropped to sea level by 21 June in 2011, signalling the start of Stage III, water continued to drain from the ice surface at a rate of 20-30 mm d^{-1} (Figure 5.9d). This volume of water could not have drained from the ice surface at macroscopic flaws after 21 June, because the hydraulic head was close to zero. Therefore vertical meltwater percolation must have become the dominant mechanism of drainage after this date.

There have been few observational or modelling studies that have directly estimated lateral (or ‘sidewall’) melt in ponds. Estimates for the *total* heat flux entering the sea ice cover (i.e. snow/ice and ponds), combining radiative and turbulent atmospheric fluxes and sometimes also the oceanic heat flux, are as high as 80 W m^{-2} [Nicolaus et al., 2010] or 120 W m^{-2} [Hudson et al., 2013] for a single day. Over a longer period (a week to a month), average estimates for the total heat flux fall to around 40-60 W m^{-2} [Perovich et al., 2003; Nicolaus et al., 2010; Hudson et al., 2013]. However, these studies provide no information on the relative partitioning of energy between the sea ice and melt ponds, or, within ponds, between vertical and horizontal (basal and lateral) ice melt at the perimeter. Skyllingstad and Paulson [2007] used a high-resolution large eddy simulation (LES) model, forced with radiative data from the SHEBA study, to demonstrate that basal and lateral melt can vary by more than 20 W m^{-2} within the same pond. To the author's knowledge, the only study that has attempted to estimate lateral melt directly is Eicken et al. [2002]. Eicken et al. calculated the mean lateral heat flux, referenced to the ice surface at the top of a melt pond wall, Q_l, as approximately 50 W m^{-2} from measurements of pond water temperatures collected over a two-month period at SHEBA.

No measurements were taken during the Arctic-ICE project of the total heat flux entering a melt pond or of the lateral heat flux acting on a pond sidewall. To estimate the maximum potential lateral melt for the period between 22 and 26 June in 2011 at our study site, we assume a relatively high constant heat flux of 50 W m^{-2} acting on the melt pond walls for 12 hours per day. This value is based on the measurements of Eicken et al. [2002] and LES results of Skyllingstad and Paulson [2007]. Lateral melt can be determined from this heat flux as:

$$\frac{\Delta x}{\Delta t} = \frac{Q_l}{\rho_i L}, \tag{5.9}$$

where ρ_i is the density of sea ice (900 kg m^{-3}) and L is the latent heat of fusion, which is estimated as 213 kJ kg^{-1} following Ono [1967] for sea ice with an average temperature of -0.3 $^{\circ}$C and bulk salinity of 2 psu. These temperature and salinity values were calculated from ice core measurements obtained on 25 June. For the four day period between 22 and 26 June (Stage III), total lateral melt is estimated as 0.045 m. This would have produced an additional 110 m^2 of pond-covered ice within the laser scanning site, corresponding to a change in coverage of 1.1 pp. Although this value is comparable with the direct observations of Eicken et al. [2002], it contributes less than one tenth of the recorded 11.3 pp change in pond coverage between these dates (Figure 5.7a).

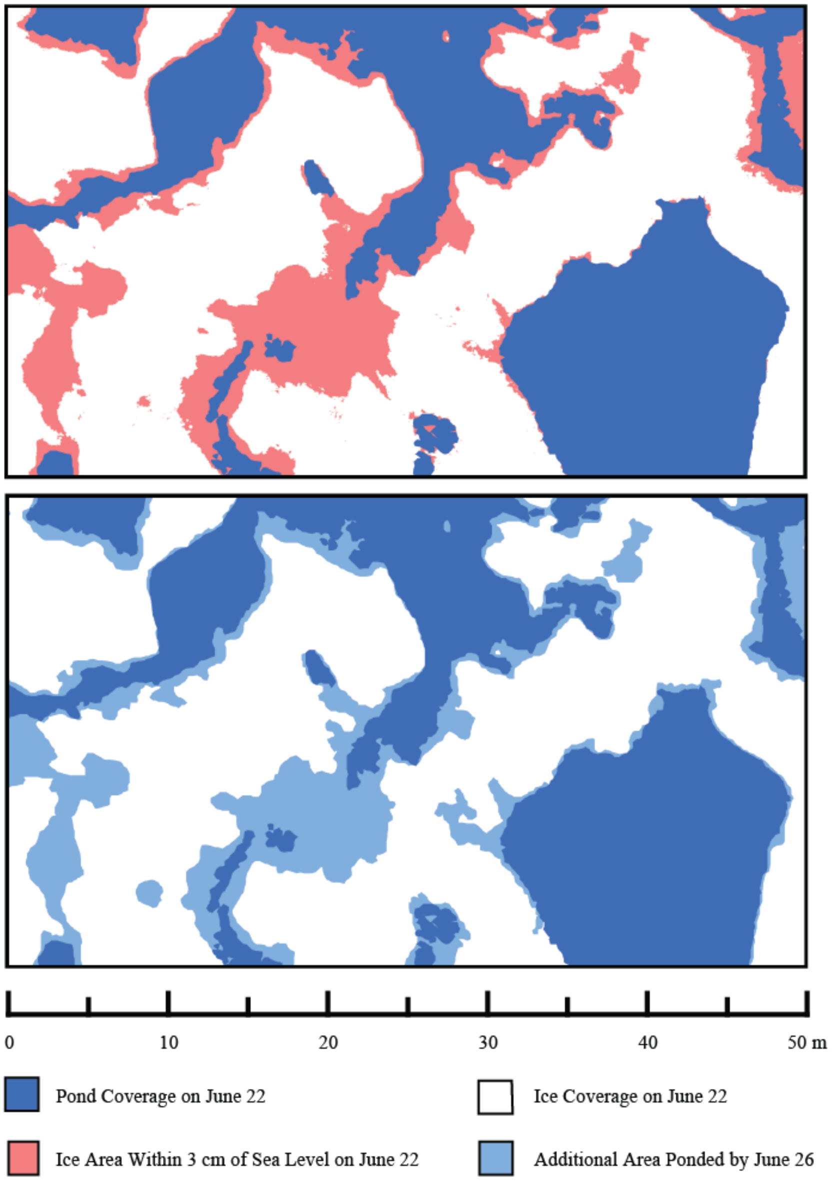

Figure 5.13 | A comparison between areas of the ice surface within 0.03 m of sea level at a subsection of the 2011 laser scanning site on June 22 and areas of melt pond growth at the same subsection between June 22 and 26. This 0.03 m threshold corresponds to the loss of freeboard measured at laser scanning platforms around the mass balance site between June 22 and 26 (Figure 5.9c).

However, the increase in pond coverage could be explained by ice freeboard loss. Throughout Stages I and II of the melt season in 2011 (and also throughout the entire sampling period in 2012), sea level dropped with respect to the fixed reference level located within the centre of the ice cover (Figure 5.7b), indicating that more mass was lost above sea level (from snow and ice melt) than below it (from ice bottom melt). But after 21 June the position of sea level above the reference level remained fairly stable, and direct measurements at the corners of the laser scanning site showed that ice thickness fell by approximately 0.18 m, with an associated decline in ice freeboard of 0.03 m, between 22 and 26 June (Figure 5.9c). All unponded areas of the ice surface within 0.03 m of sea level at a subsection of the 2011 laser scanning site on June 22 are shown in red in the upper panel of Figure 5.13 and are highly correlated with additional areas ponded by June 26, indicating that freeboard loss controlled late season melt pond growth in 2011. It is also worth noting that steepening ice at the edges of melt ponds (Figure 5.8a) resulted in almost zero change in coverage at numerous locations between these dates (e.g., the lower right pond in Figure 5.13).

5.3.2.4. Surface Energy Balance

Daily rates of meltwater production were clearly regulated by the key components of the surface energy balance, i.e. air temperature and incident shortwave and longwave radiation, throughout the melt season each year. For instance, air temperatures were on average 2-3 °C higher and the shortwave flux was 50-100 W m^{-2} greater between 17 and 22 June than between 22 and 26 June in 2011, which corresponded with the measured peak rate of meltwater production (approximately 50 mm d^{-1}) (Figure 5.9d). Likewise, production was nearly zero around 17 June 2012, which corresponded with near-zero air temperatures and a sharp fall in the shortwave flux to ~ 150 W m^{-2} from previous daily averages of almost 400 W m^{-2} (Figure 5.9h). In both years, the rate of meltwater drainage also appeared to track the rate of production closely, so that (excluding Stage I) the absolute difference between production and drainage never exceeded 10 mm d^{-1}. It is also worth noting that meltwater production rates were lowest in the few days following melt pond onset each year as higher albedo snow melted less quickly than either bare or ponded ice.

We estimated the net daily flux of radiative energy from the atmosphere to the sea ice during the 2011 and 2012 melt seasons (Q_*), from boundary layer meteorological measurements recorded at the on-ice towers, as

$$Q_* = \left[\left(1 - f_p\right)\alpha_i + f_p\alpha_p\right]K_d + L_d - L_u, \tag{5.10}$$

where K is shortwave and L longwave radiation, with subscripts d and u denoting downwelling and upwelling, respectively. The shortwave albedo of a melt pond (α_p) was assumed to be 0.21, and the shortwave albedo of sea ice (α_i) was assumed to be either 0.62 for bare white ice or 0.77 for melting snow, depending on the date, following Perovich [1996]. By assuming a latent heat of fusion of 334 kJ kg^{-1} we estimated the energy (Q_m) required to melt snow or ice and yield the daily rates of meltwater production recorded in 2011 and 2012 (Figure 5.9d and h). Comparing Q_* with Q_m (for all LiDAR sampling days in 2011 and 2012) demonstrated that, on average, surface melt accounted for the absorption of 62 ± 23% of the net flux of radiative energy entering the sea ice from the atmosphere during the melt season. For this calculation we assume that the turbulent (sensible and latent) heat fluxes were negligible. This is not an unrealistic assumption when the near-surface air temperatures are close to zero [e.g. Hudson et al., 2013].

A comparison between net daily meltwater balance (production minus drainage) and melt pond coverage (Figure 5.14) indicates that changes in pond coverage were driven by minor fluctuations in meltwater balance. If production exceeded drainage then melt ponds expanded and, conversely, if drainage exceeded production then ponds contracted. The fit between each year's measurements ($p < 0.005$) demonstrates that a shift in meltwater balance of ± 10 mm produced a change in pond coverage of 9 pp in 2011 and 17 pp in 2012. This difference reflects the variation in topographic relief between the two years.

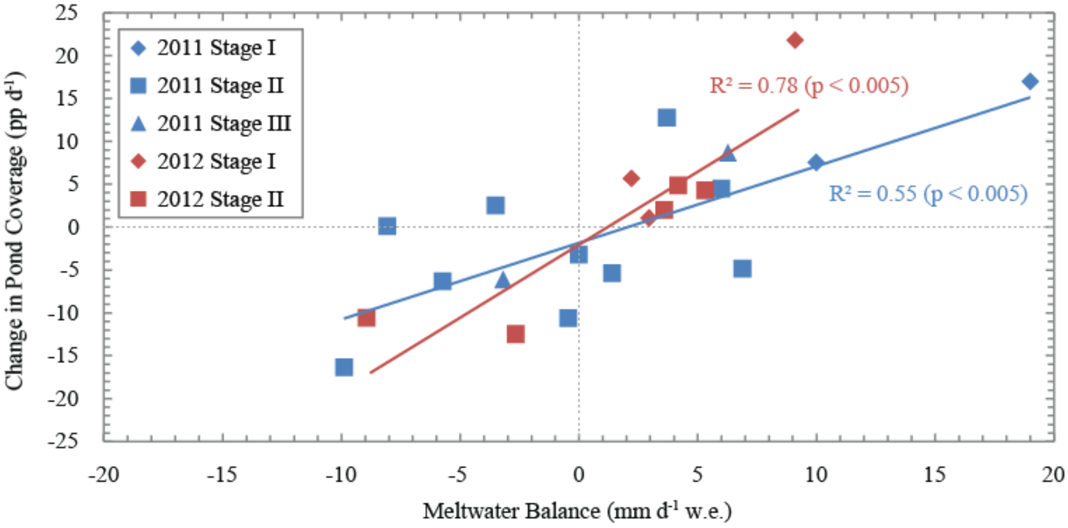

Figure 5.14 | Change in melt pond coverage (in percentage point per day) versus change in meltwater balance (in mm per day) between sequential sampling days at the 2011 and 2012 laser scanning sites. Measurements are separated for the different stages of melt pond evolution each year. Coefficients of determination (r^2) and associated p-values for best-fit linear trends between each years' measurements are presented in the top right.

5.4. Summary and Conclusions

In general, the evolution of melt pond coverage at both years' field sites conformed to the four stages defined by Eicken et al. [2002]. Within a few days of pond formation, on 10 June in both years, coverage increased to the seasonal maximum (Stage I), before fluctuating, but gradually dropping, over the following week (Stage II). In 2011, melt pond surface levels dropped to sea level almost two weeks after forming, but, in 2012, melt pond levels were still 20-30 mm above sea level at the end of our sampling period in late June. After ponds dropped to sea level in 2011, coverage rose slightly in the few subsequent days before we left the ice (Stage III). Ice break-up (Stage IV) occurred on 27 June at the 2011 field site, but was delayed until 5 July in 2012.

The key factors affecting melt pond coverage on undeformed first-year sea ice in the CAA are: (1) pre-melt surface topography; (2) the number-density of drainage features that open up through the ice cover; (3) the evolution of ice temperature; and (4) the surface energy balance.

Snow drift locations pre-condition the initial spatial distribution of melt ponds in spring, as originally suggested by Barber and Yackel [1999] and confirmed by Petrich et al. [2012]. Pre-melt topography then restricts the horizontal percolation of meltwater across the sea ice surface, thereby controlling the maximum achievable, seasonal limit in pond coverage (end of Stage I) and the connectivity between ponds. Although snow surface and thickness distributions were similar between our study sites, an interannual difference in topographic relief (height range of 0.8 m in 2011 rather than 0.3 m 2012) modified pond coverage significantly. The seasonal peak in pond coverage was almost 20 pp higher and the variation in coverage with a change in the surface meltwater balance (production minus drainage) was almost twice as high for the smoother ice in 2012. It would be useful to develop this relationship between topographic relief and parameters of melt pond coverage beyond our analysis of two years for a single ice type. Airborne LiDAR could be used to acquire large pre-and post-melt topography data sets for a range of ice types and deformation conditions, in different regions of the Arctic, to improve modelling studies of the sensitivity of pond coverage on topography [e.g. Luthje et al., 2006; Scott and Feltham, 2010]. Once this sensitivity has been established, remote sensing measurements of pre-melt sea ice surface topography, for example using satellite laser altimeters [Kwok et al., 2006], could be used to predict pond coverage in summer.

The location and density of drainage flaws affect the redistribution of meltwater at the ice surface during Stage II, with the development of channels occasionally, and somewhat counter intuitively, draining ponds that are preferentially in adjacent low lying areas. This mechanism of drainage was apparent in both years of our study, suggesting that it is common of melt ponds on first-year sea ice; however, it was not observed by Polashenski et al. [2012]. Melt ponds do not recede in the same manner they occupy topography. Considerable modification of surface topography occurs with the formation of drainage channels and the recession of meltwater from a ponded area depends on the proximity to a channel and/or drainage flaw, rather than pre-melt elevation. Scott and Feltham [2010] conclude that a fundamental limitation of current melt pond models is their inaccurate representation of the hydraulic processes governing meltwater transport in ponds. A key objective of future research should therefore be to build on the observations of this study and quantify flow patterns, friction and turbulence within melt ponds, in support of modelling studies.

Ice temperature controls the transition in permeability between Stages II and III that allows surface meltwater to percolate through the ice cover, thereby determining whether hydrostatic balance or ice freeboard loss regulates changes in late-season pond coverage. Results from sea ice cores (Figure 5.12) support the hypothesis of Polashenksi et al. [2012] that fresh meltwater percolating into the upper portion of the sea ice cover early in the melt season refreezes to form plugs of interposed ice, delaying the permeability transition by at least several weeks. Lateral melt at sidewalls does not contribute to pond growth over the short timescales (days) associated with late-season melt pond evolution on first-year ice.

Finally, the sea ice surface energy balance, in particular the radiative forcing of the sun, affects melt pond coverage throughout the entire season by regulating the rate of surface meltwater production. It is estimated that surface melt accounted for the absorption of almost two thirds (62 ± 23%) of the net radiative flux from the atmosphere to the sea ice during the melt season. We assume that turbulent heat exchanges were negligible. The remaining energy of ~38% was either absorbed within the ice cover, melting and raising its temperature in the process, or transmitted through the ice to the ocean. Our data set does not allow us to assign values to this partitioning confidently. However, if we assume a constant oceanic heat flux of 15 W m^{-2} [Stanton et al., 2012; Hudson et al., 2013], observed ice thickness and temperature changes during the two years of our study suggest that bottom melt and internal heating accounted for a further 27% of the radiative flux. This would leave a surplus of approximately 11% transmitted to the ocean, which is towards the lower limit of past observations [Ehn et al., 2011; Nicolaus et al., 2012; Hudson et al., 2013].

In this study we have demonstrated that melt pond evolution on first-year sea ice is primarily controlled by four interdependent mechanisms. The timing and/or magnitude of each of these mechanisms varied between our field sites, producing significant spatiotemporal variations in melt pond coverage. Active microwave observations demonstrate that stages of melt pond evolution in the CAA are frequently not spatially auto-correlated or correlated with radiative forcing parameters [Howell et al., 2006]. This suggests that the four mechanisms controlling melt pond variability in our *in situ* field study are representative of, at least, first-year ice in the wider CAA. The Arctic Ocean is becoming increasingly dominated by first-year, rather than multi-year, sea ice [Stroeve et al., 2011] and the date of melt onset and length of the melt season are becoming earlier and longer, respectively [Howell et al., 2009; Markus et al., 2009]. Further work is therefore required to understand how these in situ observations transfer to regional scales, so that relevant melt pond parameters can be regularly monitored across the entire Arctic through optical remote sensing [Rösel and Kaleschke, 2012] or SAR [Scharien et al., 2014].

Chapter 6. Albedo Feedback Enhanced by Smoother Arctic Sea Ice

A peer-reviewed scientific research letter published in:
Geophysical Research Letters, *42(24), 10,714–10,720,*
doi.org/2010.1002/2015GL066712

Jack C. Landy*, Jens K. Ehn, David G. Barber

* Corresponding Author

Centre for Earth Observation Science, Department of Environment and Geography, University of Manitoba, Winnipeg, Manitoba, Canada.

Summary Paragraph

The recent declining trends in summertime Arctic sea ice [Schweiger et al., 2011; Comiso, 2012] have been linked [Schröder et al., 2014] to prolonged melt season duration [Markus et al., 2009; Stroeve et al., 2014] and escalating melt pond coverage [Rösel and Kaleschke, 2012]. Melt ponds dramatically reduce the sea ice albedo [Perovich et al., 2002], allowing a larger portion of solar radiation to penetrate the ice cover [Ehn et al., 2011], thereby accelerating further melt [Curry et al., 1995] and enhancing light-limited primary productivity in the ocean [Arrigo et al., 2012]. Although melt ponds evolve in stages, coverage is generally higher on sea ice with smoother surface topography [Eicken et al., 2004; Landy et al., 2014]. However, the relationships between the topography, pond coverage and albedo have not yet been quantified. Here we show, for the first time, that the summer albedo of Arctic sea ice can be predicted several months in advance as a function of the pre-melt sea ice surface roughness. We find that our quantitative method applied to satellite observations of the end-of-winter sea ice surface roughness can explain 85% of the variance in the following summer's ice albedo. Our results reveal that an Arctic-wide reduction in sea ice roughness during the 2000s explains a drop in ice albedo that resulted in a 16% increase in solar heat input to the sea ice cover. We estimate this to be ten times the heat input contributed by earlier melt onset timing over the same period.

6.1. Research Letter

Melt ponds form on sea ice during the spring to summer transition, at a time when surface meltwater cannot percolate through the cold interior of the ice cover [Freitag and Eicken, 2003] and instead pools at the surface [Eicken et al., 2002]. The fractional coverage of ponds can vary by more than 80% over the course of a single melt season [Landy et al., 2014] and by more than 30% between locations and years [Polashenski et al., 2012; Rösel and Kaleschke, 2012], principally depending on the surface energy balance [Taylor and Feltham, 2004], permeability [Polashenski et al., 2012], and surface topography [Eicken et al., 2004] of the sea ice cover. It is known that first-year sea ice (FYI) typically has a lower albedo than multi-year sea ice (MYI) because the ice is thinner [Perovich, 1996] and because the smoother surface supports higher melt pond coverage [Eicken et al., 2004; Hunke et al., 2013]. It has therefore been suggested that a larger fraction of FYI, rather than MYI, in the Arctic basin over the past decade may have contributed to a general decrease in summer sea ice albedo, leading to a stronger ice-albedo feedback and enhanced melt [Lindsay and Zhang, 2005; Stroeve et al., 2012]. However, the relationship between the pre-melt (winter) sea ice surface roughness and melt season pond coverage has not yet been quantified. Consequently, it is not known how much influence the pre-melt roughness of the Arctic ice cover has on the summer sea ice albedo, in comparison to other factors, for instance ice type [Stroeve et al., 2012] or prolonged melt season duration [Markus et al., 2009; Stroeve et al., 2014].

The root mean square (RMS) roughness height of Arctic sea ice surface topography, calculated from laser altimeter measurements of sea ice surface elevation (ICESat; see Methods in Section 6.2), show that pre-melt (March) sea ice surface roughness decreased across the majority of the Arctic basin over the ICESat operational period 2003-2008 (Fig. 6.1a). Several of the regions which exhibited the strongest reductions in surface roughness (up to 2 cm yr-1), including the Canadian Arctic Archipelago (CAA), Central Arctic Ocean, and eastern Beaufort Sea, coincide with those regions which lost thick and old ice during this period, particularly during the summer of 2007 [Maslanik et al., 2011]. The trend of mean Arctic sea ice surface roughness was -0.5 cm yr 1 ($p = 0.05$) over the period 2003-2008. At the same time, modal sea ice surface roughness decreased from approximately 15 cm in 2003-2006, to approximately 9 cm in 2007-2008 (Fig. 6.5 in Section 6.3.1).

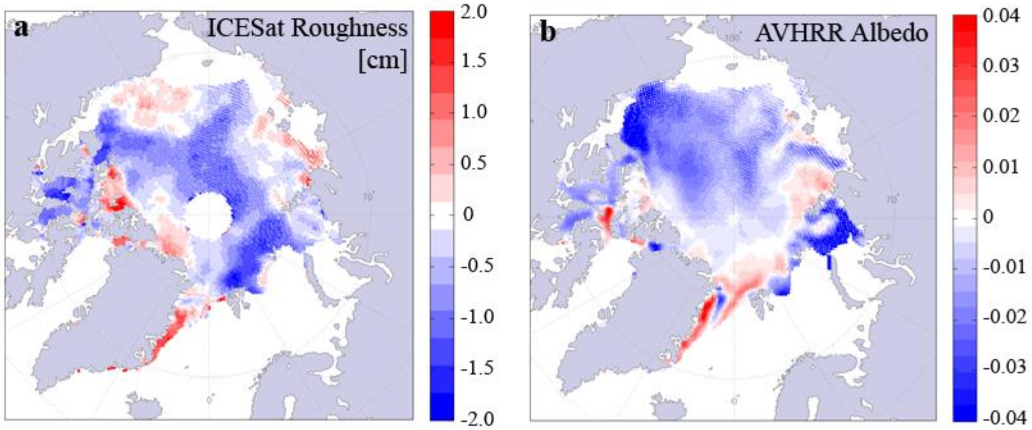

Figure 6.1 | Trends of sea ice surface roughness and surface albedo for the period 2003-2008. (a) Sea ice surface roughness σ in March, from detrended 10-km moving window ICESat observations [cm yr^{-1}]. (b) Surface albedo α (a mixture of bare sea ice, pond-covered sea ice and/or ocean) in June-August, from AVHRR (SAF-CLARA product) [yr^{-1}]. Areas which contained only seasonal sea ice for the entire period are excluded.

The general imprint of the pre-melt surface topography remains throughout the summer melt season. Rougher ice typically remains rougher compared to smoother ice, and mounds and depressions of the surface topography remain at predetermined locations [Petrich et al., 2012]. Melt ponds then form and evolve in these depressions [Polashenski et al., 2012]. Field observations on FYI in the Canadian Arctic have demonstrated that the rate of change in melt pond area, as a function of the surface meltwater balance, can vary almost two-fold between locations with marginally different pre-melt roughness [Landy et al., 2014]. This discovery suggests that relatively minor variations in the roughness of the pre-melt sea ice surface topography can instigate major variations in summer melt pond coverage.

Based on these observations, we hypothesize that recent changes in the strength of the sea ice-albedo feedback may be principally a direct result of general changes in the pre-melt roughness of Arctic sea ice surface topography. Fittingly, the strong observed smoothing of the Arctic sea ice surface topography between 2003 and 2008 (Fig. 6.1a) was accompanied by anomalously large declines in both sea ice concentration [Serreze et al., 2007; Comiso, 2012] and volume [Zhang et al., 2008]. The Arctic-wide pattern of the summer surface albedo trend (from AVHRR, see Methods in Section 6.2) over the same period generally agrees with the trend in pre-melt sea ice roughness (Fig. 6.1b). The albedo decreased by up to 0.04 yr-1 ($p = 0.02$) across the majority of the Arctic basin, including many of the regions that experienced a decrease in roughness, for instance: the CAA, western Central Arctic Ocean, Beaufort Sea, and Kara Sea. The increase in sea ice roughness observed in a few regions (the Lincoln Sea, Greenland Sea, and northern CAA) also correlates with an increase, or minimal change, in surface albedo. It is noticeable that neither the albedo nor the surface roughness, are homogenous within FYI or MYI zones (Fig. 6.5 in Section 6.3.1 and Fig. 6.6 in Section 6.3.2), which suggests that sea ice albedo in summer cannot be accurately estimated solely from the ice age, as attempted in several studies [Perovich and Polashenski, 2012; Nicolaus et al., 2012; Arndt and Nicolaus, 2014].

These discoveries prompted us to examine the influence of the pre-melt sea ice surface topography on the summer melt pond fraction in greater depth, using numerical simulations. Random rough surfaces, but with predetermined statistical parameters obtained from field observations [Rivas et al., 2006], were simulated using spectral analysis [Landy et al., 2015b] to represent the pre-melt ice surface topography. More than 19 thousand melt pond distributions were generated from 480 topography grids, with varying surface roughness, by positioning the meltwater surfaces at levels that represented specific volumes of meltwater per unit area above the sea ice surface, hereinafter h_{net} (see Section 6.3.3). Thus, we could monitor changes in various parameters of melt pond geometry, including the melt pond fraction f_p, for increasing h_{net} (Fig. 6.2a).

Simulation results demonstrate that f_p increases as a non-linear function of h_{net} and pre-melt RMS sea ice surface roughness σ (Fig. 6.2b). The rate of change in f_p with h_{net} strongly depends on σ, with the pond fraction initially increasing more rapidly on a smoother surface than on a rougher surface, in accordance with field observations [Landy et al., 2014]. We used the simulation results to develop an empirical model which quantifies f_p in terms of h_{net} and σ (see Section 6.3.4). This model can determine the areal fraction of the sea ice surface, with a certain pre-melt roughness, which is flooded by a certain volume of meltwater. Field observations of pre-melt sea ice surface roughness and melt season pond volume were collected on FYI in the Canadian Arctic, and were obtained from the literature for MYI [Eicken et al., 2002], to validate the model (Fig. 6.2b; see Section 6.3.4). In general, the model predictions describe the observed changes in f_p as a function of h_{net} very well (correlation, $r = 0.97$, $p < 0.001$).

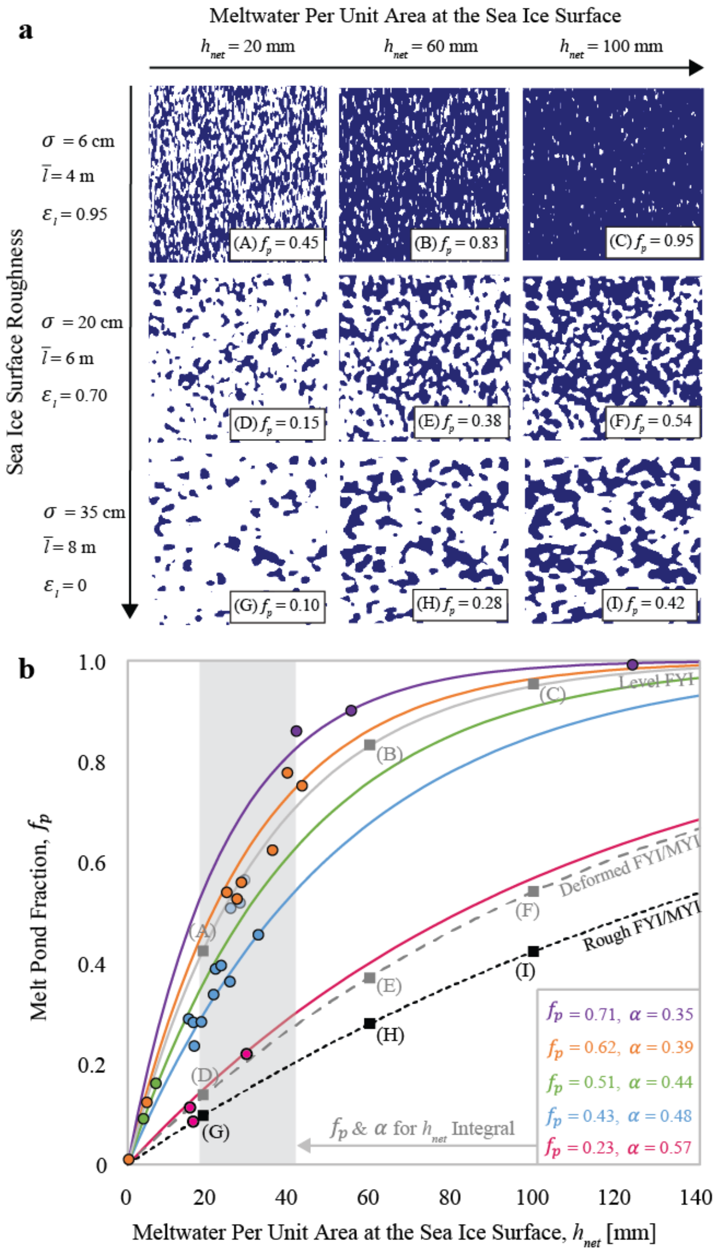

Figure 6.2 | (a) The evolution of simulated melt pond geometries is representative of natural sea ice, with a transition occurring from individual isolated ponds to interconnected pond networks as f_p rises. (b) Comparison of observed and simulated relationship between f_p and h_{net}. Model simulations (curves) and observations (points) are for the following: FYI in Dease Strait, 2014 (σ = 3.5 cm, purple); two locations on FYI in Resolute Passage, 2012 (5.2 cm, orange; 7.7 cm, green); FYI in Allen Bay, 2011 (9.6 cm, blue); MYI in the Chukchi Sea, 1998 (18 cm, pink) [Eicken et al., 2002]; characteristic level FYI (6 cm, solid gray); characteristic deformed FYI/MYI (20 cm, dashed gray); roughest FYI/MYI (35 cm, dashed black). Melt pond configurations in (A) are marked on the modelled curves by the letters in parentheses.

Our field observations reveal that h_{net} rarely exceeds 60 mm, with the majority of the observations located within a confined band of h_{net} between approximately 20 and 40 mm (Fig. 6.2b), which represents a balance between meltwater production and drainage at the sea ice surface. We therefore infer that the most significant regional/interannual differences in f_p are due to variations in σ occurring when h_{net} is within this 20 mm range. This finding is particularly important, because it restricts the upper and lower limits that the sea ice albedo can potentially attain during the summer melt period. For instance, the difference in simulated f_p between the smoothest and roughest FYI field sites, integrated over this significant band of h_{net} from 20 to 40 mm (i.e. the difference between the blue and purple curves within the gray area of Fig. 6.2b), is 0.28 (65%). The difference in simulated f_p between characteristic level FYI and characteristic deformed FYI or MYI [Rivas et al., 2006], integrated over the same significant band of h_{net} (i.e. the difference between light gray and dashed black curves within the gray area of Fig. 6.2b), is 0.38 (181%).

The importance of the pre-melt sea ice topography for the melt season ice albedo is demonstrated by the above two cases: Case 1, relatively smooth (σ = 3.5 cm) versus relatively rough (σ = 9.6 cm), but level, FYI surfaces; and Case 2, level FYI (σ = 6 cm) versus deformed FYI/MYI (σ = 20 cm) [Rivas et al., 2006]. We estimate the sensitivity of the sea ice albedo to the calculated variations in f_p given above, for each of these cases, using average end-member values for ice and melt pond albedos. The shortwave albedo for sea ice is: $\alpha_{si} = (1 - f_p)\alpha_i + f_p\alpha_p$, where the albedos for ice (average value for snow/bare white ice) α_i and melt pond α_p are assumed to be 0.68 and 0.21, respectively [Perovich, 1996]. The striking reductions in α_{si} for the smoother ice are 0.13 for Case 1 and 0.20 for Case 2, which equate to 38% and 48% more ice melt, respectively.

To evaluate the contribution of the reduction in pre-melt sea ice roughness to the observed albedo change over the ICESat period (Fig. 6.1), we first use our empirical model to calculate Arctic-wide maps of f_p using σ from ICESat, before predicting the sea ice albedo α_{si} as above. The total shortwave surface albedo is then calculated as: $\alpha = \alpha_{si}C_{si} + \alpha_{ow}(1 - C_{si})$, where C_{si} is the sea ice concentration from AMSR-E and the open water albedo α_{ow} is assumed to be 0.07 [Perovich, 1996]. The years 2005 and 2007 offer a picture of the Arctic sea ice cover in two years with contrasting roughness: relatively rough ice (modal σ = 18 cm) in 2005 and relatively smooth ice (modal σ = 11 cm) in 2007 (Fig. 6.5 in Section 6.3.1). The mean summertime (June-August) surface albedo over the entire basin, as predicted by the pre-melt roughness, is 0.05 (10%) lower in 2007 than in 2005 (Fig. 6.3a and b).

Incidentally, the average reduction in the Arctic summertime surface albedo, as observed by AVHRR, was also 10% lower in 2007 than in 2005. Furthermore, the average decrease in the thickness of the Arctic sea ice cover between March and September (i.e. summer sea ice ablation), as modelled in PIOMAS (see Section 6.3.5), was 9% higher in 2007 than in 2005. Maps of the 2005 and 2007 AVHRR June-August surface albedo (Fig. 6.3c and d) and PIOMAS modelled sea ice ablation (Fig. 6.7 in Section 6.3.5) show remarkable spatial similarities to the regional changes in surface albedo predicted by March sea ice surface roughness, as observed by ICESat. Indeed, the pixel-by-pixel correlation between the ICESat predicted surface albedo and AVHRR observed albedo (see Section 6.3.6) is r = 0.92 (rmse = 0.067, p < 0.001), for all years with coincident and available data (2003-2008) (Fig. 6.3e and f). Thus, the pre-melt sea ice surface roughness can explain 85% of the variance in the summer sea ice albedo.

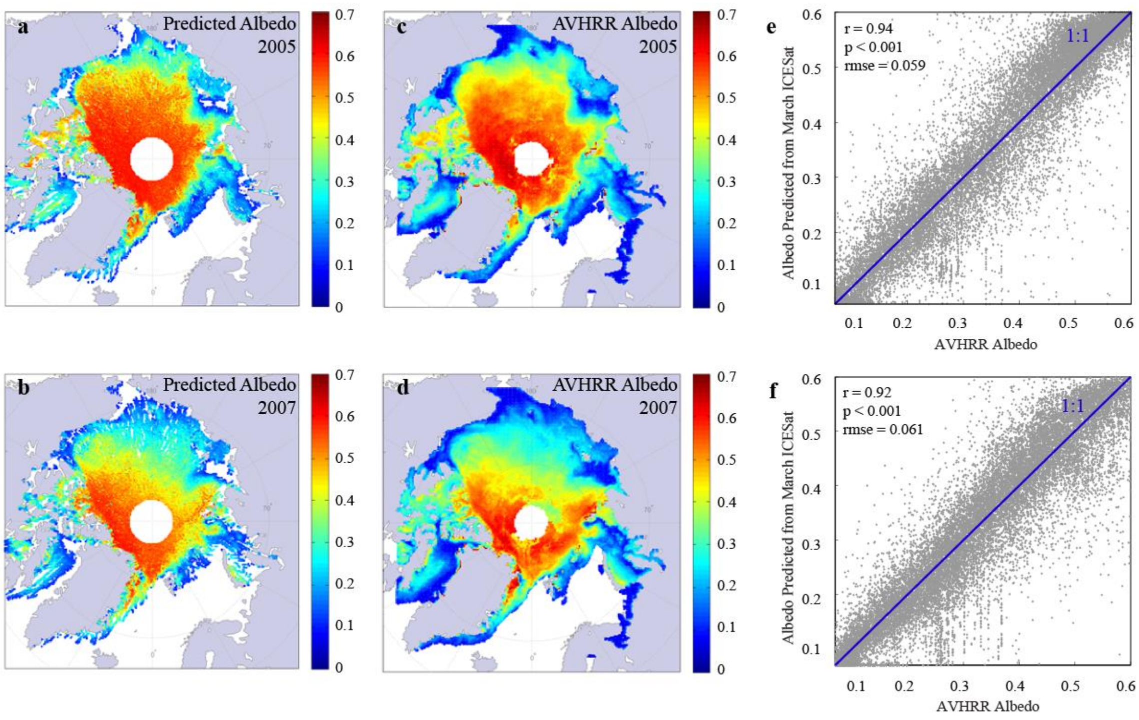

Figure 6.3 | Predicted versus observed surface albedo in 2005 and 2007. (a) and (b) Predicted shortwave albedo in June-August, based on empirical model estimates of f_p for the h_{net} integral from 20-40 mm, and using ICESat roughness observations in March and AMSR-E sea ice concentration. (c) and (d) Observed shortwave albedo in June-August, from AVHRR. (e) and (f) Comparison between predicted and observed surface albedo. One-to-one lines are highlighted in blue.

Trends towards earlier melt onset (of around 2 days decade-1) have also been documented in several studies [Markus et al., 2009; Stroeve et al., 2014], and it has been suggested that earlier melt onset timing may have contributed to recent strengthening of the ice-albedo feedback mechanism [Stroeve et al., 2014]. Indeed, over the ICESat period the average date of melt onset decreased by 2 days within the Arctic basin, approximately twice the long-term trend [Markus et al., 2009]. However, a sensitivity analysis of variations in melt onset date and sea ice surface roughness (see Section 6.3.7) indicates that decreasing Arctic sea ice roughness, between 2003 and 2008, had ten times more influence on the observed reduction in ice albedo than earlier melt onset timing.

Sea ice extent was within 10% and ice volume within 20% of their long-term climatological averages at the turn of the century (Fig. 6.4). However, by 2014, MYI extent in both March and September declined by roughly 40% (as observed by passive microwave satellites) [Comiso, 2012] and annual mean sea ice volume declined by an estimated 70% (as simulated in PIOMAS) [Schweiger et al., 2011]. The roughness of the sea ice cover also declined; however, data are only available during the ICESat operational period (Fig. 6.4). Interestingly, March roughness is significantly correlated with both the AVHRR June-August surface albedo ($r = 0.71$, $p < 0.05$), and the PIOMAS modelled sea ice volume, particularly the ‘post-melt’ ice volume in September ($r = 0.74$, $p < 0.05$). These relationships support our original hypothesis, that recent changes in the roughness of the pre-melt sea ice topography have significantly influenced the sea ice albedo, and consequently the amount of ice that has melted, during the Arctic summer. We calculate that the shift in Arctic sea ice roughness from 2003 to 2008, particularly evident in March 2007, would have reduced the ice albedo by approximately 0.08 ($p < 0.001$), from an average June-August albedo of 0.54 (f_p = 0.29) in 2003-2006 to 0.46 (f_p = 0.47) in 2007-2008. This change in albedo would have increased the solar heat input to the sea ice cover by 16%.

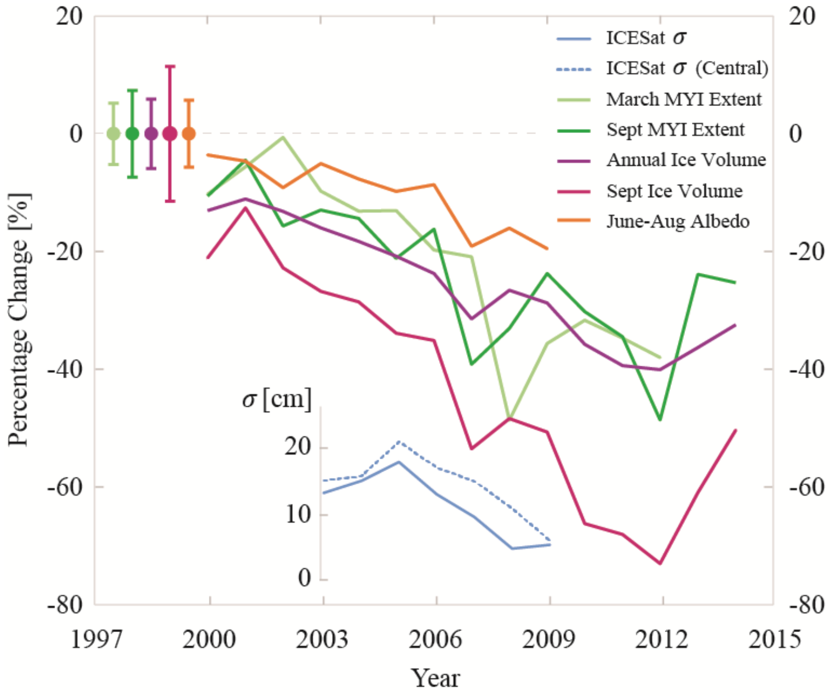

Figure 6.4 | Interannual evolution of Arctic sea ice surface roughness, extent and volume, and surface albedo, for the period 2000-2014. Including: March sea ice surface roughness σ [m] (from ICESat), for the entire Arctic and for the Central Arctic only; relative changes in March and September MYI extent (from the NSIDC sea ice age product); relative changes in September and annual average sea ice volume (from PIOMAS); relative changes in June-August surface albedo (from AVHRR). Long-term climatological means and standard deviations are illustrated as points and error bars. Climatologies are: 1985-1999 for March MYI extent; 1979-1999 for Sept MYI extent and for ice volume; and 1982-1999 for surface albedo.

Our findings reveal the possibility for an interannual feedback loop between winter sea ice roughness and summer surface melt. Summer melting either reduces the thickness of the ice cover or causes it to disappear completely. Although ICESat laser altimeter observations demonstrate that sea ice surface roughness can vary considerably within FYI or MYI zones (see Section 6.3.1), FYI is generally smoother than MYI over local scales [Rivas et al., 2006]. Therefore, if relatively thin new ice replaces thicker older ice in winter, following a summer of enhanced melting, the overall roughness of the sea ice topography will decrease. Our results have shown that melt pond coverage is higher on seasonal ice with smoother surface topography, so the albedo of the thinner and smoother ice cover will be reduced in the subsequent summer, further enhancing the rate of ice melt. Satellite observations have shown that MYI is being progressively replaced by FYI within the Arctic basin [Maslanik et al., 2011; Comiso, 2012; Stroeve et al., 2012], which is potentially both a consequence of, and contributes to, the proposed feedback loop.

We have demonstrated that observed reductions in Arctic-wide sea ice surface roughness, over the ICESat operational period, are quantitatively related to observed reductions in surface albedo, with the increasing fractional coverage of melt ponds providing the link. This finding is particularly timely, since NASA intends to launch a new satellite LiDAR: ICESat-2, in 2017. It remains to be seen whether the relationships hold in a new Arctic dominated by seasonal sea ice. However, our technique could potentially be used to predict the summer albedo of the Arctic sea ice cover, several months in advance, using surface roughness estimates obtained from the new altimetry data in the preceding winter.

6.2. Methods

Arctic-wide, long-term estimates of sea ice surface roughness were obtained from NASA's ICESat laser altimeter. The latest version of the data available at the time of analysis was Version 34 of the Level 2 GLA05 & GLA13 products, available from NSIDC at http://nsidc.org/data/icesat/. In our analysis, we only used the altimeter data collected during March, to maintain accurate comparisons of pre-melt sea ice surface roughness between years. The precision of the raw altimeter measurements is estimated to be 2 cm

[Kwok et al., 2006]. Raw data were quality controlled, corrected for geoid and ocean loading effects (see Section 6.3.1) and filtered within the area defined by March sea ice concentration >0.9 (using 25-km gridded AMSR-E data, enhanced NASA Team algorithm, available at http://nsidc.org/data/AE_SI25) [Cavalieri et al., 2014]. Finally, 10-km profiles were detrended to account for low-frequency variability caused by errors in the estimation of the sea surface height, following Kwok et al. [2007]. Surface roughness was obtained from the root mean square (RMS) height of detrended 10-km ICESat profiles. The standard error of the minimum observed roughness (σ ~ 2 cm) is 0.3 cm and the standard error of the maximum observed roughness (σ ~ 40 cm) is 5.2 cm. The standard errors of the mean annual Arctic-wide roughness, for all years between 2003 and 2008, are <1 mm.

Arctic Ocean surface albedo observations were obtained from the 25-km monthly Northern Polar Region black-sky broadband surface albedo product from the EUMETSAT CLARA-A1 dataset (available at http://dx.doi.org/10.5676/EUM_SAF_CM/CLARA_AVHRR/V001). Albedo is processed by the data provider following atmospheric and surface corrections (see Section 6.3.2). The average June-August (Arctic summer) sea ice albedo is obtained by correcting the AVHRR surface albedo for sea ice concentration. The accuracy of the processed radiance data for snow and ice is estimated to be 15 W m^{-2} [Karlsson et al., 2012]. The standard errors of the mean annual Arctic surface albedo, for all years between 2003 and 2008, are <0.01.

Sea ice volume was obtained from the PIOMAS retrospective (hindcast) results [Zhang and Rothrock, 2003], assimilating sea ice concentration data [Lindsay and Zhang, 2006], (http://psc.apl.washington.edu/zhang/IDAO/data_piomas.html). An estimate for summer sea ice ablation was obtained by taking the difference between sea ice thickness in winter

(March; i.e. equivalent to the ICESat data) and the end of summer (September) (see Section 6.3.5).

Numerical simulations were used to examine the relationships between pre-melt sea ice surface roughness and melt season pond volume and areal coverage. The method for generating random rough surfaces with predetermined statistical parameters using spectral analysis, and for simulating melt pond distributions on these surfaces, is provided in Section 6.3.3. Field observations of level and deformed, first-year and multi-year sea ice surface roughness [Rivas et al., 2006; Liu et al., 2014; Beckers et al., 2015] were used to identify realistic upper and lower roughness limits for the surface simulations. Results from the melt pond simulations were used to develop an empirical relationship between the sea ice surface roughness, pond fraction and volume of meltwater per unit area at the ice surface, through least-squares curve fitting (see Section 6.3.4).

Field observations were obtained from four field sites in the Canadian High Arctic to validate the empirical model. Three-dimensional models of the pre-melt surface topography of landfast first-year sea ice were collected at each site using a *Leica Scanstation C10* terrestrial LiDAR system [Landy et al., 2014]. After post-processing, each LiDAR model was resampled to a regular 5 cm grid, detrended, and used to calculate surface roughness parameters, following Landy et al. [2015a]. Further LiDAR scans were collected at each site for several weeks following melt onset, in addition to direct measurements of melt pond volume at transects along the edges of each site. These observations provided us with coincident estimates of mean pond depth, pond fraction and the volume of meltwater per unit area at the ice surface, which could be used to validate the empirical model.

Predictions for the Arctic summer surface albedo were calculated from March ICESat RMS roughness observations. Based on the field data, we made a simple assumption that the volume per unit area of meltwater pooling at the sea ice surface, at all locations and over a long time period (June-August), could be estimated by integrating the volume between 20 and 40 mm. The ICESat observations were then used to determine the fraction of the sea ice surface over which this volume of meltwater pooled, i.e. an estimate for average long-term pond fraction, using the empirical model. Sea ice albedo was calculated from average end-member albedos for snow/bare white ice and melt pond, as described in the main text, weighted by the pond fraction. It is important to note that ICESat observations could be used to predict the *sea ice* albedo, rather than a general *surface* albedo (i.e. ice plus open water), which could only be estimated by weighting the predicted sea ice albedo with ice concentration observations (see Section 6.3.6). Predicted albedos were resampled to AVHRR locations using nearest neighbor interpolation for comparison. No spatial filtering or smoothing was used prior to making these comparisons.

6.3. Supplementary Information

6.3.1. ICESat observations of sea ice surface roughness

Arctic-wide, long-term estimates of sea ice surface roughness were obtained from the Ice, Cloud and land Elevation Satellite (ICESat). The latest version of the data available at the time of analysis was Version 34 of the Level 2 GLA05 & GLA13 products, available from the National Snow and Ice Data Center (NSIDC) at http://nsidc.org/data/icesat/. In our analysis, we only used the altimeter data collected during March, to maintain accurate comparisons of pre-melt sea ice surface roughness between years. The precision of the raw altimeter measurements is estimated to be 2 cm [Kwok et al., 2006].

Valid elevation samples were obtained by filtering the raw data based on the laser return reflectivity, number of waveform peaks, and detector gain [Kwok et al., 2007; Farrell et al., 2009; Renganathan, 2010]. The data were corrected for geoid undulations, tides and dynamic topography of the ocean [Kwok et al., 2007], in addition to the inverted barometer effects [Farrell et al., 2009]. Finally, the data were filtered within the area defined by sea ice concentration >0.9 (using AMSR-E data, enhanced NASA Team algorithm, available at http://nsidc.org/data/AE_SI25) [Cavalieri et al., 2014]. It has been shown that, despite removing the best static geoid, modeled tides, and the effects on the ocean of atmospheric loading, in the worst case, the variation of the sea surface height can still remain >50% higher than the variation of the sea ice freeboard [Kwok et al., 2006]. Thus, the linear trend was removed from 10-km profiles along individual ICESat tracks to account for low-frequency variability caused by errors in the estimation of the sea surface height, following Kwok et al. [2007].

Surface roughness was obtained from the root mean square (RMS) height of detrended 10-km ICESat profiles. The 10-km window was large enough to include a sufficient number of samples (characteristically ~60) for estimating the roughness, but was still close to the length-scale of the simulated melt pond distributions (2 km), so that results from the empirical model are relevant at the scale of the ICESat data. The lowest estimated roughness (approximately 2-3 cm) is above the reported precision of the altimeter. The standard error of the minimum observed roughness (~2 cm) is 0.3 cm and the standard error of the maximum observed roughness (~40 cm) is 5.2 cm. The standard error of the mean annual Arctic-wide roughness, for all years between 2003 and 2008, is <1 mm. The correlation coefficient of the 2003-2008 trend in Arctic-wide sea ice surface roughness is 0.75 (p = 0.052).

Maps of the March Arctic sea ice surface roughness in 2005-2008 (Fig. 6.4) illustrate that roughness can vary considerably within FYI or MYI zones, which suggests that the sea ice albedo in summer cannot be accurately estimated solely from the ice age, as attempted in several studies [Perovich and Polashenski, 2012; Nicolaus et al., 2012; Arndt and Nicolaus, 2014]. Despite this, the mean March roughness was 7 cm (44%) lower in the FYI zone compared to the MYI zone, over the entire ICESat dataset.

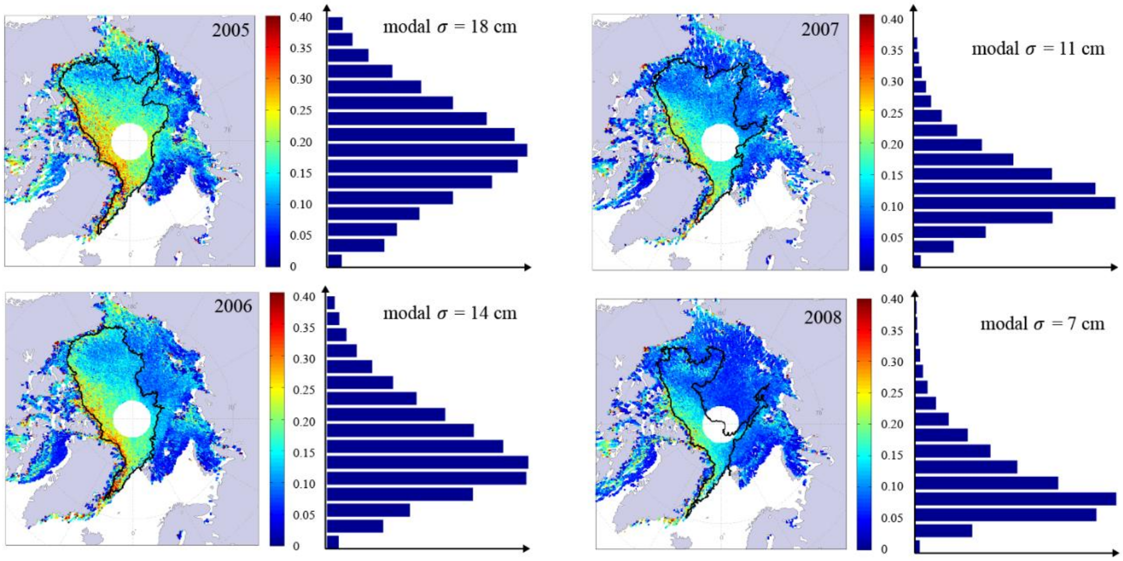

Figure 6.4 | Sea ice surface roughness in 2005-2008. Maps of the sea ice roughness in March are calculated from the RMS height of ICESat observations within a 10-km moving window. The MYI edge in March is superimposed onto each map as a solid black line. Normalized probability distributions of the ICESat surface roughness are provided alongside each map.

6.3.2. AVHRR observations of surface albedo

Arctic Ocean surface albedo observations were obtained from the 25-km monthly Northern Polar Region black-sky broadband surface albedo product from the EUMETSAT Satellite Application Facility on Climate Monitoring (CM-SAF) Cloud, Albedo, Radiation dataset (CLARA-A1, http://dx.doi.org/10.5676/EUM_SAF_CM/CLARA_AVHRR/V001). Surface albedo is processed by the data provider from Advanced Very High Resolution Radiometer (AVHRR) Channels 1 (0.58-0.68 µm) and 2 (0.73-1 µm) [Karlsson et al., 2012]. Following atmospheric, radiometric and topographic corrections, the raw radiances are expanded into hemispherical spectral albedos using a kernel-model bi-directional reflectance distribution function (BRDF) algorithm [Wu et al., 1995]. Finally, shortwave broadband albedo is obtained from the spectral albedos using a narrow-to-broadband conversion. Average June to August (Arctic summer) sea ice albedo is obtained by correcting the AVHRR surface albedo for sea ice concentration (AMSR-E data, enhanced NASA Team algorithm). The accuracy of the processed radiance data for snow and ice is estimated to be 15 W m-2 [Karlsson et al., 2012]. The standard error of the mean annual Arctic surface albedo, for all years between 2003 and 2008, is <0.01. The correlation coefficient r of the 2003-2008 trend in surface albedo is 0.87 (p = 0.022).

Maps of the summer sea ice albedo in 2005-2008 illustrate that, similar to the pre-melt sea ice roughness, the albedo can vary considerably within FYI or MYI zones (as defined in March) (Fig. 6.5). Despite this, the mean summer sea ice albedo was 0.04 cm (8%) lower in the FYI zone compared to the MYI zone, between 2003 and 2008.

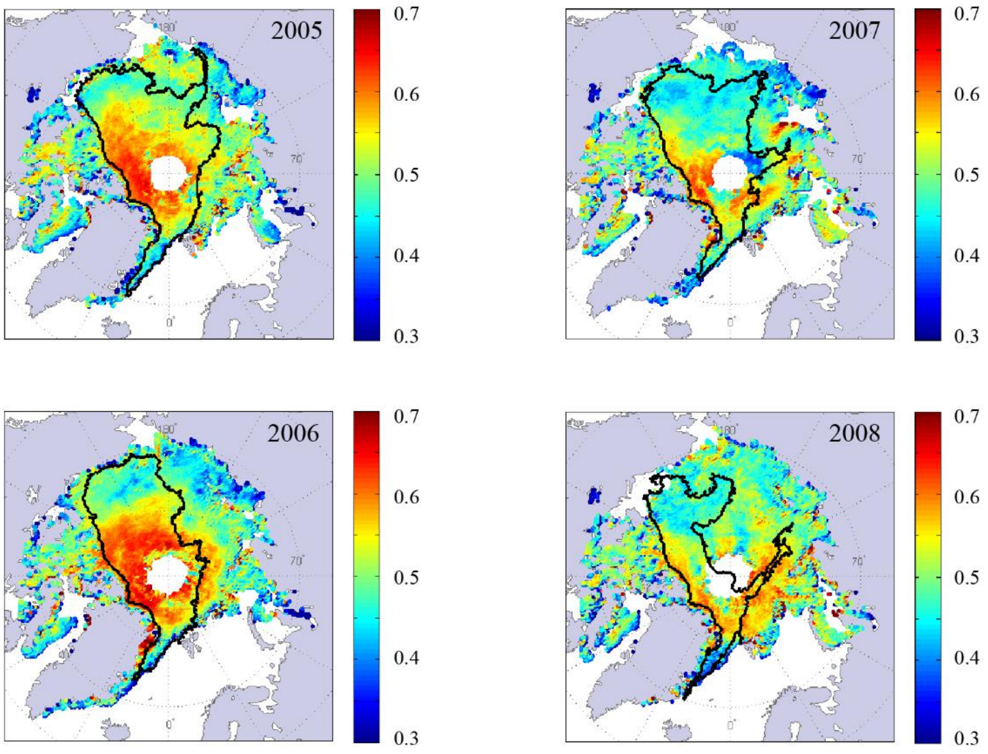

Figure 6.5 | Arctic summer (June-August) sea ice albedo in 2005-2008. Maps of the summer sea ice albedo are calculated by correcting 25-km CLARA-A1 AVHRR observations of Arctic Ocean surface albedo for sea ice concentration (using 25-km AMSR-E data). Only data within the area defined by average summer sea ice concentration >0.3 are included. The MYI edge in March is superimposed onto each map as a solid black line.

6.3.3. Melt pond simulations

Random rough surfaces, but with the predetermined statistical parameters: RMS height σ, correlation length l and autocorrelation function c, were simulated using spectral analysis [Landy et al., 2015b], to represent pre-melt sea ice surface topography. Field observations have demonstrated that the spectral behaviour of sea ice topography is best represented by a Lorentzian (exponential) power spectral density [Rivas et al., 2006] and that the correlation function of sea ice topography is characteristically strongly anisotropic [Iacozza and Barber, 1999]. Therefore, rough surfaces were generated by convolving an uncorrelated rough surface, with Gaussian height distribution and standard deviation σ, with a predetermined anisotropic exponential correlation function. It can be shown that the correlated and uncorrelated rough surfaces are linked in the Fourier domain by a simple universal relationship [Landy et al., 2015b].

The accuracy of a simulated surface depends on the size and resolution of the discretized grid. So the surface topography was generated on a 2000 x 2000 m grid, with an interval of 0.5 m, which produced errors of no more than 2% in the simulated roughness parameters and importantly, in a standard run, provided several tens of thousands of melt ponds for analysis.

Surface grids were generated for σ at 0.05 m intervals from 0.05-0.40 m and l at 1 m intervals from 1-10 m, following field observations of level and deformed, first-year and multi-year sea ice surface roughness [Rivas et al., 2006; Liu et al., 2014; Beckers et al., 2015]. Since the correlation function was anisotropic, directional correlation lengths were derived from l using the eccentricity parameter ε_l [Landy et al., 2015a]. If ε_l = 0, the surface topography is perfectly isotropic, whereas if ε_l = 0.99, the surface topography is strongly anisotropic. Melt pond distributions were created by iteratively raising the water level on a surface to a pre-determined volume. The volume per unit area of meltwater on the sea ice surface h_{net} was varied at 5 mm intervals from 5-200 mm. Thus, in total, 19,200 melt pond distributions were generated from 480 surface topography grids.

Here, we made the assumption that all melt ponds within a single grid had identical surface levels. This is valid when the pond network is well interconnected and/or ponds have drained to and are fixed at sea level [Eicken et al., 2002]. However, for a short period after melt onset, typically when f_p is low, isolated ponds can exist at a range of elevations in local topographic depressions at the ice surface, and the variance of pond surface height can be as high as 4-5 cm [Landy et al., 2014].

An example of this scenario is evident in our field observations. The three light blue observations in Fig. 6.2b were collected within 4 days of melt pond formation and are underestimated by the blue model curve. In this scenario, the original assumption does not hold: melt ponds are not restricted to the *absolute* lowest surface elevations, but rather exist in *local* topographic depressions and are poorly connected. However, field observations suggest that lateral and vertical drainage cause pond surfaces to level out relatively soon after initial formation, such that this situation can only be expected to be a potential issue for rougher ice surfaces within the first week of melt [Eicken et al., 2002].

6.3.4. Empirical model for melt pond coverage as a function of sea ice surface roughness

Results from the melt pond simulations were used to develop an empirical relationship between the sea ice surface roughness σ, pond fraction f_p and volume of meltwater per unit area at the ice surface h_{net}. The relationship between f_p and h_{net} could be modelled with a simple exponential function:

$$f_p = 1 - e^{-Rh_{net}}, \tag{6.1}$$

where R [m^{-1}] describes the attenuation of the melt pond growth rate as water is added to the sea ice surface. The limits of this relationship are fixed because f_p is always equal to zero when h_{net} is zero (no water on the surface) and f_p cannot exceed 1.

Figure 6.2b suggests that R changes as a function of σ, so we performed a least-squares fit on the model results to find:

$$R(\sigma) = R_0 e^{-\lambda\sigma} + \Gamma, \qquad (6.2)$$

where R_0 [m^{-1}] is the attenuation coefficient on absolutely level ice with σ = 0, λ [m^{-2}] is the decay constant, and Γ [m^{-1}] is the minimum possible attenuation. The coefficients R_0, λ and Γ, in addition to their ± 99% prediction intervals, are provided in Figure 6.6, and can be used in the empirical model to predict the value and precision of f_p for certain h_{net} and σ.

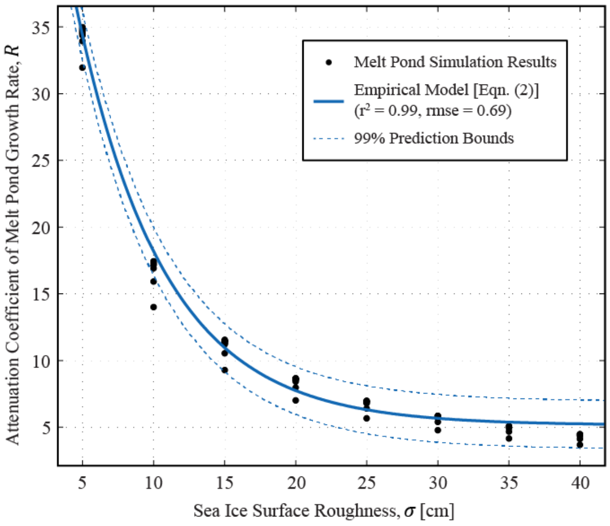

Coefficient	Mean	Prediction Intervals	
		-99%	+99%
R	65.43	64.02	66.84
λ	16.14	15.75	16.53
Γ	5.15	5.00	5.30

Figure 6.6 | Attenuation of the melt pond growth rate R as a function of the pre-melt sea ice surface roughness. The value of R for each black data point was obtained by calculating the relationship in equation (6.1) for a set of simulated melt pond distributions, i.e. the variation in f_p as a function of h_{net} for a specific σ. The empirical model in equation (6.2) is the least-squares fit on these data points, and is illustrated by the solid blue line (with 99% prediction bounds shown by the two dashed blue lines). Values for the empirical model coefficients are given in the table.

The correlation between f_p derived from the melt pond simulations and the predictions of equation (6.2) is r = 0.99 (p < 0.001). Thus, the empirical model closely describes the results of the melt pond simulations. The model can determine the areal fraction of the sea ice surface, with a certain pre-melt roughness, which is flooded by a certain volume of meltwater.

6.3.5. Model estimates of summer sea ice ablation

Sea ice volume was obtained from the Pan-Arctic Ice-Ocean Modeling and Assimilation System (PIOMAS) retrospective (hindcast) results (http://psc.apl.washington.edu/zhang/IDAO/data_piomas.html). PIOMAS consists of a multicategory thickness and enthalpy distribution sea ice model [Zhang and Rothrock, 2003] coupled with the Parallel Ocean Program (POP2) ocean model (http://www.cesm.ucar.edu/models/cesm1.0/pop2/). The model is initiated with NCEP/NCAR reanalysis atmospheric forcing data and assimilates passive microwave sea ice concentration data [Lindsay and Zhang, 2006]. PIOMAS ice thickness has been found to agree well with ICESat ice thickness observations (<0.1 m mean difference; r ~ 0.8 pattern correlation) [Schweiger et al., 2011].

An estimate for summer sea ice ablation was obtained by taking the difference between sea ice thickness in winter (March; i.e. equivalent to the ICESat data) and the end of summer (September). Maps of the modelled sea ice ablation in 2005-2008 are shown in Figure 6.7.

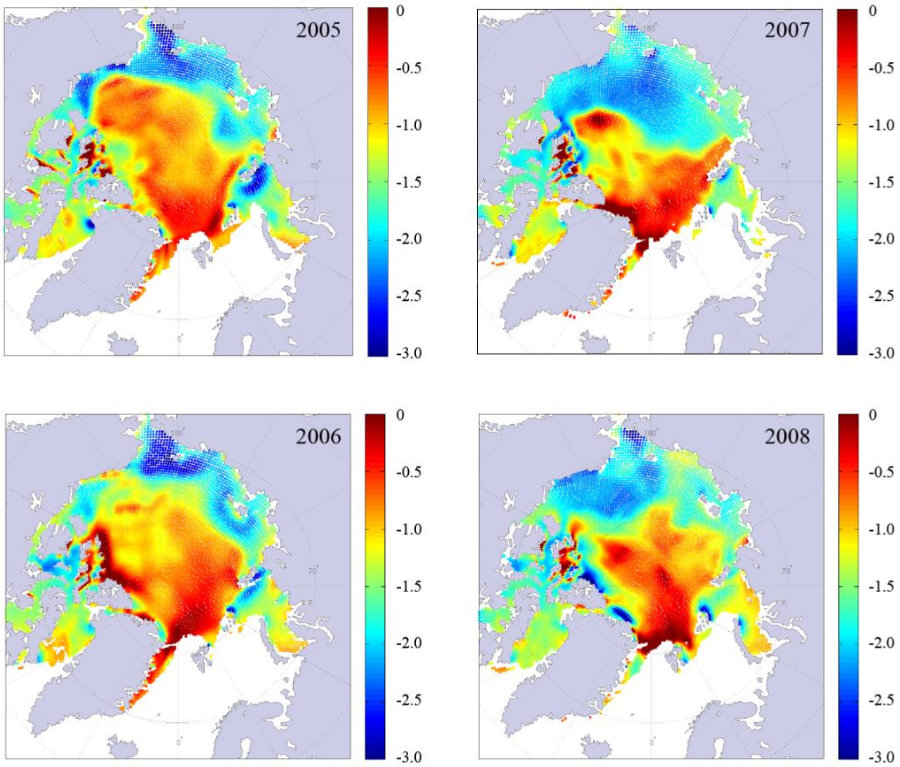

Figure 6.7 | Summer sea ice ablation in 2005-2008. Modelled change in sea ice thickness between March and September (i.e. ice ablation during summer), from PIOMAS.

6.3.6. Comparison of predicted and observed surface albedo

Predictions for the Arctic summer surface albedo, in 2005 and 2007 (Fig. 6.3a and b), were calculated from the ICESat RMS roughness observations in March each year. Based on the field observations in Fig. 6.2, we made a simple assumption that the volume per unit area of meltwater pooling at the sea ice surface, at all locations and over a long time period (June-August), could be estimated by integrating h_{net} between 20 and 40 mm. This, in itself, is an important finding with regards to understanding Arctic sea ice mass balance in summer. The ICESat observations were then used to determine the fraction of the sea ice surface over which this volume of meltwater pooled, i.e. an estimate for average long-term f_p, using the empirical model above.

Sea ice albedo was calculated from average end-member albedos for snow/bare white ice and melt pond, as described in the main text, weighted by f_p (Fig. 6.8a and b). Since the seasonal ice in many regions of the Arctic melts, breaks up and disappears completely before the end of August, sea ice concentration observations (AMSR-E; Fig. 6.8c and d) were used to convert the sea ice albedo to a general ‘surface’ albedo (i.e. including sea ice and open water) (Fig. 6.8e and f). It is important to note that ICESat observations could be used to predict the *sea ice* albedo, rather than the general *surface* albedo, which could only be estimated by weighting the predicted sea ice albedo with ice concentration observations.

The observed surface albedos presented in Fig. 6.1b, Fig. 6.3c and d, and Fig. 6.4, were calculated from the mean of June-August (i.e. Arctic summer) AVHRR CLARA-A1 albedos. Predicted albedos were resampled to AVHRR locations using nearest neighbor interpolation for the comparison in Fig. 6.3. No spatial filtering or smoothing was used prior to making these comparisons.

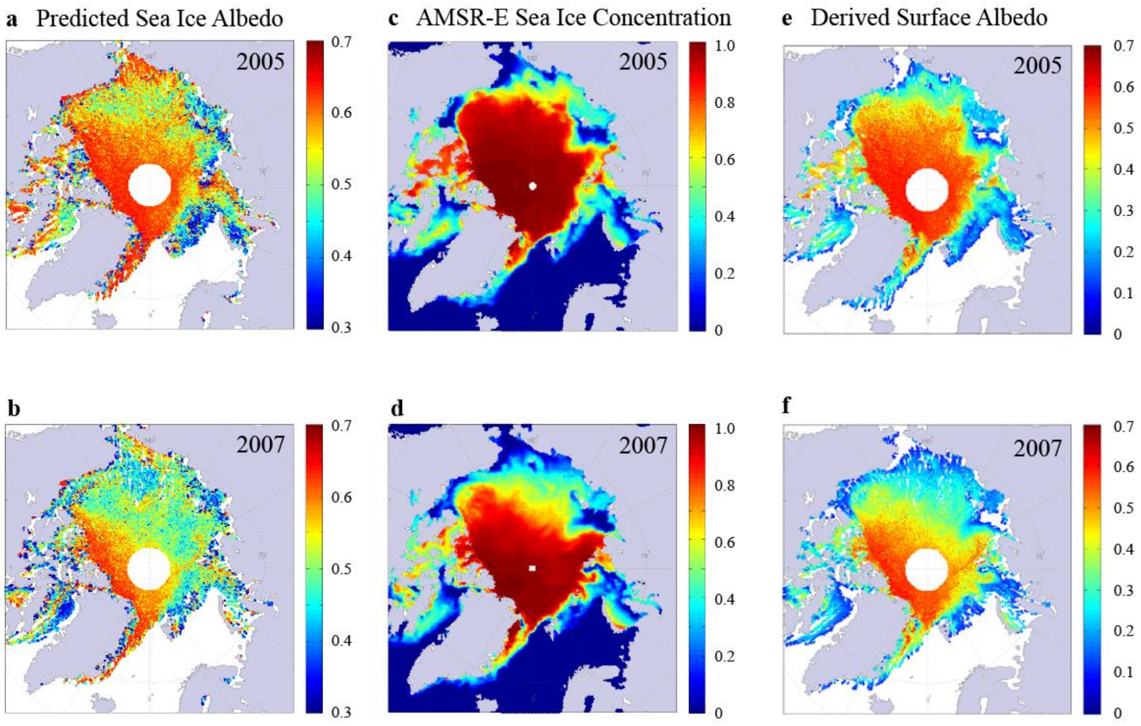

Figure 6.8 | Steps to derive predictions for the Arctic surface albedo in 2005 and 2007. Summer shortwave sea ice albedo (a) and (b) was predicted from f_p, estimated using the empirical model for the critical band of h_{net} from 20 to 40 mm, based on σ derived from ICESat observations in March, and using average end-member albedos for snow/bare ice and for melt ponds (as described in the main text). The sea ice albedo was then weighted by the mean June-August AMSR-E sea ice concentration (c) and (d) to obtain a general surface albedo (e) and (f).

6.3.7. Evaluation of the factors contributing to surface melt of Arctic sea ice during summer

Our results suggest that a reduction in pre-melt sea ice surface roughness can produce a significant decrease in summer sea ice albedo. However, trends towards earlier melt onset dates have also been observed [Markus et al., 2009; Stroeve et al., 2014] and, since peak melt pond coverage (the early flooding stage) typically occurs close to annual maximum solar irradiance [Perovich et al., 2011], the timing of melt onset may have a significant effect on solar heat input to the sea ice cover during summer [Stroeve et al., 2014]. Here, we conduct a simple sensitivity experiment to examine the relative contributions of each of these factors to the rate and amount of Arctic summer sea ice melt.

The weekly evolution of the mean Arctic sea ice albedo from May to August, for each year between 2003 and 2008, was obtained by correcting the CLARA-A1 AVHRR data for sea ice concentration (AMSR-E 25-km data). Estimates for the solar heat input to the sea ice cover, Q_S, over this spring-summer period, were calculated from: $Q_S = (1 - \alpha_{si})F_r\,\Delta t$, where F_r is the incident downwelling solar irradiance at the sea ice surface and Δt = one week, following the method of Perovich and Polashenski [2012]. Weekly downwelling solar irradiance at the sea ice surface was obtained from the NCEP/NCAR reanalysis data (Daily Downward Solar Radiation Flux, Reanalysis 1 Data, http://www.esrl.noaa.gov/psd/data/gridded/data.ncep.reanalysis.surfaceflux.html). Only data within the area defined by sea ice concentration >0.9 were used in the calculations. Examples of the seasonal evolutions of solar irradiance and sea ice albedo in 2003 are presented as black curves in Fig. 6.9a and b.

Variations in the albedo evolution owing to the date of melt onset were obtained by shifting the true albedo curve 2 and 7 days earlier (red curves in Fig. 6.9b). The value of -2 days was the observed change in melt onset date between 2003 and 2008, (from passive microwave observations, NSIDC MEaSUREs Arctic Sea Ice Characterization data, http://nsidc.org/data/NSIDC-0532). The extreme value of -7 days (one week) was approximately the range in melt onset date between 2003 and 2008 [Markus et al., 2009]. Reductions in RMS sea ice surface roughness σ of 1, 3.2 (the observed change from 2003-2008) and 5 cm from each year's mean roughness value, as observed by ICESat, were used to estimate associated mean increases in melt pond fraction, using the empirical model above, and thus decreases in sea ice albedo. New curves were obtained by scaling the true albedo curve for these calculated decreases (blue curves in Fig. 6.9b). A final curve was obtained by combining the -2 day observed shift in melt onset date with the observed -3.2 cm reduction in RMS sea ice surface roughness (green curve in Fig. 6.9b).

The total solar heat input to the sea ice cover in spring-summer 2003, for each of these scenarios, is shown in Fig. 6.9c. The percentage increase in cumulative heat input relative to the observed sea ice evolution (the standard case), for each scenario, is also given in Fig. 6.9d. Understandably, earlier melt onset dates (the red curves) result in enhanced heat input earlier in the melt season, with a peak relative increase in heating during June, which supports previous findings [Perovich et al., 2011]. However, in these scenarios the ice albedo remains similar to the standard case throughout the majority of the melt season (July and August). Increasingly smooth sea ice surface roughness also enhances heat input to the ice cover (the blue curves), but affects the ice albedo throughout the full duration of the melt season, so the integrated increase in solar heating is generally higher. The combined effect of satellite observed changes in melt onset timing and sea ice surface roughness on the ice albedo (the green curve), over the period 2003-2008, is to increase the heat input to the sea ice cover by 201 MJ m^{-2}. However, observed reductions in sea ice roughness are found to contribute approximately ten times more heat input to the ice cover than observed earlier melt onset dates (Fig. 6.9d). If we assume an ice density of 900 kg m^{-3} and latent heat of fusion of ice of 334 kJ kg^{-1}, the effect of reduced sea ice roughness is sufficient to potentially melt 55 cm more sea ice, on average, compared to the effect of earlier melt onset timing.

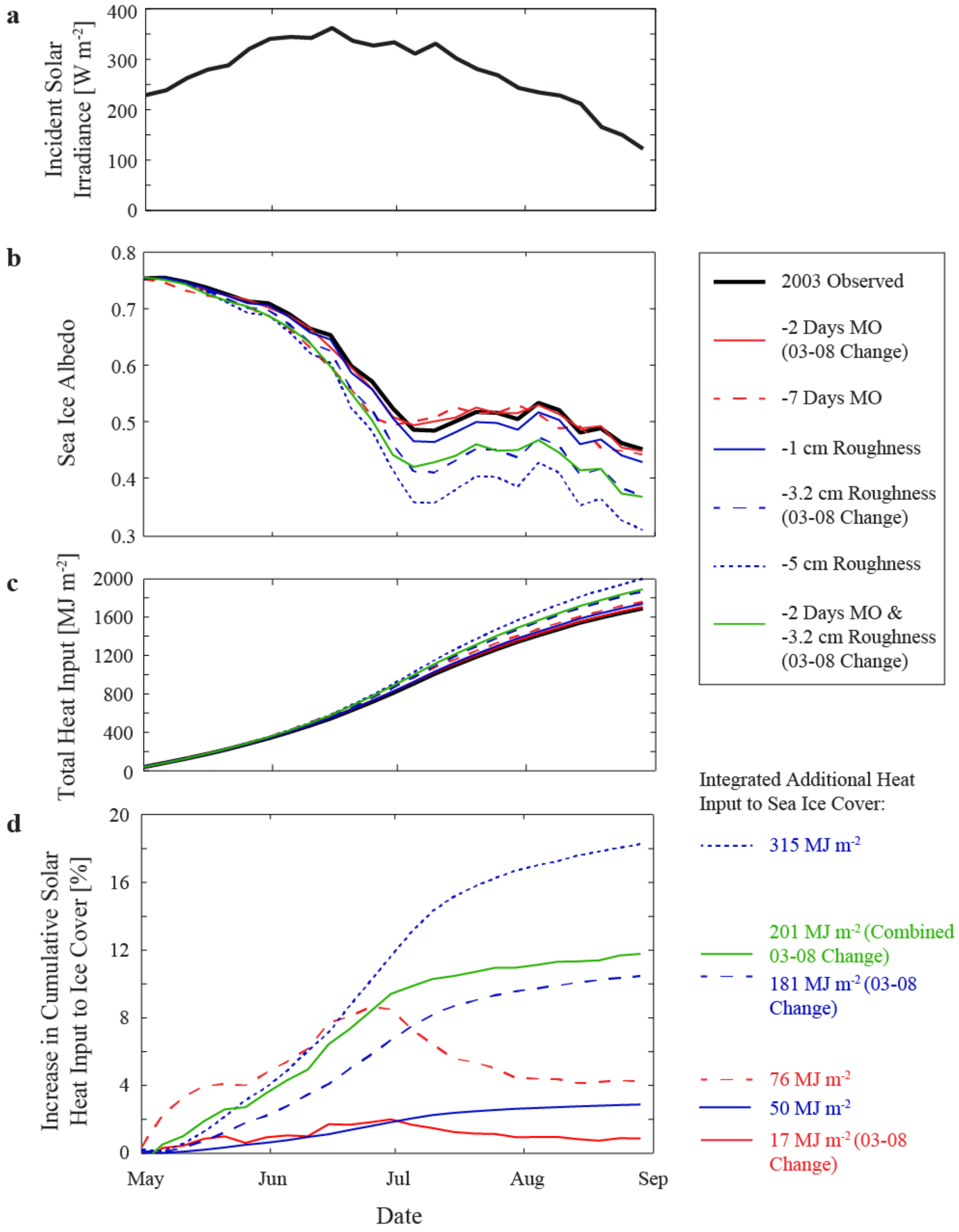

Figure 6.9 | Sensitivity of solar heat input to the Arctic sea ice cover to variations in the date of melt onset and the ice surface roughness. (a) Weekly average incident solar irradiance at the ice surface in 2003 (NCEP reanalysis data). (b) Observed Arctic sea ice albedo evolution in 2003, corrected for sea ice concentration (black line), and estimated changes in the albedo for varied melt onset dates (red lines), ice surface roughness (blue lines), and both (green line). Total solar heat input (c) and increase in cumulative heat input (d) to the sea ice cover, compared to the observed 2003 data, for each scenario.

Chapter 7. Summary and Conclusions

7.1. Summary of Major Contributions

Contribution 1: A new precise and accurate technique for parameterizing centimeter-scale sea ice surface roughness using terrestrial LiDAR

In Chapters 3 and 4 we presented new methods for parameterizing the two-dimensional surface roughness of sea ice from three-dimensional terrestrial LiDAR data. This included algorithms for: (1) preprocessing and resampling the raw data, (2) detrending the data to remove low frequency topography, (3) two-dimensional autocorrelation and curve fitting to characterize the surface rms height, correlation length and correlation function, and (4) calibrating the roughness parameters to correct for biases.

The two-dimensional approach was shown to be considerably more precise than the conventional one-dimensional profiling approach. Our technique is therefore able to characterize the roughness of a surface while satisfying an underlying assumption of stationarity, required by most microwave backscattering models. However, in spite of the precision of the technique, terrestrial LiDAR instruments are severely limited by their high inclination scanning angle with respect to nadir. So, in a particularly novel feature of this thesis, we developed and validated a numerical model to simulate the scanning process of a terrestrial LiDAR system. The model includes formulations for deriving: (1) the size and shape of the laser footprint on the surface, (2) ranging noise in the sensor, and (3) occlusion errors caused by surface self-shadowing from the sensor's perspective. Results from the model were used to calculate a unique set of calibration functions for correcting LiDAR roughness measurements for errors caused by both the known inclination angle of the sensor and the *a priori* unknown true roughness properties of the target surface.

LiDAR data can be collected over a surface, processed using the algorithms in Chapter 3 to calculate roughness parameters as ‘observed’ by the LiDAR sensor, then calibrated using the functions in Chapter 4 to calculate accurate roughness parameters. This novel technique has been applied to measure sea ice surface roughness in several studies. It has been used to develop a database of sea ice roughness statistics [Landy et al., 2015a] and to monitor the roughness of both young and mature sea ice in support of microwave remote sensing and modelling studies [Isleifson et al., 2014; Scharien et al., 2014; Firoozy et al., 2015]. Although these studies were applied to sea ice, the technique could also be used to measure the roughness of other natural surfaces, such as soil and rock.

Contribution 2: An improved understanding of the physical mechanisms controlling melt pond evolution on first-year sea ice

In Chapter 5 we identified four key physical mechanisms controlling interannual and local variations in melt pond coverage on level first-year sea ice. Although previous studies [e.g. Barber and Yackel, 1999; Eicken et al., 2002; 2004; Petrich et al., 2012; Polashenski et al., 2012] have contributed to our understanding of the mechanisms driving melt pond formation and evolution on sea ice, our study was the first to closely monitor variations in these mechanisms between two years and locations on relatively similar first-year sea ice.

(I) We found that a minor variation in the range of pre-melt topographic relief between years (0.5 m) caused melt ponds to spread or recede over an area that was almost

90% larger on the smoother ice compared to the rougher ice, as the meltwater balance varied. This has particularly significant implications for the sea ice albedo during the melt season, and prompted the study in Chapter 6.

(II) We discovered that large areas of the low-lying pre-melt sea ice surface could be unexpectedly and rapidly drained of meltwater if a macroscopic drainage flaw (melt hole) formed in the ice cover within around a hundred meters distance. It was previously expected that only higher pre-melt areas would drain as ponds recess in response to the formation of a flaw. This mechanism accounted for significant variations in pond coverage between our two study years.

(III) Another somewhat counterintuitive observation was that the timing of the sea ice cover permeability transition (i.e. the onset of percolation drainage), which controls late season pond coverage, was more than one week earlier during the year with thicker pre-melt ice thickness. We might expect the thicker ice to warm, and thus become permeable to fluid transport, less quickly. However, we found that the total energy available for internal heating of the ice cover was more than twice as high in the year with the earlier permeability transition. This allowed the central portion of the ice cover to warm to a sufficient temperature (> -0.5 °C) for the brine volume to increase past the threshold required for percolation (around 0.15-0.20). This threshold is higher than the threshold proposed by Golden et al. [1998] for the permeability transition in congelation sea ice (0.05). Our observations support the hypothesis that fresh melt pond water percolating into the coldest central portion of the ice cover refreezes, blocking pores and brine channels within the sea ice and delaying the onset of full percolation drainage [Polashenski et al., 2012].

(IV) Finally, we were able to estimate that surface melt accounted for approximately two thirds of the net radiative flux from the atmosphere to the sea ice during the melt season. The remaining energy contributed to internal heating of the ice cover and bottom melt (~25%) or was transmitted through the ice to the ocean and did not contribute to melting ice (~10%).

Our findings suggest that each of these mechanisms can affect significant variations in melt pond coverage, which helps to explain why satellite observations of melt pond coverage, timing of melt stages and sea ice albedo exhibit strong interannual and regional variability [Howell et al., 2006; Rösel and Kaleschke, 2012; Stroeve et al., 2014]. Based on the results of our study, future field and modelling efforts would provide most value by targeting the roles of the sea ice surface topography (partly accomplished in Chapter 6), meltwater drainage flaws, the timing of the ice cover permeability transition, and the surface energy balance, in driving melt pond evolution.

Contribution 3: Discovering a statistically significant relationship between the pre-melt roughness of Arctic sea ice surface topography and summer sea ice albedo

The results of Chapter 6 indicate that, of the four key mechanisms affecting variations in melt pond coverage on sea ice, the roughness of the ice surface topography is most influential. In Chapter 6 we discovered that observations of the pre-melt (winter) surface roughness of Arctic sea ice, from the ICESat laser altimeter, could explain 85% of the spatial variance in the summer sea ice albedo, as observed by the AVHRR spectral radiometer. Interannual variations in pre-melt sea ice roughness were also significantly correlated (r = 0.71) with observed variations in Arctic Ocean surface albedo during summer, over the short ICESat record (2003-2008). Thus, the albedo of Arctic sea ice in summer can be accurately predicted from the roughness of the sea ice topography several months previously, in winter – an original concept, which has not been suggested before. NASA intends to launch a new satellite LiDAR: ICESat-2, in 2017, and we will be potentially able to employ our technique to predict the Arctic sea ice albedo several months in advance, for each year of this mission.

To identify these linkages, at the outset, we developed an empirical model for predicting summer melt pond fraction (i.e. ice albedo) from pre-melt sea ice surface roughness, using melt pond distributions simulated on statistical topographies. A particularly novel and important aspect of this study was that we were able to validate the model using combined field observations of ice surface roughness and melt pond distributions, collected in the Arctic with a terrestrial LiDAR system. We could then estimate the melt pond fraction on sea ice during the Arctic summer by applying the model to satellite observations of winter sea ice roughness from ICESat.

The satellite observations demonstrated that an Arctic-wide reduction in sea ice roughness during the 2000s, centered on the year 2007, led to a drop in ice albedo that resulted in a 16% increase in solar heat input to the sea ice cover. This original finding points to a strong positive feedback mechanism between winter sea ice roughness and summer sea ice volume. Significant reductions in multi-year ice area in 2006, 2007 and 2008, following melt and ice export, caused the overall roughness of the winter Arctic sea ice cover to decrease. This led to an increase in summer melt pond fraction (a decline in ice albedo) on the smoother surface, concluding in enhanced rates of ice melt and loss of ice volume. Essentially, our results suggest that the ice-albedo feedback has been amplified as multi-year ice has been replaced by first-year ice in the Arctic Ocean, accelerating the rate of decline of the Arctic sea ice cover.

7.2. Limitations and Recommendations for Future Work

In this thesis we have provided new techniques for measuring and understanding sea ice surface topography, and the effect of the topography on dynamic and thermodynamic sea ice processes, using LiDAR. However, LiDAR technology, and the presented techniques for applying LiDAR data, are not without their limitations. Here we offer a series of recommendations for future research that are based on addressing these limitations and/or building on the major findings of this thesis.

Detecting and Monitoring Sea Ice Surface Roughness

1. We discussed in Chapters 3 and 4 that the laser pulse of a LiDAR instrument (particularly at the 532 nm [green] wavelength of the instrument used in this thesis) may penetrate slightly into snow or sea ice. Consequently, the backscattered pulse return would be a time-spread integral of surface and volume scattering contributions, potentially causing centimeter-scale surface roughness measurements to be overestimated. In our analysis, we made the fundamental assumption that the main source of the backscatter is from the surface of the ice, and justified this assumption using field observations of the polarization of visible light reflected from sea ice, obtained from the literature. However, a full-waveform resolving LiDAR system could be used to examine this phenomenon directly. A waveform resolving LiDAR can

digitize the shape and magnitude of the emitted and received laser pulses, and would therefore be able to observe the spreading of the tail of the pulse if strong volume scattering occurred. In spite of this, the range resolution of current waveform-resolving terrestrial LiDAR instruments may not yet be small enough to observe these millimeter-scale variations in the laser pulse shape. In this case, an optical radiative transfer model could be used to simulate theoretically how different types of snow and sea ice affect the scattering of a Gaussian laser pulse, at various wavelengths.

2. It is not only the micro-scale surface topography that affects microwave scattering from sea ice and the aerodynamic roughness of the ice cover. Larger (meso- and macro-scale) surface topography, if present, also strongly influences both processes. Although the technique presented in Chapters 3 and 4 can be used to parameterize surface roughness at a spatial frequency as high as 1000 m^{-1}, it is restricted by the spatial coverage of terrestrial LiDAR (up to a few hundred square meters). Airborne LiDAR could be used to detect and characterize sea ice surface roughness over a larger range of spatial frequencies, for instance between 0.01 and 100 m^{-1}, because it can provide much greater spatial coverage (up to tens of square kilometers). This has been attempted in a few studies [Rivas et al., 2006; Liu et al., 2014; Beckers et al., 2015]; however, only the study of Rivas et al. [2006] attempted to characterize the spatial covariance properties of the sea ice roughness. Satellite LiDAR, such as ICESat-2, which is currently scheduled for launch in 2017, may also be able to characterize limited statistical properties of the sea ice roughness using information derived from the laser return waveform [Kurtz et al., 2008]. Alternatively, ICESat-2 will utilize a novel photon-counting LiDAR system, operating at a high pulse-repetition frequency,

and it may be possible to extract roughness information from the distribution of photons reflected by the sea ice cover [Kowk et al., 2014].

3. An important potential application of airborne or satellite LiDAR is for characterizing sea ice surface roughness in satellite synthetic aperture radar (SAR) images. As the sea ice contained within the Arctic basin becomes increasingly seasonal, larger areas of open water will exist during summer, encouraging trans-Arctic shipping and oil and gas exploration. These infrastructure require near real-time monitoring of the thickness and movement of local sea ice floes. It is also important to detect particularly rough (i.e. heavily ridged) sea ice, which can damage infrastructure that is not ice-reinforced. SAR is already used to monitor sea ice motion; however, there is currently no convincing technique for accurately measuring properties of sea ice roughness in SAR images. A large volume of airborne LiDAR data has been collected during the NASA Operation Icebridge Campaign, which could be used to characterize the size, spacing and directional properties of pressure ridges in rough sea ice [Herzfeld et al., 2015]. These information could be compared with coincident and concurrent SAR scenes to develop empirical methods for detecting ridge properties from their backscattering characteristics [Shields et al., 2015]. Given that the dielectrics of the snow and sea ice cover strongly influence the backscatter, this would also require coincident data and/or parameterizations of the thermodynamic state of the sea ice cover.

Understanding Sea Ice Thermodynamics during the Arctic Melt Season

1. In Chapter 5 we observed how the formation of a macroscopic flaw (melt hole) in the ice cover could rapidly, and unexpectedly, drain large areas of ponded ice in nearby

locations. The obvious questions are: how do the locations and density of drainage features affect the surrounding distribution of melt ponds; does the affected area have a systematic size, shape and pattern; and does this phenomenon have a significant effect on regional-scale ice albedos? We hypothesize that the first question can be explained by one or a combination of two processes. (1) As meltwater drains from the sea ice surrounding a flaw, the ice cover rises to maintain isostatic equilibrium in response to the loss of weight, and flexes slightly over a length-scale of a few hundred meters. This process must occur during Stage II of melt pond evolution, before the ponds fall to sea level. (2) The loss of meltwater increases the ice albedo and, over a period of time (a few weeks), differential rates of melt between pond-covered and unponded areas raises the freeboard of the ice surrounding a flaw considerably relative to the overall freeboard of the ice cover. It will require field studies and possibly modelling of ice deformation/flexure to understand if either or both of these processes are significant. The second and third questions could be evaluated using aerial photographs of sea ice during the melt season. This would involve detecting drainage flaws and classifying the areas affected by the flaws using image analysis techniques, followed by statistical analysis of the geometric distributions of surrounding ponds. By comparing the statistical distributions of affected areas with those of the entire ice cover, one could identify whether the flaws have a significant effect on the ice albedo.

2. Building on the previous point, it is currently not well understood how drainage networks within melt ponds form and evolve. Furthermore, it is not known if flow within ponds significantly affects lateral and vertical rates of ice melt. Previous modelling studies have examined the partitioning of solar radiative energy between the

sea ice, melt pond and atmosphere, considering the effects of turbulent flow within ponds [Skyllingstad and Paulson, 2007]. However, field studies are required to examine the processes *in situ*. This could include studying local horizontal velocity fields in melt ponds, for instance by tracking objects as they move through the pond network in a time-series of aerial photographs, or by monitoring the spread of chemical tracers [e.g. Eicken et al., 2002]. At the same time, it would be valuable to simultaneously measure individual components of the energy and mass budget across the atmosphere-pond-ice interface, including the near-surface wind profile, pond surface energy balance, pond depth, pond current profile, pond base elevation, and pond and ice temperature profiles, over a period of time at a single location. This would require a suite of instruments, including micro-meteorological equipment, a high-resolution current profiler, thermocouple strings, and an echo sounder. With this dataset, one could simultaneously evaluate the influence of wind forcing and flow within ponds on local lateral and basal ice melt rates and on the formation of drainage channels within the pond network.

3. It has been shown that a transition occurs in the fractal geometry of the melt pond area-perimeter relationship as pond area exceeds a threshold between approximately 50 and 500 m^2 [Hohenegger et al., 2012]. Below this size, ponds are mostly isolated, whereas above this size ponds are mostly integrated within complex clusters or networks. This has important implications for understanding/modelling catchment hydrology and meltwater drainage rates within pond networks. In Chapter 6, we demonstrated that the pre-melt roughness of the sea ice surface topography regulates the melt pond fraction during summer. We might therefore expect the pre-melt topography to also affect the threshold melt pond area which causes a transition between isolated and integrated

ponds. The simple melt pond model introduced in Chapter 6 or, if necessary, a more complex time-dependent model which accounts for merging, splitting and flow between ponds, among other hydrological processes (which is currently being developed by the author), could be used to examine whether this is the case.

4. During fieldwork we observed that the properties of the sea ice under melt ponds could vary considerably between locations and years. The albedo at the base of a pond can range from 0.2 to 0.7 depending on the thickness of the underlying sea ice [Podgorny and Grenfell, 1996]. Our observations also suggest that the albedo at the base of a pond can increase significantly if a layer of superimposed ice is present between the pond and sea ice. In contrast, debris entrained within the ice cover [e.g. Polashenski et al., 2015] can reduce the albedo significantly. Existing techniques for retrieving melt pond fraction from optical satellite images [e.g. Tschudi et al., 2008; Rösel et al., 2012] typically use fixed *a priori* assumed spectral reflectance coefficients for pixel constituents, e.g. snow, bare white ice and melt pond. These techniques do not take into account variations in the reflectance of melt ponds, depending on, for instance, ice thickness. Field studies are required to examine how these physical factors affect the reflectance of melt ponds and, most importantly, whether they bias satellite estimates of melt pond fraction. A new technique for retrieving pond fraction from MERIS optical data, based on an analytical solution for the reflectance from melt pond-covered sea ice, which accounts for variations in the ice thickness directly, shows promise [Zege et al., 2015].

5. The major findings in Chapter 6 suggest that a relative increase in the areal fraction of first-year sea ice, compared to multi-year ice, within the Arctic basin should accelerate

the rate of decline of the ice cover. Since first-year ice is, on average, less rough than multi-year ice, a declining trend in the pre-melt roughness of Arctic sea ice should increase the melt pond fraction in summer, thus accelerating the rate of ice melt over time. This feedback mechanism may result in an earlier ice-free Arctic summer than previously predicted. To better understand whether this will indeed be the case, the physics of the relationship between pre-melt ice surface topography and summer pond coverage need to be incorporated into a global climate model (GCM). The sea ice surface topography is indirectly represented by the ice thickness distribution in each cell of a GCM. It may be possible to calculate the melt pond fraction (i.e. ice albedo) in the model directly from the empirical functions in Chapter 6, depending on the ice thickness distribution. Otherwise, a more sophisticated approach [e.g. Flocco et al., 2010] could be explored. The GCM could then be used to project future scenarios of the Arctic ice cover while examining the sensitivity of the ice volume to varying trends in the winter sea ice roughness.

Appendix A: Contributions of Collaborating Authors

Chapter 3

The idea for the study in this chapter was my own. I collected the LiDAR data during collaborative projects in the field and at the University of Manitoba SERF facility with Dustin Isleifson and Alexander Komarov. I developed the code for the processing algorithms to detrend surfaces and derive surface roughness parameters. The majority of the writing is my own and I created all of the figures. Dustin Isleifson provided discussion of the results and several detailed reviews of the manuscript. Alexander Komarov provided technical support and discussion of the implications of the results for microwave scattering from sea ice. David Barber provided logistical and financial support for the study, and reviewed the manuscript.

Chapter 4

The idea for the study in this chapter was my own. I designed the experimental rough surfaces, collected the LiDAR data, and developed the code for the numerical LiDAR model. Alexander Komarov developed the code for accurately simulating rough surfaces with exponential correlation function. I performed the genetic algorithm analysis for deriving surface roughness calibration functions. The majority of the writing is my own and I created all of the figures. Alexander Komarov provided discussion of the results and several detailed reviews of the manuscript. David Barber provided logistical and financial support for the study, and reviewed the manuscript.

Chapter 5

The idea for the study in this chapter was my own. I collected and processed all of the field data. Megan Shields assisted with the field data collection. The ideas for presenting the results and discussion were largely my own. The majority of the writing is my own and I created all of the figures. Jens Ehn provided ideas for presenting the results, discussion of the results and several detailed reviews of the manuscript. David Barber provided logistical and financial support for the study, and reviewed the manuscript.

Chapter 6

The idea for the study in this chapter was largely my own. Jens Ehn provided the idea for using satellite observations of sea ice albedo and model simulations of sea ice ablation. I developed the code for the numerical melt pond simulations and for processing the satellite observations. The majority of the writing is my own and I created all of the figures. Jens Ehn contributed significantly to all areas of the manuscript, including the abstract, results and discussion, and provided several detailed reviews. David Barber provided logistical and financial support for the study, and provided several reviews of the manuscript.

Appendix B: Additional Contributions to the Peer Reviewed Literature

In addition to the four papers which make up the body of this thesis, I also co-authored nine peer-reviewed journal papers while completing my Ph.D. thesis. My contributions to these papers are listed below.

Firoozy, N., Majobai, P., **Landy, J.**, and Barber, D. (2015), Landfast First-Year Snow-Covered Sea Ice Reconstruction via Electromagnetic Inversion. IEEE J. Select. Topics Appl. Earth Obs. Rem. Sens., In Review.

In this paper I processed and provided observations of sea ice surface roughness at multiple sampling frequencies, collected coincidentally to scatterometer measurements using a terrestrial LiDAR system. I provided a figure illustrating spatial variations of sea ice surface roughness within the scatterometer sampling area. I also wrote the methods section for the LiDAR observations and provided comments and suggestions on manuscript drafts prior to peer review.

Campbell, K., Rysgaard, S., **Landy, J.**, Delaforge, A., and Mundy, C.J. (2015), Evaluation of snow-depth dependent ice algal production using O2 optode and 14C incubation methods. Marine Ecology Progress Series, In Review.

In this paper I developed code for deriving photosynthesis-irradiance curves from sea ice algae incubation data. I also developed code for analyzing the optimal time for an incubation setup and provided a figure illustrating how the incubation time depends on ice algae biomass. I was also heavily involved with editing manuscript drafts prior to and during peer-review, including providing ideas for statistical and technical analysis of the data.

Firoozy, N., Komarov, A.S., Mojabi, P., Barber, D.G., **Landy, J.**, and Scharien, R. (2015), Retrieval of Young Snow-Covered Sea Ice Temperature and Salinity Evolution through Radar Cross Section Inversion, IEEE J. Oceanic Eng., In Press.

In this paper I processed and provided observations of sea ice surface roughness, collected coincidentally to scatterometer measurements using a terrestrial LiDAR system. I provided a figure illustrating the sea ice surface roughness within the scatterometer footprint. I also wrote the methods section for the LiDAR observations and provided comments and suggestions on manuscript drafts prior to peer review.

Komarov, A.S., **Landy, J.C.** and Barber, D.G. (2015), Simulation of Random Rough Surfaces with Predetermined Statistical Properties, IEEE Geosci. Rem. Sens. Lett., In Prep.

I helped the lead author to develop the theme and concept of this letter, and provided ideas for demonstrating the developed technique. I was also heavily involved with editing manuscript drafts prior to peer-review.

Firoozy, N., Komarov, A.S., **Landy, J.**, Barber, D.G., Mojabi, P., and Scharien, R. (2014), Inversion-based sensitivity analysis of snow-covered sea ice electromagnetic profiles, IEEE J. Select. Topics Appl. Earth Obs. Rem. Sens., 8(7), 3643-3655, doi: 10.1109/JSTARS.2015.2399651.

In this paper I processed and provided observations of sea ice surface roughness, collected coincidentally to scatterometer measurements using a terrestrial LiDAR system. I provided a figure illustrating the sea ice surface morphology collected with the LiDAR system. I also wrote the methods section for the LiDAR observations and provided comments and suggestions on manuscript drafts prior to peer review.

Geilfus, N. X., Galley, R. J., Crabeck, O., Papakyriakou, T., **Landy, J.C.**, Tison, J. L., and Rysgaard, S. (2014), Inorganic carbon dynamics of melt pond-covered first year sea ice in the Canadian Arctic, Biogeosciences, 12, 2047-2061, doi: 10.5194/bg-12-2047-2015.

In this paper I provided observations of melt pond coverage at the field site, obtained from terrestrial LiDAR data collected on-site and from aerial photographs, and summarized these observations in a figure. I also provided significant edits on manuscript drafts prior to peer-review and helped to develop the title.

Scharien, R. K., Hochheim, K., **Landy, J.C.**, and Barber, D. G. (2014), First-year sea ice melt pond fraction estimation from dual-polarisation C-band SAR – Part 2: Scaling in situ to Radarsat-2, The Cryosphere, 8, doi:10.5194/tc-8-2163-2014.

In this paper I worked with the lead author to develop a method for classifying melt pond fraction in aerial photographs of sea ice. I also provided comments and suggestions on manuscript drafts prior to peer-review.

Scharien, R.K., **Landy, J.C.**, Barber, D.G. (2014), First-year sea ice melt pond fraction estimation from dual-polarisation C-band SAR – Part 1: In situ observations, The Cryosphere, 8, doi:10.5194/tc-8-2147-2014.

In this paper I processed and provided observations of sea ice surface roughness, collected coincidentally to scatterometer measurements using a terrestrial LiDAR system. I developed and provided code for processing melt pond surface roughness data. I also wrote the methods section for the LiDAR observations and was heavily involved with editing manuscript drafts prior to and during peer-review.

Isleifson, D. Galley, R.J., Barber, D.G., **Landy, J.C.**, Komarov, A.S, Shafai, L. (2014). A Study on the C-band Polarimetric Scattering and Physical Characteristics of Frost Flowers on Experimental Sea Ice, IEEE Trans. Geosci. Rem. Sens., 52(3), doi: 10.1109/TGRS.2013.2255060.

In this paper I processed and provided observations of frost flower surface roughness, collected coincidentally to scatterometer measurements using a terrestrial LiDAR system. I provided two figures illustrating the LiDAR data and roughness parameters. I also wrote the methods section for the LiDAR observations and provided comments on manuscript drafts prior to and following peer-review.

References

Andreas, E. L. (1987). A theory for the scalar roughness and the scalar transfer coefficients over snow and sea ice, *Bound.-Layer Meteor.*, 38(1-2), 159-184.

Armstrong, R.L. (1980). An analysis of compressive strain in adjacent temperature-gradient and equi-temperature layers in a natural snow cover, *J. Glaciol.*, 26(94), 283-289.

Assur, A. (1958). Composition of sea ice and its tensile strength, Arctic Sea Ice. U.S. National Academy of Sciences-National Research Council, Pub. 598, 106-138.

Axelsson, P. (2000). DEM generation from laser scanner data using adaptive TIN models, *Int. Arch. Photogramm. Rem. Sens.*, 33(B4/1), 111-118.

Bae, K. H., and D. D. Lichti (2008). A method for automated registration of unorganised point clouds, *J. Photogramm. Rem. Sens.*, 63(1), 36-54.

Baltsavias, E. P. (1999). Airborne laser scanning: basic relations and formulas, *J. Photogramm. Rem. Sens.*, 54(2), 199-214.

Banke, E. G., S. D. Smith, and J. Anderson (1980). Drag coefficients at AIDJEX from sonic anemometer measurements. In: *Sea ice processes and models*, R.S. Pritchard (Ed.), Seattle: Univ. Washington Press, 430-442.

Barber, D. G. (2005). Microwave remote sensing, sea ice and Arctic climate. *Phys. Can.*, 61, 105-111.

Barber, D. G., and J. Yackel (1999). The physical radiative and microwave scattering characteristics of melt ponds on Arctic landfast sea ice. *Int. J. Remote Sens.*, 20(10), 2069–2090.

Barber, D. G., J. Ehn, M. Pućko, S. Rysgaard, J. Deming, J. Bowman, and D. Soegaard (2014). Frost flowers on young Arctic sea ice: The climatic, chemical and microbial significance of an emerging ice type. *J. Geophys. Res.*, 119(20), 11593-11612.

Barry, R. G. (1983). Arctic Ocean ice and climate: Perspectives on a century of polar research. *Ann. Assoc. Am. Geogr.*, 73(4), 485–501.

Beaven, S. G., S. P. Gogineni, A. Gow A. Lohanick, and K. Jezek (1993). Radar Backscatter Measurements from Simulated Sea Ice During CRRELEX'90. RSL Technical Report 8243-2.

Beckers, J. F., A. H. H. Renner, G. Spreen, S. Gerland, and C. Haas (2015). Sea-ice surface roughness estimates from airborne laser scanner and laser altimeter observations in Fram Strait and north of Svalbard. *Ann. Glaciol.*, 56, 235.

Beraldin, J.-A., F. Blais, and U. Lohr (2010). Laser Scanning Technology. In: *Airborne and Terrestrial Laser Scanning*, G. Vosselmann and H.-G. Maas (Eds.), 1-42, Ch. 1, Dunbeath, UK: Whittles.

Blackford, J. R. (2007). Sintering and microstructure of ice: a review. *J. Phys. D: App. Phys.*, 40(21), 355.

Boé, J., A. Hall, X. Qu (2009). September sea-ice cover in the Arctic Ocean projected to vanish by 2100. *Nature Geosci.,* 2, 341-343.

Bryant, R., M. Moran, D. Thoma, C. Holifield Collins, S. Skirvin, M. Rahman, K. Slocum, P. Starks, D. Bosch, and M. González Dugo (2007). Measuring surface roughness height to parameterize radar backscatter models for retrieval of surface soil moisture. *IEEE Geosci. Rem. Sens. Lett.,* 4(1), 137-141.

Callens, M., N. E. Verhoest, and M. W. Davidson (2006). Parameterization of tillage-induced single-scale soil roughness from 4-m profiles, *IEEE Geosci. Rem. Sens.,* 44(4), 878-888.

Carnat, G., T. Papakyriakou, N. X. Geilfus, F. Brabant, B. Delille, M. Vancoppenolle, G. Gilson, J. Zhou, and J.L. Tison (2013). Investigations on physical and textural properties of Arctic first-year sea ice in the Amundsen Gulf, Canada, November 2007–June 2008 (IPY-CFL system study). *J. Glaciol.*, 59(217), 819-837.

Cavalieri, D. J., T. Markus, and J. C. Comiso (2014). AMSR-E/Aqua Daily L3 25 km Brightness Temperature & Sea Ice Concentration Polar Grids. Version 3. Boulder, Colorado USA: NASA National Snow and Ice Data Center Distributed Active Archive Center.

Clegg, J., J. F. Dawson, S. J. Porter, and M. H. Barley (2005). The use of a genetic algorithm to optimize the functional form of a multi-dimensional polynomial fit to experimental data. IEEE Congress on Evolutionary Computation, 1. Edinburgh, Scotland.

Colbeck, S. C. (1982). An overview of seasonal snow metamorphism. *Rev. Geophys. Space Phys.*, 20(1), 45-61.

Colbeck, S. C. (1986). Classification of seasonal snow cover crystals. *Wat. Resour. Res.*, 22(9), 59-70.

Colbeck, S. C. (1991). The layered character of snow covers. *Rev. Geophys., 29*(1), 81-96.

Colbeck, S. C. (1993). The vapor diffusion coefficient for snow. *Water Resour. Res.*, 29(1), 109-115.

Cole, D.M. and L.H. Shapiro (1998). Observations of brine drainage networks and microstructure of first-year sea ice. *J. Geophys. Res.,* 103(C10), 21739-21750.

Comiso, J.C. (2010). Variability and Trends of the Global Sea Ice Cover. In: *Sea Ice: An Introduction to its Physics, Chemistry, Biology and Geology*, D.N. Thomas and G.S. Dieckmann (Eds.), Oxford, UK: Blackwell Science Ltd., 205-246.

Comiso, J. C. (2012). Large Decadal Decline of the Arctic Multiyear Ice Cover. *J. Climate*, 25, 1176-1193.

Comiso, J. C., and D. K. Hall (2014). Climate trends in the Arctic as observed from space. *WIREs Clim. Change 2014,* 5.3, 389–409.

Coon, M.D. (1974). Mechanical behaviour of compacted Arctic ice floes. *J. Petro. Tech.*, *257*, 466-479.

Cox, G. F. N., and W. F. Weeks (1983). Equations for determining the gas and brine volumes in sea-ice samples. *J. Glaciol., 29*, 306–316.

Curry, J. A., J. L. Schramm, and E. E. Ebert (1995). Sea ice-albedo climate feedback mechanism. *J. Clim.,* 8, 240-247.

Curry, J. A., J. L. Schramm, D. K. Perovich, and J. O. Pinto (2001). Applications of SHEBA/FIRE data to evaluation of snow/ice albedo parameterizations. *J. Geophys. Res.,* 106(D14), 15345-15355.

Denoth, A. (1982). The pendular-funicular liquid transition and snow metamorphism. *J. Glaciol*., 28(99), 357-364.

Derksen, C., J. Piwowar, and E. LeDrew (1997). Sea-ice melt-pond fraction as determined from low level aerial photographs. *Arct. Alp. Res.,* 29(3), 345–351.

Doble, M. J., H. Skourup, P. Wadhams, and C. A. Geiger (2011). The relation between Arctic sea ice surface elevation and draft: A case study using coincident AUV sonar and airborne scanning laser. *J. Geophys. Res.,* 116, C00E03.

Domine, F., M. Albert, T. Huthwelker, H. W. Jacobi, A. A. Kokhanovsky, M. Lehning, G. Picard, and W. R. Simpson (2008). Snow physics as relevant to snow photochemistry. *Atmos. Chem. Phys.*, 8(2), 171-208.

Douglas, T. A., et al. (2012). Frost flowers growing in the Arctic ocean-atmosphere–sea ice–snow interface: 1. Chemical composition. *J. Geophys. Res.,* 117, D00R09.

Doumani, G. A. (1966). Surface structures in snow. In: *Physics of snow and ice 1*, H. Oura (Ed.), 1119-1136, Inst. Low Temp. Sci., Hokkaido, Japan.

Drinkwater, M. R. (1989). LIMEX'87 ice surface characteristics: implications for C-band SAR backscatter signatures. *IEEE Geosci. Rem. Sens.,* 27(5), 501-513.

Ehn, J. K., T. N. Papakyriakou, and D. G. Barber (2008). Inference of optical properties from radiation profiles within melting landfast sea ice. *J. Geophys. Res.*, 113, C09024.

Ehn, J. K., C. J. Mundy, D. G. Barber, H. Hop, A. Rossnagel, and J. Stewart (2011). Impact of horizontal spreading on light propagation in melt pond covered seasonal sea ice in the Canadian Arctic. *J. Geophys. Res.,* 116, C00G02.

Eicken, H., and M. Salganek (Eds.) (2010). Field Techniques for Sea-Ice Research. University of Alaska Press.

Eicken, H., M. Lensu, M. Leppäranta, W. B. Tucker III, A. J. Gow, and O. Salmela (1995). Thickness, structure, and properties of level summer multiyear ice in the Eurasian sector of the Arctic Ocean. *J. Geophys. Res.,* 100(C11), 22697–22710.

Eiken, H., C. Bock, R. Wittig, H. Miller and H.-O. Poertner (2000). Nuclear magnetic resonance imaging of sea ice pore fluids: methods and thermal evolution of pore microstructure. *Cold Reg. Sci. Tech.,* 31, 207-225.

Eicken, H., W. B. Tucker III, and D. K. Perovich (2001). Indirect measurements of the mass balance of summer Arctic sea ice with an electromagnetic induction technique. *Ann. Glaciol.,* 33, 194–200.

Eicken, H., H. R. Krouse, D. Kadko, and D. K. Perovich (2002). Tracer studies of pathways and rates of meltwater transport through Arctic summer sea ice, *J. Geophys. Res.,* 107(C10), 8046.

Eicken, H., T. C. Grenfell, D. K. Perovich, J. A. Richter-Menge, and K. Frey (2004). Hydraulic controls of summer Arctic pack ice albedo. *J. Geophys. Res.,* 109, C08007.

Else, B. G. T., T. N. Papakyriakou, R. Raddatz, R. J. Galley, C. J. Mundy, D. G. Barber, K. Swystun, and S. Rysgaard (2014). Surface energy budget of landfast sea ice during the transitions from winter to snowmelt and melt pond onset: The importance of net longwave radiation and cyclone forcings. *J. Geophys. Res.*, 119.

Farrell, S. L., S. W. Laxon, D. C. McAdoo, D. Yi, and H. J. Zwally (2009). Five years of Arctic sea ice freeboard measurements from the Ice, Cloud and land Elevation Satellite. *J. Geophys. Res.*, 114, C04008.

Farmer, L., Drinkwater, M., Lukowski, T., Arsenault, L., Livingstone, C., Kovacs, Shapiro, L. (1991). Beaufort Sea Ice - 1. Hanover, New Hampshire: Naval Oceanographic and Atmospheric Research Laboratory.

Feltham, D. L. (2008). Sea ice rheology. *Annu. Rev. Fluid Mech., 40*, 91-112.

Fetterer, F., and N. Untersteiner (1998). Observations of melt ponds on Arctic sea ice. *J. Geophys. Res.,* 103(C11), 24821–24835.

Firoozy, N., A. S. Komarov, J. C. Landy, D. G. Barber, P. Mojabi, and R. Scharien (2015). Inversion-Based Sensitivity Analysis of Snow-Covered Sea Ice Electromagnetic Profiles. *IEEE J. Sel. Top. Appl. Earth Obs. Rem. Sens.*, In Press.

Flocco, D., D. L. Feltham, and A. K. Turner (2010). Incorporation of a physically based melt pond scheme into the sea ice component of a climate model. *J. Geophys. Res., 115*, C08012.

Flocco, D., D. Schroeder, D. L. Feltham, and E. C. Hunke (2012). Impact of melt ponds on Arctic sea ice simulations from 1990 to 2007. *J. Geophys. Res., 117*, C09032.

Freitag, J. (1999), The hydraulic properties of Arctic sea-ice – Implications for the small scale particle transport *Ber. Polarforsch. /Rep. Pol. Res.* 325. In German.

Freitag, J., and H. Eicken (2003). Meltwater circulation and permeability of Arctic summer sea ice derived from hydrological field experiments. *J. Glaciol.*, 49, 349-358.

Fung, A. K. (1994). *Microwave Scattering and Emission Models and Their Applications*. Artech House, Inc.

Fung, A. K., and K.S. Chen (2010), *Microwave scattering and emission models for users*. Norwood, MA, USA: Artech House.

Garcia, N., and E. Stoll (1984). Monte Carlo Calculation for Electromagnetic-Wave Scattering from Random Rough Surfaces. *Phys. Rev. Lett.*, 52(20), 1798-1801.

Geldsetzer, T. and J.J. Yackel (2009). Sea ice type and open water discrimination using dual co-polarized C-band SAR. *Can. J. Rem. Sens.,* 35(1), 73-84.

Golden, K. M. (2001). Brine percolation and the transport properties of sea ice. *Ann. Glaciol., 33*, 28–36.

Golden, K. M., S. F. Ackley, and V. I. Lytle (1998). The percolation phase transition in sea ice. *Science, 282*, 2238–2241.

Golden, K., H. Eicken, A. Heaton, J. Miner, D. Pringle, and J. Zhu (2007). Thermal evolution of permeability and microstructure in sea ice. *Geophys. Res. Lett.*, 34(16), L16501.

Granskog, M. A., T. Vihma, R. Pirazzini, and B. Cheng (2006). Superimposed ice formation and surface energy fluxes on sea ice during the spring melt–freeze period in the Baltic Sea. *J. Glaciol.,* 52(176), 119–127.

Grenfell, T.C. and D.K. Perovich (1984). Spectral albedos of sea ice and incident solar irradiance in the southern Beaufort Sea. *J. Geophys. Res.*, 89, 3573–3580.

Guest, P. S., and K.L. Davidson (1991). The aerodynamic roughness of different types of sea ice. *J. Geophys. Res.*, 96(C3), 4709-4721.

Gupta, M., D. Barber, R. Scharien, and D. Isleifson (2012). Detection and classification of surface roughness in an Arctic marginal sea ice zone. *Hydrol. Process.,* 28(3), 599-609.

Gutierrez, P.-C., J. Martinez-Fernandez, N. Sanchez, and J. Álvarez-Mozos (2007). Modeling of soil roughness using terrestrial laser scanner for soil moisture retrieval. Proceedings IGARSS July 2007, Barcelona, Spain, 1877-1880.

Haas, C. (2010). Dynamics versus thermodynamics: The sea ice thickness distribution. In Thomas, D.N. and G.S. Dieckmann (eds.), *Sea ice: An introduction to its physics, chemistry, biology and geology,* Ch. 4, 82-111, Blackwell Science, Oxford.

Haas, C., S. Hendricks, H. Eicken, and A. Herber (2010). Synoptic airborne thickness surveys reveal state of Arctic sea ice cover. *Geophys. Res. Lett.,* 37, L09501.

Hallikainen, M., and D.P. Winebrenner (1992). The Physical Basis for Sea Ice Remote Sensing. In: *Microwave Remote sensing of Sea Ice*, F.D. Carsey (Ed.), Washington DC: American Geophysical Union, vol. 68, Ch. 3, 29-46.

Hanesiak, J. M., D. G. Barber, R. M. de Abreu, and J. J. Yackel (2001). Local and regional observations of Arctic first-year sea ice during melt ponding. *J. Geophys. Res.,* 106(C1), 1005–1016.

Hanson, A. M. (1965). Studies of the mass budget of Arctic pack-ice floes. *J. Glaciol.,* 5, 701– 709.

Herzfeld, U. C., E. C. Hunke, B. W. McDonald, and B. F. Wallin (2015). Sea ice deformation in Fram Strait — Comparison of CICE simulations with analysis and classification of airborne remote-sensing data. *Cold Reg. Sci. Tech.,* 117, 19-33.

Hibler, W. D., Ш (1972). Removal of aircraft altitude variation from laser profiles of the Arctic ice pack. *J. Geophys. Res., 77*(36), 7190-7195.

Hibler, W.D. III (1979). A dynamic thermodynamic sea ice model. *J. Phys. Oceanogr., 9*, 815-846.

Hohenegger, C., B. Alali, K. R. Steffen, D. K. Perovich, and K. M. Golden (2012). Transition in the fractal geometry of Arctic melt ponds. *Cryosphere,* 6(3), 2161-2177.

Holt, B., and S. A. Digby (1985). Processes and imagery of first-year fast sea ice during the melt season. *J. Geophys. Res.,* 90(C3), 5045–5062.

Hopkins, M.A. (1994). On the ridging of intact lead ice. *J. Geophys. Res., 99*(C8), 16351-16360.

Hopkins, M.A. (1998). Four stages of pressure ridging. *J. Geophys. Res., 103*, 21883-21891.

Howell, S. E. L., A. Tivy, J. J. Yackel, and R. K. Scharien (2006). Application of a SeaWinds/QuikSCAT sea ice melt algorithm for assessing melt dynamics in the Canadian Arctic Archipelago. *J. Geophys. Res., 111*, C07025.

Howell, S. E. L., C. R. Duguay, and T. Markus (2009). Sea ice conditions and melt season duration variability within the Canadian Arctic Archipelago: 1979–2008. *Geophys. Res. Lett., 36*, L10502.

Hudson, S. R., M. A. Granskog, A. Sundfjord, A. Randelhoff, A. H. H. Renner, and D. V. Divine (2013). Energy budget of first-year Arctic sea ice in advanced stages of melt. *Geophys. Res. Lett.*, 40, 2679–2683.

Hunke, E. C., and W. H. Lipscomb (2010). CICE: The Los Alamos sea ice model documentation and software user's manual version 4.1, *Rep.LA-CC-06–012*, T-3 Fluid Dyn. Group, Los Alamos Natl. Lab., Los Alamos, N. M.

Hunke, E. C., D.A. Hebert, and O. Lecomte (2013). Level-ice melt ponds in the Los Alamos sea ice model, CICE. *Ocean Model.*, 71, 26-42.

Iacozza, J. and D.G. Barber (1999). An examination of the distribution of snow on sea ice. *Atmos-Ocean*, 37(1), 21-51.

Iacozza, J. and D. Barber (2010). An examination of snow redistribution over smooth land-fast sea ice. *Hydrol. Process.,* 24(7), 850-865.

Isleifson, D., B. Hwang, D.G. Barber, R.K. Scharien, and L. Shafai (2010). C-band polarimetric backscattering signatures of newly formed sea ice during fall freeze-up, *Geo. Rem. Sens., IEEE Trans. on,* 48(8), 3256-3267.

Isleifson, D., R.J. Galley, D.G. Barber, J.C. Landy, A. S. Komarov, and L. Shafai (2014). A Study on the C-Band Polarimetric Scattering and Physical Characteristics of Frost Flowers on Experimental Sea Ice. *IEEE Trans. Geosci. Rem. Sens.,* 52(3), 1787-1798.

Jacobs, G. (2006). Understanding Spot Size for Laser Scanning. Professional Surveyor Magazine, October 2006.

Jester, W. and A. Klik (2005). Soil Surface Roughness Measurement - Methods, Applicability, and Surface Representation. *Catena,* 64, 174-192.

Jin, Y.-Q. (1993). *Electromagnetic Scattering Modelling for Quantitative Remote Sensing*, Singapore: World Scientific.

Karlsson, K. G., A. Riihelä, R. Müller, J. F. Meirink, J. Sedlar, M. Stengel, M. Lockhoff, and E. Wolters (2012). CLARA-A1: CM SAF Clouds, Albedo and Radiation dataset from AVHRR data - Edition 1 - Monthly Means / Daily Means / Pentad Means / Monthly Histograms. Satellite Application Facility on Climate Monitoring.

Kay, J. E., and A. Gettelman (2009). Cloud influence on and response to seasonal Arctic sea ice loss. *J. Geophys. Res.,* 114, D18204.

Kobayashi, D. (1987). Snow accumulation on a narrow board. *Cold Reg. Sci. Technol.,* 13(3), 239-245.

Komarov, A.S., L. Shafai, and D.G. Barber (2014). Electromagnetic wave scattering from rough boundaries interfacing inhomogeneous media and application to snow-covered sea ice. *Prog. Electromag. Res.*, 144, 201-219.

Kuchiki, K., T. Aoki, M. Niwano, H. Motoyoshi, and H. Iwabuchi (2011). Effect of sastrugi on snow bidirectional reflectance and its application to MODIS data. *J. Geophys. Res.,* 116, D18110.

Kurtz, N. T., T. Markus, D.J. Cavalieri, W. Krabill, J.G. Sonntag, and J. Miller (2008). Comparison of ICESat data with airborne laser altimeter measurements over Arctic sea ice. *IEEE Trans. Geosci. Rem. Sens.,* 46(7), 1913-1924.

Kwok, R. and D. Rothrock (2009). Decline in Arctic sea ice thickness from submarine and ICESat records: 1958–2008. *Geophys. Res. Lett*., 36(15), L15501.

Kwok, R., and D. Sulsky (2010). Arctic Ocean sea ice thickness and kinematics: Satellite retrievals and modelling. *Oceanography,* 23(4), 134-143.

Kwok, R., G. F. Cunningham, H. J. Zwally, and D. Yi (2006). ICESat over Arctic sea ice: Interpretation of altimetric and reflectivity profiles. *J. Geophys. Res.,* 111, C06006.

Kwok, R., G.F. Cunningham, H.J. Zwally, D. Yi, Ice (2007). Cloud, and land Elevation Satellite (ICESat) over Arctic sea ice: Retrieval of freeboard. *J. Geophys. Res.*, 112, C12013.

Kwok, R., T. Markus, J. Morison, S. P. Palm, T. A. Neumann, K. M. Brunt, W. B. Cook, D. W. Hancock, and G. F. Cunningham (2014). Profiling Sea Ice with a Multiple Altimeter Beam Experimental Lidar (MABEL). *J. Atmos. Oceanic Technol.,* 31, 1151–1168.

Landy, J. C., J. K. Ehn, M. Shields, and D. G. Barber (2014). Surface and melt pond evolution on landfast first-year sea ice in the Canadian Arctic Archipelago. *J. Geophys. Res.,* 119, 3054–3075.

Landy, J. C., D. Isleifson, A. S. Komarov, and D. G. Barber (2015a). Parameterization of centimeter-scale sea ice surface roughness using terrestrial LiDAR, *IEE Trans. Geosci. Rem. Sens.,* 53(3), 1271-1286.

Landy, J. C., A. S. Komarov, and D. G. Barber (2015b). Numerical and experimental evaluation of terrestrial LiDAR for parameterizing centimeter-scale sea ice surface roughness. *IEEE Trans. Geosci. Rem. Sens.*, 53(9), 4887-4898.

Laxon S. W., K. A. Giles, A. L. Ridout, D. J. Wingham, R. Willatt, R. Cullen, R. Kwok, A. Schweiger, J. Zhang, C. Haas, S. Hendricks, R. Krishfield, N. Kurtz, S. Farrell and M. Davidson (2013). CryoSat-2 estimates of Arctic sea ice thickness and volume. *Geophys. Res. Lett.,* 40, 732–737.

Leica Geosystems (2009). Leica Scanstation C10 Product Specifications. Heerbrugg, Switzerland: Leica Geosystems.

Leica Geosystems (2013). Leica Scanstation P20 Product Specifications. Heerbrugg, Switzerland: Lecia Geosystems.

Leppäranta, M. (2011). *The Drift of Sea Ice*. 2nd ed., 347 pp., Springer, Berlin.

Leppäranta, M. and T. Manninen (1988). The brine and gas content of sea ice with attention to low salinities and high temperatures, Finnish Inst. Marine Res., Internal Report 88-2, Helsinki.

Lettau, H. (1969). Note on aerodynamic roughness-parameter estimation on the basis of roughness element description. *J. Appl. Meteorol*., 8(5), 828– 832.

Li, L. and J. W. Pomeroy (1997). Estimates of threshold wind speeds for snow transport using meteorological data. *J. Appl. Meteorol.,* 36(3), 205-213.

Lichti, D.D., and S. Jamtsho, S. (2006). Angular resolution of terrestrial laser scanners. *Polarimet. Rec.*, 21(114), 141-160.

Light, B., G. A. Maykut, and T. C. Grenfell (2003). Effects of temperature on the microstructure of first-year Arctic sea ice, *J. Geophys. Res.,* 108(C2), 3051.

Light, B., G. A. Maykut, and T. C. Grenfell (2004). A temperature-dependent, structural-optical model of first-year sea ice. *J. Geophys. Res.,* 109, C06013.

Lin, T., L. Blunt, and K. Stout (1993). Determination of proper frequency bandwidth for 3D topography measurement using spectral analysis, Part I: isotropic surfaces. *Wear*, 166, 221-232.

Lindsay, R. W., and J. Zhang (2005). The Thinning of Arctic Sea Ice, 1988–2003: Have We Passed a Tipping Point?, *J. Climate*, 18, 4879-4894.

Lindsay, R. W., and J. Zhang (2006). Assimilation of ice concentration in an ice–ocean model. *J. Atmos. Oceanic Technol.*, 23, 742-749.

Lindsay, R., J. Zhang, A. Schweiger, M. Steele, and H. Stern (2009). Arctic sea ice retreat in 2007 follows thinning trend. *J. Clim.,* 22(1), 165-176.

Lipscomb, W. H. (2001). Remapping the thickness distribution in sea ice models. *J. Geophys. Res., 106*(C7), 13989–14000.

Lipscomb, W. H., E. C. Hunke, W. Maslowski, and J. Jakacki (2007). Ridging, strength, and stability in high-resolution sea ice models, *J. Geophys. Res., 112*, C03S91.

Liu, C., J. Chao, W. Gu, W., L. Li, and Y. Xu (2014). On the surface roughness characteristics of the land fast sea-ice in the Bohai Sea. *Acta Oceanol. Sin.,* 33, 97-106.

Lüthje, M., D. L. Feltham, P. D. Taylor, and M. G. Worster (2006). Modeling the summertime evolution of sea-ice melt ponds*, J. Geophys. Res., 111*, C02001.

Manes, C., M. Guala, H. Löwe, S. Bartlett, L. Egli, and M. Lehning (2008). Statistical properties of fresh snow roughness. *Water Resour. Res.,* 44, W11407.

Manninen, A. T. (1997). Surface roughness of Baltic sea ice. *J. Geophys. Res.*, 102(C1), 1119-1139.

Markus, T., J. C. Stroeve, and J. Miller (2009). Recent changes in Arctic sea ice melt onset, freezeup, and melt season length. *J. Geophys. Res., 114*, C12024.

Martin, S. and P. Kauffman (1981). A field and laboratory study of wave damping by grease ice. *J. Glaciol.,* 27(96), 283-313.

Martin, S., Y. Yu, and R. Drucker (1996). The temperature dependence of frost flower growth on laboratory sea ice and the effect of the flowers on infrared observations of the surface. *J. Geophys. Res.,* 101(C5), 12111-12125.

Maslanik, J., J. Stroeve, C. Fowler, W. Emery (2001). Distribution and trends in Arctic sea ice age through spring 2011. *Geophys. Res. Lett.*, 38, L13502.

Massom, R.A., M.R. Drinkwater and C. Haas (1997). Winter snow cover on sea ice in the Weddell Sea. *J. Geophys. Res.*, 102(C1), 1101-1117.

Massom, R. A., H. Eicken, C. Hass, M. O. Jeffries, M. R. Drinkwater, M. Sturm, A. P. Worby, X. Wu, V. I. Lytle, and S. Ushio (2001). Snow on Antarctic sea ice. *Rev. Geophys.*, 39(3), 413-445.

Mathia, T. G., P. Pawlus, and M. Wieczorowski (2011). Recent trends in surface metrology. *Wear,* 271, 494-508.

Mattia, F., and T. LeToan (1999). Backscattering properties of multi-scale rough surfaces. *J. Electro. Wave. App.*, 13, 491-526.

Mattia, F., M. W. J. Davidson, T. LeToan, C. M. F. D'Haese, N. E. C. Verhoest, A. M. Gatti, and M. Borgeaud (2003). A comparison between soil roughness statistics used in surface scattering models derived from mechanical and laser profilers. *IEE Trans. Geosci. Rem. Sens.,* 41, 1659-1671.

Mätzler, C. and U. Wegmuller, (1987). Dielectric properties of fresh-water ice at microwave frequencies. *J. Phys. D: Appl. Phys.,* 20, 1623-1630.

Maykut, G. A. and T. C. Grenfell (1975). The spectral distribution of light beneath first-year sea ice in the Arctic Ocean. *Limnol. Oceanogr.*, 20, 554-563.

Nassar, E. (1997). Numerical and Experimental Studies of Electromagnetic Scattering from Sea Ice. PhD Thesis, Ohio State University.

Nghiem, S., R. Kwok, S. Yueh, and M. Drinkwater (1995). Polarimetric signatures of sea ice 2: Experimental observations. *J. Geophys. Res.*, 100(C7), 13681-13698.

Nicolaus, M., S. Gerland, S. R. Hudson, S. Hanson, J. Haapala, and D. K. Perovich (2010). Seasonality of spectral albedo and transmittance as observed in the Arctic Transpolar Drift in 2007. *J. Geophys. Res., 115*, C11011.

Nicolaus, M., C. Katlein, J. Maslanik, and S. Hendricks (2012). Changes in Arctic sea ice result in increasing light transmittance and absorption. *Geophys. Res. Lett., 39*, L24501.

Niedrauer, T. M. and S. Martin (1979). An experimental study of brine drainage and convection in young sea ice. *J. Geophys. Res.,* 84, 8C1208, 1176–1186.

Nishimoto, M. (2010). Characteristics of Rough Surface Parameters Estimated from Measured Surface Profile of Finite Length. Proceedings IGARSS July 2010, Honolulu, Hawaii, 4436-4439.

Notz, D., and M. G. Worster (2009). Desalination processes of sea ice revisited. *J. Geophys. Res.*, 114, C05006.

Notz, D., M. G. McPhee, M. G. Worster, G. A. Maykut, K. H. Schlünzen, and H. Eicken (2003). Impact of underwater-ice evolution on Arctic summer sea ice. *J. Geophys. Res.,* 108(C7), 3223.

Ogilvy, J. A. (1991), *Theory of wave scattering from random rough surfaces*. New York, USA: A. Hilger.

Ogilvy, J. and J. Foster (1989). Rough surfaces: Gaussian or exponential statistics? *J. Phys. D*: *Applied Phys.*, 22(9), 1243.

Oh, Y. and Y. C. Kay (1998). Condition for precise measurement of soil surface roughness. *IEE Trans. Geosci. Rem. Sens.,* 36(2), 691-695.

Oh, Y., and Y. Kay (1998). Condition for Precise Measurement of Soil Surface Roughness. *IEEE Trans. Geosci. Rem. Sens.*, 36(2), 691-695.

Oke, T.R. (1987). *Boundary layer climates*. London: Routledge.

Ono, N. (1967). Specific heat and heat of fusion of sea ice. In: *Physics of snow and ice 1*, H. Oura (Ed.), 599-610, Inst. Low Temp. Sci., Hokkaido, Japan.

Onstott, R.G. (1992). SAR and Scatterometer Signatures of Sea Ice. In: *Microwave Remote Sensing of Sea Ice*, F. Carsey (Ed.), Washington DC: American Geophysical Union, vol. 68, Ch. 5, 73-104.

Optech Inc. (2015). ILRIS Terrestrial Laser Scanner Datasheet. Canada: Optech Inc.

Paterson, J., B. Brisco, S. Argus, and G. Jones (1991). In situ measurements of micro-scale surface roughness of sea ice. *Arctic*, 44(5), 140-146.

Pedersen, C. A., E. Roeckner, M. Lüthje, and J. Winther (2009). A new sea ice albedo scheme including melt ponds for ECHAM5 general circulation model. *J. Geophys. Res., 114*, D08101.

Perez-Gutierrez, C., J. Alvarez-Mozos, J. Martínez-Fernández, and N. Sanchez (2010). Comparison of a multilateral-based acquisition with Terrestrial Laser Scanner and profilometer technique for soil roughness measurement. Proceedings IGARSS July 2010, Honolulu, Hawaii, 2988-2991.

Perovich, D. (1994). Light reflection from sea ice during the onset of melt. *J. Geophys. Res.*, 99(C2), 3351-3359.

Perovich, D. K. (1996). *The Optical Properties of Sea Ice.* CRREL Monograph Series, 96-1.

Perovich, D. (1998). Observations of the polarization of light reflected from sea ice. *J. Geophys. Res.*, 103(C3), 5563-5575.

Perovich, D.K. and J.A. Richter-Menge (1994). Surface characteristics of lead ice. *J. Geophys. Res., 99*(C8), 16341-16350.

Perovich, D. K. and A. J. Gow (1996). A quantitative description of sea ice inclusions. *J. Geophys. Res.,* 101(C8), 18327-18343.

Perovich, D. K., and C. Polashenski (2012). Albedo evolution of seasonal Arctic sea ice. *Geophys. Res. Lett.,* 39, L08501.

Perovich, D. K., T. C. Grenfell, B. Light, and P. V. Hobbs (2002a). Seasonal evolution of the albedo of multiyear Arctic sea ice, *J. Geophys. Res., 107*(C10), 8044.

Perovich, D. K., W. B. Tucker III, and K. A. Ligett (2002b). Aerial observations of the evolution of ice surface conditions during summer. *J. Geophys. Res.,* 107(C10), 8048.

Perovich, D. K., T. C. Grenfell, J. A. Richter-Menge, B. Light, W. B. Tucker, and H. Eicken (2003). Thin and thinner: Sea ice mass balance measurements during SHEBA. *J. Geophys. Res.,* 108(C3), 8050.

Perovich, D. K., J. A. Richter-Menge, K. F. Jones, B. Light (2008). Sunlight, water, and ice: Extreme Arctic sea ice melt during the summer of 2007. *Geophys. Res. Lett.*, 35, L11501.

Perovich, D. K., T. C. Grenfell, B. Light, B. C. Elder, J. Harbeck, C. Polashenski, W. B. Tucker III, and C. Stelmach (2009). Transpolar observations of the morphological properties of Arctic sea ice. *J. Geophys. Res.*, 114, C00A04.

Persson, P. O. G. (2012). Onset and end of the summer melt season over sea ice: thermal structure and surface energy perspective from SHEBA. *Clim. Dyn.*, 39(6), 1349-1371.

Persson, P. O. G., C. W. Fairall, E. L. Andreas, P. S. Guest, and D. K. Perovich (2002). Measurements near the Atmospheric Surface Flux Group tower at SHEBA: Near-surface conditions and surface energy budget. *J. Geophys. Res.,* 107(C10), 8045.

Pesci, A., G. Teza, and E. Bonali (2011). Terrestrial Laser Scanner Resolution: Numerical Simulations and Experiments on Spatial Sampling Optimization. *Rem. Sens.*, 3, 167-184.

Petrich, C., and H. Eiken (2010). Growth, Structure and Properties of Sea Ice. In: *Sea Ice: An Introduction to its Physics, Chemistry, Biology and Geology*, D.N. Thomas and G.S. Dieckmann (Eds.), Blackwell Science Ltd., Oxford, UK., 22-81.

Petrich, C., H. Eicken, C. M. Polashenski, M. Sturm, J. P. Harbeck, D. K. Perovich, and D. C. Finnegan (2012). Snow dunes: A controlling factor of melt pond distribution on Arctic sea ice. *J. Geophys. Res.,* 117, C09029.

Petrie, G., and C. K. Toth (2008). Introduction to laser ranging, profiling, and scanning. In: *Topographic Laser Ranging and Scanning: Principles and Processing*, Shan, J. and Toth, C. K. (Eds.), 1-28, Ch. 1, CRC Press, Taylor & Francis.

Pfeifer, N., and G. Mandlburger (2008). LiDAR Data Filtering and DTM Generation. In: *Topographic Laser Ranging and Scanning: Principles and Processing*, Shan, J. and Toth, C. K. (Eds.), 307-333, Ch. 11, CRC Press, Taylor & Francis.

Podgorny, I. A., and T. C. Grenfell (1996). Partitioning of solar energy in melt ponds from measurements of pond albedo and depth. *J. Geophys. Res.*, 101, 22737-22748.

Polashenski, C. M., D. K. Perovich, and Z. Courville (2012). The mechanisms of sea ice melt pond formation and evolution. *J. Geophys. Res.,* 117, C01001.

Polashenski et al 2015…

Pollyea, R., and J. P. Fairley (2011). Estimating surface roughness of terrestrial laser scan data using orthogonal distance regression. *Geol.*, 39(7), 623-626.

Pollyea, R., and J. P. Fairley (2012). Experimental evaluation of terrestrial LiDAR-based surface roughness estimates. *Geosphere*, 8(1), 222-228.

Pringle, D. J., H. Eicken, H. J. Trodahl, and L. G. E. Backstrom (2007). Thermal conductivity of landfast Antarctic and Arctic sea ice. *J. Geophys. Res.*, 112, C04017.

Prokop, A. (2008). Assessing the applicability of terrestrial laser scanning for spatial snow depth measurements. *Cold. Reg. Sci. Tech.,* 54(3), 155-163.

Rees, W., and N. Arnold (2006). Scale-dependent roughness of a glacier surface: implications for radar backscatter and aerodynamic roughness modelling. *J. Glaciol.*, 52(177), 214-222.

Renganathan, V. (2010). Arctic Sea Ice Freeboard Heights from Satellite Altimetry. Ph.D. Thesis, University of Calgary, UCGE 20301.

Riegl Systems (2014). Riegl VZ-400 Datasheet. Horn, Austria: Riegl Laser Measurement Systems.

Rivas, M. B., J.A. Maslanik, J.G. Sonntag, and P. Axelrad (2006). Sea ice roughness from airborne LIDAR profiles. *IEEE Trans. Geosci. Rem. Sens,* 44(11), 3032-3037.

Rösel, A., and L. Kaleschke (2012). Exceptional melt pond occurrence in the years 2007 and 2011 on the Arctic sea ice revealed from MODIS satellite data. *J. Geophys. Res., 117*, C05018.

Rösel, A., L. Kaleschke, and G. Birnbaum (2012). Melt ponds on Arctic sea ice determined from MODIS satellite data using an artificial neural network. *Cryosphere*, 6, 431-446.

Sankelo, P., J. Haapala, I. Heiler, and E. Rinne (2010). Melt pond formation and temporal evolution at the drifting station Tara during summer 2007. *Polar Res., 29*, 311-321.

Scharien, R. K., and J. J. Yackel (2005). Analysis of surface roughness and morphology of first-year sea ice melt ponds: Implications for microwave scattering. *IEEE Trans. Geosci. Remote Sens.,* 43, 2927.

Scharien, R. K., J. C. Landy, and D.G. Barber (2014). First-year sea ice melt pond fraction estimation from dual-polarisation C-band SAR–Part 1: In situ observations. *Cryosphere*, 8(6), 2147-2162.

Schmidt, R.A. (1980). Threshold wind-speeds and elastic impact in snow transport. *J. Glaciol.*, 26, 453-467.

Schröder, D., D.L. Feltham, D. Flocco, and M. Tsamados (2014). September Arctic sea-ice minimum predicted by spring melt-pond fraction, *Nature Clim. Change,* 4*,* 353-357.

Schweiger, A., R. Lindsay, J. Zhang, M. Steele, H. Stern, and R. Kwok (2011). Uncertainty in modeled Arctic sea ice volume. *J. Geophys. Res.,* 116, C00D06.

Schwerdtfeger, P. (1963). The thermal properties of sea ice. *J. Glaciol.*, *4*(36), 789-807.

Scott, F., and D. L. Feltham (2010). A model of the three-dimensional evolution of Arctic melt ponds on first-year and multi-year sea ice. *J. Geophys. Res.,* 115, C12064.

Serreze, M. C., M. M. Holland, and J. Stroeve (2007). Perspectives on the Arctic's shrinking sea-ice cover. *Science*, 315, 1533.

Sheng, Y. (2008). Quantifying the size of a Lidar footprint: A set of generalized equations. *IEEE Geosci. Rem. Sens. Lett.*, 5(3), 419-422.

Shields et al Submitted.

Sithole, G., and G. Vosselman (2004). Experimental comparison of filter algorithms for bare-Earth extraction from airborne laser scanning point clouds. *J. Photogramm. Rem. Sens.*, 59(1), 85-101.

Skyllingstad, E. D., and C. A. Paulson (2007). A numerical study of melt ponds. *J. Geophys. Res., 112*, C08015.

Skyllingstad, E. D., C. A. Paulson, and D. K. Perovich (2009). Simulation of melt pond evolution on level ice. *J. Geophys. Res., 114*, C12019.

Smith, S.L., D.A. Holland, and P.A. Longley (2005). Quantifying interpolation errors in urban airborne laser scanning models. *Geog. Analysis*, 37, 200-224.

Sommerfeld, R. A. and E. LaChapelle (1970). The classification of snow metamorphism. *J. Glaciol.*, 9, 3–17.

Sorensen, L., B. Jensen, R. Glud, D. McGinnis, M. Sejr, J. Sievers, J., and S. Rysgaard (2014). Parameterization of atmosphere-surface exchange of CO2 over sea ice. *Cryosphere*, 8, 853-866.

Sozzi, R., M. Favaron, and T. Georgiadis (1998). Method for estimation of surface roughness and similarity function of the wind speed vertical profile. *J. Appl. Meteor.*, 37, 461-469.

Stanton, T. P., W. J. Shaw, and J. K. Hutchings (2012). Observational study of relationships between incoming radiation, open water fraction, and ocean-to-ice heat flux in the Transpolar Drift: 2002–2010. *J. Geophys. Res., 117*, C07005.

Stogryn, A. and G. D. Desargant (1985). The dielectric properties of brine in sea ice at microwave frequencies. *IEEE Trans. Antennas Propag.,* 33(5), 523-532.

Stroeve, J. C., M. M. Holland, W. Meier, T. Scambos, and M. Serreze (2007). Arctic sea ice decline: Faster than forecast. *Geophys. Res. Lett.*, 34, L09501.

Stroeve, J. C., M. C. Serreze, M. M. Holland, J. E. Kay, J. Malanik, and A. P. Barrett (2012). The Arctic’s rapidly shrinking sea ice cover: a research synthesis. *Clim. Change*, 110(3-4), 1005-1027.

Stroeve, J. C., T. Markus, L. Boisvert, J. Miller, and A. Barrett (2014). Changes in Arctic melt season and implications for sea ice loss. *Geophys. Res. Lett.,* 41, 1216–1225.

Sturm, M., and C.S. Benson (1997). Vapor transport, grain growth and depth-hoar development in the subarctic snow. *J. Glaciol.*, 43(143), 42-59.

Sturm, M., J. Holmgren, and D. K. Perovich (2002). Winter snow cover on the sea ice of the Arctic Ocean at the Surface Heat Budget of the Arctic Ocean (SHEBA): Temporal evolution and spatial variability. *J. Geophys. Res.*, 107(C10), 8047.

Style, R.W. and M.G. Worster (2009). Frost flower formation on sea ice and lake ice. *Geophys. Res. Lett.,* 36(11), 16341-16350.

Swift, C., K. St. Germain, K. Jezek, S. Gogineni, A. Gow, D. K. Perovich, R. Onstott (1992). Laboratory Investigations of the Electromagnetic Properties of Artificial Sea Ice. In: *Microwave Remote Sensing of Sea Ice*, 177-200, Ch. 9, American Geophysical Union.

Tan, B., Z. Li, P. Lu, C. Haas, and M. Nicolaus (2012). Morphology of sea ice pressure ridges in the northwestern Weddell Sea in winter. *J. Geophys. Res., 117*, C06024.

Taylor, P. D., and D. L. Feltham (2004). A model of melt pond evolution on sea ice. *J. Geophys. Res.,* 109, C12007.

Thorndike, A.S., D.A. Rothrock, G.A. Maykut and R. Colony (1975). The thickness distribution of sea ice. *J. Geophys. Res., 80*(33), 4501-4513.

Tsang, L., J. Kong, and K.-H. Ding (2000). *Scattering of Electromagnetic Waves: Theories and Applications*. New York, NY, USA: Wiley.

Tschudi, M. A., J.A. Maslanik, and D.K. Perovich (2008). Derivation of melt pond coverage on Arctic sea ice using MODIS observations. *Rem. Sens. Environ., 112*, 2605–2614.

Ulaby, F., R. Moore and A. Fung (1990). *Microwave Remote Sensing: Active and Passive*, vol. II, Boston, MA, USA: Artech House.

Vancoppenolle, M., C. M. Bitz, and T. Fichefet (2007). Summer landfast sea ice desalination at Point Barrow, Alaska: Modeling and observations. *J. Geophys. Res.*, 112, C04022.

Verhoest, N. E., H. Lievens, W. Wagner, J. Álvarez-Mozos, M. S. Moran, and F. Mattia (2008). On the soil roughness parameterization problem in soil moisture retrieval of bare surfaces from synthetic aperture radar. *Sensors*, 8(7), 4213-4248.

Vosselman, G. (2000). Slope based filtering of laser altimetry data. *Int. Arch. Photogramm. Rem. Sens.,* 33(B3), 935-942.

Wadhams, P. (1980). A comparison of sonar and laser profiles along corresponding tracks in the Arctic Ocean. In: *Sea Ice Processes and Models*, R. S. Pritchard (Ed.), 283–299, Univ. of Wash. Press, Seattle, Washington.

Wadhams, P. (1994). Sea ice thickness changes and their relation to climate. In: *The Polar Oceans and Their Role in Shaping the Global Environment*. O.M . Johannessen, R.D. Muench and J.E. Overland (Eds.), 337-362, American Geophysical Union, Washington, DC. Geophysical Monograph 85.

Wadhams, P. (2000). *Ice in the ocean*. London: Gordon and Breach Science.

Wadhams, P., M. A. Lange, and S. F. Ackley (1987). The ice thickness distribution across the Atlantic sector of the Antarctic Ocean in midwinter. *J. Geophys. Res.,* 92(C13).

Wang, M., and J.E. Overland (2009). A sea ice free summer Arctic within 30 years? *Geophys. Res. Lett.*, 36, L07502.

Wang, S., A. P. Trishchenko, K. V. Khlopenkov, and A. Davidson (2006). Comparison of International Panel on Climate Change Fourth Assessment Report climate model simulations of surface albedo with satellite products over northern latitudes. *J. Geophys. Res.,* 111, D21108.

Warner, W. (1995). Mapping a three-dimensional soil surface with handheld 35 mm photography. *Soil Till. Res.*, 34, 187-197.

Weeks, W. F. (1998). Growth conditions and the structure and properties of sea ice. In: *Physics of Ice-Covered Seas*, M. Leppäranta (Ed.), vol. 1, 25-104, Helsinki University Press, Helsinki.

Weeks, W.F. and J.S. Wettlaufer (1996). Crystal orientations in floating ice sheets. In: *The Johannes Weertman Symposium*. R.J. Arsenault, D. Cole, T. Gross, G. Kostorz, P.K. Liaw, S. Parameswaran and H. Sizek (Eds.), 337–350. The Minerals, Metals and Materials Society, Warrendale, Pennsylvania.

Wehr, A., and U. Lohr (1999). Airborne laser scanning - an introduction and overview. *J. Photogramm. Rem. Sens.,* 54(2), 68-82.

Weichel, H. (1990). *Laser Beam Propagation in the Atmosphere*, vol. 3, Washington, USA: SPIE Press.

Wilchinsky, A. V., and D.L. Feltham (2012). Rheology of discrete failure regimes of anisotropic sea ice. *J. Phys. Ocean.,* 42(7), 1065-1082.

Winebrennerm D.P. et al. (1992). Microwave Sea Ice Signature Modeling. In: *Microwave Remote Sensing of Sea Ice*. F. Carsey (Ed.), Washington DC: American Geophysical Union, vol. 68, ch. 8, 137-175.

Wohl, G.M. (1995). Operational sea ice classification from synthetic aperture radar imagery. *Photogramm. Eng. Remote Sens.,* 61, 1455–1462.

World Meteorological Organization (2010). WMO Sea Ice Nomenclature, WMO/DMM/BMO 259-TP-145, Secretariat of the WMO, Geneva.

Wozencraft, J., and D. Millar (2005). Airborne lidar and integrated technologies for coastal mapping and nautical charting. *Mar. Tech. Soc. J.*, 39(3), 27-35.

Wright, B., J. Hnatiuk, and A. Kovacs (1978). Sea ice pressure ridges in the Beaufort Sea. *Proceedings of IAHR Ice Symposium,* Lulea, Sweden.

Wu, A., Z. Li, and J. Cihlar (1995). Effects of land cover type and greenness on advanced very high resolution radiometer bidirectional reflectances: Analysis and removal. *J. Geophys. Res.,* 100, 9179-9192.

Zege, E., A. Malinka, I. Katsev, A. Prikhach, G. Heygster, L. Istomina, L., G. Birnbaum, and P. Schwarz (2015). Algorithm to retrieve the melt pond fraction and the spectral albedo of Arctic summer ice from satellite optical data. *Rem. Sens. Env.*, 163, 153-164.

Zhang, J., and D.A. Rothrock (2003). Modeling Global Sea Ice with a Thickness and Enthalpy Distribution Model in Generalized Curvilinear Coordinates. *Mon. Wea. Rev.*, 131, 845–861.

Zhang, J., R. Lindsay, M. Steele, and A. Schweiger (2008). What drove the dramatic retreat of arctic sea ice during summer 2007? *Geophys. Res. Lett.*, 35, L11505.

Zhang, X., J. E. Walsh, J. Zhang, U. Bhatt, and M. Ikeda (2004). Climatology and interannual variability of Arctic cyclone activity, 1948–2002. *J. Clim.,* 17, 2300–2317.